# Cool Flames!
# Radical Reactions in Biofuels
# and the Atmosphere

Fiona Christine Whiting

PhD
University of York
Chemistry
October 2018

# Abstract

A novel apparatus for pulsed laser photolysis generation of radicals coupled with laser induced fluorescence (LIF) detection of OH has been developed at the University of York, enabling kinetic studies of atmospheric and combustion-relevant chemical reactions.

Direct LIF detection was used to identify unambiguously OH as a product of $O_2$ + RCO reactions, for the first time, where R = $CH_3CH_2CH_2$, $(CH_3)_2CH$, $(CH_3)_3C$, $CH_3CH_2CH_2CH_2$, $(CH_3)_2CHCH_2$, and $CH_3CH_2CH(CH_3)$. Pressure- dependent (13 - 120 Torr) OH yields were determined by comparison of time-resolved OH LIF profiles with those obtained from the well-characterised $CH_3CO + O_2 \rightarrow OH$ reaction. Results not only illustrate the dependency of OH yield on chain length and degree of branching within the R group, but also resolve a literature discrepancy for $CH_3CH_2CO + O_2$ .

OH produced from RCO + $O_2$ was used as a spectroscopic marker to study the kinetics of Cl + RCHO. This indirect method produced the first values for Cl + $(CH_3)_2CHCH_2CHO$ (($3.1 \pm 0.6$) $\times 10^{-10}$ $cm^3$ molecule$^{-1}$ s$^{-1}$) and $CH_3CH_2CH(CH_3)$ CHO (($1.2 \pm 0.3$) $\times 10^{-10}$ $cm^3$ molecule$^{-1}$ s$^{-1}$) at 298 K, with results for other Cl + RCHO and OH + RCHO reactions agreeing well with previous literature.

Finally, the reactions of $RC(O)O_2$ with $HO_2$ were investigated at temperatures between 293 and 400 K. Preliminary experiments in the absence of $HO_2$ recorded OH production from a previously unknown source, potentially $RC(O)O_2 + RC(O)O_2$. OH production from $RC(O)O_2 + HO_2$, identified for the first time when R = $CH_3CH_2$, $(CH_3)_2CH$, $(CH_3)_3C$, $(CH_3)_2CHCH_2$, and $CH_3CH_2CH(CH_3)$, demonstrates that significant OH production is a general feature of $HO_2 + RC(O)O_2$ reactions.

# Acknowledgements

First and foremost, I would like to give a massive thanks to my supervisor Dr. Terry Dillon, for his support and enthusiasm throughout this whole process. Thanks also to Dr. Derek Wann for his advice and supervision throughout the last three years. Thank you to Dr. Jacqui Hamilton and Dr. Richard Lidster who encouraged and first introduced me to the research world during my MChem. Also a big thank you to Prof. Paul Walton for all the support he has given me throughout the seven years I have been at York.

I would like to express my immense gratitude to Andy Goddard and Mark Blitz for all their help with LabVIEW, and also to Abby, Stuart, Chris, and Tim from workshops in the department, without whom this work would not have been possible.

I have been very fortunate to have met some wonderful people during my time at York. A special thank you to all the people in the Phys Chem office including Conor, Pedro, Tomas, Natalie, Rosaria, and Michi who helped to keep me sane during long experimental days.

Further thanks go to the University of York Swimming and Waterpolo Club for providing a fun life outside academia. There are far too many of you to mention individually but a special thank you to Becky, Harriet, Beth, Jacob, and last but not least Simon.

I am grateful to the Engineering and Physical Sciences Research Council (EPSRC) for funding my studentship.

Lastly, I would like to thank my family for their love, support and generosity; also Darwin who was always there for me.

# List of Accompanying Material

The appendices relating to the work presented in this thesis contain various codes and hundreds of plots. Therefore, they are presented in electronic format, as a CD attached to the back cover of this book.

Appendix A – Codes for Experimental Development and Analysis.

Appendix B – Chapter 3 Supplementary Data

Appendix C – Chapter 4 Supplementary Data

Appendix D – Chapter 6 Supplementary Data

# Declaration

I declare that this thesis is a presentation of original work and I am the sole author. This work has not previously been presented for an award at this, or any other, University. All sources are acknowledged as References.

'Two things are infinite: the universe and human stupidity; and I'm not sure about the universe.'

*Albert Einstein*

x

# Contents

# List of Tables

# List of Figures

6.28 Data from the experimental runs of $CH_3C(O)O_2 + DO_2$ (black diamonds), $C_2H_5C(O)O_2 + DO_2$ (red diamonds) and $(CH_3)_2CHCH_2C(O)O_2 + DO_2$ (blue circles) at 100 Torr and 360 K. The concentrations (in molecule $cm^{-3}$) were: $[RCHO] = 7 \times 10^{14}$, $[Cl_2] = 4 \times 10^{15}$, $[Cl] \approx 6 \times 10^{13}$, $[N_2] = 2 \times 10^{18}$, $[CD_3OD] = 2.0 \times 10^{15}$ and $[O_2] = 2.1 \times 10^{17}$.201

# Chapter 1

# Introduction

## 1.1 Atmospheric Chemistry

Earth's atmosphere is crucial for its ability to sustain life. Held close by gravitational interactions, it is constantly changing due to both dynamic processes and chemical reactions. Though transparent to the naked eye, the atmosphere can be classified into different layers, each having its own characteristic vertical temperature gradient (Finlayson-Pitts and James 1999). The troposphere, from the Greek word *tropos* meaning to turn or change, is the lowest layer of the atmosphere, stretching out from Earth's surface to an altitude of 17 km. Though the troposphere only reaches an altitude of 17 km it contains 85-90% of the atmosphere's mass, where the majority of the phenomena associated with weather and climate change occurs (Finlayson-Pitts and James 1999). This is the part of the atmosphere which has the most interest and where the reactions studied in this project occur.

The Earth's atmosphere is primarily composed of the gases $N_2$ (78%), $O_2$ (21%), and Ar (1%); however, the trace gases which represent less than 1% of the atmosphere play a crucial role in the atmosphere. $H_2O$, $CO_2$, $NO_x$ (nitrogen oxides) and VOCs (volatile organic compounds) are examples of trace gases which have a direct impact

on climate change and human health. Since 1975 instrumentation innovations have enabled the very sensitive identification of atmospheric trace species at levels of $10^{-12}$ parts per air – in other words 1 pptv by volume. This has allowed investigations to help understand the role of trace gases – not only their chemical reactions but also for the atmosphere's radiative balance (Seinfeld and Pandis 2006).

Trace species such $CO_2$ and $H_2O$ are key greenhouse gases. The Earth receives (on average) an energy of $1.74 \times 10^{17}$ J every second from the sun, and the atmosphere is responsible for moderating this energy to keep the climate stable (Finlayson-Pitts and James 1999). Half of this solar radiation is absorbed by the Earth's surface, 30% is reflected back out of Earth's atmosphere, with the remaining 20% absorbed by gas molecules within the atmosphere – this process mainly occurring in the troposphere. $CO_2$ and $H_2O$ are among the gas molecules that absorb solar radiation, in turn creating excited molecules with higher energy. These molecules then either emit long-wave radiation or transfer the surplus energy via collisions – this phenomenon is known as the greenhouse effect.

The hydroxyl radical, OH, is another trace gas. Though only present in small concentrations, it controls the majority of the atmosphere's oxidative chemistry (Atkinson 2000). It is crucial and has often been called the 'detergent of the atmosphere' (Riedel and Lassey 2008). The high reactivity of OH and short lifetime (less than a second) meant that the earliest recognition of its central role in the atmosphere, came less than five decades ago (Levy 1971). However, the importance of OH cannot be overstated as many trace gas species' lifetimes are solely dependent on their reactivity towards OH, with approximately 3.7 Gt of trace gases destroyed by OH each year (Forster et al. 2007).

Primary OH is formed in the troposphere by photolysis of $O_3$ which forms an O atom in an excited singlet state that goes on to react with water vapour (Reactions 1.1 and 1.2) (Talukdar et al. 1998).

$$O_3 + h\nu(\lambda < 330nm) \rightarrow O(^1D) + O_2 \tag{1.1}$$

$$O(^1D) + H_2O \rightarrow 2OH \tag{1.2}$$
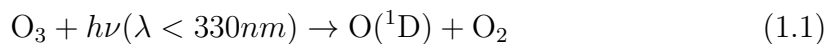
OH is closely coupled with the hydroperoxy radical ($HO_2$), two common reactions between $HO_2$ and OH are shown below (Reaction 1.3 and 1.4). Often collectively termed $HO_x$ radicals due to their close relationship, they are responsible for the oxidation of the majority of volatile organic compounds (VOCs) present in the atmosphere (Jacob 1999).

$$HO_2 + NO \rightarrow OH + NO_2 \tag{1.3}$$

$$CO + OH \xrightarrow{O_2} CO_2 + HO_2 \tag{1.4}$$

OH is key in the tropospheric oxidation of hydrocarbons, including the oxidation of CO (Reaction 1.4) which recycles $HO_2$ and the oxidation of methane (Reaction 1.5). Methane oxidation leads to the formation of methylperoxy radicals (Reactions 1.5 and 1.6) (Finlayson-Pitts and James 1999).

$$CH_4 + OH \rightarrow CH_3 + H_2O \tag{1.5}$$

$$CH_3 + O_2 + M \rightarrow CH_3O_2 + M \tag{1.6}$$

This oxidation process is the main route to the formation of peroxy radicals ($RO_2$) from hydrocarbons in the atmosphere (Figure 1.1). Once formed $RO_2$ has two main destruction pathways: the route it takes depends on the other species in that part of the atmosphere – whether it is in a clean or dirty environment. A dirty environment relates to an environment which has high concentration of NO, formed primarily by the combustion of fuels. Therefore a major city is an example of where a high [NO] environment would be found. $RO_2$ reacts rapidly with NO, forming $NO_2$ and
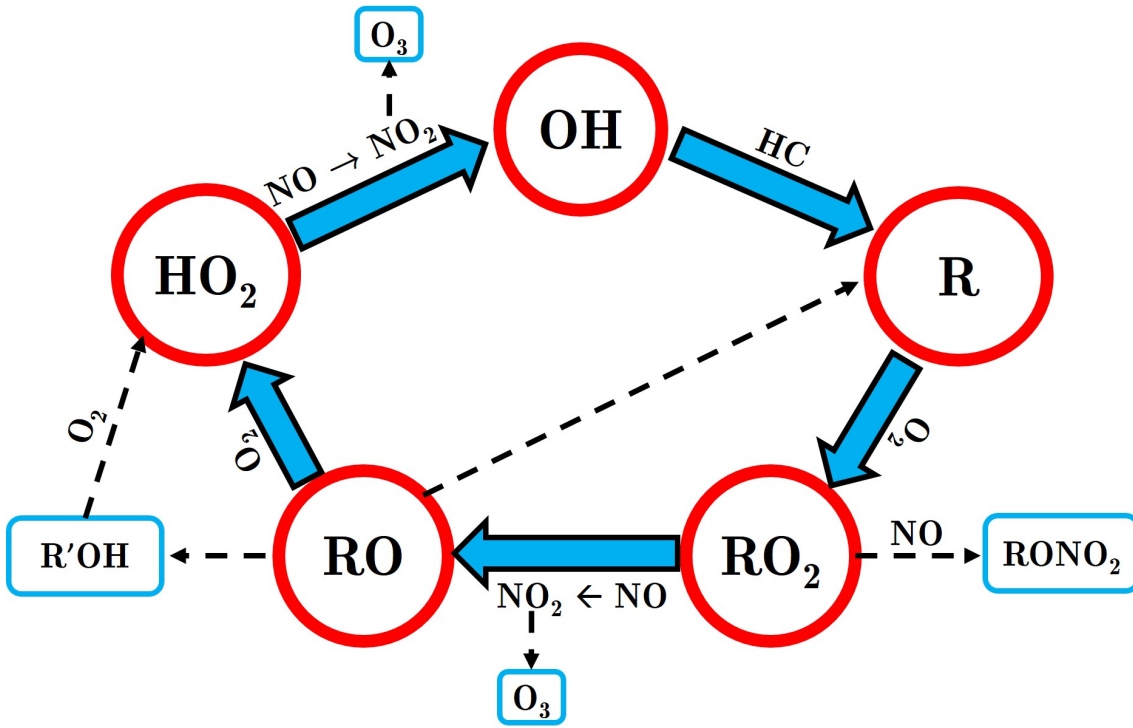
Figure 1.1: Schematic showing the $HO_x$ / $RO_x$ cycle, illustrating the main route to the formation of peroxy radicals ($RO_2$) from hydrocarbons.

recycling OH through the creation and destruction of $HO_2$ (Reactions 1.7, 1.8, 1.3) (Winiberg et al. 2016). This reaction of $RO_2$ with NO is also a pathway to the formation of acyl radicals (RCO) and aldehydes (RCHO) in the troposphere.

The $NO_2$ produced in these cycles can be converted to $O_3$ during the day, which is a primary component in photo-chemical smog. This smog is seen across mega-cities as brown haze and is primarily formed from vehicles and industrial activities. It is crucial that climate models are able to understand the smog around and in the cities due to the harmful effects it has on human health and the environment.

$$RCH_2O_2 + NO \rightarrow RCH_2O + NO_2 \tag{1.7}$$

$$RCH_2O + O_2 \rightarrow RCHO + HO_2 \tag{1.8}$$

In high $NO_x$ environments, $RO_2$ lead to the formation of peroxy nitrates($RO_2NO_2$). Peroxyacetyl nitrate (PAN, $CH_3C(O)O_2NO_2$) is the most well-known member of the

peroxy nitrates but it wasn't until the 1950s when it was first identified by Stephens et al. (1956) during a smog episode in the Los Angeles basin. PAN exists in a rapid equilibrium with its radical precursors $RO_2$ and $NO_2$, shown in Reaction 1.9 – when photo-chemistry of non-methane hydrocarbons coincides with high $[NO_x]$.

$$CH_3C(O)O_2NO_2 + M \rightleftharpoons CH_3C(O)O_2 + NO_2 + M \tag{1.9}$$

Peroxy nitrates not only contribute to photo-chemical smog, but they also act as temporary reservoirs for both $RO_2$ and $NO_x$. PAN is transported via convection into the upper troposphere where it can travel up to hundreds of km before descending in a remote location. This allows the redistribution of $NO_x$ from polluted urban environments into pristine environments where normal $NO_x$ concentrations are otherwise negligible (Ridley et al. 1990; Singh, Salas, and Viezee 1956). VOCs, $NO_x$, and $O_3$ lead to various respiratory problems and eye irritations; however, PAN is extremely toxic to plant growth reducing photosynthesis therefore can damage these pristine environments that it is able to travel to (Molina and Molina 2004).

The second destruction pathway for $RO_2$ occurs in clean environments, where there is a lack of $NO_x$ – such as remote forested areas or over the marine boundary layer. In clean environments the loss of $RO_2$ is no longer dominated by the reactions with NO, though still important, the reactions with $HO_2$ and other $RO_2$ radicals compete with the NO. These reactions with $HO_2$ and other $RO_2$ play a crucial role in the destruction of tropospheric $HO_x$ radicals (Reactions 1.10 and 1.11) (Stone, Whalley, and Heard 2012).

$$HO_2 + HO_2 \xrightarrow{M} H_2O_2 + O_2 \tag{1.10}$$

$$HO_2 + RO_2 \rightarrow ROOH + O_2 \tag{1.11}$$
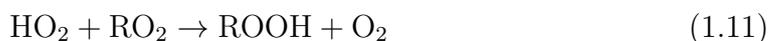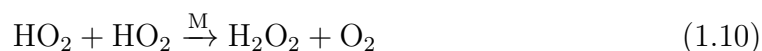
This project examined the OH produced by the reactions of $RCO + O_2$ and $RC(O)O_2$

+ $HO_2$. As explained in this section OH has great importance in the atmosphere and therefore understanding the amount of OH coming from these reactions is crucial to help monitor air quality worldwide. Also shown in this section is how critical the reactions of hydrocarbon radicals are in the atmosphere, not just with their own decomposition but also how they in turn affect air quality due to propagation reactions, for example via $O_3$ production.

The compounds that are investigated in this study come from aldehyde precursors which enable us easily to form acyl compounds such as $C_2H_5C(O)O_2$ - peroxy radicals which have a C=O bond. These peroxys are formed easily in the atmosphere via the oxidation of hydrocarbons emitted from anthropogenic sources. Aldehydes are not only used in this project for the ease of which they form peroxy radicals but they are a group of reactive compounds that can cause problems in both humans and animals (Cassee, Groten, and Feron 1996; Cassee, Arts, et al. 1996). There are both primary and secondary sources of aldehydes in the atmosphere, they can be: directly emitted into the atmosphere from the incomplete combustion of biomass and fossil fuels; or formed from photo-chemical oxidation of reactive hydrocarbons (Zhang and Smith 1999; Altemose et al. 2015). It is crucial to know the lifetimes of these species in the atmosphere as they have a significant impact within global climate models, hence the rate coefficients of OH with aldehydes need to be known.

In recent years, knowledge of the powerful influence that halogens have on the chemical composition of the troposphere has increased. The high reactivity of atomic chlorine radicals means that they are potent oxidisers for both organic and inorganic compounds, therefore affecting the fate of pollutants (Simpson et al. 2015). Modelling studies first indicated that the marine boundary layer was impacted by reactive halogens in 1993 (Pszenny et al. 1993) though the first substantial evidence for the importance of Cl reactions in the troposphere was provided by Jobson et al. (1994). They concluded that the changes in alkane concentrations during ozone depletion events in the high Arctic were due to Cl reactions (Jobson et al. 1994; Ariya et al. 1998; Simpson et al. 2015). Reactive halogens were subsequently detected

above bodies of water including salt lakes, saline seas, tidal coastal areas and the open sea; and also in pollution plumes and in the free troposphere (Simpson et al. 2015).

Chlorine has also been observed to impact the nocturnal $NO_x$ chemistry. Though dominated by reactions of $NO_3$ and $N_2O_5$, aerosols containing Cl are able to react with $N_2O_5$ to form $ClNO_2$ (Reaction 1.12). $ClNO_2$ is sufficiently long-lived at night to photo-dissociate in the morning to yield $NO_2$ and Cl atoms which can accelerate $O_3$ production in the troposphere (Mielke, Furgeson, and Osthoff 2011).

$$N_2O_5 + Cl \rightarrow ClNO_2 + NO_3 \tag{1.12}$$
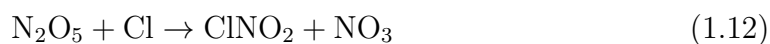
This mechanism was initially believed to be of significance only in areas with sources of sea salt aerosol, forming Cl containing aerosols – i.e. marine boundary areas. Recently, however, observations of high concentrations of $ClNO_2$ over continental Europe and America have been recorded (Mielke, Furgeson, and Osthoff 2011; Thornton et al. 2010; Phillips et al. 2012). Thornton et al. (2010) observed high concentrations of $ClNO_2$ in Boulder, Colorado – 1400 km from the nearest coastline; Mielke, Furgeson, and Osthoff (2011) presented results showing $ClNO_2$ in Calgary, Canada – 700 km from the coast; Phillips et al. (2012) presented measurements of $ClNO_2$ from Essen which were the first over continental Europe – approximately 250 km from the coast. These observations highlight the fact that there is an unknown anthropogenic source of chloride in the troposphere, responsible for the formation of continental $ClNO_2$. Increasing the number of known Cl rate coefficients will allow the formation of better equipped models, which are able to constrain the Cl loss more accurately and to help understand where this unknown Cl is coming from.

Recently, surface snow-pack was shown to be a significance source of $Cl_2$. This is extremely relevant in current climate conditions as the Arctic is currently undergoing rapid sea ice transformation. The production of $Cl_2$ and BrCl from the snow-pack

increases the photolytic production of Cl radicals (Custard et al. 2017). As Cl is highly reactive towards hydrocarbons, Cl rate coefficients are crucial in understanding and simulating future atmospheric conditions and compositions. Therefore in this project both the Cl and OH rate coefficients will be examined.

### 1.1.1    Atmospheric Relevant Compounds Studied in this Project

This project studies numerous RCO compounds including various $RC(O)O_2$: $C_2H_5C$ $(O)O_2$, $C_3H_7C(O)O_2$, $C_4H_9C(O)O_2$, $(CH_3)_2CHC(O)O_2$, $(CH_3)_2CHCH_2C(O)O_2$, $(CH_3)_3CC(O)O_2$, and $C_2H_5CH(CH_3)C(O)O_2$. These compounds can be all found in the atmosphere from multiple sources, such as the photolysis of ketones. Ketones are released from both anthropogenic and biogenic sources and also can be formed as intermediates in the oxidation of many hydrocarbons (Jacob et al. 2002). At around 300 nm the photodissociation of ketones results in the formation of an alkyl fragment and the associated acyl radical - Equation 1.13a and 1.13b. The RCO radical formed from the photolysis then reacts with $O_2$ to form the corresponding peroxy radical (Romero et al. 2005).

$$CRCOR' + h\nu \rightarrow R + R'CO \qquad (1.13a)$$

$$\rightarrow RCO + R' \qquad (1.13b)$$
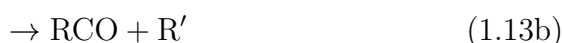
Another way to form $RC(O)O_2$ in the atmosphere is via H-abstraction from aldehydes. Aldehydes have been recognised for many years as an important group of compounds in the troposphere. They are emitted as primary pollutants from the partial oxidation of hydrocarbon fuels in internal combustion engines, and the secondary pollutants from the atmospheric oxidation of hydrocarbons. As mentioned previously OH is the most common oxidiser and therefore combined with the short lifetime and high reactivity of aldehydes the majority of aldehydes react with OH to form RCO +

$H_2O$. However, when the OH concentration is low other oxidisers can replace the role of OH, such as $NO_3$. These species are also able to abstract hydrogen from the aldehyde, forming RCO which can then go on to form $RC(O)O_2$ from the reaction with $O_2$. The photolysis of aldehydes can also form RCO compounds though this is only a minor source (Reaction 1.14).

$$RCHO \xrightarrow{h\nu} H + RCO \tag{1.14}$$

## 1.2   Combustion Chemistry and Biofuels

The finitude of fossil fuels is well-known, but with them contributing around 80% of total world energy supply we still have a heavy dependence on them (Goldemberg 2007). The known fossil fuel reserves could last anywhere between 41 and 700 years, depending on production and consumption rates (Goldemberg 2007). Therefore, coupled with the response to climate change, the concern for energy security has driven worldwide interest in renewable energy sources (Koh and Ghazou 2008).

Renewable energy sources such as biomass, wind, solar , hydro-power, and geothermal can provide sustainable energy based on available resources. Out of these renewable energy sources, hydro-power gives the largest contribution to the global electricity supply – nearly 20%; however, in developing countries biomass has a more significant role (Herzog et al. 2001; Shin et al. 2016). Biomass energy has fuelled the world's economy for thousands of years in the form of wood before the fossil fuel era. Liquid fuels from biomass (biofuels) are not a recent thing: in 1890 ethanol was used for the first time as a motor fuel and shortly after ethanol engines became fairly common in Germany (Lewis and Unit 1981). In recent years biofuels have been investigated with new rigour to help alleviate the pressure from fossil fuels, especially in the area of transportation. Biomass energy has been suggested to be one of the most

promising among renewable energy sources due to its spread and its availability worldwide (Demirbas 2008). Biomass has the unique advantage among the other renewables to be able to provide solid, liquid and gaseous fuels that can be stored, transported and utilised far away from the point of origin (Demirbas 2008).

Biofuels are biomass-based components for transport fuels. Both liquid and gaseous fuel can be produced; they can be pure biofuels for dedicated vehicles or blend fuels in such a proportion that they can substitute conventional motor fuels without affecting car performance (Demirbas 2008). Biofuels include bio-alcohols, bio-diesels, bio-gas, and bio-hydrogen. Initially biofuels were met with excitement since not only do they help combat climate change by reducing carbon emissions of traffic, they can help the world respond to a higher energy consumption, and also by using waste and residue as raw materials for biofuels, are an excellent example of answering to the needs of a circular economy. However, political and public support for biofuels has been undermined due to environmental and food security concerns. The diversion of food crops or croplands to produce biofuels has been blamed for global food shortages and associated increasing costs of staple food crops such as maize and rice (Koh and Ghazou 2008). Bio-ethanol and bio-diesel differ in the crops that are used to produce them (Figure 1.2). Even though crops grown for biomass feed-stocks take up less than 2% of the world's arable land, many authorities have agreed that some first generation biofuels have contributed to food price increases (Sims et al. 2010). The competition with food crops will remain an issue as long as the first generation biofuels produced from food crops dominate total biofuel production.

Nevertheless some policy makers and scientists remain optimistic about the development of next generation of biofuels – second generation biofuels which are produced from non-food biomass (Koh and Ghazou 2008; Sims et al. 2010). These new biofuels include fuels which are based on the conversion of lignocellulosic biomass, to improve rate, cost and efficiency (Welz, Zádor, Savee, Martin, et al. 2012).

Medium-chain alcohols, such as isopentanol, are among the compounds produced
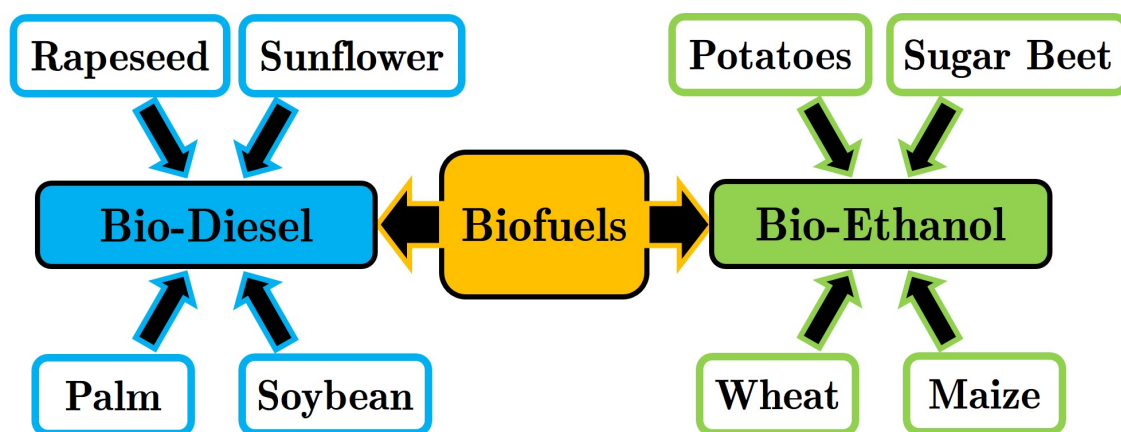
Figure 1.2: Illustrating the sources of bio-ethanol and bio-diesel.

from endophytic fungi that can directly digest cellulosic biomass (Strobel et al. 2011; Singh, Strobel, et al. 2011; Welz, Zádor, Savee, Martin, et al. 2012). A couple of potential candidates for second generation biofuels are isobutanol (($CH_3)_2CHCH_2OH$) and isopentanol (($CH_3)_2CHCH_2CH_2OH$) (Welz, Zádor, Savee, Martin, et al. 2012; Welz, Savee, et al. 2013). As potential candidates for biofuels these compounds need extensive chemical studies performed on them, allowing their oxidation to be well understood and combustion conditions optimised.

Such studies have included examining the low-temperature oxidation chemistry of alkanes, where the formation of R radicals occurs by slow reactions such as the abstraction of H atoms from a fuel molecule (RH) by $O_2$, also producing $HO_2$ at the same time (Zádor, Taatjes, and Fernandes 2011). These reactions are endothermic and reactions of the products rapidly overwhelm the overall reaction as it is well known that the reaction of initial fuel radicals R with $O_2$ forms $RO_2$ (Zádor, Taatjes, and Fernandes 2011; Welz, Zádor, Savee, Martin, et al. 2012). Peroxy species have been previously discussed as key intermediates in the troposphere, but they are also key intermediates in combustion chemistry (Kuwata 2014). The majority of peroxys are formed from the addition of $O_2$ to alkyl radicals, forming chemically activated (vibrationally excited) peroxy radical.

There are, however, other sources of peroxy radicals, including via a Markovnikov addition of OH to the C=C bond of an alkene leading to $\beta$–hydrocyalkylperoxy

radicals and also attack from $O_3$ to the C=C bond oso-substituted alkylperoxy radicals via the intermediate carbonyl oxides (Kuwata 2014).

There are three main fates of peroxy radicals in low-temperature combustion: $HO_2$ elimination to form an alkene species with the HOO radical; formation of hydroperoxyalkyl (QOOH) radicals by internal hydrogen abstraction; or formation back to separated alkyl radicals and $O_2$ (Figure 1.3). The QOOH species formed by a hydrogen shift can subsequently decompose to form either alkene + $HO_2$ or cyclic ether + OH products. However, this QOOH radical can react with $O_2$ to be converted into three radicals (two OH and one alkoxy radical). The OH that is produced here is exceptionally important as it is more reactive than $HO_2$ and therefore enhances chain propagation (Zádor, Taatjes, and Fernandes 2011; Kuwata 2014). This chain branching is an exponential growth in radical concentration found in combustion which leads to auto-ignition (Welz, Zádor, Savee, Martin, et al. 2012).
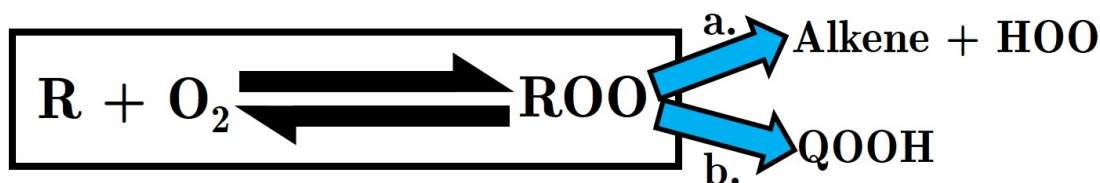


Figure 1.3: Schematic of the main fate of peroxy radicals in low-temperature combustion, where a = $HO_2$ elimination, and b = hydrogen shift.

The chemistry of peroxy radicals in low-temperature combustion, discussed above, can occur with either chemically activated or thermalised peroxy radicals. Chemical activation occurs when an energised unimolecular reactant is formed by a chemical reaction rather than by thermal equilibration (Klippenstein, Pande, and Truhlar 2014).

For a species to be chemical activated, they must possess energy in excess of the threshold energy of at least one reaction pathway available to that species. This allows chemically activated reactions to occur several orders of magnitude faster than thermally activated reactions. A chemically activated peroxy radical is able to

form QOOH in a single elementary step (Kuwata 2014).

Chemically activated reactions have a higher importance in low-temperature combustion chemistry than in the troposphere. This is due to the conditions found in the troposphere ranging from 100 Torr to 1 atm and 200-300 K causing the dominant fate of most chemically activated peroxy radicals to be thermalisation - the loss of chemical activation energy due to collisions. At the temperature range of low-temperature combustion (500-1000 K) a number of important unimolecular reaction channels become thermally accessible, increasing the number of chemically activated reactions.

Figure 1.4 illustrates the main pathway that an alcohol biofuel compound takes during combustion. It shows clearly how important RCO and $RC(O)O_2$ radicals are in combustion chemistry, playing a critical role in auto-ignition at low temperatures.
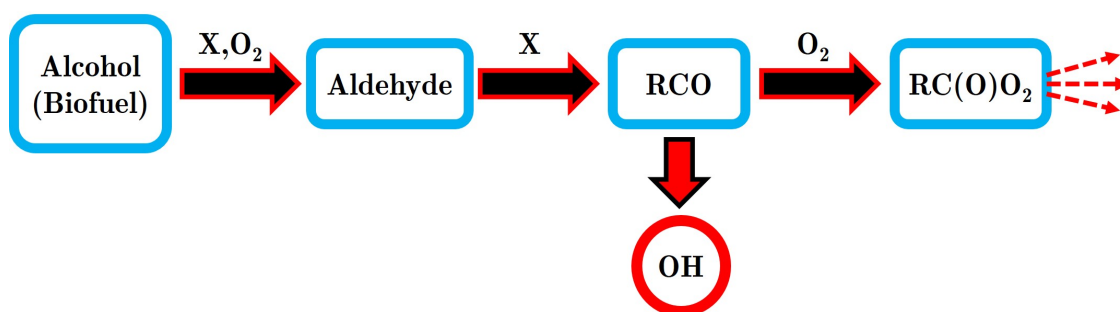


Figure 1.4:   Schematic of the main route of an alcohol compound biofuel in low-temperature combustion.

The interest in low-temperature combustion (LTC) has increased in recent years, as it is a way of to increase fuel efficiency while decreasing the amount of harmful emissions. LTC engines operate in regions where they avoid producing $NO_x$ and soot, unlike conventional diesel engines (Daley 2015). Figure 1.5 illustrates how the main species in the auto-ignition of n-butanol change with temperature and time. The sharp increase in temperature, around 50 ms, which occurs in auto-ignition emphasizes the importance of understanding the chemistry of the species below 1000 K.
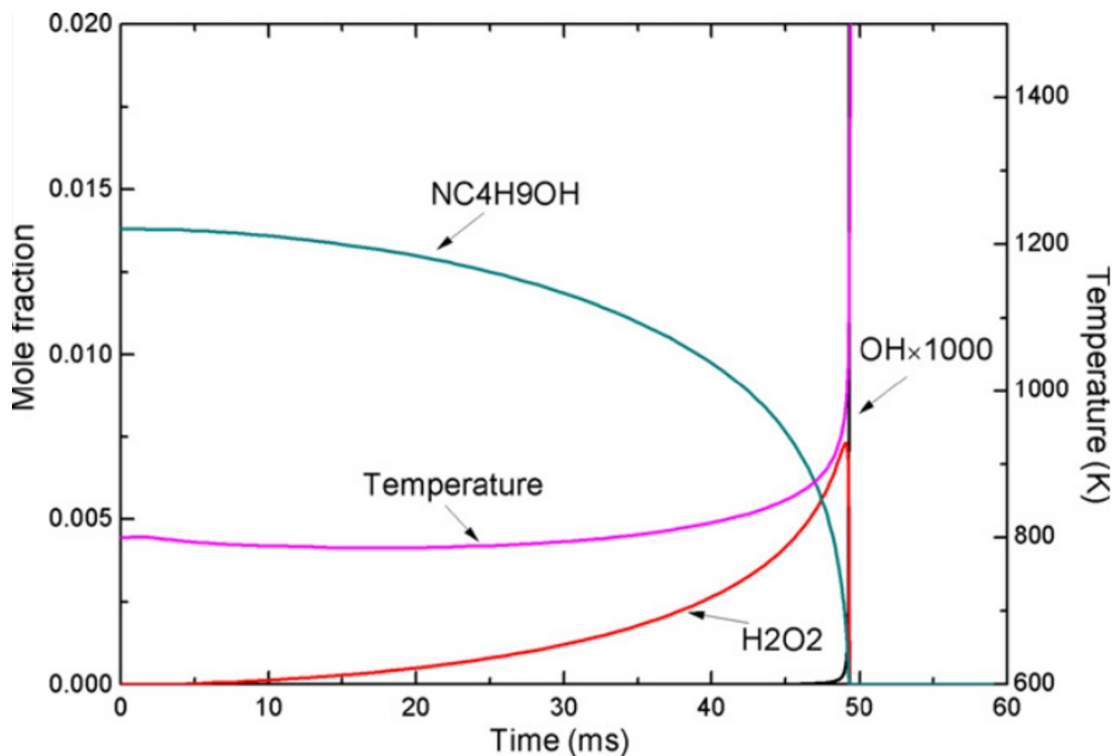
Figure 1.5: Computed temperature and species concentrations for auto-ignition of neat n-butanol at $p = 20$ atm and $T = 800$ K. - image from (Zhang, Niu, et al. 2013).

### 1.2.1 Biofuel Relevant Compounds Studied in this Project

Recently, longer chain molecules have been investigated for second generation of biofuels, discussed briefly in the previous section. These biofuels include n-butanol ($C_4H_9OH$), isobutanol (($CH_3)_2CHCH_2OH$) and isopentanol (($CH_3)_2CHCH_2CH_2OH$). These larger compounds are promising biofuels due to their higher energy content, lower vapour pressure and lower solubility in water when compared to ethanol (Welz, Zádor, Savee, Martin, et al. 2012; Welz, Savee, et al. 2013; Welz, Zádor, Savee, Sheps, et al. 2013; Zhang, Niu, et al. 2013).

These larger compounds have the same reaction mechanisms as the smaller compounds therefore: n-butanol ($C_4H_9OH$) leads to the formation of $C_3H_7C(O)O_2$; isobutanol (($CH_3)_2CHCH_2OH$) leads to the formation of ($CH_3)_2CHC(O)O_2$; and isopentanol (($CH_3)_2CHCH_2CH_2OH$) leads to the formation of ($CH_3)_2CHCH_2C(O)O_2$.

This project has investigated these larger peroxy radicals and has recorded their OH yields for the decomposition of peroxy radicals and from the reactions of chemically activated acyl peroxy radicals with $HO_2$. The new experimental set-up will test the viability for future high-temperature studies.

As mentioned previously this project studies numerous RCO including: $C_2H_5CO$, $C_3H_7CO$, $C_4H_9CO$, $(CH_3)_2CHCO$, $(CH_3)_2CHCH_2CO$, $(CH_3)_3CCO$, and $C_2H_5CH(CH_3)CO$. All these compounds and their corresponding $RC(O)O_2$ species are relevant in the atmosphere but a few of them are also relevant in biofuels.

Older biofuels which are primarily from food crops such as grains and sugar cane use shorter compounds (e.g. $C_2H_5OH$) which lead to the formation of $C_2H_5CHO$ and $CH_3CHO$. These aldehydes can react with an oxidising compound, such as OH or $O_2$ or $HO_2$ to abstract the H on the aldehyde. After H-abstraction the amount of $O_2$ found in an engine enables the rapid formation of $RC(O)O_2$ compounds.

## 1.3  Reaction Kinetics

As alluded to in the previous sections, it is critical to know how fast reactions occur in all branches of chemistry – reaction kinetics simply refers to the measurements these reaction rates (Pilling and Seakins 1996). The rate of a reaction can be simply described by the rate that reactants are used up, or the products are formed, and so by monitoring the concentration of one of the products or reactants as a function of time the rate can be calculated. This means that the rate has the units concentration per unit time.

In this project the experimental analysis was based on simple kinetics, with the calculation of rate coefficients and the determination of branching ratios in reaction. Therefore this section will explain and show the kinetics that form the basis of the analysis. Reactions can be grouped depending on the molecularity of the process

(number of molecules involved) and two types of reactions will be discussed here: unimolecular and bimolecular.

A reaction that proceeds with just a single species is considered to be an unimolecular reaction. For example, a unimolecular reaction with species A proceeds with the rate constant $k_A$ (Equation 1.15). Since the reaction is solely dependent on species A, the rate coefficient can be seen to be directly proportional to the change in concentration of A with time. The rate law is an expression relating the rate of reaction to the concentrations of the chemical species present, with the constant of proportionality $k$ called the rate constant. The power to which a particular concentration is raised is called the order of the reaction with respect to that reactant, with the sum of the powers being called the overall rate. Therefore a unimolecular reaction with species A has a rate equal to $k_A$ and is overall first order. The rate law describes the rate of change of a reactant (or product) concentration with time, therefore it can be expressed in a differential form (Equation 1.16).

$$A \xrightarrow{k_A} Products \tag{1.15}$$

$$\frac{d[A]}{dt} = -k_A[A] \tag{1.16}$$

The integration of this differential equation forms an expression for the concentration as a function of time: the first-order rate reaction (Equation 1.17). It displays how the concentration of the reactant decays exponentially with time when there are no other compounds involved. Where $[A]_t$ represents the concentration of A at time $t$, and $[A]_0$ represents the original concentration of A. This equation shows that the rate coefficient for a simple first-order reaction can be obtained experimentally by simply measuring the change in the concentration of species A – or a property of species A which is proportional to it such as fluorescence.

$$[A]_t = [A]_0 exp(-k_A t) \tag{1.17}$$

A reaction that proceeds via two species, for example A and B, is called a bimolecular reaction (Reaction 1.18). For a bimolecular reaction the rate is dependent on $k$[A][B] and therefore is called a second-order reaction. Equation 1.19 displays the differential rate law where $k_{AB}$ is the bimolecular rate coefficient for the reaction.

$$A + B \xrightarrow{k_{AB}} Products \tag{1.18}$$

$$\frac{d[A]}{dt} = -k_{AB}[A][B] \tag{1.19}$$

The integrated form of the second-order rate law is more complex than the first-order equation – the concentrations of both reactants need to be known (Equation 1.20).

$$[A]_t = \frac{[A]_0[B]_t}{[B]_0}exp(-([B]_0 - [A]_0)k_{AB}t) \tag{1.20}$$

A technique of simplifying the raw law for a second-order reaction is by having one of the reactants in such large excess that its concentration can be considered to be constant throughout the reaction. Sometimes known as an isolation method, it simplifies the rate law in order to determine its dependence on the concentration of a single reactant. In a reaction of A + B, when the reagent B is in excess the rate law will be reduced to a pseudo first-order rate law (Equation 1.21), where $k_{obs}$ is $k_{AB}$[B].

$$\frac{d[A]}{dt} = -k_{obs}[A] \tag{1.21}$$

Pseudo first-order conditions are routinely used for laboratory kinetics in order to study kinetics of bimolecular reactions. In this work it will be used to allow the kinetics of the reactions of aldehydes with radicals to be studied.

## 1.3.1   Temperature Dependence

The fact that some chemical reactions occur more rapidly at higher temperatures has been common knowledge for many years. It has been accepted for decades that as the temperature rises, molecules move faster and collide more vigorously therefore increasing the likelihood of bond cleavages and rearrangements greatly. It was in 1850 that Wilhelmy's pioneering investigations led to the first empirical equation relating the rate constant to temperature; however, it was not able to show the temperature dependence which was consistent with that of equilibrium constant for reversible reactions (Truhlar and Horowitz 1978). Investigations carried on to improve this empirical equation and in 1892 Berhelot proposed the equation, where $A$ and $D$ are constants (Equation 1.22) (Eyring and Polanyi 1931).

$$k = Ae^{DT} \tag{1.22}$$

However it wasn't till 1889 that Arrhenius combined the concepts of activation energy and the Boltzmann distribution law to create the Arrhenius equation, based on experiments where reaction coefficients were found to increase with temperature (Equation 1.23). The Boltzmann distribution law is represented in the Arrhenius equation by: $E_a$ / $RT$ where $E_a$ is the activation energy of the reaction, $R$ is the gas constant (8.314 J K$^{-1}$ mol$^{-1}$) and $T$ is the temperature (K). The Arrhenius equation enables the determination of $A$ and $E_a$ by plotting experimental data: $\ln k$ against $1/T$.

The activation energy is related to the relative energy between the transition state (the maximum on the minimum energy pathway of a reaction) and the reactants. Transition state theory (TST) explains this pathway between reactants and activated transition states which are at a higher energy level. If the energy of the reactants is lower than the $E_a$, the reaction will simply not proceed as it is unable to form the transition state. Therefore a reaction with a large activation energy requires much

more energy to reach the transition state than one with a smaller activation energy.

$A$ is the pre-exponential factor, which corresponds to the collision frequency of the reactant molecules - it quantifies how many molecules collide with the correct orientation to initiate a reaction. It is related to both transition state theory and collision theory. Collision theory represents how not every collision between molecules leads to a reaction, therefore directly impacts the value of $A$.

$$k = Aexp\frac{-E_a}{RT} \tag{1.23}$$

The Arrhenius equation is the only two-parameter temperature-dependent equation to survive, though it is not the most accurate equation. The Harcout-Esson equation proposed in 1912 was seen to be empirically better, fitting experimental data more reliably (Equation 1.24). The reason why the Arrhenius equation survived was due to the fact it is able to provide insight on how reactions proceed – the activation energy ($E_a$) relates to the energy barrier height. In comparison the parameter $m$ that appears in the Harcout-Esson equation and the parameter $D$ in Berhelot's equation cannot be related to any physical quantity (Johnston, Oudemans, and Cole 1960).

$$k = AT^m \tag{1.24}$$

It has been found experimentally that some reactions have rate coefficients that follow the Arrhenius relationship, allowing $A$ and $E_a$ to be determined as an Arrhenius plot can be created: $\ln(k)$ versus $1/T$. Even if a straight line is not observed from the plot other information can be determined; therefore, in this project Arrhenius plots will be created to analyse the relationship observed between the rate coefficients and temperature.

## 1.4    Kinetics Experimental Techniques

Reaction timescales vary greatly, from millennia to femtoseconds, and therefore various highly specialised techniques have been devised to measure them. A kinetic experiment can essentially be spilt into two parts: the first consists of mixing the reactants and initiating reactions; the second is the monitoring of the concentrations of one or more of the reactants or/and products as a function of time. A couple of examples of each will be discussed here including the technique which was used in this project (flash photolysis coupled to laser-induced fluorescence).

### 1.4.1    Kinetic Techniques

A simple technique which utilises the velocity of species to calculate concentrations is the flow method. This method simply mixes the reactants at one end of the flow tube and the composition of the reaction mixture is monitored at a position or positions further along the tube. To allow the reactions of radical species to occur the flow method was altered slightly to a discharge flow method, where a microwave discharge generates the radical species immediately prior to injection into the flow tube. However, this simple method has a few disadvantages: large quantities of reactants are needed; very fast velocities are needed to study fast reactions; kinetics can be complicated by surface reactions occurring on the walls of the flow tube. These large quantities mean that this method is usually used to study reactions that occur on timescales of seconds and milliseconds, and so it is not applicable for this project.

Another method that is used to initiate kinetic reactions is the shock tube method. More commonly found in combustion reaction studies, it is able to produce a highly reactive species through rapid dissociation of a molecular precursor without the use of a discharge laser pulse. The shock tube has two major compartments with

a diaphragm separating them - one containing a high pressurised inert gas and the other a low pressurised reaction mixture. When the reaction is initiated the diaphragm is broken, causing a shock wave which passes through the low pressure gas. Since a rapid increase of pressure causes an increase of temperature, the shock wave will cause a temperature step. This initiates the reaction, with the temperature rise controlled by the pressure and composition of the inert gas. Composition of the reaction mixture is monitored usually with spectroscopy, and is often used to study combustion reactions. There are a lot of drawbacks to this method, it can lead to a complicated mixture of reactive species and since each experiment is essentially a one off no signal averaging is possible – therefore data can be very noisy.

To overcome the mixing and pressure limitations of flow systems in kinetics, Norrish and Porter developed the technique of flash photolysis in the 1940s which earned them the Nobel prize in 1967 (Laidler 1987). In flash photolysis premixed reactants and precursors flow into a photolysis cell where a pulse of light produces a transient species. Premixing the reactants produces a homogeneous concentration of the reactants which the light interacts with. Effects from wall catalysed reactions are also reduced with flash photolysis, since reactant species are generated and monitored in the centre of the reactor cell. The concentration of the species of interest is recorded as a function of time (Pilling and Seakins 1996).

Flash lamps produced the pulse of light for the first experiments, which limited the number of studied reactions due to its long pulse duration of several milliseconds. The chromatic nature of these lamps also meant that various chemical effects were caused by the light over a range of wavelengths confusing results. The development of lasers, with their short pulse duration and monochromatic nature, enhanced the technique of flash photolysis (Pilling and Seakins 1996). The monochromatic nature of lasers meant that the wavelength now had to be suitable for the excitation of the compound to be studied, reducing the chance of other unwanted reactions occurring. Laser beams also have a high intensity, high repetition rate and are coherent. Their high intensity beams are important as a significant quantity of transient species can

be produced from a low precursor concentration, simplifying the overall kinetics of the system studied (Logan 1996).

This project uses flash photolysis to initiate the reactions that are studied; as reactants are produced from well-mixed precursors there is no mixing time to reduce the time resolution of the technique, and also since the reactants are generated and monitored in the centre of the cell there are no wall reactions to complicate kinetics.

## 1.4.2   Detection Techniques

Techniques for monitoring the concentration vary greatly with the timescale of the reaction that is studied. For example, in slow reactions the composition of the reaction mixture can be analysed while the reaction is in progress; however fast reactions require a fast measurement technique.

One example is absorption spectroscopy, which is widely used to track reactions where the reactants and products have different absorption spectra. Full spectra of either the reactant or product can be recorded via diode array or a charged coupled device (CCD) camera, to determine the yield of the reaction. Another common technique is resonance fluorescence which is widely used for detecting atomic species such as N, O or H. The light source is a discharge lamp filled with a mixture of helium and a molecular precursor for the atom of interest; excited atoms produced from a microwave discharge emit photons as they return to the ground state. This is used to excite atoms of the same species in the reaction mixture, and by monitoring the intensity of the radiation given off in the reaction mixture this provides a measure of their concentration.

Laser induced fluorescence (LIF) is is a powerful spectroscopic method, which is a highly sensitive and commonly used in kinetic studies. LIF provides a relative measure of concentration of the transient species, not an absolute concentration, which less sensitive methods such as absorption spectroscopy can provide. The

species to be detected by LIF is excited to an upper electronic state; this project used a dye laser as the excitation source. The output of a dye laser is high intensity radiation, giving the technique high sensitivity, and the wavelength can be precisely tuned to match a particular transition so is highly selective. The excited molecules then relax down to the ground state, emitting fluorescence which can be detected by a photomultiplier tube (PMT). The intensity of this fluorescence is proportional to the number of the molecules in the ground state, and so it is proportional to the concentration of the transient species.
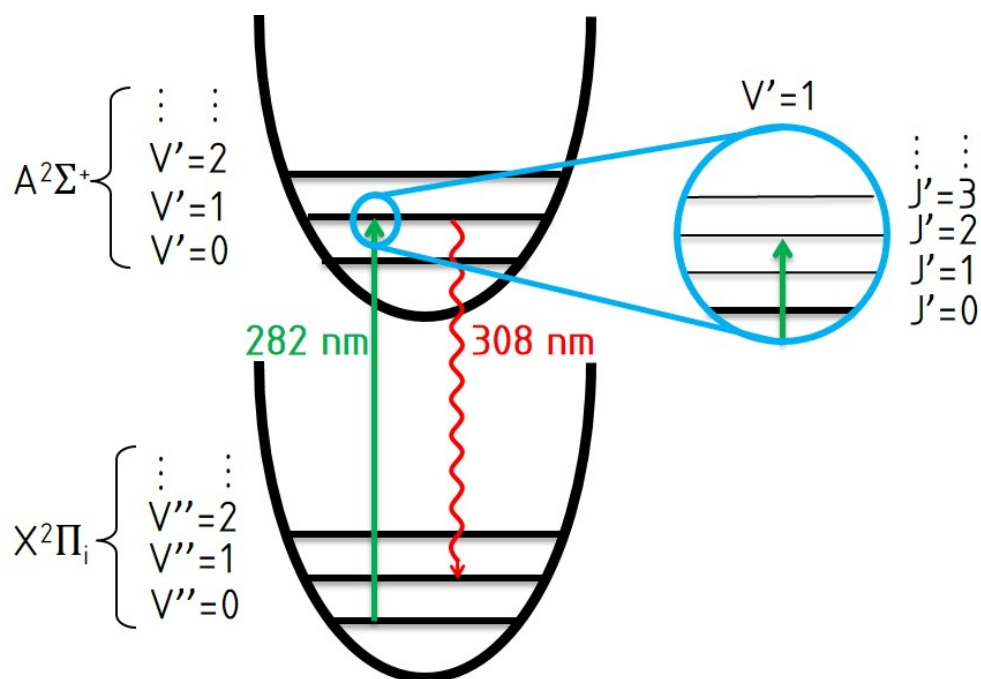


Figure 1.6: Schematic diagram of laser induced fluorescence of the OH radical. The OH excitation (green arrow) uses a 282 nm photon beam, OH is excited to a particular rovibrational level in an upper electronic state which the dye laser is tuned to (blue circle). Collisional energy transfer occurs with the red arrow representing the off resonance fluorescence at 308 nm, in this work the OH $A^2\Sigma+(v\prime=1) \leftarrow X^2\Pi$ 3/2 $(v\prime\prime=0)$ transition is used.

OH is ideal for LIF studies, due to its excellent absorption coefficient and high quantum yield of fluorescence for its excited state. LIF exploits the specific energy levels in OH: when OH relaxes back down from its excited state to its ground state it emits a photon. Relaxation can occur to several vibrational levels in the ground state and hence the fluorescence can be detected at a different wavelength from the excitation wavelength. The relaxation can occur in two main ways where the

photon emitted can be either on-resonance, the same wavelength as the excitation wavelength, or off-resonance. This project employs off-resonance relaxation, which is key for LIF as the wavelength of the emitted photon is longer than the excitation wavelength. Interference filters block the excitation wavelength, so only signal from the off-resonance wavelength is detected, allowing a high signal-to-noise ratio. The fluorescence scheme which is commonly used for LIF detection of OH is shown in Figure 1.6. LIF is ideal for the studies carried out in this project as it is sensitive, selective, fast, and direct; however, it it not an absolute method and therefore back-to-back reactions are necessary for calibrations.

## 1.5   Overview of Thesis

This thesis will focus on certain gas-phase reaction kinetics which are relevant to the Earth's atmosphere and to the biofuels which were discussed in this chapter. Since the reactions that were studied are fast and produce the short-lived OH radical a new experimental set-up was created during this project, which enabled the detection of OH radicals using pulsed-laser-photolysis combined with laser-induced-fluorescence (PLP-LIF). Chapter 2 will give detailed explanations this new experimental set-up and how experimental runs were carried out.

Chapter 3 describes the results from the first investigation carried out on the new experiment, recording the OH yields of $RCO + O_2$ reactions where the decomposition of the hot chemically activated acyl peroxy radicals led to OH formation.  As discussed previously in this chapter, the reactions of $RCO + O_2$ are critical in the atmosphere and combustion chemistry; therefore, knowing the OH yield from these reactions is important to be able to predict conditions. To analyse these results with greater accuracy, experiments were carried out to determine rate coefficients for aldehyde with OH or Cl. This allowed the calculation of two new rate coefficients which are discussed in Chapter 4.

Experimental tests were carried out when the interest of the project shifted from the OH yield of $RCO + O_2$ reactions to the OH yield from $RC(O)O_2 + HO_2$. It was with these experiments that a new source of OH was detected. Chapter 5 discusses the experiments carried out to interrogate this new source of OH alongside the results and data from these experiments.

Chapter 6 examines the OH yields from the reactions of acyl peroxy radicals with $HO_2$. The reaction of $CH_3C(O)O_2 + HO_2$ has been studied before to show that OH is produced with a yield of $0.61 \pm 0.009$ at room temperature (Gross et al. 2014). This chapter will discuss the results from other $RC(O)O_2$ species to determine OH yields for different R groups and the first preliminary high temperature experiments.

The final chapter, Chapter 7, will give a brief summary of the key findings from the previous chapters and outline possible future work.

# Bibliography

Altemose et al. (2015). "Aldehydes in Relation to Air Pollution Sources: A Case Study around the Beijing Olympics". In: *Atmospheric Environment* 109, pp. 61–69.

Ariya et al. (1998). "Measurement of C2-C7 hydrocarbons during the Polar Sunrise Experiment 1994: further evidence for halogen chemistry in the troposphere". In: *Journal of Geophysical Research Atmospheres* 103.D11, pp. 13169–13180.

Atkinson (2000). "Atmospheric chemistry of VOCs and NOx". In: *Atmospheric Environment* 34, pp. 2063–2101.

Cassee, Arts, et al. (1996). "Sensory irritation to mixtures of formaldehyde, acrolein, and acetaldehyde in rats". In: *Archives of Toxicology* 70.6, pp. 329–337.

Cassee, Groten, and Feron (1996). "Changes in the nasal epithelium of rats exposed by inhalation to mixtures of formaldehyde, acetaldehyde, and acrolein". In: *Toxicological Sciences* 29.2, pp. 208–218.

Custard et al. (2017). "Production and Release of Molecular Bromine and Chlorine from the Arctic Coastal Snowpack". In: *ACS Earth and Space Chemistry* 1.3, pp. 142–151.

Daley, Shane (2015). "Chemometrics-based Approach for Predicting Low Temperature Combustion Engine Fuel Performance". PhD thesis. Oregon State University, p. 11. URL: http://pubs.rsc.org/en/content/articlepdf/2008/dt/b806358c.

Demirbas (2008). "Biofuels sources, biofuel policy, biofuel economy and global biofuel projections". In: *Energy Conversion and Management.*

Eyring and Polanyi (1931). "On simple gas reactions". In: *Zeitschrift fur Physikalische Chemie* 227.11, pp. 1221–1245.

Finlayson-Pitts and James (1999). *Chemistry of the upper and lower atmosphere : theory, experiments, and applications.* 1st ed. Elsevier Science.

Forster et al. (2007). *Changes in Atmospheric Constituents and in Radiative Forcing.*

Goldemberg (2007). "Ethanol for a Sustainable Energy Future". In: *Science* 315.5813, pp. 808–810.

Gross et al. (2014). "Direct kinetic study of OH and $O_3$ formation in the reaction of $CH_3C(O)O_2$ with $HO_2$." In: *The Journal of Physical Chemistry. A* 118.6, pp. 974–85.

Herzog et al. (2001). "Renewable Energy: A Viable Choice". In: *Environment: Science and Policy for Sustainable Development* 43.10, pp. 8–20.

Jacob (1999). *Introduction to atmospheric chemistry.* Princeton University Press.

Jacob et al. (2002). "Atmospheric budget of acetone". In: *Journal of Geophysical Research: Atmospheres* 107.D10.

Jobson et al. (1994). "Measurements of C 2 -C 6 hydrocarbons during the Polar Sunrise 1992 Experiment: Evidence for Cl atom and Br atom chemistry". In: *Journal of Geophysical Research Atmospheres* 99.D12, pp. 25355–25368.

Johnston, Oudemans, and Cole (1960). "Dielectric Constants of Imperfect Gases. I. Helium, Argon, Nitrogen, and Methane". In: *The Journal of Chemical Physics* 33.5, pp. 1310–1317.

Klippenstein, Pande, and Truhlar (2014). "Chemical kinetics and mechanisms of complex systems: A perspective on recent theoretical advances". In: *Journal of the American Chemical Society* 136.2, pp. 528–546.

Koh and Ghazou (2008). *Biofuels, biodiversity, and people: Understanding the conflicts and finding opportunities.*

Kuwata (2014). "Computational Treatments of Peroxy Radicals in Combustion and Atmospheric Reactions". In: *PATAI'S Chemistry of Functional Groups.*

Laidler (1987). *Chemical Kinetics.* 3rd Editio. Harper Collins Publishers.

Levy (1971). "Normal atmosphere: large radical and formaldehyde concentrations predicted." In: *Science (New York, N.Y.)* 173.3992, pp. 141–143.

Lewis and Energy Studies Unit (1981). "Biomass Through the Ages". In: *Biomass* 1, pp. 5–15.

Logan (1996). *Fundamentals of Chemical Kinetics*. Longman.

Mielke, Furgeson, and Osthoff (2011). "Observation of $ClNO_2$ in a mid-continental urban environment". In: *Environmental Science and Technology* 45.20, pp. 8889–8896.

Molina and Molina (2004). "Megacities and atmospheric pollution." In: *Journal of the Air & Waste Management Association (1995)* 54.February 2015, pp. 644–680.

Phillips et al. (2012). "Significant concentrations of nitryl chloride observed in rural continental Europe associated with the influence of sea salt chloride and anthropogenic emissions". In: *Geophysical Research Letters* 39.10, pp. 1–5.

Pilling and Seakins (1996). *Reaction Kinetics*. Oxford Science Publications.

Pszenny et al. (1993). "Evidence of inorganic chlorine gases other than hydrogen chloride in marine surface air". In: *Geophysical Research Letters*.

Ridley et al. (1990). *The Behavior of Some Organic Nitrates at Boulder and Niwot Ridge, Colorado*. Tech. rep. D9, p. 99.

Riedel and Lassey (2008). "Detergent of the atmosphere". In: *Water & Atmosphere* 16.1, pp. 22–23.

Romero et al. (2005). "Photolysis of methylethyl, diethyl and methylvinyl ketones and their role in the atmospheric HOxbudget". In: *Faraday Discussions* 130, pp. 73–88.

Seinfeld and Pandis (2006). *Atmospheric chemistry and physics : from air pollution to climate change*. 2nd ed. Wiley.

Shin et al. (2016). "An Assessment of the Association Between Renewable Energy Utilization and Firm Financial Performance". In: *Journal of Business Ethics* 151.4, pp. 1–18.

Simpson et al. (2015). "Tropospheric Halogen Chemistry: Sources, Cycling, and Impacts". In: *Chemical Reviews* 115.10, pp. 4035–4062.

Sims et al. (2010). *An overview of second generation biofuel technologies.*

Singh, Salas, and Viezee (1956). "Global distribution of peroxyacetyl nitrate". In: *Nature* 321.6080, pp. 588–591.

Singh, Strobel, et al. (2011). "An Endophytic Phomopsis sp. Possessing Bioactivity and Fuel Potential with its Volatile Organic Compounds". In: *Microbial Ecology.*

Stephens et al. (1956). "Reactions of Nitrogen Dioxide and Organic Compounds in Air". In: *Industrial and Engineering Chemistry* 48.9.

Stone, Whalley, and Heard (2012). "Tropospheric OH and $HO_2$ radicals: field and model comparisons". In: *Chemical Society Reviews* 41.19, p. 6348.

Strobel et al. (2011). "An endophytic/pathogenic Phoma sp. from creosote bush producing biologically active volatile compounds having fuel potential". In: *FEMS Microbiology Letters.*

Talukdar et al. (1998). "Quantum yields of $O(^1D)$ in the photolysis of ozone between 289 and 329 nm as a function of temperature". In: *Geophysical Research Letters* 25.2, pp. 143–146.

Thornton et al. (2010). "A large atomic chlorine source inferred from mid-continental reactive nitrogen chemistry". In: *Nature* 464.7286, pp. 271–274.

Truhlar and Horowitz (1978). "Functional representation of Liu and Siegbahn's accurate ab initio potential energy calculations for $H + H_2$". In: *The Journal of Chemical Physics* 68.5, pp. 2466–2476.

Welz, Savee, et al. (2013). "Low-temperature combustion chemistry of biofuels: Pathways in the low-temperature (550-700 K) oxidation chemistry of isobutanol and tert-butanol". In: *Proceedings of the Combustion Institute* 34.1, pp. 493–500.

Welz, Zádor, Savee, Martin, et al. (2012). *Low-temperature combustion chemistry of biofuels: pathways in the initial low-temperature (550 K–750 K) oxidation chemistry of isopentanol.*

Welz, Zádor, Savee, Sheps, et al. (2013). "Low-temperature combustion chemistry of n-butanol: Principal oxidation pathways of hydroxybutyl radicals". In: *Journal of Physical Chemistry A* 117.46, pp. 11983–12001.

Winiberg et al. (2016). "Direct measurements of OH and other product yields from the HO$_2$ + CH$_3$C(O)O$_2$ reaction". In: *Atmospheric Chemistry and Physics* 2.2, pp. 4023–4042.

Zádor, Taatjes, and Fernandes (2011). *Kinetics of elementary reactions in low - temperature autoignition chemistry*. DOI: `10.1016/j.pecs.2010.06.006`.

Zhang, Niu, et al. (2013). "Experimental and modeling study of the auto-ignition of n-heptane/n-butanol mixtures". In: *Combustion and Flame* 160.1, pp. 31–39.

Zhang and Smith (1999). "Emissions of carbonyl compounds from various cookstoves in China". In: *Environmental Science and Technology* 33.14, pp. 2311–2320.

# Chapter 2

# Experimental and Instrument Development

The apparatus was designed and constructed to enable the detection of OH yields by pulsed laser induced fluorescence (LIF). The OH yield was recorded for target reactions of $RO_2$, generated by pulsed laser photolysis (PLP) of $Cl_2$ inside the glass reactor cell. This chapter will explain how the apparatus was used to detect OH, including how conditions such as the gas concentration, temperature and the pressure of the system were controlled. The technique of LIF has been used for many years for the detection of the OH radical (Baardsen and Terhune 1972). A common method, LIF will be briefly explained alongside PLP, describing how these techniques were used in this work and why they are suitable for the reactions investigated.

## 2.1 Apparatus

Experiments were carried out using a glass reactor with a volume of approximately 400 $cm^3$, with the gas mixture entering the reactor cell 30 cm upstream of the photolysis region. The pressure in the cell was held constant during each experimental
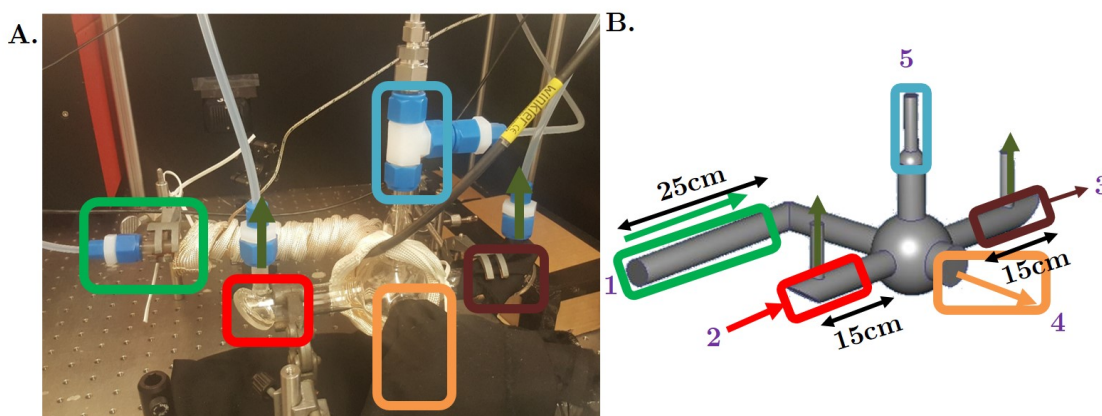
Figure 2.1: A - The reactor cell where: the gases enter (light green) and exit (dark green); laser pulses enter (bright red) and exit (dark red); the position of the photomultiplier tube to detect OH photolysis (orange); the connection for the Baratron capacitance manometers and the temperature probe (blue). The arms of the reactor cell are labelled and these numbers are referred to in the text. B - A sketch of the reactor cell to scale, the colours match up to A.

run; calibrated mass flow controllers (MFCs) regulated the flow rates of the gases, ensuring fresh gas was photolysed at each laser pulse. This section explains how all aspects of the apparatus are controlled including the temperature and pressure control of the cell. The apparatus was modified throughout the project, enabling the investigation of a greater number of reactions.

## 2.1.1   Reactor Cell

The reactor cell, manufactured in-house (Figure 2.1), was based on a 200 ml round bottom flask, with four cylinder arms glass-blown on one axis and another perpendicular. The longest arm (1) is the gas inlet; it is approximately 40 cm in length and changes diameter - from 1 cm to 2 cm at the 90° bend. Heating tape was wrapped around the longer arm, allowing the gases to heat for a longer length of time before entering the middle of the cell. Heat transfers through the glass by conduction and then to the gases via convection, the smaller diameter at the start allowed a more uniform heating of the gas molecules.

The gas is pumped through the reactor and passes out via the two arms, each

approximately 15 cm in length, through which the laser beams pass (2 and 3). Outlets on both arms provide quick and effective removal of gas from the centre of the cell, which ensures that a fresh supply of gas is available for each photolysis pulse. These two arms, where the laser beams enter and exit the cell, have quartz windows at the Brewster angle of 45°, fixed with Loctite EA 3430 glue. Windows at the Brewster angle are 14 cm away from the centre of the cell, minimising the effect that scattered light has on the fluorescence signal.

The fresh gas from the inlet meets the laser beams at the centre of the cell. The photomultiplier tube (PMT) is placed opposite the inlet and orthogonal to the laser beams on the fourth arm of the cell, approximately 5 cm in length (4). The fifth arm from the centre of the cell (5) contains the connectors for both the pressure gauges and the thermocouple (Type K - 310 stainless steel sheath (1100° C)). The thermocouple is contained in a glass sheath so it did not come into contact with any of the gases, especially chlorine which is corrosive. This sheath contained a small amount of silica oil, which allowed efficient heat transfer to take place from the glass sheath to the thermocouple. A vacuum-tight seal on this sheath is achieved by o-rings and a special Swagelok fitting which has a larger bore size, allowing the glass sheath to fit through it. Figure 2.2, shows the position of the reactor cell in relation to the rest of the apparatus.

## 2.1.2 Reaction Conditions

The temperature and pressure controls in the reactor were crucial, as the reactions that were studied in this project have both a temperature and a pressure dependence.

Pressure was monitored by two Baratron capacitance manometers (MKS) with different pressure ranges: one was 10 Torr (model: 622A11TAD) and the other 1000 Torr (model: 626A13TAE), this gave not only a wide range but also high accuracy at low pressures. The calibration for the 1000 Torr Baratron capacitance manometer was checked frequently using an atmospheric pressure value from the
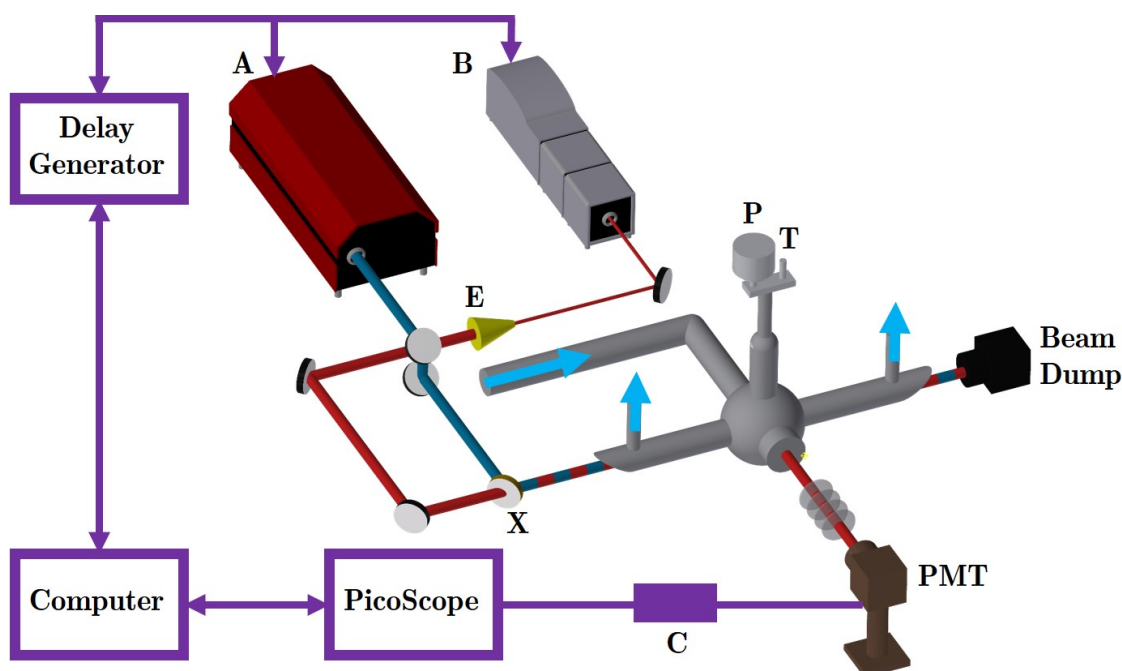
Figure 2.2: Schematic view of experimental set-up. Key: 282 nm Nd:YAG pumped dye probe laser (A); 355 nm Nd: YAG photolysis laser (B); pre-amp connected to a PicoScope (C); Photomultiplier tube (PMT); Pressure gauges (P); Thermocouple (T); beam expander (E); dichroic mirror (X) was highly reflective at 282 nm and transmits at 355 nm to allow laser pulses to enter the cell co-linearly; blue arrows represent gas flow.

University of York weather station, and a low-pressure reading from the 10 Torr gauge; these checks gave a reliable calibration for pressure with an uncertainty of $\pm$ 0.5 Torr for the 1000 Torr gauge and $\pm$ 0.1 Torr for the 10 Torr gauge.

Pressure was controlled in the reactor cell by the flow of gases which were set on the mass flow controllers, and by a needle valve which is situated on the outlet tube from the cell to the pump, to regulate pumping speed. These controls allowed pressures of between 4 and 300 Torr to be maintained. During an experimental run both the mass flow controllers and the needle value were unchanged, this kept the pressure constant. In the absence of gas flow, the lowest pressure the cell could achieve was 4 Torr. The lowest pressure experiments that were run were at 10 Torr, while the highest pressure experiments were at 300 Torr.

The apparatus was located in a temperature-controlled laboratory, kept constant at (294 $\pm$1) K. To run experiments at higher temperatures the reactor cell was

heated. Heating tape (Winkler, 375 W, 1.5m) was wrapped around the inlet tube and the middle section of the reactor cell. The heating tape controller box (made by University of York Electronics Workshops) allowed precise control over the heating of the tape, ranging from 0-400 °C. Once the heat tape reached the temperature set on the controller, the experimental run had a constant temperature due to the good temperature stability of the heat tape. Time was allowed for the surfaces to equilibrate so the thermocouple was reading the temperature in the middle of the cell; this time changes depending on the temperature and pressure set in the reactor cell.

## 2.2   Chemicals

Information regarding the chemicals and gases used in this project is presented in Table 2.1. Two different chlorine ($Cl_2$) mixtures were used in experiments: $Cl_2$ (BOC, 5%) either in nitrogen or argon depending on availability. As $Cl_2$ played such a critical role in these experiments, it was important to know its precise concentration at all times. Two different nitrogen oxide (NO) concentrations were used: 10 ppm and 1000 ppm, both were obtained from BOC.

For the room temperature $RCO + O_2$ experiments (Chapter 3), the 5% $Cl_2$ in $N_2$ mixture was diluted to 0.5% in $N_2$ and stored in a stainless steel canister (Restek - SilcoCan, L5861). For the experiments on the Cl and OH rate coefficients (Chapter 4), the new source of OH (Chapter 5), and $RC(O)O_2 + HO_2$ reactions (Chapter 6) the 5% $Cl_2$ in Ar mixture was used.

### 2.2.1   Mixtures

The concentrations of the different aldehydes used in this project were calculated from the vapour pressures of the aldehydes and the total pressure in the container.

Table 2.1: Information on the chemicals used in this project, including which company supplied each chemical.

| Chemical Name | Chemical Formula | Manufacturer | Purity |
|---|---|---|---|
| Nitrogen | $N_2$ | BOC | 99.995% |
| Oxygen | $O_2$ | BOC | 99.999% |
| Chlorine (5% in $N_2$ or Ar) | $Cl_2$ | BOC | 99.999% |
| Nitrogen Oxide (1000 ppm in $N_2$) | NO | BOC | 99.999% |
| Nitrogen Dioxide* | $NO_2$ | BDH | 99.5% |
| Ethanal* | $CH_3CHO$ | Sigma-Aldrich | $\geq$ 99.5% |
| Propanal* | $CH_3CH_2CHO$ | Acros Organics | 99+% |
| Butanal* | $CH_3CH_2CH_2CHO$ | Acros Organics | 99% |
| Pentanal* | $CH_3CH_2CH_2CHO$ | Acros Organics | 97% |
| Nonanal* | $C_8H_{17}CHO$ | Sigma-Aldrich | 95% |
| 2-Methylpropanal* | $(CH_3)_2CHCHO$ | Merck Millipore | 95% |
| 3-Methylbutanal* | $(CH_3)_2CHCH_2CHO$ | Fluorochem | 99% |
| 2-Methylbutanal* | $CH_3CH_2CHO$ | Acros Organics | 95% |
| Decane* | $C_{10}H_{22}$ | Fluka | $\geq$99.8% |
| Methanol* | $CH_3OH$ | VWR | 99.9% |
| Deuterated Methanol* | $CD_3OD$ | Sigma-Aldrich | $\geq$99.8% |

*Notes:* The chemicals that were purified via a freeze-pump-thaw process are marked with *, the others were all used as supplied.

A glass vial containing the concentrated aldehyde was attached to the Schlenk line, allowing the preparation of dilute aldehyde mixtures (Figure 2.3). The process of freeze-pump-thaw-degassing was carried out to purify the sample, removing any dissolved gases and impurities, before the organic mixture was used in the experiment. This technique involves freezing the aldehyde at 77 K, pumping on it while it is still frozen by opening it up to a vacuum, then thawing the aldehyde with a tepid water bath. This process of freezing, pumping and thawing was repeated until the evolution of gas was no longer seen, usually after three cycles. After freeze-pump-thaw-degassing the manifold was closed off to the pump and the aldehyde vial was opened to the manifold. The vial was closed once the aldehyde vapour had built up in the manifold, allowing the manifold to be opened to the pump. Pumping away the first couple of evolutions of the aldehyde vapour increased the purity of the aldehyde mixture when the bulb is filled.

The glass bulb was filled with a small amount of organic vapour, 1-11 Torr, then diluted with $N_2$ to 800-1100 Torr. This was achieved by using the Schlenk line, under vacuum, to transport the organic vapour from a glass vial to a bulb. The bulbs were stored at pressures higher than 1 atm, to reduce the chance of impurities entering the bulb. The bulbs were regularly filled with different organics, therefore at each filling the bulb was cleaned. This was accomplished by heating the bulb, which contained clean $N_2$, with a heat gun before pumping on it by opening it up to a vacuum – this could be repeated multiple times until the bulb was not contaminated by any previous organic mixture.

The concentrations of aldehyde in the bulbs varied for each aldehyde due to their rate of reaction with OH: the more reactive the aldehyde, the less concentrated the bulb was for that aldehyde. This increased the accuracy of the analysis, since the decay of OH will be similar for each organic and therefore a more direct comparison could be made for the production of OH. The uncertainties in the concentration of these organic mixtures was calculated to be approximately $\pm$ 5% of the concentration.
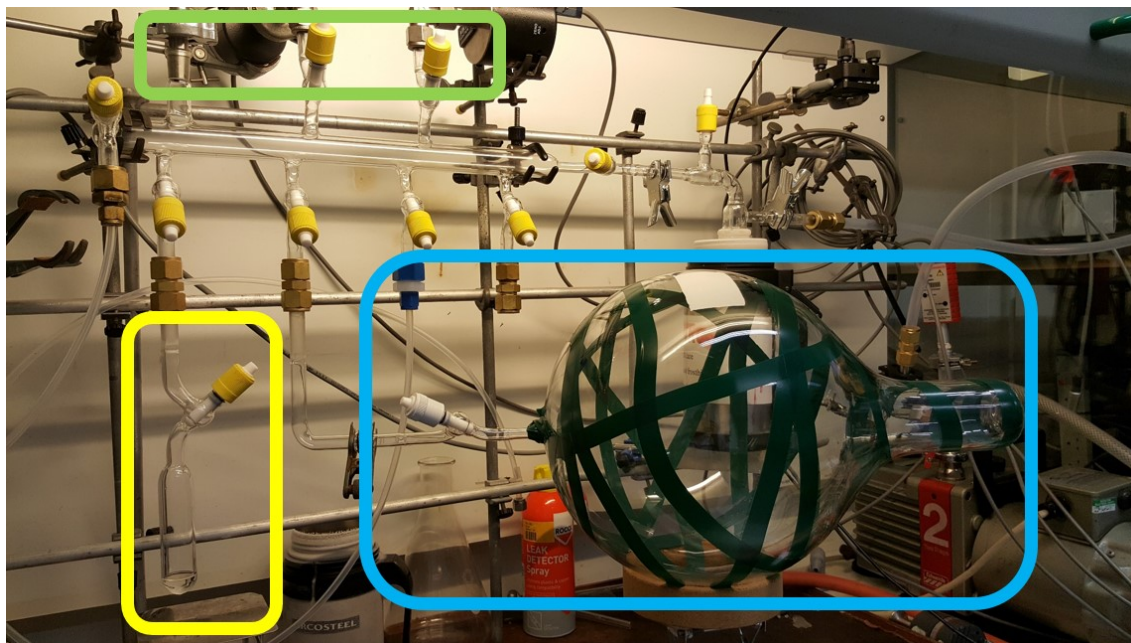


Figure 2.3: The Schlenk line, where the yellow, blue and green boxes show the locations of the vial, the bulb and the three pressure gauges on the line, respectively. There are two Baratron capacitance manometers (10 and 1000 Torr gauges) and a Pirani gauge to measure the gas pressure. This line uses a rotary pump with an $N_2$ (l) trap, reaching a vacuum of $<10^{-1}$ Torr.

## 2.2.2   Gas Flows

Figure 2.4 depicts the five MFCs used to control flows, in standard cubic centimetre per minute (sccm), of $N_2$, $O_2$, and $Cl_2$ and two from aldehydes, methanol or NO mixtures. This arrangement allowed for the ability to flush the MFCs out with nitrogen, or argon after each use. Flushing not only increased the lifespan of the MFCs but also reduced the chance of residue build up, in both the lines and the reactor cell. This flushing facility was crucial to ensure $Cl_2$ removal, and to allow rapid switching between experimental runs using different organics. In later experiments, when investigating $RC(O)O_2$ + $HO_2$ reactions (Chapter 6), a sixth MFC was added which was solely used for NO but was also connected to the $N_2$ line for the MFC to be flushed out.
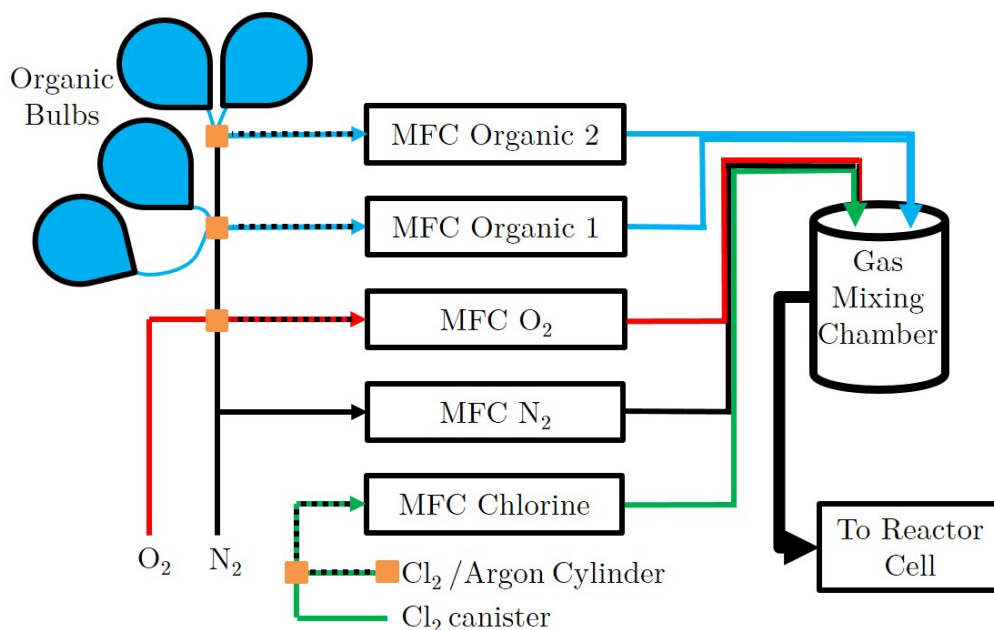


Figure 2.4: Schematic of the gas flow control; three-way taps (orange squares) allowed the organic (blue) and oxygen (red) lines to be flushed with $N_2$; the $Cl_2$ lines (green) were flushed with $N_2$ or Ar. Glass bulbs (not to scale) stored and supplied 12 L of dilute organic in $N_2$ mixtures.

A Gilian Gilibrator-2 NIOSH Primary Standard Air Flow Calibrator (Sensidyne) was used to calibrate the MFCs, Figure 2.5 shows the data from $O_2$, $Cl_2$, and the two organic MFCs. The gas used for the calibrations was $N_2$, then conversions

were applied for the $O_2$ and $Cl_2$ MFCs to convert the $N_2$ flow rate. Calibration is important as the accuracy of the MFCs was relied on to calculate the concentrations of all the species in the reactor cell, which were used as the inputs in the theoretical simulations of the experiments. During the project the MFCs were recalibrated three times, ensuring that the correct calibrations were used throughout the project. The calibrations used for the last set of experiments are shown in Table 2.2.
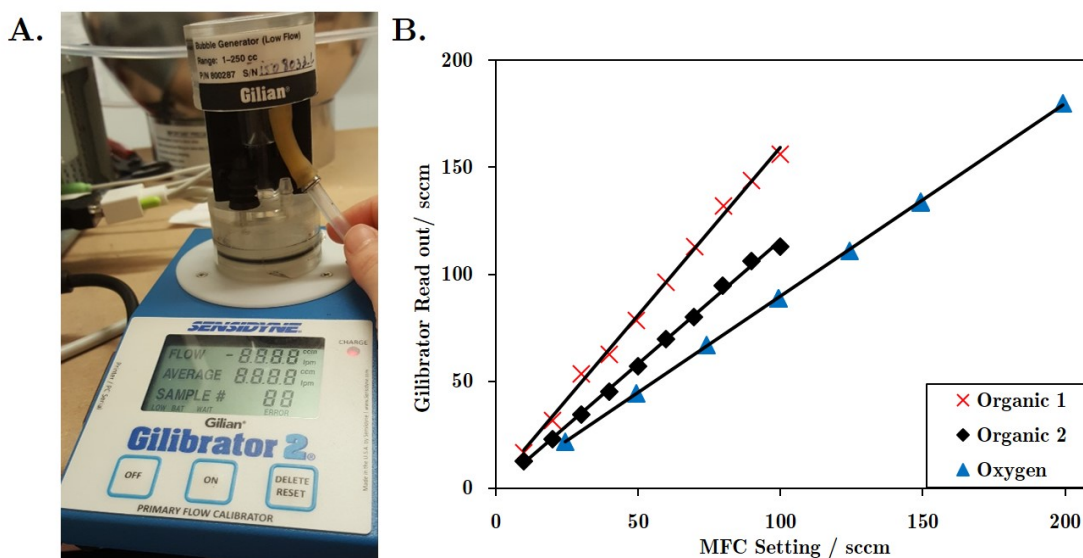


Figure 2.5: A - The Gilian Gilibrator-2 NIOSH Primary Standard Air Flow Calibrator (Sensidyne) which was used to calibrate the MFCs. B - The results of MFC calibration using the Gilian Gilibrator, showing the true value of the gas flow on the $x$ axis and what the MFCs reads out on the $y$ axis.

The error in the gradient of these calibrations were combined with the uncertainties of the bulb concentration ($\approx 5\%$) and pressure gauges ($\approx 1\%$). This gives an uncertainty of less than 5% for mixtures using the $N_2$ and NO MFCs which have the lowest calibration error; however, for the $Cl_2$ MFC it has the largest calibration error associated to it ($\approx 9\%$) giving an uncertainty of 10%. Although when calculating the uncertainty in the concentration of Cl radicals the uncertainty in the power of the photolysis laser and the overlap between the two beams has to be taken into account. The uncertainty in these laser conditions can be as great as 40%, which combined with the uncertainty in the $[Cl_2]$ increases the uncertainty of the $[Cl]$ to up to 50%. This illustrates how critical running experiments back-to-back is, removing the necessity to be able to determine $[Cl]$ with high accuracy and low error.

Table 2.2: The calibration of the MFCs; each MFC has a calibration equation where $y$ is the value it reads out and $x$ is its true value.

| Gas | Range of MFC / sccm | Calibration Equation |
|---|---|---|
| Nitrogen | 0-1000 | $y = (0.9187 \pm 0.0021)x - 4.7469$ |
| Oxygen | 0-200 | $y = (1.1105 \pm 0.0037)x - 0.4131$ |
| Chlorine | 0-50 | $y = (2.2099 \pm 0.1982)x - 0.0651$ |
| Organic-1 | 0-100 | $y = (0.6330 \pm 0.0116)x - 1.1491$ |
| Organic-2 | 0-100 | $y = (0.8653 \pm 0.0133)x - 0.1594$ |
| NO | 0-10 | $y = (0.9712 \pm 0.0064)x + 0.061$ |

*Notes:* These equations are included in all the data sheets allowing the accurate calculations of the concentrations of the gases in the reactor cell.

## 2.3 Lasers

Two laser systems, both controlled externally by a delay generator (BNC 575), were used: 355 nm pulses for $Cl_2$ photolysis and the other 282 nm beam for OH LIF. These laser systems are described below, including details of optics, pulsed laser photolysis and pulsed laser induced fluorescence.

### 2.3.1 Laser Systems

The photolysis laser was a Nd:YAG Laser (Quantel Q-Smart) operating at the third harmonic, 355 nm (200 mJ per 6 ns pulse), used to initialise the reaction by photolysis of $Cl_2$. The power of the laser pulse was closely monitored due its effect on radical concentrations. Experimental runs used a deliberately low optimal power of 0.20 W, equivalent of 20 mJ per pulse. The Q-switch of the laser needed a warm-up time of approximately 10 minutes, as the power of the laser beam could decrease by 0.05 W within the first few minutes. The delay time between the flashlamp and Q-switch of the laser was kept constant at 380 $\mu$s. The photolysis of $Cl_2$ is used as a source of Cl radicals due to its absorption cross section of $1.4 \times 10^{-19}$ cm$^{-2}$ molecule at 355 nm (Reaction 2.1). As $Cl_2$ photolysis occurs at 300 - 370 nm, away from the photolysis of aldehydes, it importantly does not photolyse the aldehydes in

the reactor cell (Keller-Rudek et al. 2013). Figure 2.6 shows the absorption spectra
of three different aldehydes and also $Cl_2$ to illustrate the advantage of using $Cl_2$
photolysis which occurs away from aldehyde photolysis.

$$Cl_2 \rightarrow 2Cl \qquad (2.1)$$
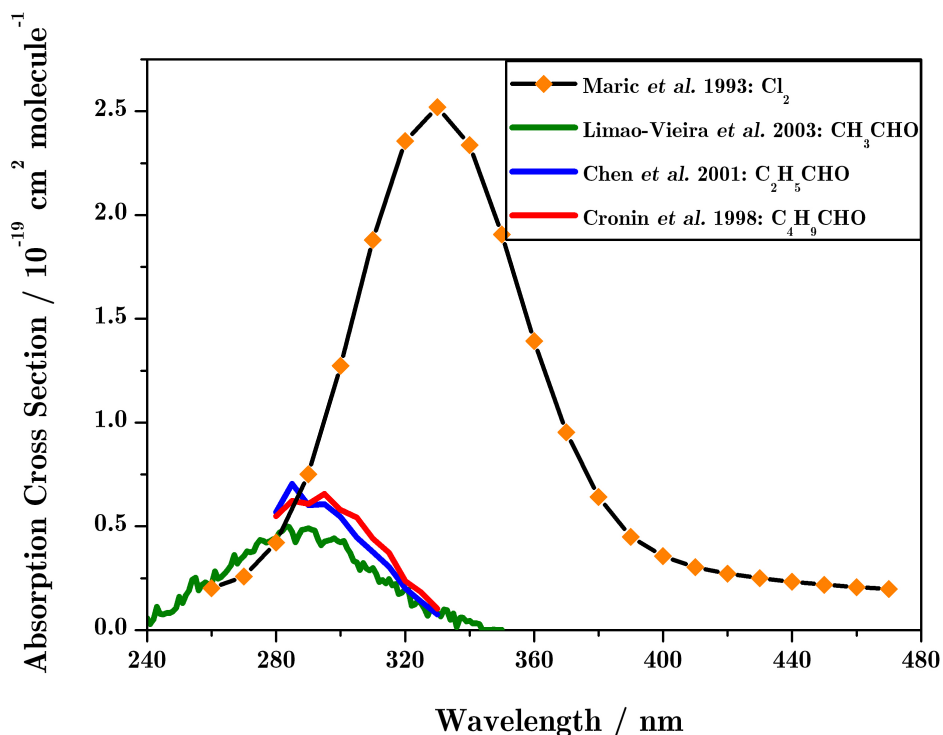


Figure 2.6: Absorption spectra of $Cl_2$ (orange diamonds), $CH_3CHO$ (green line),
$C_2H_5CHO$ (blue line) and $C_4H_9CHO$ (red line) illustrating that the photolysis of
$Cl_2$ at 355 nm will minimise unwanted aldehyde photolysis (Maric et al. 1993; Chen
and Zhu 2001; Limao-Vieira et al. 2003; Cronin and Zhu 1998).

Chlorine radicals react with the aldehyde to form an acyl radical which in turn
reacts with $O_2$; this is the more simple $RCO + O_2$ reaction which can either form
the stabilised $R(O)O_2$ or $OH$ + products (Reactions 2.2 and 2.3). Subsequent, more
complex reactions of $RO_2$ can occur: Reactions 2.4, 2.5, and 2.6.

$$Cl + RCHO \rightarrow HCl + RCO \qquad (2.2)$$

$$RCO + O_2(+M) \rightarrow RC(O)O_2(+M) \; or \; OH \; and \; products \tag{2.3}$$

$$Cl + CH_3OH \rightarrow HCl + CH_2OH \tag{2.4}$$

$$CH_2OH + O_2 \rightarrow HO_2 + CHOH \tag{2.5}$$

$$HO_2 + RC(O)O_2 \rightarrow OH + Products \tag{2.6}$$
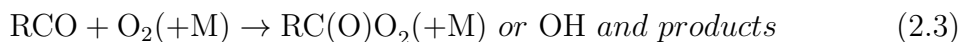
A Nd:YAG laser (Continuum Powerlite Precision) operating at the second harmonic (532 nm, 400 mJ per 6 ns pulse) was used to pump Radiant Dye NarrowScan pulsed dye at 564 nm for OH detection, doubled to a central wavelength of 282 nm by a potassium dihydrogen phosphate (KDP) crystal. The time between the flashlamp and the Q-switch of the Powerlite was kept constant at 350 $\mu$s throughout the project. A recharge pulse for the flashlamp was also required for the Powerlite, set to 3000 $\mu$s after the flashlamp and kept constant throughout. The NarrowScan pulsed dye laser used Rhodamine 6G dye with methanol as the solvent, to produce a broad range of 552 - 580 nm for the lasing wavelength. Two different solutions were required: $2.2 \times 10^{-4}$ M for the oscillator cell, and $3.2 \times 10^{-5}$ M for the amplifier. The KDP doubling crystal in the NarrowScan laser lacked an insulating jacket, impacting the output of the laser since the crystal warmed when the laser beam passed through. Therefore, before tuning the doubling crystal for an experiment, the crystal was allowed approximately 20 minutes to warm up. This is crucial since the 282 nm beam needed to be stable throughout the experiment; any change directly impacted the amount of OH detected. The 282 nm beam was isolated from the parent 564 nm wavelength by a filter.

In later experiments the fluorescence of the deuterated hydroxyl radical (OD) was recorded from the excitation at 287.7 nm (Chapter 6) - the $A^2\Sigma^+(\nu'=0) \leftarrow X^2\Pi^+(\nu''=0)$ transition. The difference in wavelengths between OH and OD fluorescence, illustrated in Figure 2.7, shows that it is possible to run traces at wavelengths which only excite OH or OD (Luque and Crosley 1999). Fortunately for these experiments the concentrations of the two dyes were kept the same and only the crystal needed to

be tuned once the grating crystal has moved to the dye laser output to the different wavelength.
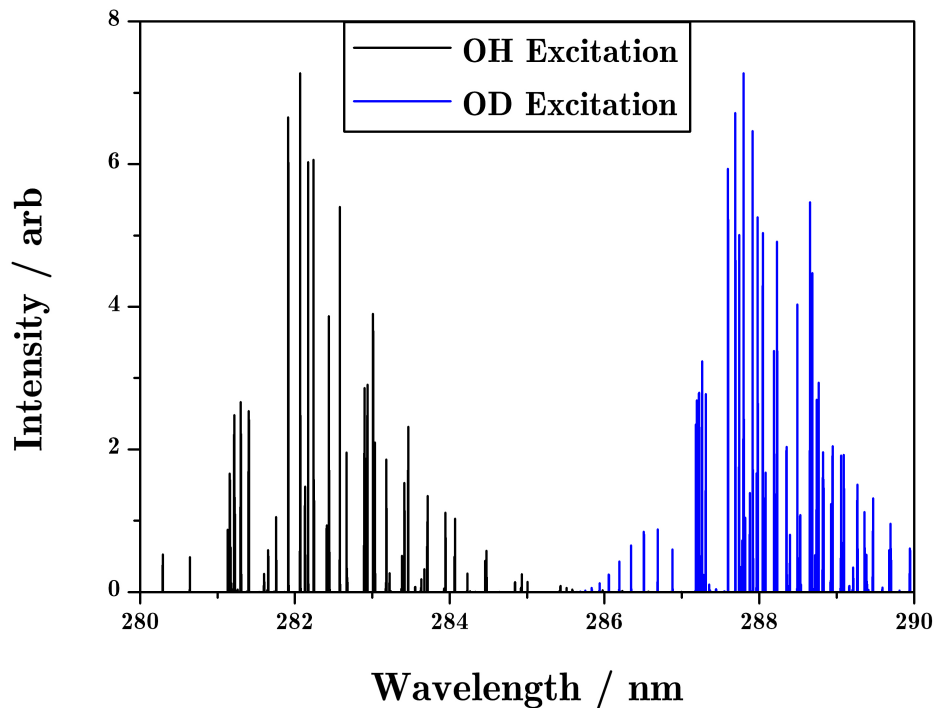


Figure 2.7: Excitation spectra of OH (black) and OD (blue) - data from LIFBASE (Luque and Crosley 1999).

## 2.3.2 Laser Optics

The periscope, Figure 2.8, lowers the 282 nm beam from the dye laser to the same height as the 355 nm beam. This periscope was created in-house, using two 282 nm mirrors (OptoSigma, TFM-25.4C05-282), angling the beam downwards. The iris diaphragm, placed after the periscope, set the 282 nm beam to a circular diameter of 2 mm. A dichroic mirror (OptoSigma, TFM-25.4C05-282), placed after this iris, has a high transmission (low reflectivity) for 355 nm and a high reflectivity at 282 nm, allowing the overlap of the two beams through the mirror. Three 355 nm mirrors (OptoSigma, TFM-25.4C05-352/355) angle the 355 nm beam in the correct place to pass through this dichroic mirror. The beams were assumed to be overlapped in
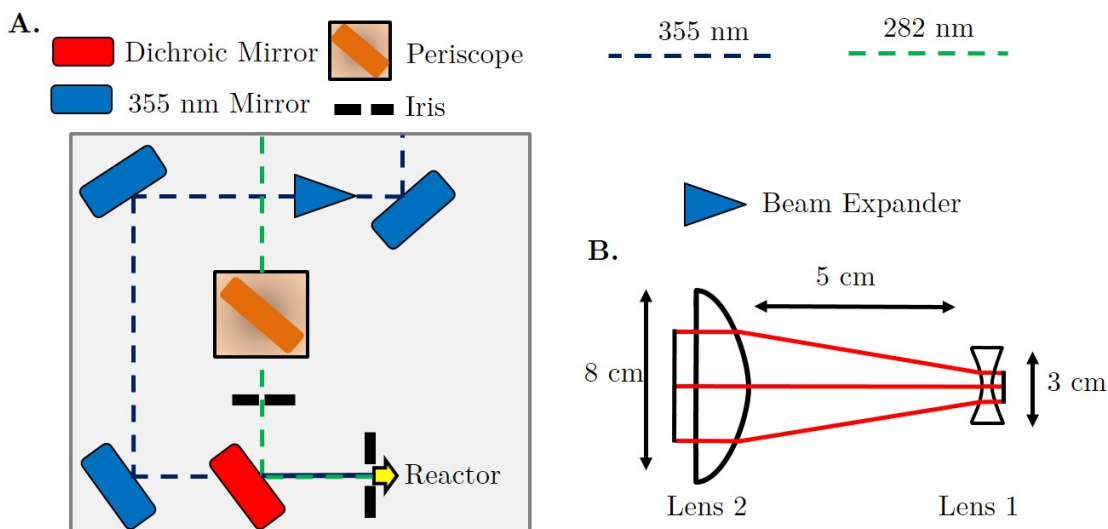
Figure 2.8: A - Schematic view of the optics set-up, a dichroic mirror allows the two laser beams to enter the reactor cell overlapped. B - Schematic of the Galilean Beam Expander, consists of two lenses - one with a positive focal length (lens 2, diameter = 8 cm) and the other with a negative (lens 1, diameter = 3 cm). The distance between the two lenses is equal to the sum of the focal lengths of the two lenses (Newport 2011)

the centre of the cell if they overlapped before and after the cell. Beam overlap was extremely important; the 282 nm beam was aligned to the centre of the 355 nm, so the OH fluorescence recorded was only from the reaction which the 355 nm beam has initialised. The beam dump was carefully positioned slightly off perpendicular after the cell, as the PMT was able to pick up reflected laser light which interfered with the results.

The 355 nm laser beam original diameter is approximately 6 mm; a beam expander is used to increase the beam diameter to approximately 11 mm which gave the 282 nm a greater area to probe the photolysis. Two lenses, one convex and one concave, were used to construct a Galilean-type beam expander (Newport 2011). The focal length of the lenses determined the distance at which they were set from each other: $f_2 + f_1$, where $f_2$ is the focal length of the larger exit lens (convex) and $f_1$ of the smaller input lens (concave - a negative value). The lenses were 3 cm and 8 cm in diameter, therefore the distance set between the two lenses was 5 cm, giving a magnification of 2.63. The beam expander gave a small amount of scatter so there

is a final iris, 1 cm in diameter, before the beams pass into the cell.

The photomultiplier tube (PMT, Hamamatsu R11540), positioned orthogonally to both laser beams, detected photons emitted from the OH radical. Being orthogonal to the beams is ideal as it reduces the pick up from the laser beams, helping to increase the signal-to-noise ratio. This fluorescence signal was focused onto the PMT by two plano-convex lenses (OptoSigma, SLSQ-25.4-50p), converging the signal to a point, Figure 2.9. Noise from the laser beams was reduced by two filters: a 309 nm interference filter (OptoSigma, VPF-25C-10-15-30710) and a 305 nm cut-off filter (Materion 8M848 - F-NB-0009650). These filters blocked any light above 309 nm and below 305 nm, this range included both laser beams. A PicoScope 5443B collects the voltage from the PMT which corresponds to the fluorescence signal, where the PicoScope software converts the signal from the PMT into a data file for analysis. An Oscilloscope (Tektronix MSO 2024B) was also used to display the fluorescence signal, when tuning the KDP doubling crystal on the dye laser.
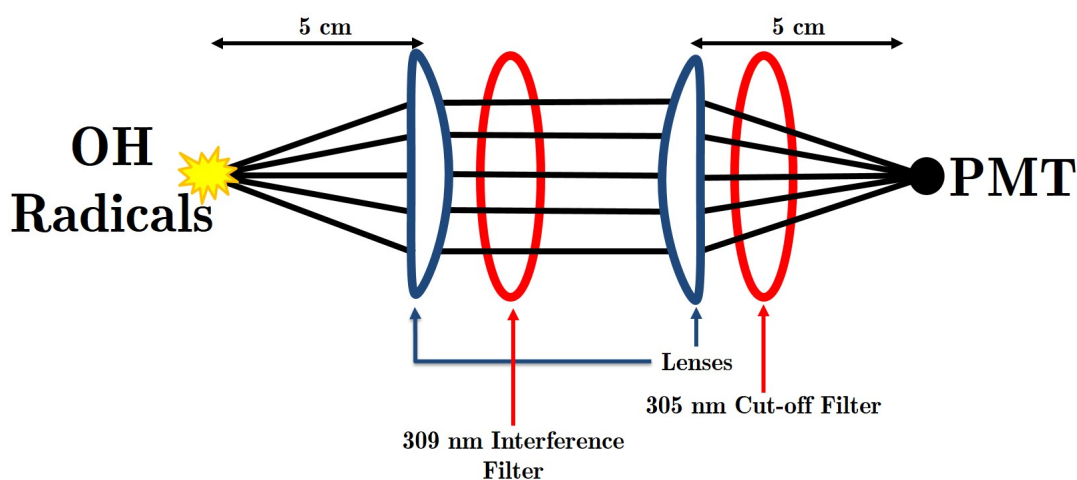


Figure 2.9: Schematic showing the position of the two plano-convex lenses and the two filters (a 309 nm interference filter and a 305 nm cut-off filter). This arrangement was able to converge the fluorescence signal onto the PMT and to block out unwanted noise from the lasers. This allowed the PMT to be located away from laser scatter and heated reactor cell.

## 2.4    Data Collection

Two types of experiments were carried out in this project: laser excitation spectra (Figure 2.10) and kinetic traces. Laser control was essential for both these experiments, and was achieved by connecting both lasers to the delay generator which precisely controlled pulse durations and trigger times. Initially the delay generator was controlled manually, and this yielded good results for laser excitation spectra but poor results for the kinetic traces. To improve the kinetic traces LabVIEW code was developed, which was key for running experiments with greater control, higher accuracy and on a faster time scale, increasing the efficiency of experiments. The main problem when LabVIEW was first set up was compatibility issues between the older YAG laser and the PicoScope; there was no existing software available for this so the code was developed from basics. Therefore a lot of time was spent developing software to work with our experimental set-up. Two LabVIEW codes were developed in this project, allowing more data points to be recorded which increased the accuracy of results. To extract and analyse data, python and MATLAB codes were developed alongside the improvements in automating the experimental system (Appendix A).

### 2.4.1    Laser Excitation Data Collection

Laser excitation spectra were produced to allow the confirmation of fluorescence to be OH (or OD) (Heard and Henderson 1999; Bailey et al. 1999). This meant that the fluorescence was recorded while the wavelength was scanned using the dye laser, so spectra codes were required to calculate the area of the fluorescence peak for each wavelength buffer (Figure 2.11) and assign each data point to its corresponding wavelength.

The delay time between the two lasers was kept consistent throughout these

experiments as it was the change in the fluorescence over different wavelengths that was examined. This meant no LabVIEW code was needed, PicoScope software was used to recorded the fluorescence signal from the PMT. The dye laser was connected to the NarrowScan Laser Control, Rev.1.2 2002 software where parameters were set to control the scan speed and the wavelengths that were scanned. For the PicoScope to start recording data at the same time as the scan was started, the start buttons were simply pressed together manually.

To minimise noise in the results, data extraction took into account the signal from the corresponding blank run, collected straight after the run with the fluorescence data, this improved the signal-to-noise ratio. Since there was no auto-tracker in the dye laser, a full spectrum experiment used six runs rather than one large run. This also allowed the KDP doubling crystal to be tuned throughout the experiment to give a clearly defined spectra. The code was developed so that the smaller runs were combined to produce a full spectrum with the spectral database spectrum 'LIFBASE' overlaid, allowing direct comparison between our results and numerical simulations. The results of these are described and explained in greater detail in Chapters 3 and 6.

## 2.4.2   Basic Manual Kinetics

For kinetic experiments the pulses controlling the 282 nm laser were maintained with the Q switch firing at 1000 $\mu$s after $T_0$, while the pulses which controlled the 355 nm laser were moved so the Q-switch fired between 500 and 1050 $\mu$s after $T_0$. This allowed the rise and decay of OH to be observed, which in turn allowed the calculation of OH yields. In preliminary experiments, the timing of the probe laser was kept constant while the photolysis laser timings were changed manually. For this, the photolysis laser trigger was turned off, the time on the delay generator was altered, then the trigger was turned back on. The photolysis laser was chosen for this role as it had a shorter warm-up time than the older probe laser. Once on,
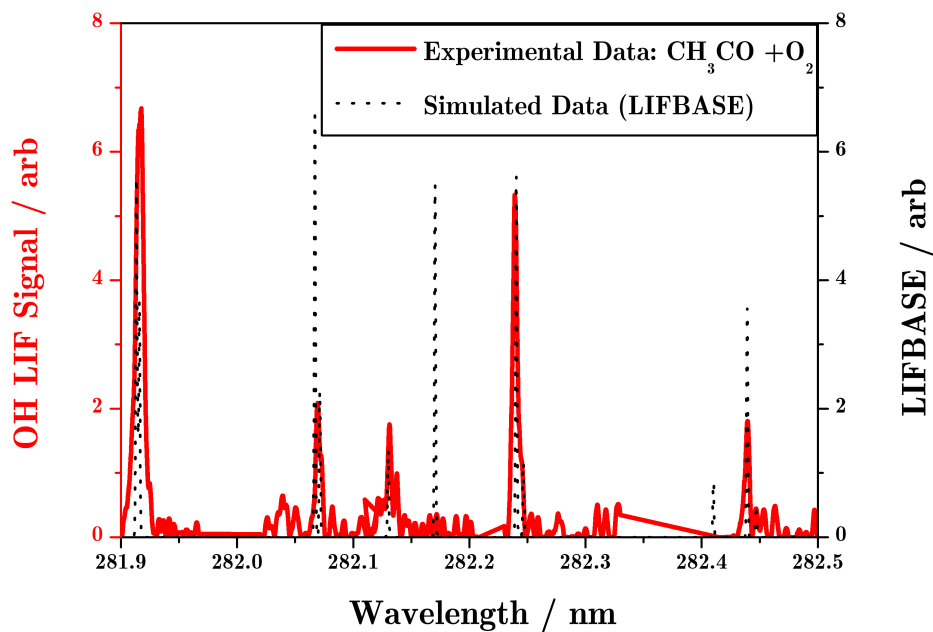
Figure 2.10: LIF Excitation Spectra of $CH_3CO + O_2$ (red line) alongside LIFBASE (dotted black line) (Luque and Crosley 1999). Carried out at 18 Torr and concentrations (in molecule $cm^{-3}$): $CH_3CHO = 1.8 \times 10^{-14}$, $O_2 = 1.0 \times 10^{-17}$, $Cl_2 = 6.5 \times 10^{-14}$, $Cl = 9.3 \times 10^{-12}$.
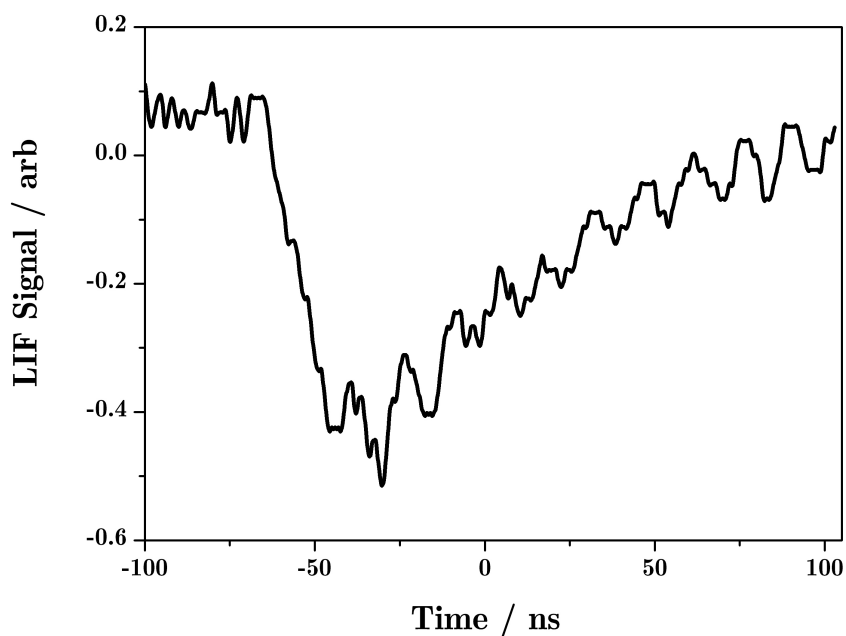


Figure 2.11: A typical OH LIF signal recorded from PicoScope for a LIF Excitation Spectra.

the fluorescence at this specific time period was recorded using the PicoScope. This was a very lengthy and laborious process so only eight data points were recorded for each decay. However, this meant the fitting function had trouble fitting the decay curve through the sparse data points. The fit of the OH rise and decay was used for the OH yield calculation, meaning more data points were needed to obtain a more accurate result.

### 2.4.3   First Generation LabVIEW

To speed up and automate data collection, a simple LabVIEW code was created which interfaced the delay generator with the computer, as shown in Figure 2.12. The code kept the probe laser trigger at a constant delay throughout the experiment but altered the photolysis laser trigger after a set amount of time, moving the photolysis pulse fourteen times in total. The PicoScope was not connected to LabVIEW for this code, which meant at the start of each experimental run PicoScope and LabVIEW were manually pressed to start at the same time, with PicoScope recording the data as a whole set.

This code was a great improvement from the first experimental set-up but it was not ideal as LabVIEW did not control PicoScope. This gave slower data extraction, with data points in the middle of each time period only used for the analysis, as they were the readings that were certain to be at that specific time period. It also affected how expansive the data collection was, with more points being collected to allow for a better average to be calculated. This affected experimental runs, as they are ideally recorded quickly using back-to-back reactions over a short space of time - a calibration reaction run either side of an unknown reaction. Therefore data collection was concentrated on the rise of OH more than the decay, since the OH decay is known to be well constrained by the aldehyde reacting with OH.
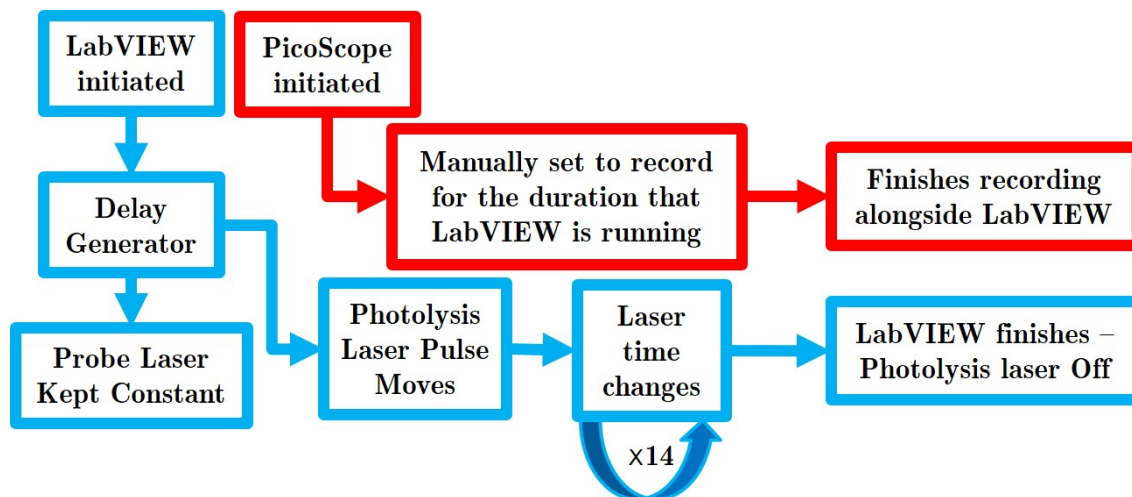
Figure 2.12: Schematic of first generation of LabVIEW code, which connected the delay generator to the computer. At the start of a run, both the LabVIEW code and the PicoScope software were manually initialised at the same time.

### 2.4.4   Second Generation LabVIEW

The Dainton Laboratory at the University of Leeds developed a more complex LabVIEW code which was generously shared with us. The code was able to interface and control both the delay generator and the PicoScope, as shown in Figure 2.13. This was more complicated and at first was not suitable for our different instruments, but once parts of the code were modified it worked well. This code allowed greater control and accuracy of the experimental runs than the previous code due to the range of options embedded in it. The options included: scan length, number of laser shots per time point, number of time points per scan and number of scans for each run. This made it easier when different reactions were looked at, for example a time-scale of 500 $\mu$s for one type of reaction could be changed to 10,000 $\mu$s for another with a simple click. Another advantage was the way the data were outputted and how it allowed the user to see the data in real time, therefore reducing the need to repeat experiments - if the run is going badly it can be simply restarted.

The inclusion of LabVIEW software improved the data substantially, as shown in Figure 2.14. The first set of experiments which ran without LabVIEW have few data points with a lot of scatter. This is mostly just due to the noise of the experiment,
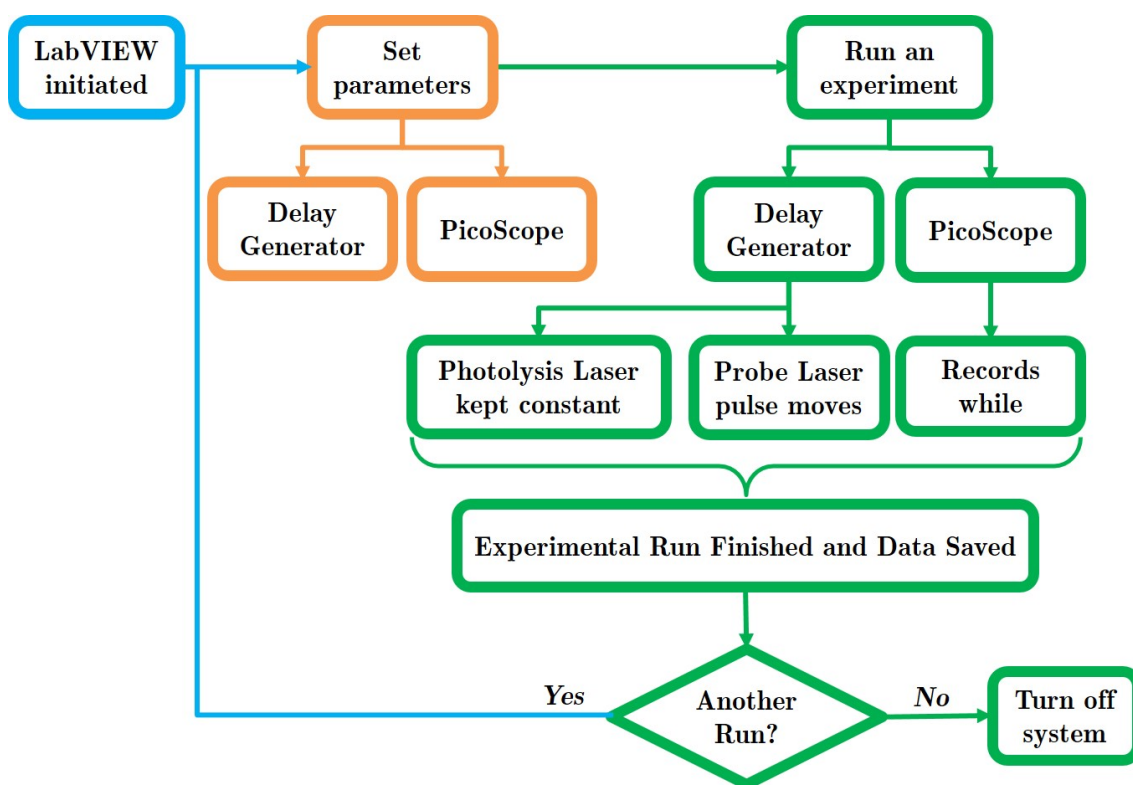
Figure 2.13: Schematic of second generation of LabVIEW code, which connected both the delay generator and PicoScope to the computer.

including electrical noise from other experiments occurring in the laboratory. This scatter improved when LabVIEW was used as it recorded more data points which were averaged in data extraction. The first LabVIEW code, more data points can be seen enabling the rise and decay of OH to be constrained more accurately. The more complex and sophisticated LabVIEW code gave the best results, with the whole OH profile displayed it allowed the OH yield to be determined with higher accuracy and less uncertainty. The improvement in the data quality was not the only advantage with using LabVIEW, it also enabled the time for each data acquisition to decrease substantially, for example: the no LabVIEW runs took approximately 30 mins, while first generation LabVIEW took approximately 5 mins and second generation LabVIEW around approximately 3 mins.

The codes for the extraction and analysis of data from kinetic traces evolved alongside the development of LabVIEW code which simplified the extraction. In all kinetic traces background noise was taken into account, recorded when no OH fluorescence
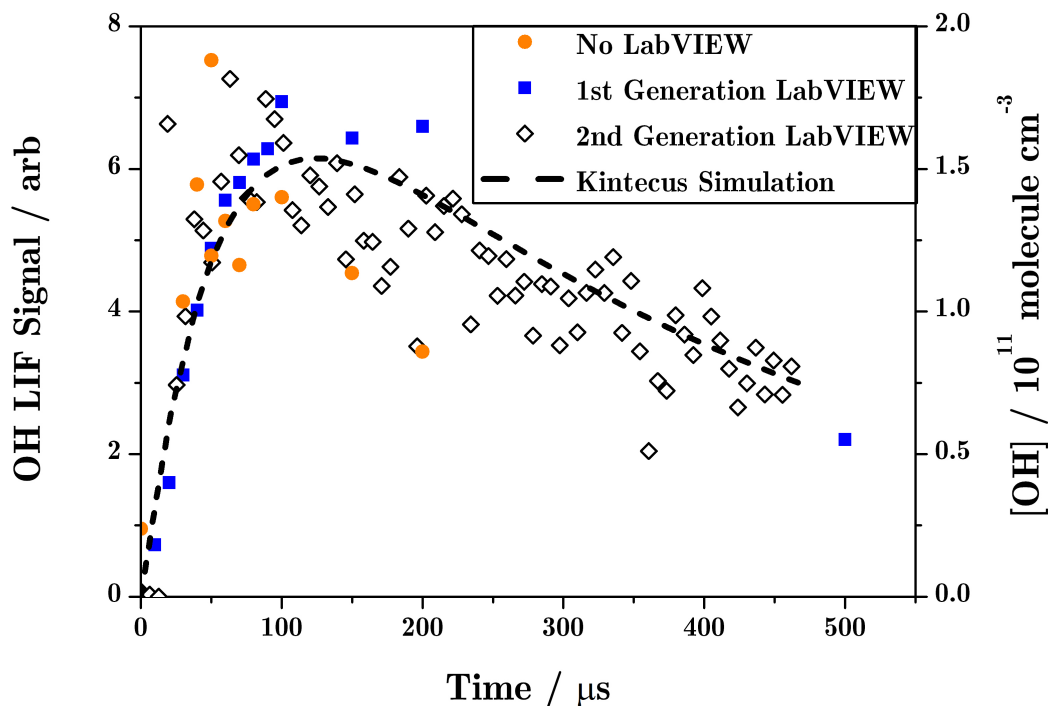
Figure 2.14: Comparison how kinetic data differs when different codes are used. These traces are all for the reaction $CH_3CO + O_2$ at approximately $(30 \pm 2)$ Torr at 294 K, collected over a year's span - can be compared to the Kintecus simulation as all had similar experimental conditions.

occurred, this increased the signal-to-noise ratio. For the first set of kinetic traces, no LabVIEW is used so for each time point there is a corresponding file output from PicoScope. Similar to the spectra code, this code summed the area of the fluorescence peaks as each time point recorded an average of twenty wavelength buffers - each buffer contains the fluorescence peak at that specific time. The kinetic traces which used the first generation LabVIEW code, recorded 3000 wavelength buffers. The middle 100 wavelength buffers of each time period were averaged to calculate a LIF intensity associated for that particular time period, therefore giving an output of a LIF intensity value for each time period. Since the second generation LabVIEW code connects to both the PicoScope and LabVIEW at the same time, the data outputs two columns - one the time and the other the intensity. The only necessary data extraction is taking into account the noise of the intensities and the fitting of the graph to the curve. All kinetic data were fitted to obtain a value for

the OH yield, the same fitting function was used throughout in MATLAB for all the results - discussed in more detail in Chapter 3 (Section 3.4).

# Bibliography

Baardsen and Terhune (1972). "Detection of OH in the atmosphere using a dye laser". In: *Applied Physics Letters* 21.1972, pp. 209–211.

Bailey et al. (1999). "Collisional quenching of OH by $N_2$, $O_2$ and $CO_2$ between 204 and 294 K. Implications for atmospheric measurements of OH by laser-induced fluorescence". In: *Chemical Physics Letters* 302.1, pp. 132–138.

Chen and Zhu (2001). "The wavelength dependence of the photodissociation of propionaldehyde in the 280-330 nm region". In: *Journal of Physical Chemistry A* 105.42, pp. 9689–9696.

Cronin and Zhu (1998). "Dye Laser Photolysis of n-Pentanal from 280 to 330 nm". In: *The Journal of Physical Chemistry A* 102.50, pp. 10274–10279.

Heard and Henderson (1999). "Quenching of OH by several collision partners between 200 and 344 K. Cross-section measurements and model comparisons". In: *Physical Chemistry Chemical Physics* 2.1, pp. 67–72.

Keller-Rudek et al. (2013). "The MPI-Mainz UV/VIS spectral atlas of gaseous molecules of atmospheric interest". In: *Earth System Science Data* 5.2, pp. 365–373.

Limao-Vieira et al. (2003). "Electronic state spectroscopy of acetaldehyde, $CH_3CHO$, by high-resolution VUV photo-absorption". In: *Chemical Physics Letters* 376.5-6, pp. 737–747.

Luque and Crosley (1999). "LIFBASE: Database and Spectral Simulation Program (Version 1.5), SRI International Report MP 99-009". In:

Maric et al. (1993). "A Study of the UV Visible Chlorine Absorption Spectrum of Molecular Chlorine". In: *Journal of Photochemistry and Photobiology A: Chemistry* 70, pp. 205–214.

Newport (2011). "Optical Components: How to Build a Beam Expander". In: *Optics Technical Note 1.*

# Chapter 3

# Reactions of Acyl Radicals with Oxygen

Acyl radicals play a key role in atmospheric chemistry and were discussed fully in Chapter 1. Involved in a rich and diverse chemistry, acyl radicals are central in numerous reactions both in the atmosphere and in combustion chemistry (Chapter 1).

There have been multiple studies of the OH yield from $CH_3CO + O_2$, however the OH yields from other RCO compounds reacting with $O_2$ are barely known. This project applies the literature knowledge of $CH_3CO + O_2$, to construct a relative OH yield experiment to determine OH yields for other RCO compounds. This chapter discusses the results from seven different $RCO + O_2$ reactions – stating the first OH yields for six of these reactions. By building on the previous literature knowledge, this chapter will show how the OH yield changes with different R groups on the $RCO + O_2$ .

## 3.1 Previous Studies of Acetyl with Oxygen

The reaction of acetyl with oxygen has been extensively studied, with the majority of the rate coefficients reported in good agreement. The first study of $CH_3CO + O_2$ (Reaction 3.1a) occurred in 1982, using photo-ionization mass spectrometry – a direct kinetic measurement (McDade, Lenhardt, and Bayers 1982). Limited to low pressure studies (1 – 4 Torr) with a helium carrier gas, acetyl radicals were formed by the photolysis of acetone using a xenon flash lamp – ideal since the lifetime of the flash (20 $\mu$s) is shorter than that of the radicals. The observed acetyl radicals had a mass charge ratio of 43, though only the ions with accumulations of $10^3$ – $10^4$ flashes were able to give enough signal for data analysis. This amount of signal needed for the mass spectrometry could be the reason why, unsurprisingly, no OH radicals were seen.

Employing a non-linear least-squares method to a double-exponential equation, McDade, Lenhardt, and Bayers (1982) observed the rate coefficient to be $(2.0 \pm 0.4) \times 10^{-12}$ cm$^3$ molecule$^{-1}$ s$^{-1}$ at 1 - 4 Torr, which differs from the recent IUPAC evaluated value: $(5.0 \pm 0.3) \times 10^{-12}$ cm$^3$ molecule$^{-1}$ s$^{-1}$ at 1 atm (Atkinson, Baulch, Cox, Crowley, Hampson, Hynes, Jenkin, Kerr, et al. 2007). This difference between the two rate coefficients suggests a low accuracy for the study by McDade, Lenhardt, and Bayers (1982), although this discrepancy could be caused by the pressure dependency of the reaction. It wouldn't be till the study of Tyndall, Orlando, Wallington, and Michael (1997) that a pressure dependency would be suggested from their investigations between 0-1100 Torr.

$$CH_3CO + O_2 + M \rightarrow CH_3C(O)O_2 + M \qquad (3.1a)$$

$$\rightarrow OH + CH_2C(O)O \qquad (3.1b)$$
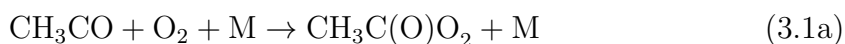
The formation of OH was still unknown until 1985, when OH production was first

observed but not quantified (Michael, Keil, and Klemm 1985). Michael, Keil, and Klemm (1985) measured the absolute rate coefficients of the reaction $CH_3CHO + OH$ using the discharge flow – resonance fluorescence (DF–RF) method. In results of preliminary scavenger experiments, if $[O_2]$ was large enough, the reformation of OH was so great that the OH radical first-order rate constant was comparable to wall loss only, suggesting that OH regeneration was occurring in their system. This OH regeneration via $CH_3CO + O_2$ was evident again by Tyndall, Staffelbach, et al. (1995) when they were studying the $CH_3CHO + OH$ rate coefficient; however, chamber experiments using fourier transform – infrared spectroscopy (FT–IR) were unable to observe OH regeneration directly.

The later study by Tyndall, Orlando, Wallington, and Michael (1997) analysed the $CH_3CO + O_2$ reaction in two different experimental chambers, both equipped with FT–IR systems enabling the calculation of the $CH_3CO + O_2$ rate coefficient as a function of pressure from 0.1 to 1100 Torr. The study gave a constant value of $(7 \pm 2) \times 10^{-13}$ molecule$^{-1}$ s$^{-1}$ cm$^3$ from 0.1 to 2 Torr for the rate coefficient, which then increased to a high-pressure limiting value of $(3.2 \pm 0.6) \times 10^{-12}$ molecule$^{-1}$ s$^{-1}$ cm$^3$ – consistent with present literature (Atkinson, Baulch, Cox, Crowley, Hampson, Hynes, Jenkin, Kerr, et al. 2007). Tyndall, Orlando, Wallington, and Michael (1997) gave two possible explanations for this pressure dependence. The first suggested that the dependence came from the competition between the stabilisation and the decomposition of the excited acetylperoxy species. Tyndall, Orlando, Wallington, and Michael (1997) linked this competition to the formation of OH from the excited acetylperoxy species. The second explanation they suggested was that a pressure-independent bimolecular reaction occurs concurrently with the pressure-dependent formation of acetylperoxy reaction.

To achieve OH product yields, Tyndall, Orlando, Wallington, and Michael (1997) carried out the oxidation with and without NO or $NO_2$, giving OH yield to be near 10% at 60 Torr and about 50% at approximately 6 Torr. The system was also chemically modelled to show how the reaction system would perform if OH was produced,

which gave the OH branching ratio to be 0.85 at a pressure of 1.2 Torr. Tyndall, Orlando, Wallington, and Michael (1997) completed the first study of $CH_3CO + O_2$ reaction in a bath gas of $N_2$, but it was almost a decade later that Hou, Li, et al. (2005) made a comparison between their theoretical results and the results of Tyndall, Orlando, Wallington, and Michael (1997). Hou, Li, et al. (2005) calculated the potential energy surface of the $CH_3CO + O_2$ reaction by using *ab initio* methods. They suggested that the acetylperoxy radical $(CH_3C(O)OO)$ is the initial adduct with the only energetically accessible decomposition channel forming the $\alpha$–lactone and OH. There is good agreement between the OH yields calculated by this theory and the experimental data from Tyndall, Orlando, Wallington, and Michael (1997).

The first temperature-dependent study and the first direct measurement of the OH yield in the $CH_3CO + O_2$ reaction was carried out by Blitz, Heard, and Pilling (2002), who observed the OH formation directly using laser induced fluorescence (LIF). The study was carried out in a He bath gas and the results follow the previous study of Tyndall, Orlando, Wallington, and Michael (1997), showing the OH yield to decrease with increasing pressure. Two temperatures were investigated (295 and 213 K), suggesting the OH yield increased slightly with lower temperature: at [He] $\approx 1 \times 10^{19}$ molecule $cm^{-3}$ the OH yield is $(0.090 \pm 0.008)$ at 295 K but is $(0.183 \pm 0.005)$ at 213 K.

Carr, Baeza-Romero, et al. (2007) studied the OH yields from $CH_3CO + O_2$ using an internal standard – the flash photolysis of $CH_3C(O)OH$ which creates equal amounts of OH and $CH_3CO$ at time zero. This study examined the bath gas effect, carrying out an experimental run with He and another with $N_2$. A comparison between the $N_2$ bath gas data of Carr, Baeza-Romero, et al. (2007) and Tyndall, Orlando, Wallington, and Michael (1997) showed the more recent Carr, Baeza-Romero, et al. (2007) data gave a higher OH yield, indicating that quenching occurs at a lower rate than previously thought. This, however, could be due to the error within the internal standard, since the previous experimental results from Tyndall, Orlando, Wallington, and Michael (1997) agree with the theoretical data from Hou, Li, et al.

(2005). On the other hand Carr, Baeza-Romero, et al. (2007) agree with the previous yields reported by Blitz, Heard, and Pilling (2002) who assumed a unity yield of OH at zero pressure for $CH_3CO + O_2$. Figure 3.1 illustrates this discrepancy in the literature, showing results of five studies carried out in a He bath gas. The studies of Blitz, Heard, and Pilling (2002), Carr, Baeza-Romero, et al. (2007), and Carr, Glowacki, et al. (2011) are shown to agree closely, but disagree substantially with the results of Kovacs et al. (2007) and Gross, Dillon, and Crowley (2014). This discrepancy has been probed by a more recent study from Papadimitriou et al. (2015) to examine the OH yield in both He and $N_2$ bath gas, which agrees with the original Tyndall, Orlando, Wallington, and Michael (1997) study and also the studies of Kovacs et al. (2007) and Gross, Dillon, and Crowley (2014).
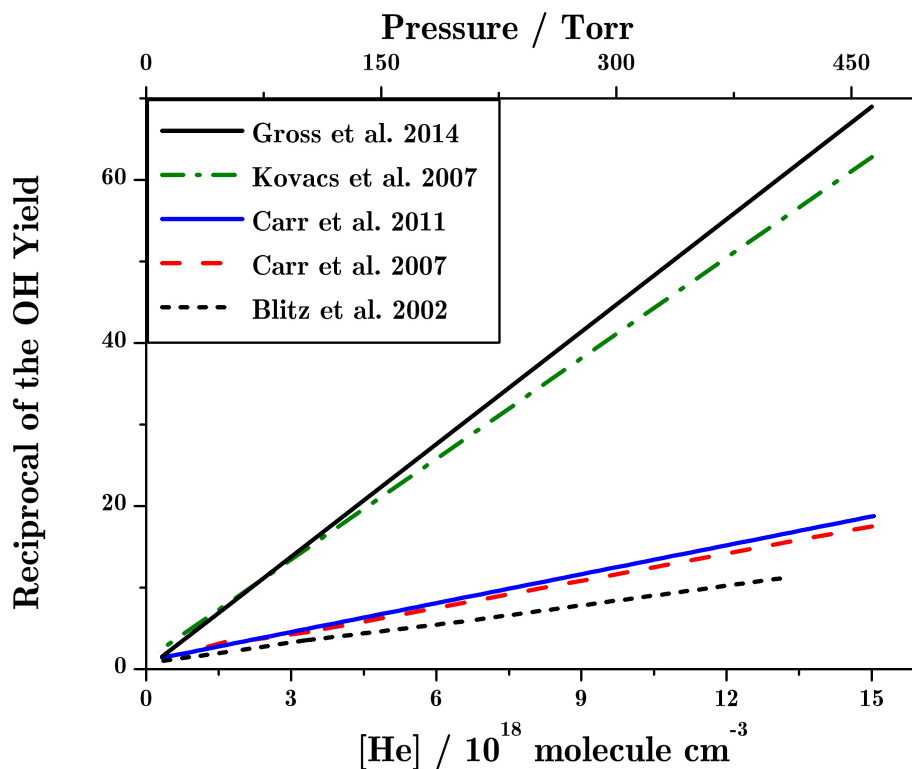


Figure 3.1: Plot of the reciprocal of the OH yield against bath gas number density [He] or pressure.

Though this reaction has been studied extensively by experiment there have only been a couple of theoretical investigations, the first theoretical investigations of $CH_3CO + O_2$ occurred via density functional and *ab initio* calculations by (Lee,

Chen, and Bozzelli 2002). This allowed the reaction pathways and kinetics of the system to be evaluated and these evaluations agreed with later studies by Hou, Li, et al. (2005) and Maranzana, Barker, and Tonachini (2007). However, when Maranzana, Barker, and Tonachini (2007) calculated a potential energy surface for this reaction, they were unable to locate a transition state for $CH_3CO + O_2$ and questioned the accuracy of the transition state calculated by Hou, Li, et al. (2005). Since this project has not investigated the theoretical side of this reaction, it will not be discussed in great detail; however, the $\alpha$–lactone co–product which was first suggested by the theoretical investigations was first observed directly by (Chen and Lee 2010) using pulsed photolysis coupled with step scan FT–IR. Though the yield they obtained for the $\alpha$–lactone at a pressure of 100 Torr is less than the yields of OH observed in the previous literature, it was suggested this could be due to the fragmentation of the $\alpha$–lactone.
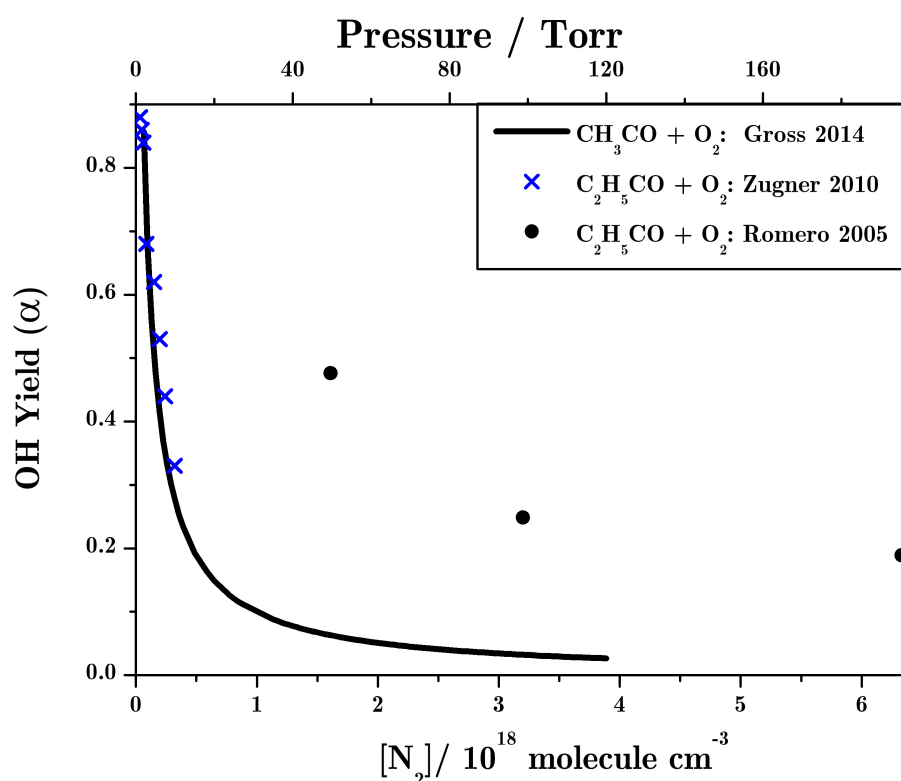


Figure 3.2: Plot of the OH yield against bath gas number density $[N_2]$ or pressure, for the two literature studies of $C_2H_5CO + O_2$: Romero et al. 2005 (black circles) and Zugner et al. 2010 (blue crosses); along with results from Gross et al. 2014 of $CH_3CO + O_2$.

Other acyl radical reactions with $O_2$ have not been studied so much. Only one theoretical study has been carried out on a different acyl radical and that is $C_2H_5CO$ + $O_2$ by Hou and Wang (2007). Using full coupled cluster theory with the complete basis set they were able to show $C_2H_5CO$ + $O_2$ produces a propionylperoxy radical which decomposes to form OH and the three-centre $\alpha$–lactone, or sometimes the four–centre $\beta$–lactone. They gave the OH yield to be close to unity at low pressure but it decreases rapidly as pressure increases. They carried out the study at two temperatures: 295 and 213 K, which showed at the lower temperature the OH yield decreased – this is the opposite of the results from the study of $CH_3CO$ + $O_2$ by Blitz, Heard, and Pilling (2002) which gave the lower temperature a higher OH yield. There have been two experimental studies on the $C_2H_5CO$ + $O_2$ reaction: Zügner et al. (2010) and Romero et al. (2005). Figure 3.2 illustrates the difference between the two studies: Zügner et al. (2010) examine the low-pressure OH yields while Romero et al. (2005) investigate higher pressure yields. They both agree that $C_2H_5CO$ + $O_2$ gives a much higher OH yield than $CH_3CO$ + $O_2$; however, they disagree substantially on the amount of OH. These studies will be discussed in more detail alongside the results from this project later on in the chapter.

## 3.2   Experimental

Seven RCO + $O_2$ reactions were investigated with the results of their OH yields analysed in this chapter – Reactions 3.2, 3.3, 3.4, 3.5, 3.6, 3.7 and 3.8. The reaction of $CH_3CO$ + $O_2$ was used as the calibration reaction throughout for the room temperature experiments, where data were collected for pressures of: 12 – 120 Torr. Some preliminary high-temperature experiments and results are also discussed in this chapter, where a different calibration method had to be found; this is discussed in more detail later on (experimental set-up explained in detail in Chapter 2).

$$C_2H_5CO + O_2 \rightarrow OH + \textit{other products} \tag{3.2}$$

$$C_3H_7CO + O_2 \rightarrow OH + \textit{other products} \tag{3.3}$$

$$C_4H_9CO + O_2 \rightarrow OH + \textit{other products} \tag{3.4}$$

$$(CH_3)_2CHCO + O_2 \rightarrow OH + \textit{other products} \tag{3.5}$$

$$(CH_3)_3CCO + O_2 \rightarrow OH + \textit{other products} \tag{3.6}$$

$$(CH_3)_2CHCH_2CO + O_2 \rightarrow OH + \textit{other products} \tag{3.7}$$

$$C_2H_5(CH_3)CHCO + O_2 \rightarrow OH + \textit{other products} \tag{3.8}$$
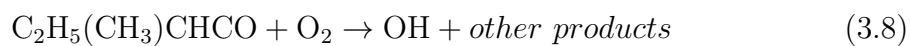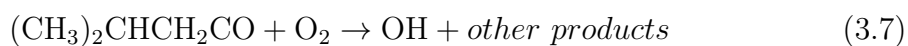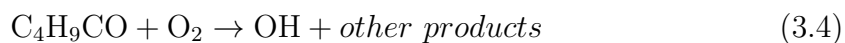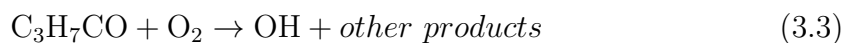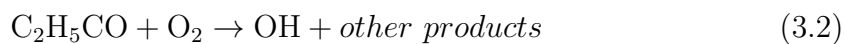
## 3.3    OH LIF Excitation Spectra

LIF was detected for all reactions; therefore, to confirm the fluorescence signal recorded was OH, LIF excitation spectra were carried out – see Figures 3.3 and 3.4. The LIF excitation spectra experiments were necessary as the apparatus was designed and used for the first time in this project, and so these experiments were a test to check what signal the PMT was recording. The probe laser was scanned across various absorption lines, while the delay between the photolysis and probe laser was kept to 50 $\mu$s, as this time period was where the maximum fluorescence was recorded in most cases.

The rotational distribution of OH appears in a relatively narrow frequency interval but the individual lines are well separated and do not strongly interfere with each other. This means that the spectrum can be highly resolved and ideal for an experiment to confirm OH fluorescence (Luque and Crosley 1999).

The spectra were recorded for all eight reactions (Reactions: 3.1 – 3.8) at room temperature (294 K) with all showing similar results; therefore, only two spectra are shown here for the reactions: $C_2H_5CO + O_2$ (Figure 3.3) and $(CH_3)_2CHCH_2CO + O_2$ (Figure 3.4). The spectra for the other reactions can be found in Appendix B. Figure 3.3 was recorded at 18 Torr with the concentrations in molecule cm$^{-3}$ as follows: $[C_2H_5CHO] = 1.8 \times 10^{14}$, $[Cl_2] = 6.5 \times 10^{14}$, $[Cl] \approx 9 \times 10^{12}$, $[N_2] = 4.1 \times 10^{17}$ and $[O_2] = 1.0 \times 10^{17}$. Figure 3.4 was recorded at 14 Torr with concentrations in molecule cm$^{-3}$ of: $[(CH_3)_2CHCH_2CHO] = 1.8 \times 10^{14}$, $[Cl_2] = 1.7 \times 10^{14}$, $[Cl] \approx 6 \times 10^{11}$, $[N_2] = 3.0 \times 10^{17}$ and $[O_2] = 6.9 \times 10^{16}$. The data from such experiments indicate that the fluorescence seen is OH, since the experimental data are in line with the simulated data from LIFBASE with the peaks overlapping well (Luque and Crosley 1999). Experiments were also carried out on $C_{10}H_{21} + O_2$, predicted to show no OH fluorescence, to confirm the OH production was from the RCO + $O_2$ reaction.
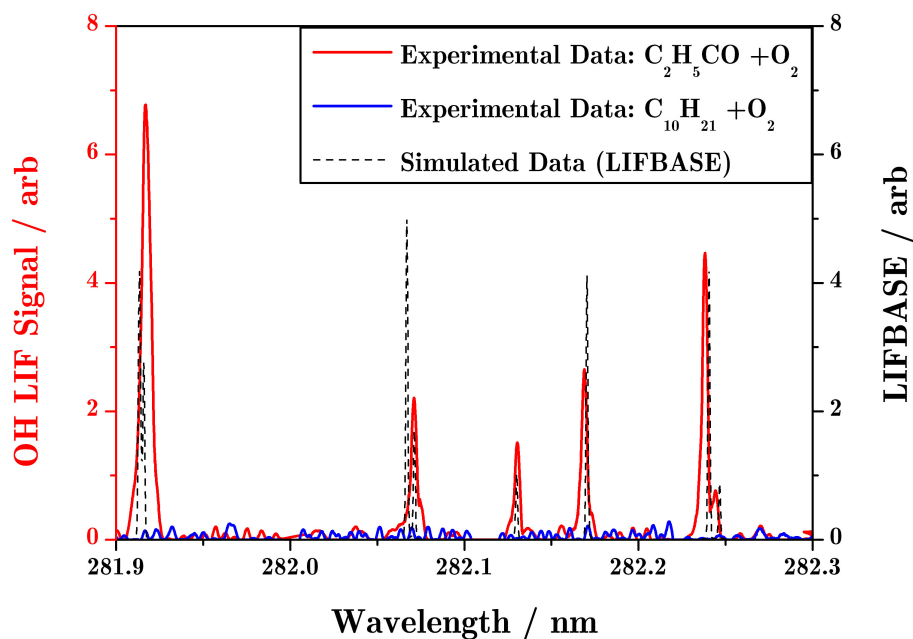
Figure 3.3: LIF Excitation Spectra of $C_2H_5CO + O_2$ (red line) alongside $C_{10}H_{21}$ (blue line) and LIFBASE (dotted black line). Recorded at 13 Torr and 294 K with concentrations (in molecule $cm^{-3}$): $C_2H_5CHO = 1.8 \times 10^{14}$, $O_2 = 1.0 \times 10^{17}$, $Cl_2 = 6.5 \times 10^{14}$, $Cl \approx 9 \times 10^{12}$.
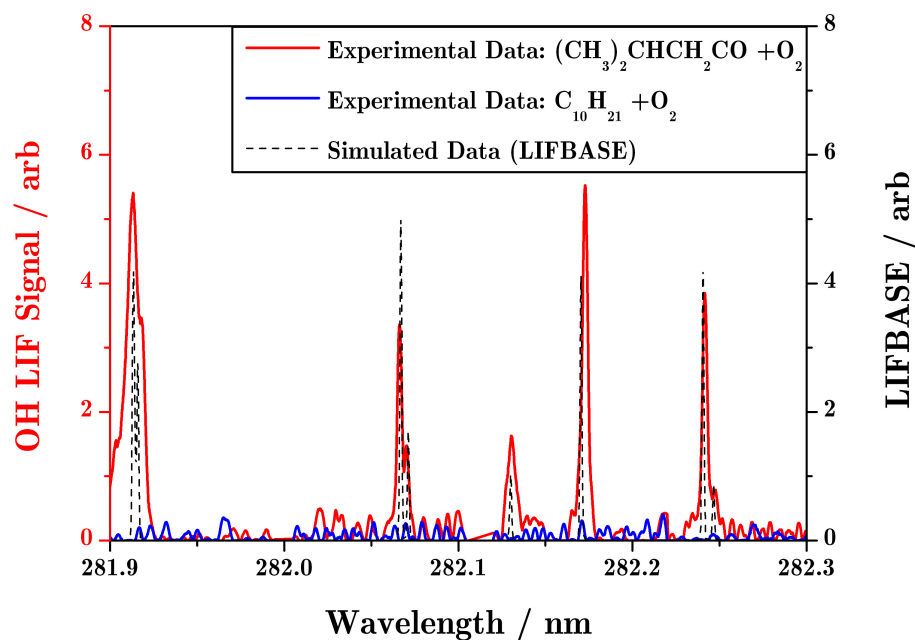


Figure 3.4: LIF Excitation Spectra of $(CH_3)_2CHCH_2CO + O_2$ (red line) alongside $C_{10}H_{21}$ (blue line) and LIFBASE (dotted black line). Recorded at 13 Torr and 294 K with concentrations (in molecule $cm^{-3}$): $(CH_3)_2CHCH_2CHO = 1.8 \times 10^{14}$, $O_2 = 6.9 \times 10^{17}$, $Cl_2 = 1.7 \times 10^{16}$, $Cl \approx 6 \times 10^{11}$.

The intensities of the signals from the experimental data vary from the theoretical data due to a number of factors such as the filters and the dye used in the dye laser. There was minimal change between compounds: the little differences are mostly due to manually tuning the dye crystal. For each spectrum, six scans were completed allowing for the crystal to be tuned between each scan. The results of each scan were stitched together to produce the full spectrum. For each of the scans a spectrum of 2000 laser shots was recorded, immediately after the photolysis laser was blocked enabling a noise spectrum to be recorded. This allowed the results to take into account the noise, helping to produce spectra with high signal-to-noise ratios.

These spectra show which wavelength the OH radical production for this apparatus works best at, the largest peak in the spectra at 281.9 nm which corresponds to the $A^2\Sigma^+$ $(\nu\prime = 1) \leftarrow X^2\Pi$ $(\nu\prime\prime = 0)$ transition. This is the wavelength that the dye laser is tuned to for the kinetic traces. The largest difference between the experimental data and the simulated data from LIFBASE was the peak broadening seen in the experimental data (Luque and Crosley 1999). This difference was unlikely due to the experimental noise since the signal took into account any noise - each run was repeated by blocking the photolysis beam; therefore, noise for each run was recorded. However, the dye laser resolution could cause this difference, along with peak broadening effects from the increase of the pressure that the data were recorded at – a well-known phenomenon (Larkins 1984). This difference was not examined in great detail since this experiment was carried out as a check, to confirm OH fluorescence. It was not used to produce any quantitative results.

## 3.4 OH Yield Calculation

This section will explain the calculations used to determine the OH yield of RCO + $O_2$ reactions. Back-to-back PLP-LIF experiments were performed on $CH_3CO$ + $O_2$ (Reaction 3.1) and an unknown RCO + $O_2$ (for example $C_2H_5CO$ + $O_2$ – Reaction 3.2). This allowed the OH yield from Reaction 3.2 to be compared to the well-characterised reaction of $CH_3CO$ + $O_2$, Figure 3.5, since $CH_3CHO$ and RCHO are kinetically very similar.
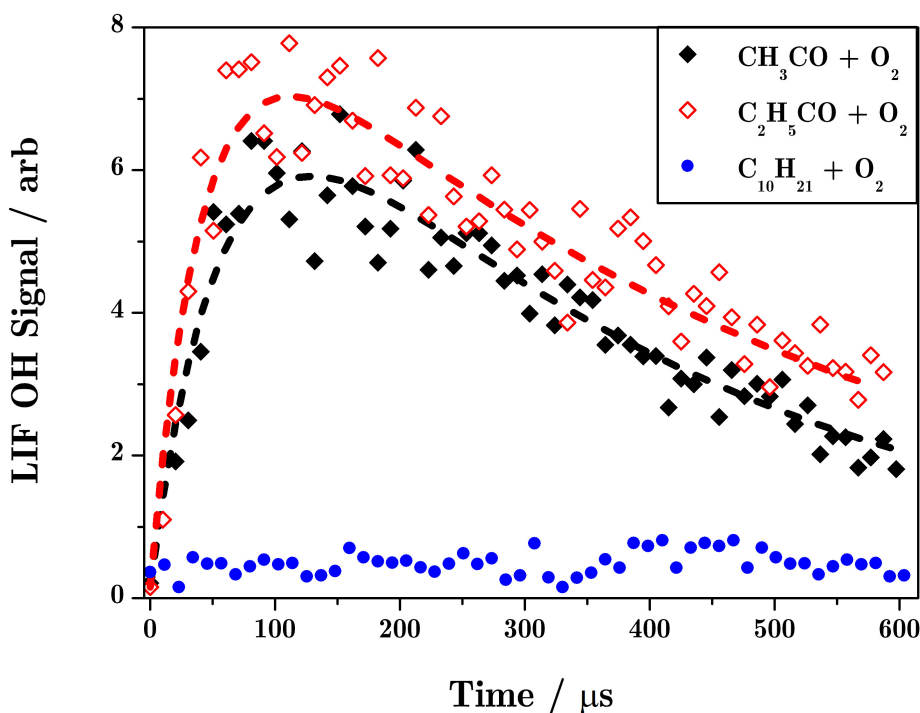


Figure 3.5: Back-to-back OH–LIF profiles measured for $CH_3CO$ + $O_2$ (black diamonds) and $C_2H_5CO$ + $O_2$ (red diamonds), with their associated fits of Equation 3.9 – shown as the dotted lines. The concentrations used (in molecule $cm^{-3}$) : Cl $\approx 1 \times 10^{12}$ , $O_2 = 7.0 \times 10^{16}$, $C_2H_5CHO = 3.6 \times 10^{14}$, $CH_3CHO = 4.1 \times 10^{14}$, at P = 13 Torr and 294 K. No OH was observed from $C_{10}H_{21}$ + $O_2$ (blue circle points; $[C_{10}H_{22}] = 1.3 \times 10^{14}$).

The LIF signal observed from each experiment can be represented by: $\Upsilon$ [OH]$(t)$, where $\Upsilon$ expresses the physical experimental conditions. These conditions include the power of the probe laser, the efficiency of the optics, the alignment of the two

laser beams and the PMT settings. These factors are extremely hard to calibrate therefore to overcome this, experiments were recorded back-to-back allowing these factors to be cancelled out. The quenching of the LIF signal is also expressed in $\Upsilon$; the amount that it changes when different organics are investigated is negligible since the amount of $N_2$ and $O_2$ is so large.

$$LIF = \Upsilon[\text{OH}](t) = A(e^{(-Bt)} - e^{(-Ct)}) \tag{3.9}$$

To obtain the OH yield ($\alpha$) for a reaction each experimental run was plotted, with the data fitted to a function, Equation 3.9. This analytical expression for the OH radical concentration contains three parameters and to explain it the reaction of $CH_3CO + O_2$ is used. The two critical rate constants in this reaction are $k_{10}$ from the Reaction 3.10 which forms the $CH_3CO$ that the $O_2$ reacts with; and are $k_{11}$ from the Reaction 3.11 which is the main OH loss pathway.

$$CH_3CHO + Cl \rightarrow CH_3CO + HCl \tag{3.10}$$

$$CH_3CHO + OH \rightarrow CH_3CO + H_2O \tag{3.11}$$
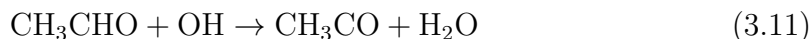
Two assumptions are employed in the analysis for this thesis. The first is that the production of OH is a pseudo first-order reaction; this is achieved by using excess $O_2$, causing parameter $B$ to be solely dependent on the RCO radical - Equation 3.12. Parameter $B$ is dependent on the rate coefficient of Reaction 3.10, $[CH_3CHO]$, and the transport coefficient - represented by $k_D$.

$$B = k_{10}[CH_3CHO] + k_D \tag{3.12}$$

The second assumption is that the start of the OH decay is also a pseudo first-order reaction. The reaction rate of aldehyde + OH is greater than the other OH decay routes and therefore it is assumed that aldehyde + OH controls the start of the

decay rate. Parameter $C$ (Equation 3.13) takes into account the rate coefficient of Reaction 3.11, [CH$_3$CHO], and the transport coefficient - represented by $k_D$. However, as $C$ represents the decay of OH it also includes the OH yield for CH$_3$CO + O$_2$ ($\alpha$) and the yield of Reaction 3.11 ($\beta$) as it is important to know how much CH$_3$CO is recycled from the reaction of CH$_3$CHO + OH (Reaction 3.11. The $C$ parameter can also include the rate coefficients of other OH loss channels for example the reaction of OH with Cl. These other reactions are not included as Reaction 3.11 is the dominant reaction occurring at $1.2 \times 10^{-11}$ cm$^3$ molecule$^{-1}$ s$^{-1}$, whereas for example Cl$_2$ + OH occurs at $6.0 \times 10^{-14}$ cm$^3$ molecule$^{-1}$ s$^{-1}$ (Atkinson et al. 2007).

$$C = (1 - \alpha \ \beta) \ k_{11}[CH_3CHO] + k_D \qquad (3.13)$$

Parameter $A$ (Equation 3.14) represents the numerical OH yield of the RCO + O$_2$ reaction taking into account the rate of CH$_3$CHO + OH ($k_{11}$) and the CH$_3$CHO + Cl rate ($k_{10}$). It also includes the initial Cl radical concentration formed via photolysis ([Cl]$_0$) and the reaction yields of CH$_3$CHO + OH ($\beta$), CH$_3$CHO + Cl ($\gamma$), and finally the OH yield from CH$_3$CO + O$_2$ ($\alpha$). The $\gamma$ yield is crucial as this is the yield of the initial formation of CH$_3$CO.

$$A = \frac{\alpha \ \gamma \ k_{10}[CH_3CHO] \ [Cl]_0}{(1 - \alpha \ \beta)k_{11}[CH_3CHO] \ k_{10}[CH_3CHO]} \qquad (3.14)$$

The numerical yield, $A$, calculated from the fit of Equation 3.9 to the data, was corrected to form the relative OH yield with the $B$ and $C$ values, shown in Equation 3.15. This correction allows the yield to take into account the amount of OH that is not observed, due to the short lifetime of OH because of its reaction with the aldehyde.

$$\text{Relative \ OH \ Yield} = A\frac{(C - B)}{B} \qquad (3.15)$$

The difference between the relative OH yield from our $CH_3CO + O_2$ reaction and Gross, Dillon, and Crowley (2014), is quantified – Gross, Dillon, and Crowley (2014) calibrated their system using a known OH radical reaction, this accurate calibration is required for this works relative method.
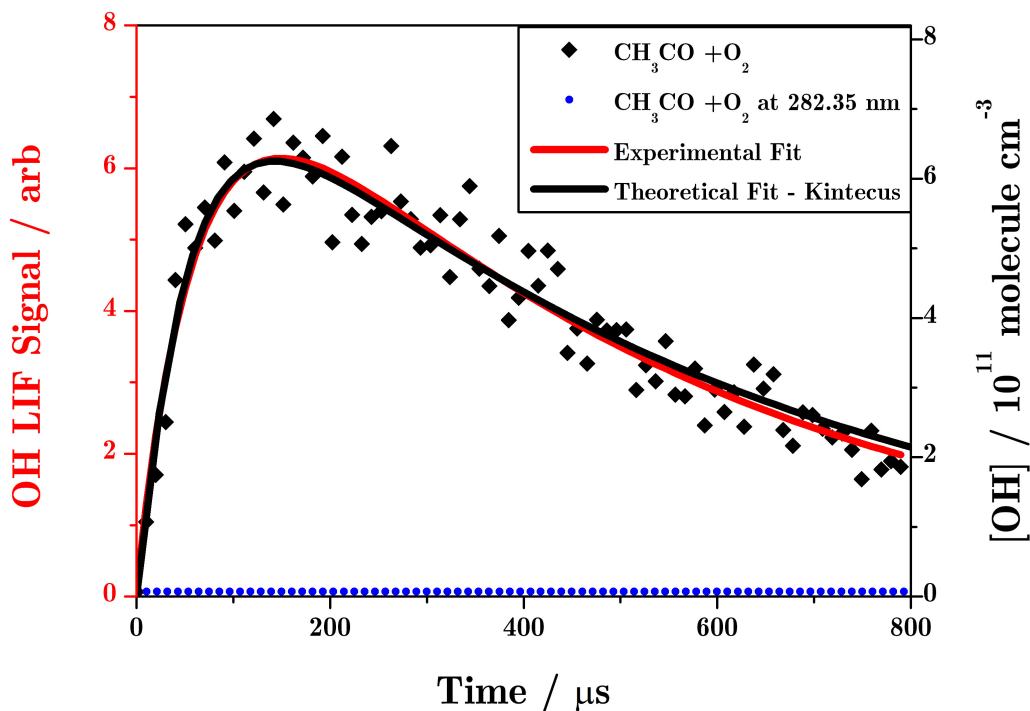


Figure 3.6: OH–LIF profile measured for the reaction of $CH_3CO + O_2$ (black diamonds), with concentrations (in molecule $cm^{-3}$) : $O_2 = 6.6 \times 10^{16}$, $N_2 = 2.2 \times 10^{17}$, $Cl \approx 2 \times 10^{12}$, $P = 13$ Torr and $T = 293$ K. The black line represents a fit of Equation 3.9 to the data, overlaid with the Kintecus model (red line) and an off-resonance trace at 282.35 nm (blue circles).

To obtain the OH yield for an unknown reaction this conversion is performed on the relative OH yield from the unknown reaction. Figure 3.5 displays experimental results for the reactions of $CH_3CO + O_2$ and $C_2H_5CO + O_2$ with the analytical fits of both data sets. The calibration of the relative OH yield from $CH_3CO + O_2$ to Gross, Dillon, and Crowley (2014) allowed the calculation of the OH yield for $C_2H_5CO + O_2$.

The assumptions reviewed in this section can be examined when the fit, using Equation 3.9, is compared to results from a kinetic simulated model (Kintecus),

Figure 3.6. Kintecus is a simulation software which is able to model reactions, the rate constants that are used in the $CH_3CO + O_2$ reaction model are listed in Table 3.1. Figure 3.6 illustrates how the experimental fit follows the theoretical fit, indicating that the assumptions hold true.

Table 3.1: The reactions with their associated rate coefficients (in $cm^3$ molecule$^{-1}$ s$^{-1}$) at 298 K that were included in the $CH_3CO + O_2$ Kintecus model.

| Reaction | Literature | Rate Coefficients |
|---|---|---|
| $CH_3CHO + Cl \rightarrow CH_3CO + HCl$ | Atkinson et al. (2006) | $8.00 \times 10^{-11}$ |
| $CH_3CHO + OH \rightarrow CH_3CO + H_2O$ | Atkinson et al. (2006) | $1.47 \times 10^{-11}$ |
| $CH_3CHO + OH \rightarrow CH_2CHO + H_2O$ | Atkinson et al. (2006) | $7.72 \times 10^{-13}$ |
| $CH_3CO + O_2 \rightarrow CH_3C(O)O_2$ | Gross et al. (2014) | $9.70 \times 10^{-12}$ |
| $CH_3CO + O_2 \rightarrow OH + product$ | Gross et al. (2014) | $3.00 \times 10^{-13}$ |
| $CH_3CO + Cl_2 \rightarrow CH_3COCl + Cl$ | Tyndall et al. (1999) | $4.30 \times 10^{-11}$ |

*Notes:* Literature used: Atkinson et al. (2006), Gross, Dillon, and Crowley (2014), and Tyndall, Orlando, Wallington, and Hurley (1999).

## 3.5    Results of Acyl Radicals with Oxygen

### 3.5.1    OH Yield from Propionyl Radical

Back-to-back experiments were performed on Reactions 3.1a and 3.2, using $CH_3CHO$ and $C_2H_5CHO$ as RCO precursors. Each pair of experiments was conducted using different concentrations of precursors, at eight pressures between 12 and 120 Torr – Figure 3.5 displays an example from 13 Torr. A summary of these experimental conditions is presented in Table 3.2, alongside the results obtained from these traces. The OH yield shown in Table 3.2 is the value for the OH yield once the conversion using the Gross, Dillon, and Crowley (2014) data has been performed. It is the yield per Cl radical not the yield per $C_2H_5CO$ radical, as to obtain the yield for per $C_2H_5CO$ a conversion using a chlorine SAR needs to be applied – this will be explained and discussed in a Section 3.6.

Table 3.2:   Summary of the experimental conditions and results from the investigation of the OH yield from the reaction of $C_2H_5CO + O_2$ at 294 K.

| Pressure/ | No. | Concentration / molecule $cm^{-3}$ | | | | OH |
|---|---|---|---|---|---|---|
| Torr | Traces | $O_2$/ $10^{16}$ | $C_2H_5CHO$/ $10^{14}$ | $Cl_2$/ $10^{14}$ | Cl/ $10^{12}$ | Yield |
| 12.8 | 8 | $6.5 - 6.7$ | $4.7 - 4.9$ | $1.3 - 1.7$ | $2 - 3$ | 0.33 |
| 13.8 | 12 | $6.9 - 7.3$ | $4.5 - 5.0$ | $0.9 - 1.0$ | $1 - 2$ | 0.36 |
| 15 | 6 | $5.2 - 5.4$ | $3.2 - 3.4$ | $0.6 - 0.6$ | $1 - 1$ | 0.36 |
| 21 | 2 | $5.8 - 6.0$ | $4.5 - 4.7$ | $1.0 - 1.2$ | $1 - 2$ | 0.19 |
| 30 | 12 | $4.8 - 6.3$ | $2.6 - 5.0$ | $0.6 - 1.2$ | $1 - 2$ | 0.14 |
| 50 | 7 | $5.0 - 5.3$ | $3.7 - 3.9$ | $0.5 - 0.9$ | $1 - 1$ | 0.07 |
| 80 | 13 | $7.6 - 8.0$ | $4.4 - 6.0$ | $1.2 - 1.5$ | $2 - 2$ | 0.05 |
| 120 | 6 | $6.6 - 14.2$ | $4.8 - 6.6$ | $0.6 - 2.6$ | $1 - 4$ | 0.03 |

*Notes:* The no. of traces column represents how many pairs of back-to-back experiments were performed at each pressure. The concentrations of $CH_3CHO$ were typical similar to $C_2H_5CHO$ though sometimes a bit larger; the yields presented here are mean values of multiple results; pressure quoted was mostly all $N_2$.

Figure 3.7 displays the results from this study, showing the OH yield ($\alpha$) decreased when the bath gas pressure was increased – this follows the trend of the OH yield

from $CH_3CO + O_2$ (black line in Figure 3.7). The difference between the OH yields of $CH_3CO + O_2$ and $C_2H_5CO + O_2$ is only the amount of OH produced, with the yield from $C_2H_5CO + O_2$ shown to be slightly larger. The rate that the OH yield decreases due to pressure between the two reactions is shown to be very similar with both reaching close to an OH yield of 0.01 at the higher pressures – discussed later in this section.

Further confidence was given when the results were examined alongside the two previous literature studies: Zügner et al. (2010) and Romero et al. (2005) shown together with results in Figure 3.7. The two studies differ greatly from one another, with different pressure ranges used to record data; however, the pressure range this project works at is able to bridge the gap – data were recorded in-between the pressure ranges of the two previous studies. All data from the studies of the OH yield from the reaction of $C_2H_5CO + O_2$ agree qualitatively – the OH yield decreases with increasing pressure. However, the results from this work agree closely with the trend set by Zügner et al. (2010), clearly shown in Figure 3.7, and not to the previous results of Romero et al. (2005). The comparison between the four data sets (including the Gross, Dillon, and Crowley (2014) $CH_3CO + O_2$ data) shows that they all follow a similar linear pattern apart from the data of Romero et al. (2005) which differs substantially.

When the literature was further examined, the group that published the study by Romero et al. (2005) have also published previous work on the reaction of $CH_3CO$ $+ O_2$. These studies, which have been mentioned in the previous section, have produced higher OH yields than all other literature and therefore it is no surprise that this study has disagreed with Romero et al. (2005) values. It has been suggested that their calibration method is slightly off, with the source of the discrepancy coming from the decomposition of hot propionyl radicals from acetone photolysis, although there is still no obvious reason why this difference exists (Papadimitriou et al. 2015).

The results from this study of the OH yield from $C_2H_5CO + O_2$ showed the ability of this project to record OH yields at different pressures. The comparisons with previous literature studies allowed the reliability of this study to be examined, and therefore showed that the new experimental set-up could record accurate and reliable data. This allowed the project to continue investigating the OH yield for different RCOs.
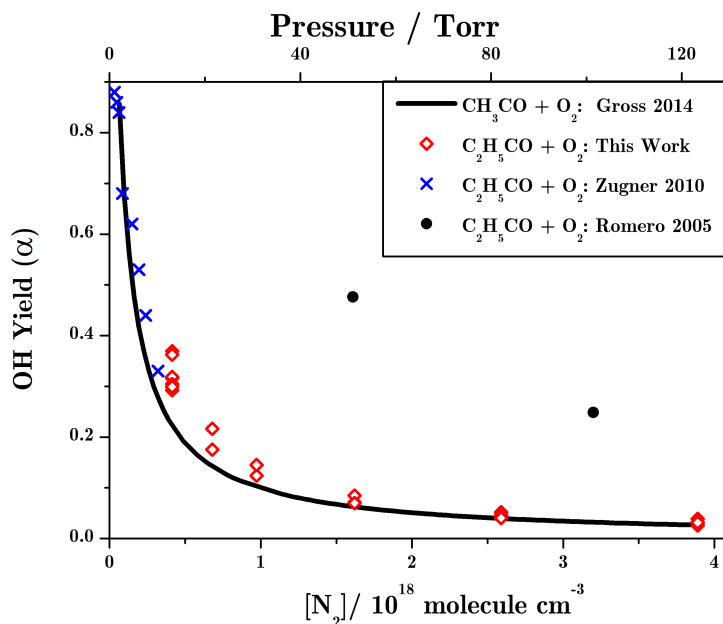


Figure 3.7: Plot of the OH yield versus pressure for the reaction of $C_2H_5CO + O_2$ (red diamonds) together with the previous literature: Romero et al. (2005) (black circles) and Zügner et al. (2010) (blue crosses). Relative OH yields per Cl radical for this work were placed on an absolute scale using $CH_3CO + O_2$ results from Gross, Dillon, and Crowley (2014) (solid black line).

## 3.5.2  Straight Chain Acyl Radicals

Similar back-to-back experiments were carried out to study reactions of $O_2$ with two larger acyl radical fragments derived from $C_3H_7CHO$ and $C_4H_9CHO$ precursor aldehydes, with the temperature kept constant at 293 K while the pressure was altered between 13 and 122 Torr. The summary of all the experimental conditions and results can be found in Table 3.3. The results from these sets of experiments were combined with the results from the previous experiment on $C_2H_5CO + O_2$; this enabled the study of how chain length affects the OH yield. Similar to the previous section the OH yields here are presented as per Cl not per RCO - discussed in Section 3.6.

As expected the reactions of $C_3H_7CO + O_2$ and $C_4H_9CO + O_2$ differ from $CH_3CO$ $+ O_2$ and $C_2H_5CO + O_2$, shown as a plot of OH yield against pressure in Figure 3.8. The results showed that all four reactions follow the same trend with the OH yield decreasing while the pressure was increased, which indicated that the mechanism could be the same for all RCO + $O_2$ reactions. Figure 3.8 also shows clearly which RCO out of the four compounds gave the lowest OH yield – $C_4H_9CO +$ $O_2$ gave the lowest OH yield at all pressures; and the highest yield – $C_2H_5CO$ $+ O_2$ gave the highest yield at all pressures. The results at each pressure were averaged taking into account the standard error of the fit (error bars shown on each data point), to produce a weighted average data point which can be represented on a Stern-Volmer plot – see Figure 3.9. A Stern-Volmer plot displays the data by plotting the reciprocal of the OH yield ($\alpha^{-1}$) against the bath gas number density ($[N_2]$). This allowed a more quantitative analysis than solely plotting the OH yield against pressure as linear regression can be performed to give a value for the gradient of the plot allowing the yield to be calculated at any pressure – Table 3.3.
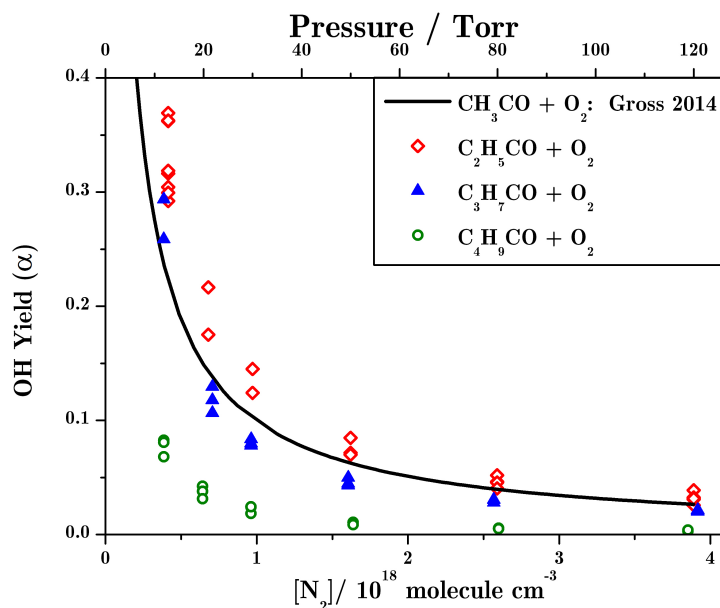
Figure 3.8: Plot of the OH yield versus pressure for reactions of $O_2$ with three straight chain acyl radicals: $C_2H_5CO + O_2$ (red diamonds), $C_3H_7CO + O_2$ (blue triangles) and $C_4H_9CO + O_2$ (green circles). Relative OH yields were places on an absolute scale using $CH_3CO + O_2$ results from Gross, Dillon, and Crowley (2014) (solid black line).
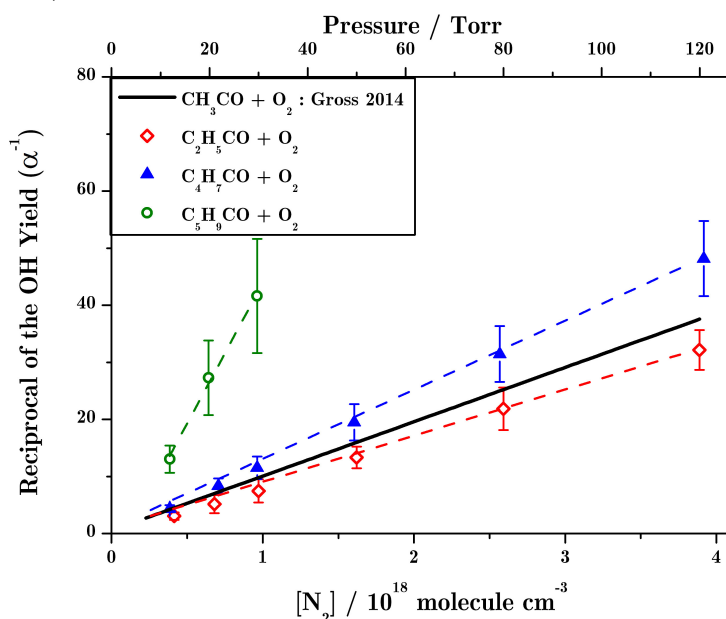


Figure 3.9: Stern-Volmer plot to show the reciprocal of the OH yields versus pressure for reactions of $O_2$ with three straight chain acyl radicals: $C_2H_5CO + O_2$ (red diamonds), $C_3H_7CO + O_2$ (blue triangles) and $C_4H_9CO + O_2$ (green circles). Relative OH yields were places on an absolute scale using $CH_3CO + O_2$ results from Gross, Dillon, and Crowley (2014) (solid black line).

Table 3.3: Summary of the experimental conditions and results for the RCO + $O_2$ investigation of the OH production at 294 K of three straight chain acyl radicals: **3.2** = $C_2H_5CO + O_2$, **3.3** = $C_3H_7CO + O_2$ and **3.4** = $C_4H_9CO + O_2$.

| Rxn | $P$ / Torr | Concentration / molecule $cm^{-3}$ | | | | $\alpha^{-1}$ |
|---|---|---|---|---|---|---|
| | | $O_2$/ $10^{16}$ | RCHO/ $10^{14}$ | $Cl_2$/ $10^{14}$ | Cl/ $10^{12}$ | |
| **3.2** | 12-120 | 4.8-14.2 | 2.6 -6.6 | 0.5-2.6 | 1-4 | $(7.9 \pm 0.21) \times 10^{-18}$ |
| **3.3** | 12-122 | 4.7-6.8 | 3.0-5.0 | 4.3-8.5 | 1-3 | $(1.2 \pm 0.23) \times 10^{-17}$ |
| **3.4** | 12-120 | 4.2-14 | 2.87.6 | 0.3-2.2 | 1-3 | $(7.1 \pm 0.32) \times 10^{-17}$ |

*Notes:* The column containing $\alpha^{-1}$ is the gradient from the Stern-Volmer plot with the units $cm^3$ molecule$^{-1}$, for the full Stern-Volmer relationship the gradient is multiplied by [M] and then 1 is added.

These data show that lengthening the carbon chain in the acyl radical causes the OH yield to decrease; however, the propionyl radical ($C_2H_5CO$) does not follow this trend. Mechanistic insight into the decomposition of the propionylperoxy radical ($C_2H_5C(O)O_2$) helps to determine the reasoning behind this difference. Two theoretical studies on the $CH_3CO + O_2$ reaction have calculated the potential energy surfaces – Hou, Li, et al. (2005) and Maranzana, Barker, and Tonachini (2007). They both agree on how the hydroxyl group is formed: the oxygen radical attacks a hydrogen on the terminal -$CH_3$. This is the same pathway that Hou and Wang (2007) theorised with their study on the propionylperoxy radical, Figure 3.10. However, the propionylperoxy radical could decompose to form OH with either the three-centre $\alpha$-lactone or the four-centre $\beta$-propiolactone. The 6-membered ring intermediate is more favourable than the 5-membered ring formed by $CH_3C(O)O_2$, therefore an increase in the OH yield is observed when the carbon chain is increased from two carbons to three carbons.

When the chain length increases from three carbons in $RC(O)O_2$, a decrease in the OH yield is observed, with $C_4H_9CO + O_2$ having the smallest OH yield. This is due to the increased chain length increasing the radical stability and therefore causing a decrease in the OH yield. The results in this thesis have given the first analysis of
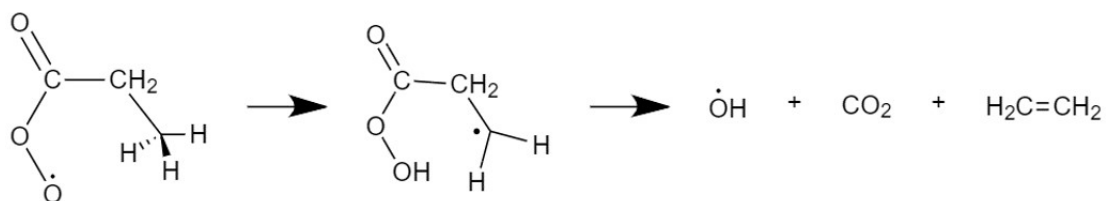
Figure 3.10: Formation of the hydroxyl group on the propionylperoxy radical $(C_2H_5C(O)O_2)$ from the reaction of $C_2H_5CO + O_2$.

the trend in OH yield due to lengthening the carbon chain in acyl radicals. It has shown that the larger the acyl radical is the smaller the OH yield with the OH yield of $C_{10}H_{19}CO + O_2$ becoming negligible. This study has not only shown a trend to OH production in the $RCO + O_2$ reactions but it was the first study to show that these reactions produce OH – proved by the OH fluorescence excitation spectra which were recorded for each reaction, mentioned previously in Section 3.3.

### 3.5.3 Branched Acyl Radicals

Back-to-back experiments were carried out to study the reaction of $O_2$ with four branched acyl radical fragments derived from: $CH_3CHO$, $(CH_3)_2CHCHO$, $C_2H_5CH(CH_3)CHO$, $(CH_3)_2CHCH_2CHO$ and $(CH_3)_3CCHO$ as the precursor aldehydes, with the temperature kept constant at 293 K while the pressure was altered between 13 and 122 Torr. The summary of all the experimental conditions and results can be found in Table 3.4. The results from these sets of experiments were combined with the results from the previous experiments on straight-chain acyl radicals, this enabled the study of how branching on the acyl radical chain effects the OH yield. Similar to the previous sections the OH yields here a presented as per Cl not per RCO - discussed in Section 3.6.

The results showed that all reactions follow the same trend with the OH yield decreasing while the pressure was increased; Figure 3.11 also shows that all the branched RCOs give a lower OH yield at all pressures compared to $CH_3CO + O_2$. Similar to the straight-chain $RCO + O_2$ analysis, a Stern-Volmer plot was created and the gradient of the straight line was calculated for each $RCO + O_2$ reaction which allowed the OH yield of each reaction to be compared quantitatively – Figure 3.12. The Stern-Volmer plot clearly displays that the OH yield is greatest in the reaction of $(CH_3)_2CHCH_2CO + O_2$ (orange circles) and is least in $(CH_3)_3CCO + O_2$ (pink triangles).

The results show that for acyl radicals which contain four carbons ($C_3H_7CO$ and $(CH_3)_2CHCO$), the OH yield was lower for the branched acyl radical. This could be due to the difference in the carbon-hydrogen bond strength. For the 6-membered intermediate, for $C_3H_7CO + O_2$, a secondary hydrogen is attacked to form the OH, whereas, a primary hydrogen is attacked in $(CH_3)_2CHC(O)O_2$. This can explain the difference in the OH yield that is observed. For acyl radicals which contain five carbons ($C_4H_9CO$, $C_2H_5CH(CH_3)CO$, $(CH_3)_2CHCH_2CO$ and $(CH_3)_3CCO$) the
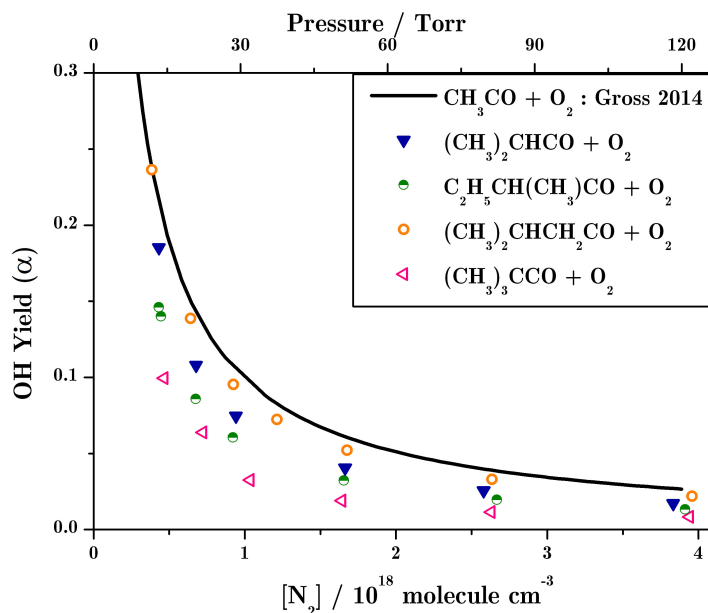
Figure 3.11: Plot of the OH yield versus pressure for reactions of $O_2$ with four branched acyl radicals: $(CH_3)_2CHCO + O_2$ (blue triangles), $C_2H_5CH(CH_3)CO + O_2$ (green circles), $(CH_3)_2CHCH_2CO + O_2$ (orange circles) and $(CH_3)_3CCO + O_2$ (pink triangles). Relative OH yields were places on an absolute scale using $CH_3CO + O_2$ results from Gross, Dillon, and Crowley (2014) (solid black line).
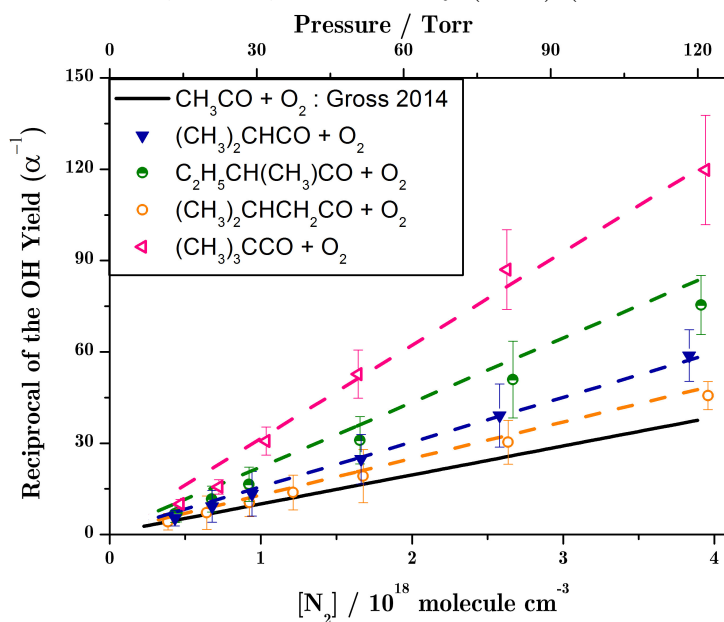


Figure 3.12: Stern-Volmer plot to show the reciprocal of the OH yields versus pressure for reactions of $O_2$ with four branched acyl radicals: $(CH_3)_2CHCO + O_2$ (blue triangles), $C_2H_5CH(CH_3)CO + O_2$ (green circles), $(CH_3)_2CHCH_2CO + O_2$ (orange circles) and $(CH_3)_3CCO + O_2$ (pink triangles). Relative OH yields were places on an absolute scale using $CH_3CO + O_2$ results from Gross, Dillon, and Crowley (2014) (solid black line).

opposite is true: the straight-chained radical has the lowest yield. This can also be explained by the difference in the carbon-hydrogen bond that is attacked by the oxygen to form OH. The reaction of $(CH_3)_2CHCH_2CO + O_2$ gave the highest OH yield out of the C5 compounds, has a tertiary hydrogen which is attacked in the intermediate. Whereas $C_2H_5CH(CH_3)C(O)O_2$ has a secondary hydrogen and $(CH_3)_3CC(O)O_2$ only has primary hydrogens, therefore the type of hydrogens can predict the difference in the OH yield of the branched C5 compounds.

Table 3.4: Summary of the experimental conditions and results for the $RCO + O_2$ investigation of the OH production at 294 K of four branched acyl radicals: labelled **3.5** $= (CH_3)_2CHCO + O_2$, **3.8** $= C_2H_5CH(CH_3)CO + O_2$, **3.7** $= (CH_3)_2CHCH_2CO + O_2$ and **3.6** $= (CH_3)_3CCO + O_2$.

| Rxn | Pressure / Torr | Concentration / molecule cm$^{-3}$ | | | | $\alpha^{-1}*$ |
|---|---|---|---|---|---|---|
| | | $O_2$/ $10^{17}$ | RCHO/ $10^{14}$ | $Cl_2$/ $10^{14}$ | Cl/ $10^{12}$ | |
| 3.5 | 13 – 119 | 0.5–1.4 | 2.0–3.6 | 0.7–2.1 | 1–3 | $(1.5 \pm 0.03)$ $\times 10^{-17}$ |
| 3.8 | 13 – 121 | 0.6–1.4 | 2.1–3.2 | 0.9–2.5 | 1– 4 | $(2.4 \pm 0.07)$ $\times 10^{-17}$ |
| 3.7 | 12 – 123 | 0.7 –1.4 | 2.7 –6.6 | 0.9–2.6 | 1–4 | $(1.2 \pm 0.03)$ $\times 10^{-17}$ |
| 3.6 | 12 – 119 | 1.3-4.3 | 0.7–1.8 | 2.1– 6.0 | 3–9 | $(3.1 \pm 0.1)$ $\times 10^{-17}$ |

*Notes:* The column containing $\alpha^{-1}$ is the gradient from the Stern-Volmer plot with the units cm$^3$ molecule$^{-1}$, for the full Stern-Volmer relationship the gradient is multiplied by [M] and then 1 is added.

The interesting result is the large difference between $C_2H_5CH(CH_3)C(O)O_2$ and $C_4H_9CO(O)O_2$ since for both compounds a secondary hydrogen is attacked, this is due to the stabilising effect that the straight chain has. When the intermediate $RC(O)O_2$ is formed it can either be stabilised via collisions with other molecules or can decompose to form OH with other organic by-products. The increase in chain length means a greater surface for collisions to occur, stabilising the intermediate. Though the study has been able to display and explain the results seen by the addition of methyl groups on the acyl radical, further theoretical studies are needed to quantify these relationships and underpin the understanding of how the methyl groups vary the reactivity of the $RCO + O_2$.

# 3.6    Structure Activity Relationships

All previous yields have been presented as a yield per Cl radical therefore to be able to make direct comparisons to literature it would be useful to be able to convert these yields into OH yields per RCO radical. This can be achieved by using chlorine structure activity relationships (SARs) to investigate where the Cl radical abstracts the H in the aldehyde to form the RCO. The larger the aldehyde becomes, the less likely that RCO will be formed – the hydrogen more likely be abstracted from part of the increasingly large alkyl chain rather than the carbonyl group. If the probability of Cl abstracting the H from the carbonyl group is known, a conversion can be calculated to convert the OH yield from per Cl radical to per alkyl radical.

There was only one SAR available which could calculate the H-abstraction rate by chlorine for the carbonyl group of each aldehyde studied (Carter 2010). Calculating the H-abstraction rate for the carbonyl group of each aldehyde allowed an estimation to be made for the probability of the Cl radical abstracting the H from the CHO group rather than elsewhere in the aldehyde. As all the OH yield calculations were calculated relative to the yield of $CH_3CO + O_2$, the conversion was also calculated relative to the H abstraction of $CH_3CHO$ – made equal to 1. The values calculated for this conversion are shown in Table 3.5; also shown is a comparison between the total rate coefficient of aldehyde + Cl calculated by the SAR and the literature rate coefficients. This gave an indication on how accurately the SAR could determine the aldehyde + Cl rate coefficient and therefore how accurate this conversion was. In general the SAR predicts the rate coefficients well, with them matching up well with the literature values for $CH_3CHO + Cl$ and $C_2H_5CHO + Cl$. However, when the aldehyde becomes larger so does the discrepancy, which suggests that the SAR needs to be expanded to be able to determine what lengthening and branching factors affect the accuracy. This was the reason why the OH yield per Cl has been presented throughout this chapter, as if a new Cl SAR is developed the OH yield

per Cl can be easily converted to a new OH yield per RCO.

The rate coefficients for $C_2H_5(CH_3)CHCHO + Cl$ and $(CH_3)_2CHCH_2CHO + Cl$ which are shown in the literature column are the results calculated in this project, discussed in Chapter 4. It illustrates that the value that we have suggested for $C_2H_5(CH_3)CHCHO + Cl$ seems to be in line although for $(CH_3)_2CHCH_2CHO + Cl$ there is a large difference. This could be due to something missing from the SAR since there are no factors to add when the chain gets longer or from any branching effects.

Table 3.5: Rate coefficients all have the units $10^{-11}$ cm$^3$ molecule$^{-1}$ s$^{-1}$ (shown in the SAR calculation and the literature rate coefficient columns.

| Aldehyde | SAR Calculation | | | Literature Rate Coefficient | Amount from CHO | Ratio |
|---|---|---|---|---|---|---|
| | CHO | Rest | Total | | | |
| $CH_3CHO$ | 6.64 | 1.37 | 8.01 | 8.00[1] | 83 % | 1.00 |
| $C_2H_5CHO$ | 6.31 | 5.97 | 12.3 | 13.0[1] | 51 % | 0.62 |
| $C_3H_7CHO$ | 6.31 | 12.4 | 18.7 | 14.4[2] | 34 % | 0.41 |
| $C_4H_9CHO$ | 6.31 | 18.8 | 25.1 | 25.1[3] | 25 % | 0.31 |
| $(CH_3)_2CHCHO$ | 6.31 | 8.30 | 14.6 | 15.3[4] | 43 % | 0.52 |
| $C_2H_5(CH_3)CHCHO$ | 6.31 | 14.7 | 21.0 | 14* | 30 % | 0.36 |
| $(CH_3)_2CHCH_2CHO$ | 6.31 | 11.0 | 17.3 | 31* | 36 % | 0.44 |
| $(CH_3)_3CCHO$ | 6.31 | 9.78 | 16.1 | 13.8[4] | 40 % | 0.47 |

*Notes:* Literature values from: [1] =Atkinson et al. (2004); [2] = Renbaum-Wolff and Smith (2012); [3] = Thévenet, Mellouki, and Bras (2000);[4] = weighted average of Thévenet, Mellouki, and Bras (2000) and LeCrâne et al. (2004); * = results from this work, discussed in Chapter 4.

Table 3.6 displays the original Stern-Volmer gradient, indicating the pressure dependent OH yield for each RCO + O$_2$ reaction studied, and the new converted Stern-Volmer gradient. The CH$_3$CO + O$_2$ was used as the calibration reaction and therefore stays the same, since the value taken from Gross, Dillon, and Crowley (2014) is per CH$_3$CO radical. Out of eight RCO + O$_2$ reactions only four stay in the same order: C$_2$H$_5$CO + O$_2$ (1$^{st}$ - most OH produced); C$_4$H$_9$CO + O$_2$ (8$^{th}$ - least OH produced); (CH$_3$)$_3$CCO + O$_2$ (7$^{th}$); (CH$_3$)$_2$CHCH$_2$CO + O$_2$ (3$^{rd}$).

The difference that the SAR conversion makes to this project's results for C$_2$H$_5$CO

Table 3.6: The order shown in the table indicates where each RCO falls with the amount of OH each RCO + $O_2$ reaction produces, $1^{st}$ is the most and $8^{th}$ is the least. The converted Stern-Volmer gradient was calculated by using the conversion shown in Table 3.5 for each OH yield at each pressure for that particular RCO + $O_2$.

| Acyl Radical | OH Yield per Cl | | OH Yield per RCO | |
|---|---|---|---|---|
| | Stern-Volmer Gradient / $10^{-17}$ | Order | Stern-Volmer Gradient / $10^{-17}$ | Order |
| $CH_3CO$ | $0.9 \pm 0.2$ | $2^{nd}$ | $0.9 \pm 0.2$ | $6^{th}$ |
| $C_2H_5CO$ | $0.8 \pm 0.2$ | $1^{st}$ | $0.5 \pm 0.1$ | $1^{st}$ |
| $C_3H_7CO$ | $1.2 \pm 0.2$ | $4^{th}$ | $0.5 \pm 0.1$ | $2^{nd}$ |
| $C_4H_9CO$ | $7.1 \pm 0.3$ | $8^{th}$ | $2.1 \pm 0.1$ | $8^{th}$ |
| $(CH_3)_2CHCO$ | $1.5 \pm 0.3$ | $5^{th}$ | $0.8 \pm 0.2$ | $4^{th}$ |
| $C_2H_5(CH_3)CHCO$ | $2.4 \pm 0.1$ | $6^{th}$ | $0.8 \pm 0.3$ | $5^{th}$ |
| $(CH_3)_2CHCH_2CO$ | $1.2 \pm 0.3$ | $3^{rd}$ | $0.5 \pm 0.1$ | $3^{rd}$ |
| $(CH_3)_3CCO$ | $3.1 \pm 0.1$ | $7^{th}$ | $1.4 \pm 0.4$ | $7^{th}$ |

*Notes:*  The Stern-Volmer gradient has units of molecule$^{-1}$ cm$^3$ and to obtain the yield from the Stern-Volmer gradient the gradient is multiplied by the bath gas number density and 1 is added, the reciprocal of this value is the OH yield for that particular pressure.

+ $O_2$ is shown in Figure 3.13 alongside the two previous literature studies (Zügner et al. 2010; Romero et al. 2005). The change that the SAR conversion has made the experimental results increase the OH yield; however, when examining this change against the previous literature studies this increase in OH yield is minimal. The results from Romero et al. (2005) are still significantly different from this study with or without the SAR conversion.

The difference that the SAR conversion makes for all the RCO + $O_2$ that were studied in this chapter can be illustrated in Figure 3.14. It shows how much the conversion impacts the OH yields at 50 Torr, with the filled data points representing the OH yield per RCO and the empty data points representing the OH yield per Cl radical.  The conversion increases the numerical yield for all the reactions; however, the largest change comes from $C_3H_7CO + O_2$, $(CH_3)_2CHCO + O_2$, and $(CH_3)_2CHCH_2CO + O_2$. Though it could be expected that the largest change should occur from the largest compounds (e.g. $C_4H_9CO + O_2$) this is not the case, though
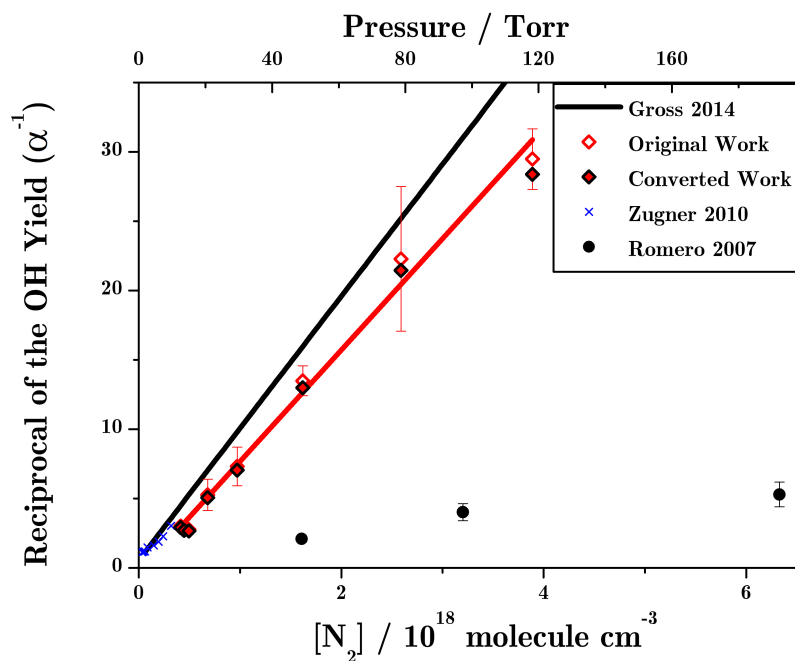
Figure 3.13: Plot displays the significance of the SAR conversion on the OH yields from the reaction of $C_2H_5CO + O_2$. The original dataset (empty red diamonds) and the converted dataset (red diamonds with black outline) are both shown together with the two previous literature studies on $C_2H_5CO + O_2$: Romero et al. (2005) (black circles) and Zügner et al. (2010) (blue crosses). The results from the study of $CH_3CO + O_2$ by Gross, Dillon, and Crowley (2014) (black line) are also shown for a comparison.
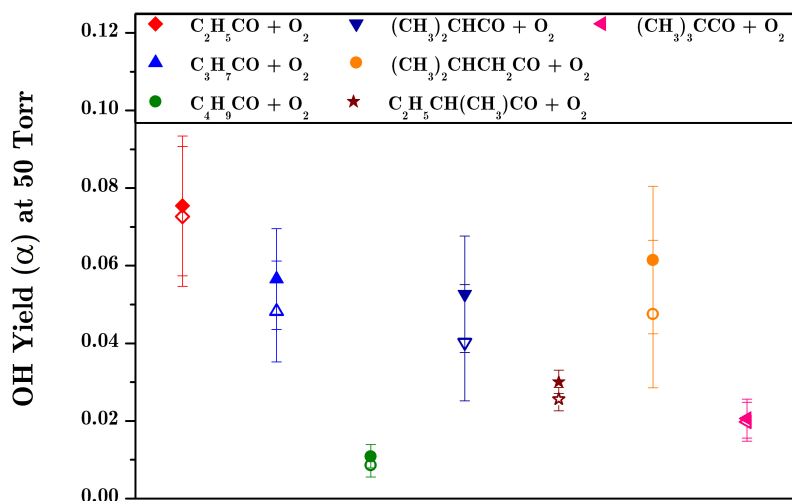


Figure 3.14: Plot displays the significance of the SAR conversion on the OH yields at 50 Torr, the filled points represent the OH yield per RCO and the empty data points represent the OH yield per Cl radical.

it could be due to the fact they have such low OH yields in the first place.

## 3.7   Summary

The results from this chapter demonstrated that OH generation is a general feature of RCO + $O_2$ reactions, when R = acyl chain. For the reaction of $C_2H_5CO$ + $O_2$ the two previous literature studies disagree substantially with Romero et al. (2005) presenting a much larger yield than Zügner et al. (2010). This study has enabled a clarification of this literature discrepancy, showing that although the OH yield of $C_2H_5CO$ + $O_2$ is definitely larger than $CH_3CO$ + $O_2$, the values from Romero et al. (2005) are far too large. The results from this study agree with the values from Zügner et al. (2010), who suggested that the source of $C_2H_5CO$ in study by Romero et al. (2005) produced very 'hot' radicals and so the OH yield was significantly over-estimated because $C_2H_5CO$ was formed directly from the photolysis of 3-pentanone which photolyses to produce $C_2H_5CO$ and ethyl radicals.

The study then carried on investigating how the OH yield was dependent on the length and shape of the carbon chain. Pressure-dependent (13 to 120 Torr - $N_2$) OH yields were determined for the first time for R = $CH_3CH_2CH_2$, $(CH_3)_2CH$, $(CH_3)_3C$, $CH_3CH_2CH_2CH_2$, $(CH_3)_2CHCH_2$, and $CH_3CH_2CH(CH_3)$. The OH yield was observed to decrease with increasing chain length and to display a complex dependency on the degree of branching within the R group. The studies on different branched RCO gave rise to the conclusion that the OH yield is dependent on two properties: the energy of the transition state and the carbon-hydrogen bond strength. To illustrate how the C-H bond affected the OH yield, the formation of the 6-membered immediate was key. In the formation of the intermediate, if a primary hydrogen is attacked rather than a secondary or tertiary hydrogen, the OH yield is higher; the lowest yield came from the attack of a tertiary hydrogen. It is the combination of both effects that controls the OH yield in the RCO + $O_2$ reaction.

# Bibliography

Atkinson, Baulch, Cox, Crowley, Hampson, Hynes, Jenkin, Kerr, et al. (2007). *IUPAC Subcommittee for Gas Kinetic Data Evaluation*. URL: `www.iupac-kinetic.ch.cam.ac.uk`.

Atkinson et al. (2004). "Evaluated kinetic and photochemical data for atmospheric chemistry: Part 1 - gas phase reactions of $O_x$, $HO_x$, $NO_x$ and $SO_x$ species". In: *Atmospheric Chemistry and Physics Discussions* 3.6, pp. 6179–6699.

— (2006). "Evaluated kinetic and photochemical data for atmospheric chemistry: Volume II; gas phase reactions of organic species". In: *Atmospheric Chemistry and Physics* 6.11, pp. 3625–4055.

— (2007). "Evaluated kinetic and photochemical data for atmospheric chemistry : Volume III – gas phase reactions of inorganic halogens". In: *Atmospheric Chemistry and Physics* 7, pp. 981–1191.

Blitz, Heard, and Pilling (2002). "OH formation from $CH_3CO + O_2$: A convenient experimental marker for the acetyl radical". In: *Chemical Physics Letters* 365.5-6, pp. 374–379.

Carr, Baeza-Romero, et al. (2007). "OH yields from the $CH_3CO + O_2$ reaction using an internal standard". In: *Chemical Physics Letters* 445.4-6, pp. 108–112.

Carr, Glowacki, et al. (2011). "Experimental and modeling studies of the pressure and temperature dependences of the kinetics and the OH yields in the acetyl with $O_2$ reaction". In: *Journal of Physical Chemistry A* 115.6, pp. 1069–1085.

Carter (2010). "Development of the SAPRC-07 chemical mechanism". In: *Atmospheric Environment* 44.40, pp. 5324–5335.

Chen and Lee (2010). "Transient infrared absorption of t -CH$_3$C(O)OO, c-CH$_3$C(O)OO, and $\alpha$ -lactone recorded in gaseous reactions of CH$_3$CO and O$_2$". In: *Journal of Chemical Physics.* 132.11.

Gross, Dillon, and Crowley (2014). "Pressure dependent OH yields in the reactions of CH$_3$CO and HOCH$_2$CO with O$_2$." In: *Physical Chemistry Chemical Physics* 16.22, pp. 10990–10998.

Hou, Li, et al. (2005). "Mechanistic and kinetic study of the CH$_3$CO + O$_2$ reaction". In: *The Journal of Chemical Physics* 122.22, p. 224304.

Hou and Wang (2007). "Ab initio study of the reaction of propionyl (C$_2$H$_5$CO) radical with oxygen (O$_2$)." In: *The Journal of Chemical Physics* 127.5, p. 054306.

Kovacs et al. (2007). "Kinetics and mechanism of the reactions of CH$_3$CO and CH$_3$C(O)CH$_2$ radicals with O$_2$. Low-pressure discharge flow experiments and quantum chemical computations". In: *Physical Chemistry Chemical Physics* 9.31, pp. 4142–4154.

Larkins (1984). "The effect of pressure broadening and line shift on the determination of lead isotopic ratios by atomic absorption and fluorescence spectroscopy". In: *SpechochMlierr Acre* 39, p. 4.

LeCrâne et al. (2004). "Atmospheric chemistry of pivalaldehyde and isobutyraldehyde: Kinetics and mechanisms of reactions with Cl atoms, fate of (CH$_3$)$_3$CC(O) and (CH$_3$)$_2$CHC(O) radicals, and self-reaction kinetics of (CH$_3$)$_3$CC(O)O$_2$ and (CH$_3$)$_2$CHC(O)O$_2$ radicals". In: *Journal of Physical Chemistry A* 108.5, pp. 795–805.

Lee, Chen, and Bozzelli (2002). "Thermochemical and Kinetic Analysis of the Acetyl Radical (CH$_3$CO) with O$_2$ Reaction system". In: *Journal of Physical Chemistry A* 106.31, pp. 7155–7170.

Luque and Crosley (1999). "LIFBASE: Database and Spectral Simulation Program (Version 1.5), SRI International Report MP 99-009". In:

Maranzana, Barker, and Tonachini (2007). "Master equation simulations of competing unimolecular and bimolecular reactions: application to OH production in the

reaction of acetyl radical with $O_2$". In: *Physical Chemistry Chemical Physics* 9.31, pp. 4291–4300. URL: http://xlink.rsc.org/?DOI=B614502G.

McDade, Lenhardt, and Bayers (1982). "The Rate of Reaction of Acetyl and Benzoyl Radicals with $O_2$". In: *Journal of Photochemistry* 20.1, pp. 1–7.

Michael, Keil, and Klemm (1985). "Rate Constants for the Reaction of Hydroxyl Radicals with Acetaldehyde from 244–528 K". In: *The Journal of Chemical Physics* 83.4, p. 1630.

Papadimitriou et al. (2015). "$CH_3CO + O_2 + M$ (M = He, $N_2$) Reaction Rate Coefficient Measurements and Implications for the OH Radical Product Yield". In: *Journal of Physical Chemistry A* 119.28, pp. 7481–7497.

Renbaum-Wolff and Smith (2012). "Virtual Injector Flow Tube Method for Measuring Relative Rates Kinetics of Gas-Phase and Aerosol Species". In: *Journal of Physical Chemistry A* 116.25, pp. 6664–6674. ISSN: 10895639.

Romero et al. (2005). "OH formation from the $C_2H_5CO + O_2$ reaction: An experimental marker for the propionyl radical". In: *Chemical Physics Letters* 408.4-6, pp. 232–236.

Thévenet, Mellouki, and Le Bras (2000). "Kinetics of OH and Cl reactions with a series of aldehydes". In: *International Journal of Chemical Kinetics* 32.11, pp. 676–685.

Tyndall, Orlando, Wallington, and Hurley (1999). "Rate Coefficients for the Reactions of Chlorine Atoms with Methanol and Acetaldehyde". In: *International Journal of Chemical Kinetics* 31.11, pp. 776–784.

Tyndall, Orlando, Wallington, and Michael (1997). "Pressure Dependence of the Rate Coefficients and Product Yields for the Reaction of $CH_3CO$ Radicals with $O_2$". In: *International Journal of Chemical Kinetics* 2.1.

Tyndall, Staffelbach, et al. (1995). "Rate coefficients for the reactions of OH radicals with Methylglyoxal and Acetaldehyde". In: *International Journal of Chemical Kinetics* 27.10, pp. 1009–1020.

Zügner et al. (2010). "OH yields for $C_2H_5CO + O_2$ at low pressure: Experiment and theory". In: *Chemical Physics Letters* 495.4-6, pp. 179–181.

# Chapter 4

# Rate Coefficients Determinations: Radical and Aldehyde Reactions

This chapter outlines the work undertaken to support and underpin research from Chapters 3 (RCO + O$_2$) and 6 (RC(O)O$_2$ + HO$_2$), specifically to investigate the kinetics of Cl and OH radicals with aldehyde precursors. Previous chapters have shown the importance of aldehydes (Chapters 1 and 3), therefore this will not be discussed in detail in this chapter. Instead this chapter reports the study of rate coefficients for six aldehydes: CH$_3$CHO, C$_2$H$_5$CHO, (CH$_3$)$_2$CHCHO, (CH$_3$)$_3$CCHO, C$_2$H$_5$CH(CH$_3$)CHO and (CH$_3$)$_2$CHCH$_2$CHO. The room-temperature results for RCHO + Cl rate coefficients are reviewed in Section 4.1, while the RCHO + OH are in Section 4.3. The rate coefficients were also analysed at higher temperature, with results for the Cl coefficients examined in Section 4.2 and for OH coefficients in Section 4.3.

New-room temperature coefficients for C$_2$H$_5$CH(CH$_3$)CHO + Cl and (CH$_3$)$_2$CHCH$_2$CHO + Cl are reported in Table 4.5 alongside other Cl + aldehyde rate coefficients which do have previous literature values.

# 4.1 Aldehyde with Chlorine Radicals at Room Temperature

Aldehydes are important trace constituents in the atmosphere, where the main degradation pathway which leads to the formation of RCO and $RC(O)O_2$ radicals is initiated by OH abstracting the aldehydic H-atom (Chapter 1). The importance of this pathway's subsequent reactions has led to various laboratory studies in past years; however, replicating the pathway in the laboratory was problematic due to problems in creating the RCO radicals. The traditional OH radical sources were photolysis of $H_2O_2$ or $HNO_3$, at a wavelength lower than 300 nm where interference from aldehyde photolysis could complicate kinetic analysis – enabling the reaction of $H + CH_3CO$ which produces $CH_3 + HCO$ (Rayez, Rayez, and Villenave 2011; Martinez et al. 1992).

To avoid this interference, Cl radicals were often used instead to create the RCO radical, allowing the study of RCO and $RC(O)O_2$ species without photolysis interference since $Cl_2$ photolysis occurs at 300 - 370 nm, away from the photolysis of aldehydes (Keller-Rudek et al. 2013)(Chapter 2). The rate coefficients for aldehydes with Cl need to be known to interpret these laboratory studies with high accuracy and precision (LeCrâne et al. 2004; Seakins, Orlando, and Tyndall 2004; Thévenet, Mellouki, and Bras 2000).

Chlorine rate coefficients are also critical for understanding the chemistry of the troposphere. In recent years, knowledge of the powerful influence that halogens have on the chemical composition of the troposphere has increased. Chlorine radicals are not only potent oxidisers for both organic and inorganic compounds, but have recently been shown to impact the nocturnal $NO_x$ chemistry (Chapter 1). As Cl is highly reactive towards hydrocarbons, Cl rate coefficients are crucial in understanding and simulating future atmospheric conditions and compositions.

### 4.1.1 Background and Previous Studies

The rate coefficient for $CH_3CHO$ + Cl has been the subject of numerous kinetic studies, with values calculated from both absolute and relative methods. One of the first measurements of this rate coefficient came from Niki et al. (1985), who carried out an FTIR study of $CH_3CHO$ + Cl alongside the reaction of $C_2H_6$ + Cl, allowing a relative decay rate for $CH_3CHO$ + Cl to be calculated: $(7.9 \pm 1.2)$ $\times$ $10^{-11}$ $cm^3$ molecule$^{-1}$ s$^{-1}$. A further seven studies have been carried out since then with consistent results, ranging from $(6.1 \pm 1.4)$ $\times$ $10^{-11}$ $cm^3$ molecule$^{-1}$ s$^{-1}$ to $(8.8 \pm 1.5)$ $\times$ $10^{-11}$ $cm^3$ molecule$^{-1}$ s$^{-1}$ (Tyndall, Orlando, et al. 1999; Kegley-Owen et al. 1999; Smith and Ravishankara 2002; Seakins, Orlando, and Tyndall 2004; Wallington et al. 1988; Payne et al. 1990; Bartels, Hoyermann, and Lange 1989). More recently a comprehensive review of these values for the $CH_3CHO$ + Cl rate coefficient recommended a value of $(8.0 \pm 0.6)$ $\times$ $10^{-11}$ $cm^3$ molecule$^{-1}$ s$^{-1}$ (Atkinson, Baulch, Cox, Crowley, Hampson, Hynes, Jenkin, Rossi, et al. 2004).

The rate coefficient for $C_2H_5CHO$ + Cl has been the subject of a number of kinetic studies, with the first measurement of this rate coefficient coming from Wallington et al. (1988) who carried out a relative rate study of $C_2H_5CHO$ + Cl alongside the reaction of $C_2H_6$ + Cl. The results were analysed by gas chromatography with flame ionisation detection (GC–FID) allowing a relative decay rate for $C_2H_5CHO$ + Cl to be determined: $(1.1 \pm 0.1) \times 10^{-10}$ $cm^3$ molecule$^{-1}$ s$^{-1}$. A further two relative rate studies have been carried out since then, providing consistent results ranging from $1.16 \times 10^{-10}$ $cm^3$ molecule$^{-1}$ s$^{-1}$ to $1.50 \times 10^{-10}$ $cm^3$ molecule$^{-1}$ s$^{-1}$(Thévenet, Mellouki, and Bras 2000; LeCrâne et al. 2004). Cuevas et al. (2006) carried out the first absolute kinetic study, giving a value of $1.10 \times 10^{-10}$ $cm^3$ molecule$^{-1}$ s$^{-1}$. A review of two of these values (Wallington et al. 1988; Thévenet, Mellouki, and Bras 2000) for the $C_2H_5CHO$ + Cl rate coefficient, gave the value to be $(1.3 \pm 0.3)$ $\times$ $10^{-10}$ $cm^3$ molecule$^{-1}$ s$^{-1}$ (Atkinson, Baulch, Cox, Crowley, Hampson, Hynes, Jenkin, Rossi, et al. 2004).

Studies on larger aldehydes are rare with the rate coefficients for $(CH_3)_3CCHO$ + Cl and $(CH_3)_2CHCHO$ + Cl only being studied twice before. Both studies used relative rate methods, though with different reference compounds – comparison is shown in Table 4.1 (Thévenet, Mellouki, and Bras 2000; LeCrâne et al. 2004). LeCrâne et al. (2004) carried out experiments in a FT–IR smog chamber, with the loss of $(CH_3)_3CCHO$ and the formation of products being monitored by FT–IR spectroscopy, whereas Thévenet, Mellouki, and Bras (2000) used GC–FID detection for quantitative analysis of the reactants. Assuming that the aldehyde and reference compound were only consumed by Cl, it was possible to determine relative rate constants of the aldehydes. Although there is a slight discrepancy with their results, both agree that $(CH_3)_2CHCHO$ + Cl has a faster rate coefficient than $(CH_3)_3CCHO$ + Cl.

Table 4.1: A comparison of the literature rate coefficients of $(CH_3)_2CHCHO$ + Cl and $(CH_3)_3CCHO$ + Cl; both studies used the relative rate method so their reference compounds have been included (LeCrâne et al. 2004; Thévenet, Mellouki, and Bras 2000).

| Literature | Reference Compounds | Cl Rate Coefficients / $10^{-10}$ cm$^3$ molecule$^{-1}$ s$^{-1}$ | |
|---|---|---|---|
| | | $(CH_3)_3CCHO$ | $(CH_3)_2CHCHO$ |
| Thévenet et al. (2000) | $C_2H_6$ ; $C_3H_8$ $n$-$C_4H_{10}$; $n$-$C_5H_{12}$ $n$-$C_6H_{14}$ | $1.6 \pm 0.3$ | $1.7 \pm 0.3$ |
| LeCrâne et al. (2004) | $C_2H_4$ $C_2H_{12}$ (cyclohexane) | $1.15 \pm 0.30$ | $1.33 \pm 0.25$ |

In this investigation, back-to-back PLP-LIF experiments, using a set-up as explained in Chapter 2, were carried out on six aldehydes ($CH_3CHO$, $C_2H_5CHO$, $(CH_3)_2CHCHO$, $(CH_3)_3CCHO$, $C_2H_5CH(CH_3)CHO$, $(CH_3)_2CHCH_2CHO$) to probe the rate coefficients of Cl + RCHO. Four rate coefficients ($CH_3CHO$ + Cl, $C_2H_5CHO$ + Cl, $(CH_3)_2CHCHO$ + Cl, $(CH_3)_3CCHO$ + Cl) have literature values with $CH_3CHO$ + Cl being the most reliable. Therefore these served as a good test of the indirect method used in this work whereby OH acted as a 'spectroscopic marker' for Cl kinetics.

Two previously unknown rate coefficients were determined for the first time in this project: $C_2H_5CH(CH_3)CHO + Cl$ and $(CH_3)_2CHCH_2CHO + Cl$.

## 4.1.2  Experimental

OH profiles were recorded at six different aldehyde concentrations ($0.79 - 4.21 \times 10^{14}$ molecule cm$^{-3}$), repeated at three different bath gas, $N_2$, pressures (13 Torr, 30 Torr and 50 Torr); see Table 4.2 for the concentrations of the other species.

Table 4.2:  The range of the concentration of $O_2$, $Cl_2$, $Cl$, and $N_2$ used in the experiments to determine rate coefficients of Cl with RCHO.

| Concentrations / molecule cm$^{-3}$ | | | |
|---|---|---|---|
| $O_2$ | $Cl_2$ | $Cl$ | $N_2$ |
| $0.54 - 1.85 \times 10^{17}$ | $0.60 - 1.53 \times 10^{14}$ | $0.5 - 2 \times 10^{12}$ | $0.11 - 1.37 \times 10^{18}$ |

The reactions (Equations 4.1, 4.2, 4.3, 4.4, 4.5, and 4.6) were studied under pseudo-first order conditions with aldehyde concentrations in excess over Cl: [RCHO] >> [Cl] >> [OH]. The products from the RCHO +Cl reactions are unknown, since the Cl can abstract a hydrogen atom from anywhere in the molecule. Structure activity relationships (SARs – Chapter 3) are able to predict the ratio of the products; however, since this chapter is examining just the rate coefficients of Cl + RCHO the ratio of the products do not matter, and therefore are not discussed further.

$$CH_3CHO + Cl \rightarrow CH_3CO \textit{ or } CH_2CHO + HCl \tag{4.1}$$

$$C_2H_5CHO + Cl \rightarrow \textit{products} \tag{4.2}$$

$$(CH_3)_2CCHO + Cl \rightarrow \textit{products} \tag{4.3}$$

$$(CH_3)_2CHCHO + Cl \rightarrow \textit{products} \tag{4.4}$$

$$C_2H_5CH(CH_3)CHO + Cl \rightarrow \textit{products} \tag{4.5}$$

$$(CH_3)_2CHCH_2CHO + Cl \rightarrow \textit{products} \tag{4.6}$$
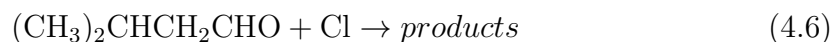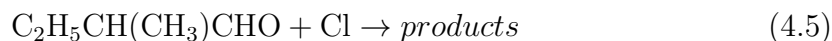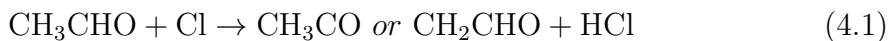
### 4.1.3 Preliminary Results

The results at each pressure were fitted with the expression shown in Equation 4.7 and explained in detail in Chapter 3. The results were analysed with a 'natural fit' and a 'constrained fit' – where one of the parameters of the fit is known. Parameter $B$ in Equation 4.7 can be estimated when the RCHO + OH rate coefficient is multiplied by the [RCHO]. This parameter $B$ can be explained by Equation 4.8, where $k_2$ is the rate constant for Reaction 4.1, explained previously in Chapter 3. Equation 4.8 shows the importance of recording the rate at different [$CH_3CHO$], as when the rate is plotted against [$CH_3CHO$], the gradient will be the rate coefficient whereas the $y$-intercept would be the $k_D$ which represents the transport coefficients and Cl loss channels which are negligible.

However, a problem with this analysis is that the RCHO + OH rate coefficient was only well known for the smaller aldehydes and an estimate for the unknown $C_2H_5CH(CH_3)CHO$ + OH and $(CH_3)_2CHCH_2CHO$ + OH rate coefficients, calculated by SARs (Chapter 3), were used. Therefore, this constrained fit was only used as a test to confirm the validity of the data – giving confidence in the results if both fits produce similar values.

$$[OH](t) = A(e^{-Bt} - e^{-Ct}) \tag{4.7}$$

$$B = k_2[CH_3CHO] + k_D \tag{4.8}$$

Figure 4.1 shows a typical kinetic trace from the data collected at 13 Torr. The scatter of the data has caused a difference between the two methods of fitting, with the constrained fit suggesting a faster decay of OH for both reactions. This could be an indication that the high number of radicals in the system has made the system's kinetics too complex for it to be constrained by two simple exponentials. The results shown in Figure 4.1 could also suggest that, for the constrained fit, the OH decay
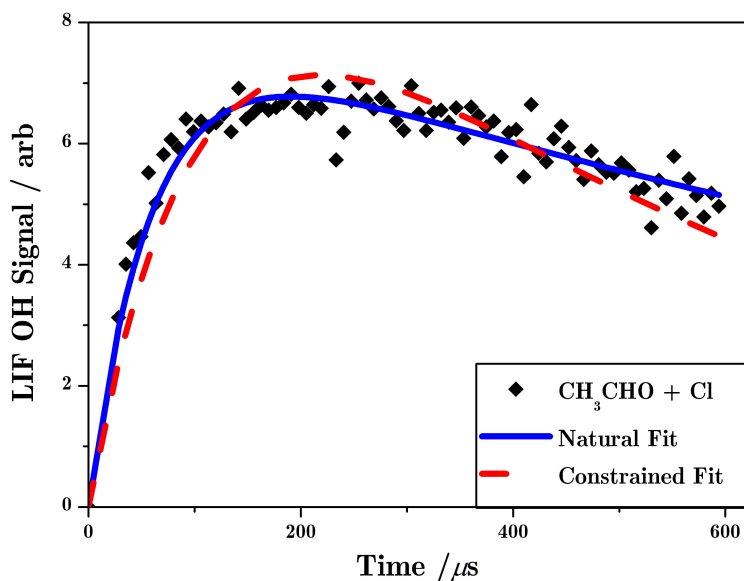
Figure 4.1: Kinetic trace of the production and decay of OH from the reaction of $CH_3CHO + Cl$ at 13 Torr with $[CH_3CHO] = 2.1 \times 10^{14}$ molecule$^{-1}$ cm$^3$ (black diamonds) with both the natural (blue line) and the constrained (dashed red line) non-linear fit.
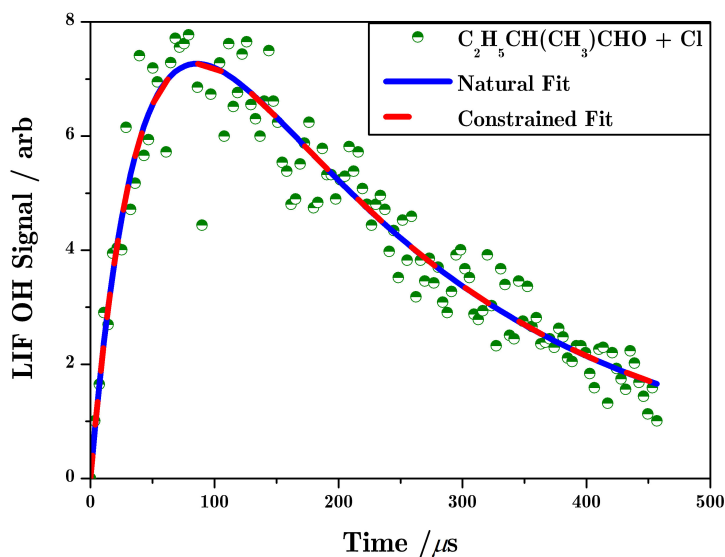


Figure 4.2: Kinetic trace of the production and decay of OH from the reaction of $C_2H_5CH(CH_3)CHO + Cl$ at 50 Torr with $[C_2H_5CH(CH_3)CHO] = 1.4 \times 10^{14}$ molecule$^{-1}$ cm$^3$ (green circles), with both the natural (blue line) and the constrained (dashed red line) non-linear fit.

is too fast. The OH yield at 13 Torr is a lot higher than the yield at 30 Torr:
0.3 compared to 0.1. The OH yield follows a Stern-Volmer relationship (Chapter
3) meaning that it follows an exponential relationship, therefore small pressure
fluctuations at the lower pressures cause a larger change in the OH yield than at
higher pressures. Since the results at 13 Torr were not reliable when investigating the
Cl + RCHO rate coefficients they were not used in the calculation of the coefficients.

Figure 4.2 displays a typical kinetic trace from the data collected at 50 Torr. This
trace was compared to the 13 Torr trace (Figure 4.1). The difference in these plots
show that the two fits are able to constrain the data better for the results at 50 Torr
than at 13 Torr.

The close agreement between the two fits in Figure 4.2 for $C_2H_5CH(CH_3)CHO + Cl$,
indicates that the system's kinetics can be constrained by two exponentials, giving
confidence in the results. The difference between the three parameters ($A$, $B$, and
$C$) for the 13 and 50 Torr results, Table 4.3, is illustrated by the numerical difference
between the parameters: the values for 13 Torr differ greatly, compared to the 50
Torr values. This indication from the two fits, that the 13 Torr data were was worse
than the 30 and 50 Torr, was backed up when the rate coefficients were calculated.
The rate coefficient for $CH_3CHO + Cl$ has a well-known literature value of (8.00
$\pm$ 0.6) $\times$ $10^{-11}$ cm$^3$ molecule$^{-1}$ s$^{-1}$ (Atkinson, Baulch, Cox, Crowley, Hampson,
Hynes, Jenkin, Kerr, et al. 2007). The data at 13 Torr gave the rate coefficient to be
(4.1 $\pm$ 1.8) $\times$ $10^{-11}$ cm$^3$ molecule$^{-1}$ s$^{-1}$, whereas the data at 50 Torr gave a value of
(8.3 $\pm$ 0.9) $\times$ $10^{-11}$ cm$^3$ molecule$^{-1}$ s$^{-1}$, a more accurate value – as predicted from
the kinetic trace fits.

There was, however, more scatter in the higher pressure results than in the 13 Torr
results, which could be due to the increased concentration of bath gas. This increase
in bath gas increases the quenching rate of the OH radical, decreasing the signal so
there is a lower signal-to-noise ratio. Unfortunately, the only way to combat this was
to increase the number of scans that gave the average signal, which consecutively

Table 4.3: The results of the two different fits (natural and constrained) at two different pressures: 13 and 50 Torr, illustrating the difference between the results.

| Fit Parameters | 13 Torr | | 50 Torr | |
|---|---|---|---|---|
| | **Normal** | **Constrained** | **Normal** | **Constrained** |
| $A$ | $1.14 \times 10^6$ | $1.77 \times 10^6$ | $3.14 \times 10^5$ | $2.64 \times 10^5$ |
| $B$ | $8.02 \times 10^2$ | $1.76 \times 10^3$ | $3.01 \times 10^3$ | $2.02 \times 10^3$ |
| $C$ | $1.68 \times 10^4$ | $9.46 \times 10^3$ | $2.55 \times 10^4$ | $2.97 \times 10^4$ |

increased the time between the experimental runs. Therefore a compromise was reached to achieve less scatter but to still be able to assume nothing had changed in between experimental runs.

In all the analyses when the rate coefficients for the reactions of RCHO + Cl were investigated, comparisons between the natural and the constrained fits were carried out. This comparison acted as a test, with only the results which had the constrained and natural fit overlapping used for future analysis. This comparison also gave evidence that it was possible to analyse the kinetics by two simple exponentials. In all future sections where RCHO + Cl results are discussed, this stage of the analysis has been carried out even though it is not mentioned again. Only the results which have overlapping natural and constrained fit are shown and discussed.

### 4.1.4 Rate Coefficients of Cl with Aldehyde - Results

Figure 4.3 displays the results from the non-linear fits at 50 Torr with their corresponding least-squares fit for the rate coefficients of: $CH_3CHO$ + Cl (black diamonds), $C_2H_5CHO$ + Cl (red diamonds), $(CH_3)_2CHCH_2CHO$ + Cl (orange circles) and $C_2H_5CH(CH_3)CHO$ + Cl (green circles). The results are exceptionally similar to the 30 Torr results and therefore they are not shown here but can be found in Appendix C. As discussed in the previous section, although data were collected at 13 Torr it was not possible to include the results in rate coefficient calculations due to not being able to validate them. The results at both 30 and 50 Torr gave a linear trend, which was expected of rate coefficients at different concentrations of precursor – the higher the concentration the faster the rate. There was scatter with both data sets which was expected for such an indirect method; however, there was no indication whether the scatter improves with changing concentrations of aldehyde or pressure changes.

Table 4.4 shows the results from the least square analysis from experimental runs of varying the aldehyde concentration for the rate coefficients: $CH_3CHO$ + Cl, $C_2H_5CHO$ + Cl, $(CH_3)_3CCHO$ + Cl, $(CH_3)_2CHCHO$ + Cl, $C_2H_5CH(CH_3)CHO$ + Cl and $(CH_3)_2CHCH_2CHO$ + Cl at two pressures (30 and 50 Torr). The results of 30 and 50 Torr for $CH_3CHO$ + Cl and $C_2H_5CHO$ + Cl follow closely to the literature. Comparing the results of 30 and 50 Torr in Table 4.4, shows that on average the experimentally calculated rate coefficients at 50 Torr are closer to the literature than the 30 Torr results. In general, the experimental results of four rate coefficients which have literature values, follow the literature within their errors – except for two values: $CH_3CHO$ + Cl at 30 Torr and $(CH_3)_2CHCHO$ + Cl at 50 Torr.

The 30 Torr results agree with the literature trend with the fastest to slowest order being: $CH_3CHO$ + Cl, $C_2H_5CHO$ + Cl, $(CH_3)_2CHCHO$ + Cl then $(CH_3)_3CCHO$ +

Cl; however, the 50 Torr results have the order slightly changed so $(CH_3)_2CHCHO$ + Cl and $(CH_3)_3CCHO$ + Cl are inverted. They both, nonetheless, agree that out of the six rate coefficients $(CH_3)_2CHCH_2CHO$ + Cl is the slowest and $CH_3CHO$ + Cl is the fastest. The one rate coefficient they disagree on the most is $(CH_3)_2CHCHO$ + Cl from $(21.0 \pm 3.1) \times 10^{-11}$ $cm^3$ $molecule^{-1}$ $s^{-1}$ at 30 Torr to $(10.0 \pm 1.6) \times 10^{-11}$ $cm^3$ $molecule^{-1}$ $s^{-1}$ at 50 Torr.

The room-temperature rate coefficient was calculated by using a weighted average of the results from the two different pressures, shown by Figure 4.4 with the values in Table 4.4. Only the results at 30 and 50 Torr are used for the weighted average since the data at 13 Torr were previously shown not to be reliable enough – though the data from 13 Torr are still shown in Figure 4.4 as the empty data points. The error associated with the room temperature rate coefficient was calculated by the statistical error of the weighted average, as the weighted average took into account the errors at each pressure.

Table 4.4: Results for Cl rate coefficients with: $CH_3CHO$; $C_2H_5CHO$; $(CH_3)_3CCHO$; $(CH_3)_2CHCHO$; $C_2H_5CH(CH_3)CHO$; and $(CH_3)_2CHCH_2CHO$ at 30 and 50 Torr (293 K).

| Reaction (+ Cl) | Rate Coefficient / $10^{-11}$ $cm^3$ $molecule^{-1}$ $s^{-1}$ | | | |
|---|---|---|---|---|
| | Literature | Experimental | | |
| | | 30 Torr | 50 Torr | Combined |
| $CH_3CHO$ | $8.0 \pm 0.6$ [1] | $10.0 \pm 0.2$ | $8.3 \pm 0.9$ | $8.8 \pm 1.3$ |
| $C_2H_5CHO$ | $13 \pm 3$ [1] | $14.2 \pm 3.4$ | $13.5 \pm 0.9$ | $13.8 \pm 1.5$ |
| $(CH_3)_2CHCHO$ | $15.3 \pm 2.0$ [2] | $21.0 \pm 3.1$ | $10.6 \pm 1.6$ | $15.1 \pm 6.8$ |
| $(CH_3)_3CCHO$ | $13.8 \pm 2.1$ [2] | $13.2 \pm 3.0$ | $14.6 \pm 2.3$ | $13.8 \pm 1.6$ |
| $C_2H_5CH(CH_3)CHO$ | Unknown | $11.2 \pm 3.8$ | $1.7 \pm 0.2$ | $14.2 \pm 3.0$ |
| $(CH_3)_2CHCH_2CHO$ | Unknown | $24.3 \pm 7.6$ | $38.5 \pm 3.5$ | $30.7 \pm 6.4$ |

*Notes:* Combined values represent the weighted average of the 30 and 50 Torr data; [1] =(Atkinson, Baulch, Cox, Crowley, Hampson, Hynes, Jenkin, Rossi, et al. 2004); [2] = weighted average of Thévenet, Mellouki, and Bras (2000) and LeCrâne et al. (2004).
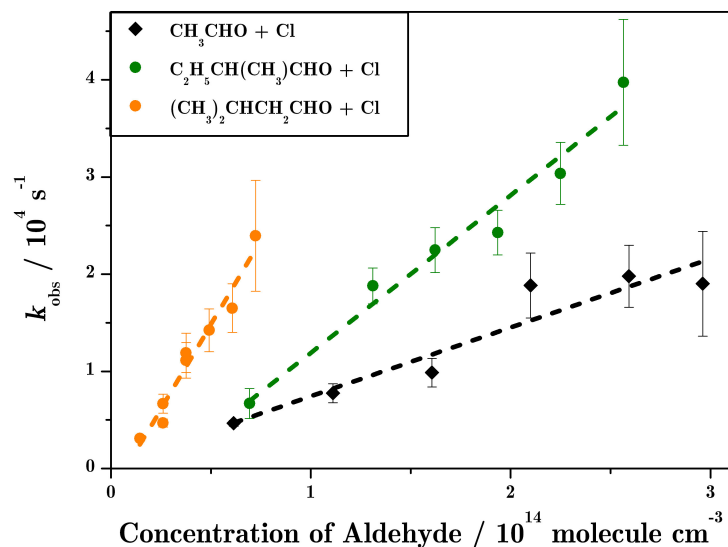
Figure 4.3: Results from the non-linear fits at 50 Torr, three different RCHO + Cl are shown at six concentrations: $CH_3CHO$ + Cl (black diamonds), $C_2H_5CH(CH_3)CHO$ + Cl (green circles), and $(CH_3)_2CHCH_2CHO$ + Cl (orange circles). The dash lines represent the fit lines to the corresponding colour data points.
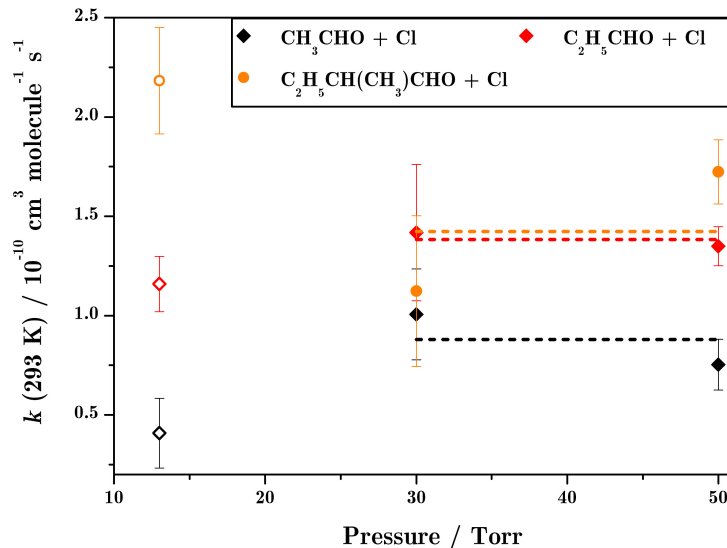


Figure 4.4: The experimentally calculated rate coefficients of: $CH_3CHO$ + Cl (black diamonds), $C_2H_5CHO$ + Cl (red diamonds), $C_2H_5CH(CH_3)CHO$ + Cl (green circles) and $(CH_3)_2CHCH_2CHO$ + Cl (orange circles). The results at the three pressures are shown (13, 30 and 50 Torr), with the 13 Torr results shown in empty data points as they were not used in the final rate coefficient calculation.

Previous literature has shown that there is no pressure dependence with these rate coefficients, and therefore any fluctuations between the different pressures must be due to the experimental conditions (Cuevas et al. 2006). This experimental set-up is unable to test the pressure dependence as it cannot work at low (too much OH) or high enough pressures (too few OH).

More importantly, no systematic changes were observed over the pressure range examined: results from 50 Torr were not always greater or smaller than 30 Torr, therefore these experiments had no pressure dependency.

The experimentally determined rate coefficients can be compared to both the literature rate coefficients and also rate coefficients calculated by structure activity-relationships (SARs), discussed further in Chapter 3. These comparisons are found in Table 4.5. The agreement between the experimental results and the literature, gives confidence in this indirect method, showing that the rate coefficient can be estimated this way. The rate coefficient increases with the number of $CH_x$ groups in the aldehyde molecule, except for the reaction of $(CH_3)_2CHCHO + Cl$. This same trend has been observed by previous literature studies (Cuevas et al. 2006; Thévenet, Mellouki, and Bras 2000; Rodríguez et al. 2005), though for those studies the straight-chain aldehydes were mostly studied, and saw an increase from $k_{propanal} < k_{butanal} < k_{pentanal} < k_{hexanal} < k_{heptanal}$.

In general the experimental results are lower than the SAR calculated results, except for the rate coefficient of $(CH_3)_2CHCH_2CHO + Cl$ where the experimental result is significantly higher. This could be an indication of a deactivating effect of the aldehydic group, which has been suggested by Cuevas et al. (2006). This deactivating carbonyl group can withdraw the electron density from the chain, which could decrease the rate of reaction. It would lead to the Cl SAR having a larger value than the experimental results that are shown in this study, since the SAR calculation does not take this deactivation into account. The difference between the experimental values and the SAR calculated values could also be due to how the rate becomes

Table 4.5: Results from the least-square analysis for Cl rate coefficients with: $CH_3CHO$; $C_2H_5CHO$; $(CH_3)_3CCHO$; $(CH_3)_2CHCHO$; $C_2H_5CH(CH_3)CHO$; and $(CH_3)_2CHCH_2CHO$ alongside literature and SAR values.

| Reaction (+ Cl) | Rate Coefficient / $10^{-10}$ cm$^3$ molecule$^{-1}$ s$^{-1}$ | | |
| --- | --- | --- | --- |
| | Literature | SAR [3] | This Work |
| $CH_3CHO$ | 0.80 ±0.06 [1] | 0.801 | 0.88 ± 0.13 |
| $C_2H_5CHO$ | 1.30 ± 0.3 [1] | 1.23 | 1.4 ± 0.15 |
| $(CH_3)_2CHCHO$ | 1.53 ± 0.20 [2] | 1.46 | 1.5 ± 0.7 |
| $(CH_3)_3CCHO$ | 1.38 ± 0.21 [2] | 1.61 | 1.4 ± 0.2 |
| $C_2H_5CH(CH_3)CHO$ | Unknown | 2.10 | 1.4 ± 0.3 |
| $(CH_3)_2CHCH_2CHO$ | Unknown | 1.73 | 3.1 ± 0.6 |

*Note:* Literature values from: [1] = Atkinson, Baulch, Cox, Crowley, Hampson, Hynes, Jenkin, Rossi, et al. (2004); [2] = weighted average of Thévenet, Mellouki, and Bras (2000) and LeCrâne et al. (2004).[3] SAR calculation (Carter 2010).

limited by the collision frequency of the Cl with the molecule rather than the collision frequency of the Cl at a specific site of the molecule (Cuevas et al. 2006).

A comparison between the results given for the OH rate coefficients from the SAPRC-07 SAR, (Carter 2010), to the recently updated Jenkin SAR, (Jenkin et al. 2018), can give an insight into how accurate the SAPRC-07 Cl SAR is – see Table 4.6. There is good agreement between the values for straight-chained aldehydes; however, for branched aldehydes the differences become more significant. This difference can easily be the same with the Cl coefficients, which suggests that the difference in the Cl rate coefficients for the experimental results and the SAPRC-07 SAR in Table 4.5 is to be expected.

To check that the calculated rate coefficients are plausible, it is possible to add these new calculated values into Kintecus. Figure 4.5 shows a kinetic trace of $C_2H_5CH(CH_3)CHO$ + Cl at 30 Torr overlaid with two Kintecus plots. Both Kintecus plots use a simple model – see the reactions shown in Table 4.7. Originally the rate coefficient for $C_2H_5CH(CH_3)CHO$ + Cl was unknown, therefore the value which was used instead was $n$-$C_4H_9CHO$ + Cl since that is well known and the aldehyde has the same number of carbons and hydrogens.

Table 4.6: Comparison of experimental literature to theoretical SAR calculations of OH rate coefficients with six aldehydes: $CH_3CHO$, $C_2H_5CHO$, $(CH_3)_3CCHO$, $(CH_3)_2CHCHO$, $C_2H_5CH(CH_3)CHO$, and $(CH_3)_2CHCH_2CHO$.

| Reaction (+ OH) | Rate Coefficient/ $10^{-11}$ cm$^3$ molecule$^{-1}$ s$^{-1}$ | | |
| --- | --- | --- | --- |
| | Literature | SAR Jenkin [3] | SAR SAPRC-07[4] |
| $CH_3CHO$ | $1.50 \pm 0.06$ [1] | 1.50 | 0.697 |
| $C_2H_5CHO$ | $1.90 \pm 0.1$ [1] | 2.20 | 1.17 |
| $(CH_3)_2CHCHO$ | $2.56 \pm 0.21$ [2] | 2.94 | 1.29 |
| $(CH_3)_3CCHO$ | $2.68 \pm 0.12$ [2] | 2.83 | 1.18 |
| $C_2H_5CH(CH_3)CHO$ | $3.28 \pm 0.09$ [2] | 3.22 | 1.84 |
| $(CH_3)_2CHCH_2CHO$ | $2.79 \pm 0.07$ [2] | 2.73 | 3.72 |

*Notes:* Literature values from: [1] Atkinson, Baulch, Cox, Crowley, Hampson, Hynes, Jenkin, Kerr, et al. (2007) and [2] = D'Anna et al. (2001). SAR calculation[3] = (Jenkin et al. 2018); [4] = (Carter 2010).

Table 4.7: The reactions included in the Kintecus simple model to examine the OH production from $C_2H_5CH(CH_3)CO + O_2$.

| Reaction | Rate Coefficient / cm$^3$ molecule$^{-1}$ s$^{-1}$ | Reference |
| --- | --- | --- |
| $C_2H_5CH(CH_3)CHO + Cl$* | $1.9 \times 10^{-10}$ | Cuevas et al. (2006) |
| $C_2H_5CH(CH_3)CO + O_2$ $\rightarrow$ OH +products | $3.3 \times 10^{-13}$ | Chapter 3 |
| $C_2H_5CH(CH_3)CO + O_2$ $\rightarrow C_2H_5CH(CH_3)C(O)O_2$ | $6.7 \times 10^{-12}$ | Chapter 3 |
| $C_2H_5CH(CH_3)CO + Cl_2$* | $4.3 \times 10^{-11}$ | Atkinson et al. (2007) |
| $C_2H_5CH(CH_3)CHO + OH$ | $3.3 \times 10^{-11}$ | D'Anna et al. (2001) |

*Notes:* $C_2H_5CH(CH_3)CHO + Cl$* the reaction of $C_4H_9CHO + Cl$ was used instead; $C_2H_5CH(CH_3)CO + Cl_2$* the reaction of $CH_3CHO + Cl$ was used instead.

The original trace which uses an estimate of the $C_2H_5CH(CH_3)CHO + Cl$ is the dashed black line in Figure 4.5; this trace rises quicker than the data. When the value which has been calculated in this study was used (the blue line) it produces a trace which fits much better – it clearly follows the rise of the OH in the data. This shows that the new rate coefficient determined for $C_2H_5CH(CH_3)CHO + Cl$ does follow the experimental data.

The rate coefficient for the reaction of $C_2H_5CH(CH_3)CO + O_2$ used the rate of $CH_3CO + O_2$ but with the branching ratio determined from Chapter 3. It was
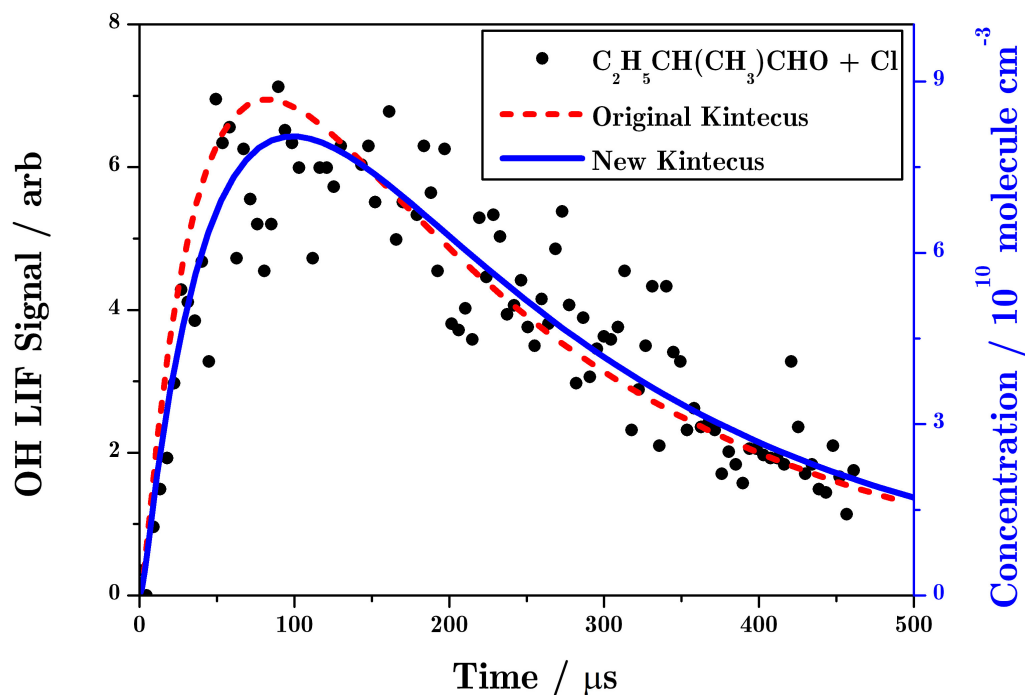
Figure 4.5: An experimental trace of $C_2H_5CH(CH_3)CO + O_2$ (black circles) at 30 Torr alongside two Kintecus traces. The red dashed line represented the original Kintecus which only had an estimate for the rate coefficient of $C_2H_5CH(CH_3)CHO + Cl$ whereas the blue line represents the Kintecus model which included the rate coefficient of $C_2H_5CH(CH_3)CHO + Cl$ determined in this study.

assumed that because the $O_2$ was in excess, the reaction would proceed via pseudo first-order reaction. This was shown to be true since altering the $C_2H_5CH(CH_3)CO + Cl$ rate coefficient had the desired effect of being able to constrain the rise of OH from this rate coefficient and not having to alter the $C_2H_5CH(CH_3)CO + O_2$ rate.

## 4.2 Rate Coefficients of Cl with Aldehydes at High Temperature

Rate coefficients of Cl + RCHO at higher temperatures are of interest as studies use Cl to initiate the chemistry. To allow the reduction of uncertainties in these higher temperature studies, it is important to understand as much as possible about the kinetics. This section will discuss the results of the high temperature studies, carried out to increase the knowledge of Cl rate coefficients at higher-temperatures.

### 4.2.1 Background

Two previous higher temperature studies have been carried out on the rate coefficients of Cl with six straight-chained aldehydes. Payne et al. (1990) examined $CH_3CHO$ + Cl at a temperature range of 210 to 343 K, while Cuevas et al. (2006) carried out studies on $C_2H_5CHO$, $C_3H_7CHO$, $C_4H_9CHO$, $C_5H_{11}CHO$, and $C_6H_{13}CHO$ at a range of 265 to 381K. When Atkinson, Baulch, Cox, Crowley, Hampson, Hynes, Jenkin, Rossi, et al. (2004) completed their review, they came to the conclusion that up to 340 K the rate coefficient for $CH_3CHO$ + Cl was temperature independent, staying at $8 \times 10^{-11} cm^3$ molecule$^{-1}$ s$^{-1}$.

In this investigation, back-to-back PLP–LIF experiments were carried out to probe the temperature effect on rate coefficients of Cl + RCHO, with the set-up explained in Chapter 2. The reactions of Cl with various aldehydes: $CH_3CHO$, $(CH_3)_2CHCHO$, $(CH_3)_3CCHO$, $C_2H_5CH(CH_3)CHO$, and $(CH_3)_2CHCH_2CHO$), were investigated to obtain temperature-dependent Cl rate coefficients. For each study, the aldehyde concentration was varied at each different pressure, whilst the conditions of temperature, pressure, [Cl], [Cl$_2$], and [O$_2$] were kept constant. Since the rate coefficient of $CH_3CHO$ + Cl has the most extensive literature database, it was used for the comparison reaction. The analysis was kept the same throughout, with

both the constrained and natural fit used to determine the reproducibility and the quality of the data. The results discussed here all have had both fits overlap each other, validating the data; since this analysis procedure was examined in detail in the previous section it is not discussed again here.

## 4.2.2 Temperature Dependency of Ethanal, Pivaldehyde, 2-Methylpropanal and 2-Methylbutanal with Cl

The four rate coefficients which were investigated at the higher temperatures of 330 and 410 K were: $CH_3CHO + Cl$, $(CH_3)_2CHCHO + Cl$, and $C_2H_5CH(CH_3)CHO + Cl$, while $(CH_3)_3CCHO + Cl$ was only investigated at 330 K. At 330 K, results from three pressures were recorded (13, 30 and 50 Torr) – Figure 4.6 shows a typical kinetic trace of the OH fluorescence as a function of time.
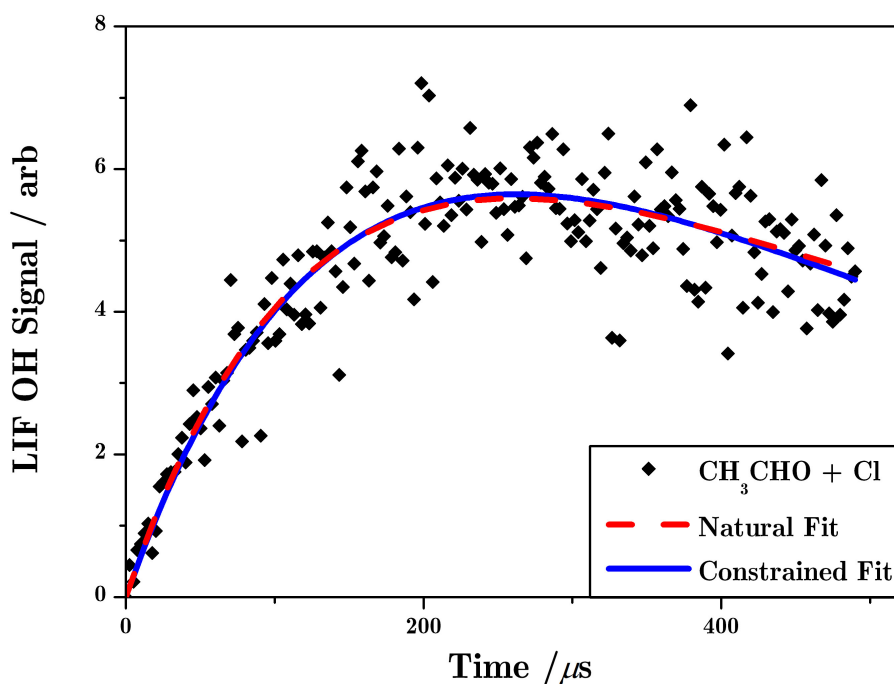


Figure 4.6: Kinetic trace of the production and decay of OH from the reaction of $CH_3CHO + Cl$ (black diamonds) at 13 Torr and 330 K with $[CH_3CHO] = 1.9 \times 10^{14}$ molecule cm$^{-3}$. Both types of the non-linear fits from the equation 4.7 are seen – natural fit in blue and the constrained fit in red.

The analysis of the kinetic traces was the same as for the previous room-temperature rate coefficients – Figure 4.7 displays the results from the non-linear fits at 13 Torr of $CH_3CHO + Cl$, $(CH_3)_2CHCHO + Cl$, and $C_2H_5CH(CH_3)CHO + Cl$. Similar to the results at room temperature, the data from each pressure at 330 K gave linear plots of $k_{obs}$ versus aldehyde concentration. Only the data from 13 Torr are presented here, in Figure 4.7. The results from the data collected at 30 and 50 Torr are similar to the 13 Torr results, with $R^2$ values all above 0.9 – these linear plots can be found in Appendix C.
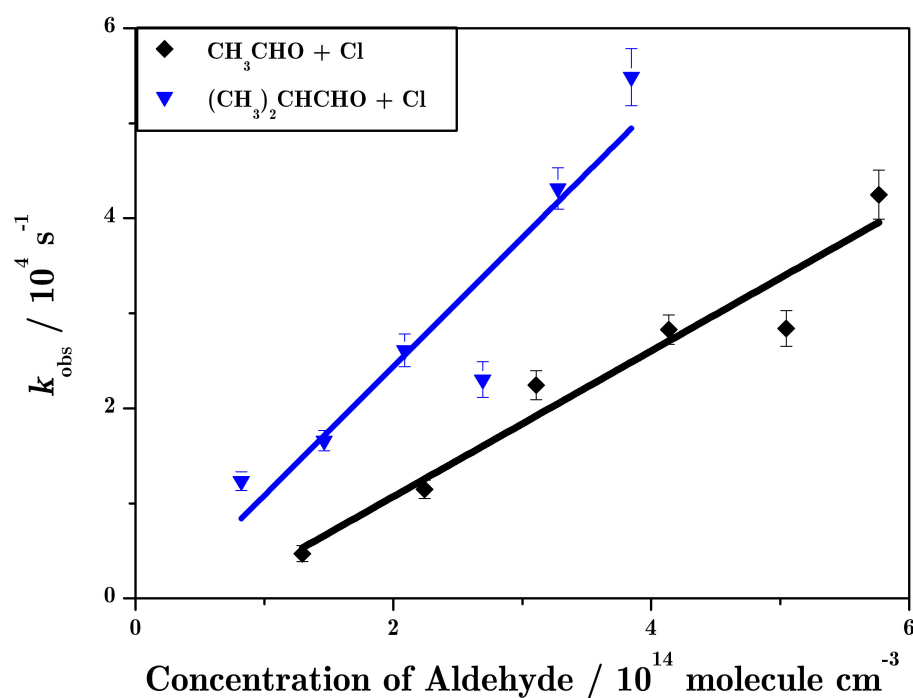


Figure 4.7: Results from the non-linear fits at 13 Torr and 330 K, of two different RCHO + Cl: $CH_3CHO + Cl$ (black diamonds) and $(CH_3)_3CHCHO + Cl$ (blue triangles). The lines represent the least-squares analysis and the error bars are not included to allow a clearer plot.

Table 4.8 shows the results from the least-square analysis of the results from the investigation of the Cl rate coefficients at the three pressures (13, 30 and 50 Torr) at 330 K.

Table 4.8: Results from the least-square analysis of Cl rate coefficients with: $CH_3CHO$, $(CH_3)_3CCHO$, $(CH_3)_2CHCHO$, and $C_2H_5CH(CH_3)CHO$ at 330 K for three pressures (13, 30 and 50 Torr).

| Reaction +Cl | Rate Coefficient / $10^{-11}$ cm$^3$ molecule$^{-1}$ s$^{-1}$ | | | |
| | Literature at 298 K | Experimental at 330 K | | |
| | | 13 Torr | 30 Torr | 50 Torr |
|---|---|---|---|---|
| $CH_3CHO$ | $8.0 \pm 0.07$ [1] | $7.7 \pm 1.0$ | $12.6 \pm 7.2$ | $3.6 \pm 1.4$ |
| $(CH_3)_2CHCHO$ | $15.3 \pm 2.0$ [2] | $13.6 \pm 2.5$ | $11.4 \pm 2.8$ | $12.9 \pm 2.3$ |
| $(CH_3)_3CCHO$ | $13.8 \pm 2.1$ [2] | $2.9 \pm 1.3$ | $16.7 \pm 6.5$ | $8.7 \pm 0.2$ |
| $C_2H_5CH(CH_3)CHO$ | Unknown | $7.7 \pm 2.2$ | $15.7 \pm 10.0$ | $14.2 \pm 3.9$ |

*Notes:* Literature values at 1 atm from: [1] = Atkinson, Baulch, Cox, Crowley, Hampson, Hynes, Jenkin, Rossi, et al. (2004); [2] = weighted average of Thévenet, Mellouki, and Bras (2000) and LeCrâne et al. (2004).

The results for each pressure show the deviation that occurs from using this indirect method to determine rate coefficients – as it is known that there is no pressure dependence over the range that was investigated in this study.

The rate coefficient which gave the largest deviations between the results was $CH_3CHO$ + Cl; however, the literature value falls inside the range that this work has calculated. The results for the $(CH_3)_2CHCHO$ + Cl rate coefficient gave a range from $(11.4 \pm 2.8)$ to $(13.6 \pm 2.5) \times 10^{-11}$cm$^3$ molecule$^{-1}$ s$^{-1}$, this indicates that it is possible to obtain accurate and reliable results at the higher temperature.

The data for the rate coefficient $(CH_3)_3CHCHO$ + Cl also had a lot of scatter giving a wide range of results but $C_2H_5CH(CH_3)CHO$ + Cl seems to have more reliable results with less scatter. Increasing the temperature from 293 to 330 K affected the reliability of the results: it increased the scatter of the data. For future experiments this scatter needed to be reduced to improve the results. As the room-temperature results had worse data at the lower pressures (notably the 13 Torr data which could not be used), the next set of high-temperature data collection was recorded at higher pressures to improve the reproducibility of the data.

The temperature was increased to 410 K, where two pressures were investigated: 80 and 120 Torr. Figures 4.8 and 4.9 display the results from the non-linear fits

of $CH_3CHO$ + Cl, $(CH_3)_2CHCHO$ + Cl and $C_2H_5CH(CH_3)CHO$ + Cl. Table 4.9 shows the results from the least-square analysis of the results from the investigation of the Cl rate coefficients at the two pressures (50 and 80 Torr) at 410 K.

Table 4.9: Results from the least-square analysis of Cl rate coefficients with: $CH_3CHO$, $(CH_3)_2CHCHO$, and $C_2H_5CH(CH_3)CHO$ at 410 K with two pressures (50 and 80 Torr).

| Reaction (+ Cl) | Rate Coefficient / $10^{-11}$ cm$^3$ molecule$^{-1}$ s$^{-1}$ | | |
|---|---|---|---|
| | Literature | Experimental at 410 K | |
| | at 298 K | 80 Torr | 120 Torr |
| $CH_3CHO$ | $8.0 \pm 0.07$ [1] | $3.8 \pm 0.6$ | $5.1 \pm 2.1$ |
| $(CH_3)_2CHCHO$ | $15.3 \pm 2.0$ [2] | $5.3 \pm 1.0$ | $3.1 \pm 0.3$ |
| $C_2H_5CH(CH_3)CHO$ | Unknown | $5.7 \pm 0.8$ | $2.4 \pm 0.1$ |

*Notes:* Literature values from: [1] = Atkinson, Baulch, Cox, Crowley, Hampson, Hynes, Jenkin, Rossi, et al. (2004); [2] = weighted average of Thévenet, Mellouki, and Bras (2000) and LeCrâne et al. (2004).

In comparison to the 330 K results, the increase in pressure has reduced the scatter of the data. The values in Table 4.9 show less deviation between the values than the results at 330 K – an improvement for the data reliability. The results, however, indicate that the rate increases substantially for all three rate coefficients at higher temperatures. This does make sense as at higher temperatures as reactions generally occur faster. The results suggest that the rates for $(CH_3)_2CHCHO$ + Cl and $C_2H_5CH(CH_3)CHO$ + Cl increase significantly at higher temperature, so they are faster than $CH_3CHO$ + Cl. An increase of this magnitude seems unlikely, and so future work should include more repeats so the data are more reliable.
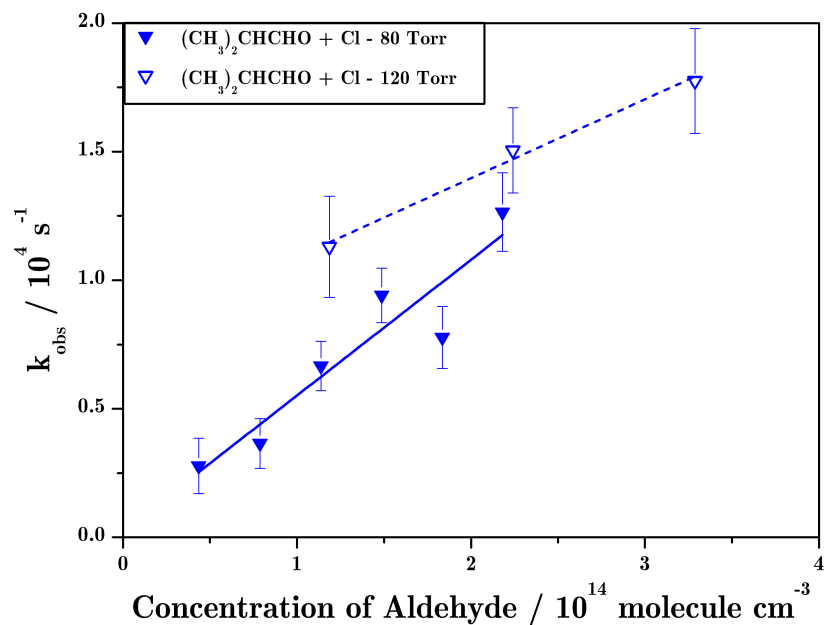
Figure 4.8: Results from the non-linear fits at 80 (filled triangles) and 120 Torr (unfilled triangles) at 410 K of the reaction $(CH_3)_2CHCHO + Cl$.
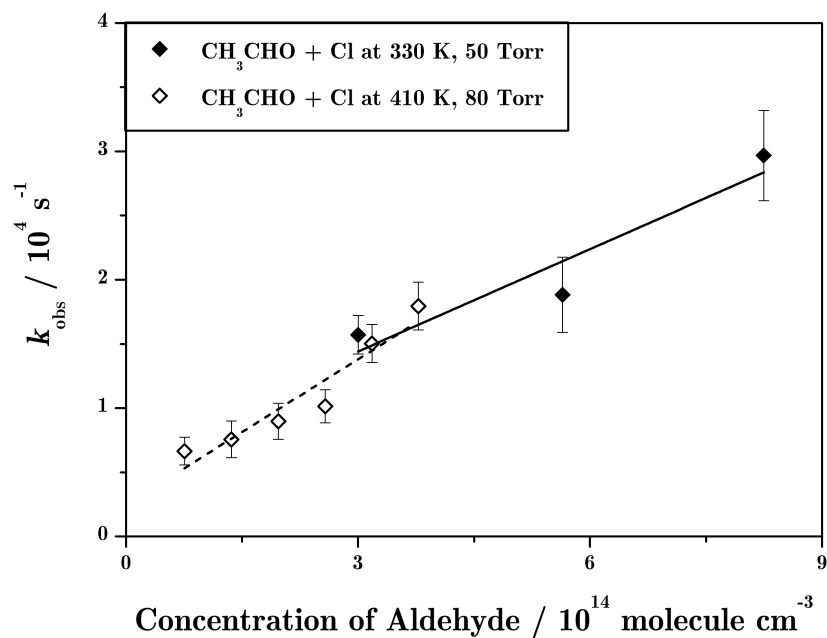


Figure 4.9: Comparison between the results of $(CH_3)_3CCHO + Cl$, the filled data points represent 410 K and 80 Torr while the unfilled represent 330 K at 15 Torr.

To examine the temperature dependence that the rate coefficients of aldehyde with Cl have, an Arrhenius plot was created (Figure 4.10) from the values given in Table 4.10.

Table 4.10: Results from the least square analysis of Cl rate coefficients with: $CH_3CHO$, $(CH_3)_3CCHO$, $(CH_3)_2CHCHO$, and $C_2H_5CH(CH_3)CHO$ at three temperatures: 293 K, 330 K, and 410 K.

| Reaction (+ Cl) | Rate Coefficient / $10^{-10}$ cm$^3$ molecule$^{-1}$ s$^{-1}$ | | | |
| --- | --- | --- | --- | --- |
| | Literature | 293 K | 330 K | 410 K |
| $CH_3CHO$ | $0.80 \pm 0.06$ [1] | $0.7 \pm 0.2$ | $0.7 \pm 0.1$ | $0.45 \pm 0.07$ |
| $(CH_3)_2CHCHO$ | $1.53 \pm 0.20$ [2] | $1.3 \pm 0.8$ | $1.3 \pm 0.6$ | $0.42 \pm 0.1$ |
| $(CH_3)_3CCHO$ | $1.38 \pm 0.21$ [2] | $1.2 \pm 0.2$ | $0.9 \pm 0.4$ | N/A |
| $C_2H_5CH(CH_3)CHO$ | Unknown | $1.8 \pm 0.14$ | $1.3 \pm 0.3$ | $0.41 \pm 0.2$ |

*Notes:* Literature values from: [1] = Atkinson, Baulch, Cox, Crowley, Hampson, Hynes, Jenkin, Rossi, et al. (2004); [2] = weighted average of Thévenet, Mellouki, and Bras (2000) and LeCrâne et al. (2004). Due to time constraints no data was recorded at 410 K for $(CH_3)_3CCHO$ + Cl.

Both the figure and the values found in the table indicate that there is a general trend, suggesting the rate coefficient to become slightly greater with the increase in temperature. Though the experimental results are lower than the literature values, shown in Table 4.10, there is still a decrease when the temperature increases. The Arrhenius plot allows the determination of the $A$ and $E_a$, with the results shown in Table 4.11. Figure 4.10 clearly shows this with the most substantial change coming from the temperature increase from 330 to 410 K – this is expected since it is a large temperature range. To determine this Arrhenius relationship, more experiments need to be conducted at the temperatures between 330 and 410 K.

Table 4.11: Results from the Arrhenius of $CH_3CHO$ + Cl, $(CH_3)_2CHCHO$ + Cl, and $C_2H_5CH(CH_3)CHO$ + Cl at three temperatures: 293 K, 330 K, and 410 K.

| Reaction (+ Cl) | Pre-Exponential factor $A$ | Activation Energy $Ea$ / J mol$^{-1}$ |
| --- | --- | --- |
| $CH_3CHO$ | $(6.8 \pm 1.8) \times 10^{10}$ | $58 \pm 24$ |
| $(CH_3)_2CHCHO$ | $(4.2 \pm 0.8) \times 10^{11}$ | $147 \pm 62$ |
| $C_2H_5CH(CH_3)CHO$ | $(1.0 \pm 0.6) \times 10^{12}$ | $187 \pm 35$ |
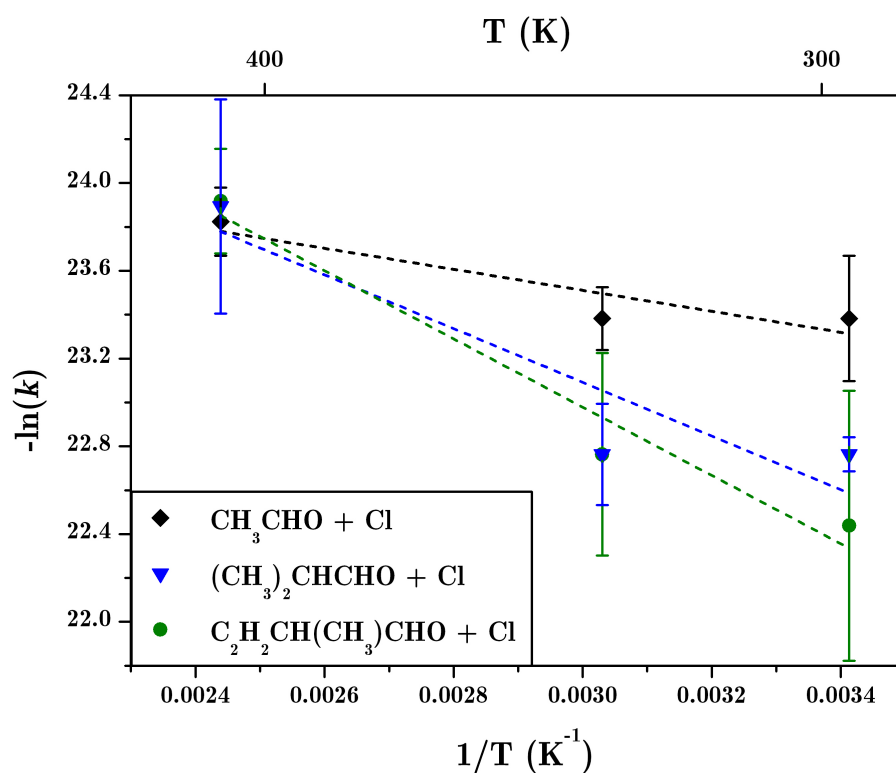
Figure 4.10: Arrhenius plot of three different RCHO + Cl at three different temperatures: $CH_3CHO$ + Cl (black diamonds), $(CH_3)_2CHCHO$ + Cl (blue triangle), and $C_2H_5CH(CH_3)CHO$ + Cl (green circles).

## 4.2.3   Temperature Dependency of 3-Methylbutanal with Cl

Experimental restrictions meant it was not possible to examine the temperature dependency for the rate coefficient of $(CH_3)_2CHCH_2CHO$ + Cl alongside the other branched aldehydes; therefore, it was investigated alongside $CH_3CHO$ + Cl and $(CH_3)_2CHCHO$ + Cl. Two temperatures were investigated: 360 K (at 50 and 80 Torr) and 420 K (at 30, 50 and 80 Torr). The first temperature investigated was 360 K – Figure 4.11 shows a typical kinetic trace from the data collected at 50 Torr. Similar to previous data, scatter was visible in the data but the non-linear fit was still able to produce a result which was in-line with the data. The same analysis was used as previously, with the results from the non-linear plots used to determine a linear fit, shown in Figure 4.12 – which indicates results from the non-linear fits at 50 and 80 Torr.

Figure 4.12 illustrates the reproducibility of the data: the data points follow a clear linear trend. Table 4.12 includes the results from the least-square analysis from experimental runs of $CH_3CHO$ + Cl, $(CH_3)_2CHCHO$ + Cl and $(CH_3)_2CHCH_2CHO$ + Cl at the two pressures.

Table 4.12:  Results from the least-square analysis of Cl rate coefficients with: $CH_3CHO$, $(CH_3)_2CHCHO$ and $(CH_3)_2CHCH_2CHO$ at 360 K, alongside results at 293 K

| Reaction ( + Cl) | Rate Coefficient / $10^{-11}$ cm$^3$ molecule$^{-1}$ s$^{-1}$ | | | |
|---|---|---|---|---|
| | 293 K | 360 K | | |
| | | 50 Torr | 80 Torr | Average |
| $CH_3CHO$ | 7.0 ± 1.5 | 6.4 ± 0.4 | N/A | N/A |
| $(CH_3)_2CHCHO$ | 12.9 ± 7.8 | 8.2 ± 0.4 | 7.6 ± 1.5 | 7.7 ± 0.2 |
| $(CH_3)_2CHCH_2CHO$ | 37.2 ± 4.5 | 17.2 ± 1.5 | 16.7 ± 1.7 | 17.0 ± 2.3 |

*Notes:* Due to time constraints no data were recorded at 80 Torr for $CH_3CHO$ + Cl.
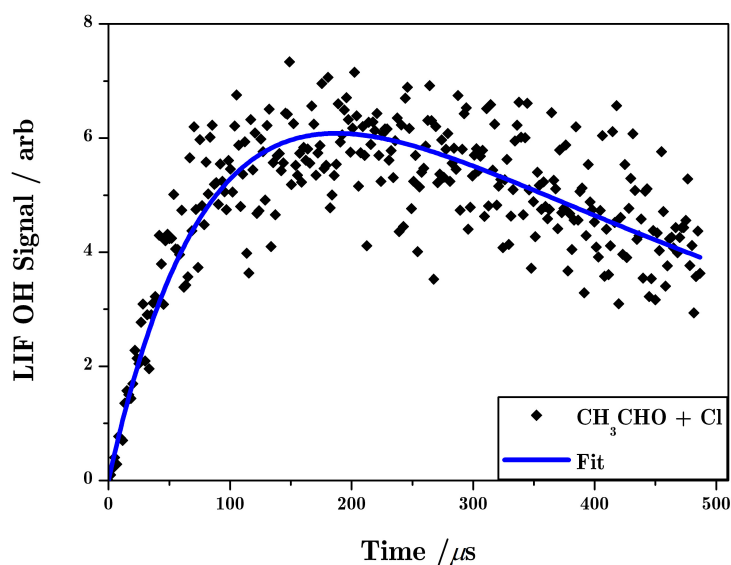
Figure 4.11: Kinetic trace of the production and decay of OH from the reaction of $CH_3CHO + Cl$ at 50 Torr and 360 K with $[CH_3CHO] = 1.8 \times 10^{14}$ molecule $cm^{-3}$, black filled diamonds indicate data points and the blue line shows the non-linear fits from the equation 4.7.
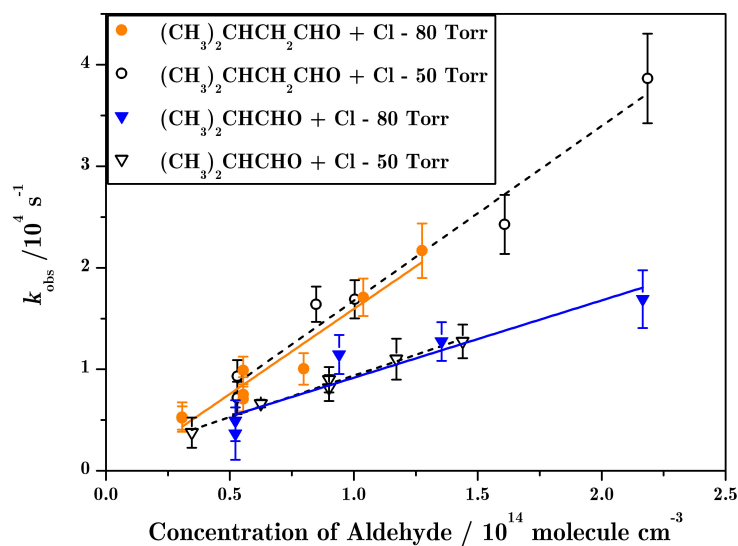


Figure 4.12: Results from the non-linear fits at 360 K, for $(CH_3)_2CHCHO + Cl$ (blue triangle) and $(CH_3)_2CHCH_2CHO + Cl$ (orange circles). The filled data points represent data from 50 Torr while the empty points correspond to the 80 Torr.

The results of $(CH_3)_2CHCHO$ + Cl and $(CH_3)_2CHCH_2CHO$ + Cl at the two pressures are very similar, with a low deviation between them giving them a good degree of certainty. The trend from the 293 K results to 360 K agrees with the previous set of data: a temperature increase causes an increase in the rate coefficient.

420 K was the second temperature investigated, with Figure 4.13 showing a typical kinetic trace from the data collected at 420 K, similar to all other traces shown in previous sections. Figure 4.14 displays the results from the non-linear fits at the pressures of 50 and 80 Torr, with linear least-square analysis. Similar to previous results, these give slight scatter but there is a clear linear fit to the values. Table 4.13 shows the results from the least-square analysis from experimental runs of $CH_3CHO$ + Cl and $(CH_3)_2CHCH_2CHO$ + Cl at the three different pressures at 420 K. The values given for the rate coefficient of $(CH_3)_2CHCH_2CHO$ + Cl at the three different pressures are in close agreement with each other; however, the values for the results of $CH_3CHO$ + Cl have a bit more spread. The value given for 30 Torr is the same as the room temperature result, but 50 and 80 Torr results are significantly lower than this and are very similar, therefore it is possible that the 30 Torr result can be considered to be an outlier.

Table 4.13: Results from the least-square analysis of Cl rate coefficients with: $CH_3CHO$ and $(CH_3)_2CHCH_2CHO$ at 420 K, alongside results at 293 K.

| Reaction (+ Cl) | Rate Coefficient / $10^{-11}$ cm$^3$ molecule$^{-1}$ s$^{-1}$ | | | |
| --- | --- | --- | --- | --- |
| | 293 K | 420 K | | |
| | | 30 Torr | 50 Torr | 80 Torr |
| $CH_3CHO$ | $7.0 \pm 1.5$ | $7.0 \pm 1.7$ | $4.3 \pm 0.9$ | $3.8 \pm 1.2$ |
| $(CH_3)_2CHCH_2CHO$ | $37.2 \pm 4.5$ | $10.2 \pm 1.7$ | $11.9 \pm 1.7$ | $11.2 \pm 2.1$ |
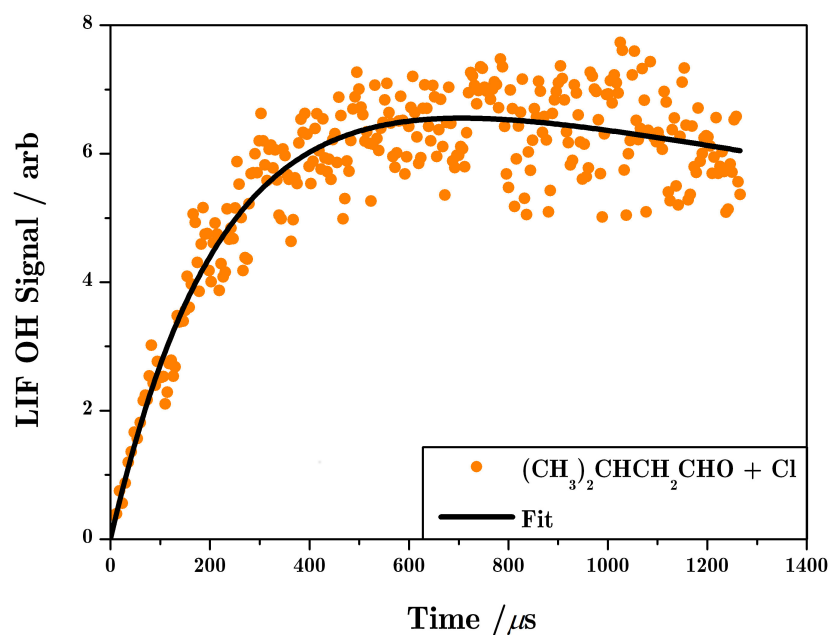
Figure 4.13: Kinetic trace of the production and decay of OH from the reaction of $(CH_3)_2CHCH_2CHO$ + Cl at 30 Torr and 420 K with $[(CH_3)_2CHCH_2CHO] = 5.1 \times 10^{13}$ molecule $cm^{-3}$, orange circles indicate data points with the black line showing the non-linear fit from the equation 4.7.
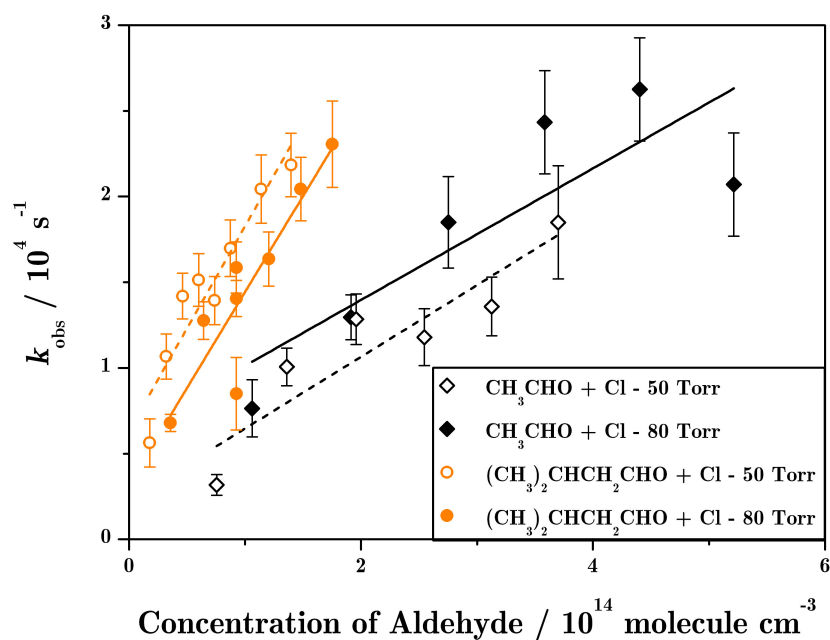


Figure 4.14: Results from the non-linear fits at 420 K, for $CH_3CHO$ + Cl (black diamond) and $(CH_3)_2CHCH_2CHO$ + Cl (orange circles). The filled data points represent data from 50 Torr while the empty points correspond to the 80 Torr.

The results for each pressure are shown in Figure 4.15, which illustrates the weighted average calculation. The gradient is set to zero, so therefore the $y$-intercept is the averaged rate coefficient.

To examine the temperature dependence of the rate coefficients, an Arrhenius plot was created – see Figure 4.16 from the values given in Table 4.14. The Arrhenius plot allowed the determination of the pre-exponential factor and the activation energy for the RCHO + Cl reactions, these values are found in Table 4.15. Figure 4.16 and the values found in Tables 4.14 and 4.15 indicate that there is a general trend, suggesting the rate coefficient becomes slightly faster with the increase in temperature – agreeing with the previous set of results. The Arrhenius plot also shows the data from $(CH_3)_2CHCHO$ + Cl; though there are no results at 420 K it does have results from 360 K and these, together with the results from the previous study, can show if these data are in-line with the previous study. The results do follow each other, indicating that this technique is precise enough to give these measurements.

Table 4.14: Results from the least-square analysis of Cl rate coefficients with: $CH_3CHO$ and $(CH_3)_2CHCH_2CHO$ at three temperatures: 293, 360, and 420 K.

| Reaction (+ Cl) | Rate Coefficient / $10^{-11}$ cm³ molecule$^{-1}$ s$^{-1}$ | | | |
| --- | --- | --- | --- | --- |
| | Literature | 293 K | 360 K | 420 K |
| $CH_3CHO$ | $8.0 \pm 0.07$ [1] | $7.0 \pm 1.5$ | $6.4 \pm 0.4$ | $5.3 \pm 1.1$ |
| $(CH_3)_2CHCH_2CHO$ | N/A | $37.2 \pm 4.5$ | $17.0 \pm 2.3$ | $11.0 \pm 4.9$ |

*Notes:* Literature value from: [1] = Atkinson, Baulch, Cox, Crowley, Hampson, Hynes, Jenkin, Rossi, et al. (2004).

Table 4.15: Results from the Arrhenius of $CH_3CHO$ + Cl, $(CH_3)_2CHCHO$ + Cl, and $(CH_3)_2CHCH_2CHO$ + Cl.

| Reaction (+ Cl) | Pre-Exponential factor $A$ | Activation Energy $Ea$ / J mol$^{-1}$ |
| --- | --- | --- |
| $CH_3CHO$ | $(5.0 \pm 1.4) \times 10^{10}$ | $46 \pm 16$ |
| $(CH_3)_2CHCHO$ | $(3.9 \pm 1.9) \times 10^{11}$ | $145 \pm 42$ |
| $(CH_3)_2CHCH_2CHO$ | $(1.6 \pm 1.1) \times 10^{11}$ | $143 \pm 5$ |
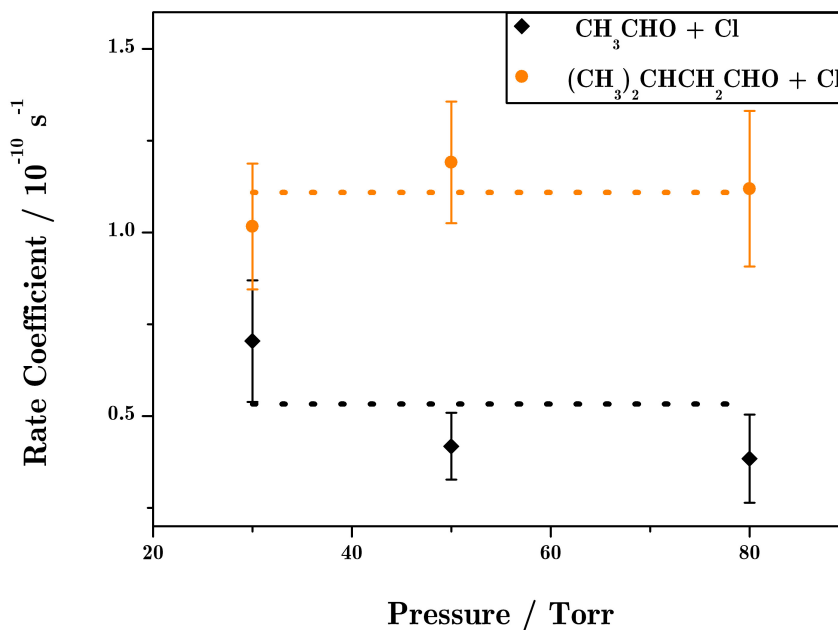
Figure 4.15: Figure showing the rate coefficients of CH$_3$CHO + Cl (black diamonds) and (CH$_3$)$_2$CHCH$_2$CHO + Cl (orange circles) at 420 K with the three results at the different pressures (30, 50 and 80 Torr). The dotted line is the linear least-squares regression which takes into account the errors.
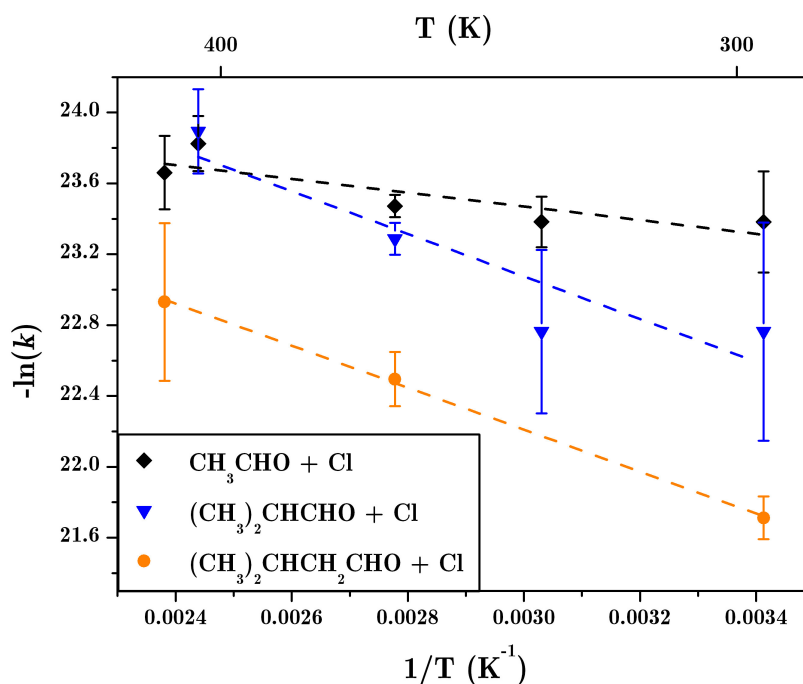


Figure 4.16: Arrhenius plot of four different RCHO + Cl at three different temperatures: CH$_3$CHO + Cl (black diamonds), (CH$_3$)$_2$CHCHO + Cl (blue triangle) and (CH$_3$)$_2$CHCH$_2$CHO + Cl (orange circles).

## 4.3 Rate Coefficients of OH with Aldehydes

The atmospheric importance of aldehyde reactions with OH has led to extensive kinetics studies at ambient temperature. Aldehydes are not only emitted from both biogenic and anthropogenic sources but are also formed *in situ* in the troposphere due to the atmospheric photo-oxidation reactions of VOCs, notably alkenes, alkanes and alcohols (Atkinson and Arey 2003). Once in the troposphere, aldehydes undergo photolysis and react with OH radicals, which has been discussed in Chapter 1.

### 4.3.1 Background and Previous Studies

This part of the study will focus on two reactions, $CH_3CHO$ with OH (Equation 4.9) and $(CH_3)_2CH\,CH_2CHO$ with OH (Equation 4.10). The reactions of aldehydes with OH proceed via a hydrogen abstraction mechanism, which can occur on different hydrogens causing the reactions to exhibit parallel product channels. The products always contain $H_2O$ and the major reaction channel is expected to be H-atom abstraction from the CHO group (Atkinson, Baulch, Cox, Crowley, Hampson, Hynes, Jenkin, Rossi, et al. 2004).

$$CH_3CHO + OH \rightarrow CH_3CO + H_2O$$
$$\rightarrow CH_2CHO + H_2O$$

$$(4.9)$$

$$(CH_3)_2CHCH_2CHO + OH \rightarrow (CH_3)_2CHCH_2CO + H_2O$$
$$\rightarrow (CH_3)_2CHCHCHO + H_2O$$
$$\rightarrow (CH_3)(CH_2)CHCH_2CHO + H_2O$$
$$\rightarrow (CH_2)(CH_3)CHCH_2CHO + H_2O$$

$$(4.10)$$
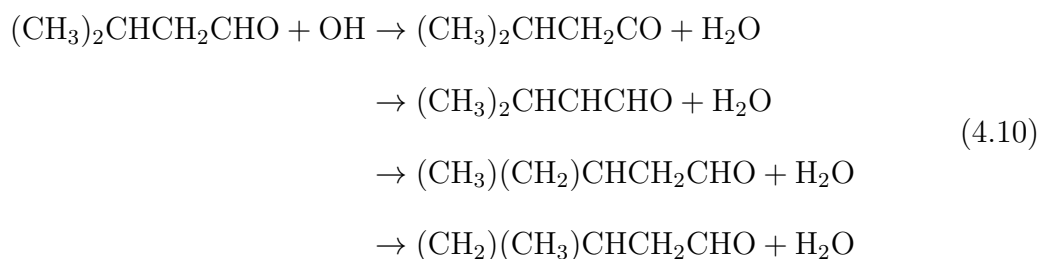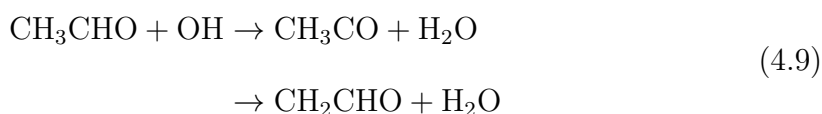
The reaction of $CH_3CHO$ + OH has been studied extensively, with approximately twenty studies between 1971 and 2006 (Atkinson, Baulch, Cox, Crowley, Hampson,

Hynes, Jenkin, Kerr, et al. 2007). The first study by Morris, Stedman, and Niki (1971), coupled a flow-discharge apparatus with a time-of-flight mass spectrometer to measure the rate coefficients of not only $CH_3CHO + OH$, but also $C_2H_4 + OH$ and $CH_3CHCH_2 + OH$. Two methods were applied: the first measured the OH decay as a function of [RH], whereas the second determined the rate coefficient directly from the decay of RH in an excess of OH – OH was created by the titration of H atoms with $NO_2$. The combination of these two methods obtained a rate coefficient of $(1.55 \pm 0.39) \times 10^{-11}$ cm$^3$ molecule$^{-1}$ s$^{-1}$ at a temperature of 300 K for $CH_3CHO$ + OH. The combination of these methods has meant that throughout the years this value has always stood up to literature examination, with the latest evaluated data giving a rate coefficient of $(1.5 \pm 0.2) \times 10^{-11}$ cm$^3$ molecule$^{-1}$ s$^{-1}$ agreeing with the first measurement (Atkinson, Baulch, Cox, Crowley, Hampson, Hynes, Jenkin, Kerr, et al. 2007).

Soon after that first study Atkinson and Pitts (1978) completed the first temperature-dependent study of $CH_3CHO$ + OH, using flash photolysis-resonance fluorescence obtaining Arrhenius expressions for both $CH_3CHO$ + OH and HCHO + OH. The room temperature value of $(1.60 \pm 0.16) \times 10^{-11}$ cm$^3$ molecule$^{-1}$ s$^{-1}$ for $CH_3CHO$ + OH is in close agreement with the previous study by Morris, Stedman, and Niki (1971), and the Arrhenius expression $(6.87 \times 10^{-12} \exp[(257 \pm 151)/T]$ agrees with more recent measurements and reviews such as Sivakumaran and Crowley (2003), Zhu et al. (2008), and Atkinson, Baulch, Cox, Crowley, Hampson, Hynes, Jenkin, Kerr, et al. (2007).

The range of room temperature rate coefficients of $CH_3CHO$ + OH is $(1.2 - 1.7) \times 10^{-11}$ cm$^3$ molecule$^{-1}$ s$^{-1}$ with the absolute rate coefficients calculated by: Atkinson and Pitts (1978), Michael, Keil, and Klemm (1985), Tyndall, Staffelbach, et al. (1995), Sivakumaran and Crowley (2003), Wang et al. (2003), Taylor, Yamada, and Marshall (2006), Vöhringer-Martinez et al. (2007), and Zhu et al. (2008) all being in reasonable agreement. Therefore the rate coefficient of $CH_3CHO$ + OH is extremely well-known and constrained and is, therefore, a good rate coefficient to benchmark

this study's accuracy and reliability.

In comparison, there have only been five studies on the rate coefficient for the reaction of $(CH_3)_2CHCH_2CHO + OH$, at room temperature: the values range from $1.83 - 3.09 \times 10^{-11}$ $cm^3$ molecule$^{-1}$ s$^{-1}$. This range is much larger than the $CH_3CHO$ + OH studies recorded, but when examined further it is possible to see that there are two extreme values which distort the results: the study from Audley, Baulch, and Campbell (1981) gave the lowest value of $(1.83 \pm 0.1) \times 10^{-11}$ $cm^3$ molecule$^{-1}$ s$^{-1}$, whereas Jiménez et al. (2009) gave the highest value of $(3.09 \pm 1.7) \times 10^{-11}$ $cm^3$ molecule$^{-1}$ s$^{-1}$. The other three studies are in close agreement, however, giving the rate coefficient a range of $2.57 - 2.79 \times 10^{-11}$ $cm^3$ molecule$^{-1}$ s$^{-1}$ (Semmes et al. 1985; Kerr and Sheppard 1981; D'Anna et al. 2001).

This difference could be due to the techniques used. Audley, Baulch, and Campbell (1981), who gave the first measurement, used a flow tube, which contained the reaction of $H_2O_2 + NO_2$, then as OH + CO gives $CO_2$ the variation in the yield of $CO_2$ was monitored by gas chromatography. This allowed a rate constant ratio to be derived when different amounts of $(CH_3)_2CHCH_2CHO$ were added. Kerr and Sheppard (1981) soon after presented their value for the rate to be $(2.7 \pm 0.1) \times 10^{-11}$ $cm^3$ molecule$^{-1}$ s$^{-1}$, which was $1.1 \times 10^{-11}$ larger than Audley, Baulch, and Campbell (1981) value. Kerr and Sheppard (1981) calculated their rate coefficient by observing the rates of consumption of $C_2H_4$ and $CH_3CHO$ by GC, which allowed the measurement of their relative rate constants. The OH radicals were generated by the photolysis of nitrous acid (HONO).

To solve this discrepancy in the literature between Audley, Baulch, and Campbell (1981) and Kerr and Sheppard (1981), Semmes et al. (1985) carried out a study which used time-resolved resonance fluorescence spectroscopy. Flash photolysis of $H_2O$ at wavelengths greater than 165 nm generated OH, which reacted with different concentrations of the aldehyde to produce a plot of the first-order decay rates against the $[(CH_3)_2CHCH_2CHO]$ which allowed the calculation of the bimolecular rate

constant. The extensive study by D'Anna et al. (2001), where they recorded the OH rate coefficients of 14 aliphatic C2 to C6 aldehydes, also helped solve the discrepancy of the $(CH_3)_2CHCH_2CHO$ + OH rate coefficient. The OH radicals were generated by the photolysis of different organic nitrates, including: $CH_3ONO$, 2-propylnitrite, and 2-propylnitrite. The relative rates were measured with propene and but-1-ene used as reference compounds, while the concentrations were monitored by FTIR. As these two later studies agreed with the rate coefficient calculated by Kerr and Sheppard (1981), a value in the range of $2.57 - 2.79 \times 10^{-11}$ cm$^3$ molecule$^{-1}$ s$^{-1}$ is more likely and reliable than the original value given by Audley, Baulch, and Campbell (1981).

There has only been one temperature-dependence study on $(CH_3)_2CHCH_2CHO$ + OH which was carried out by Jiménez et al. (2009). The study showed that there is a temperature dependence for the rate coefficient between the range of 263 – 353 K, with the rate increasing as temperature increases. However, this study gave a room temperature value which was higher than the four previous studies. For this work, the study by Jiménez et al. (2009) was used as a comparison since it has an Arrhenius expressions for when comparisons were made at higher temperature. However, since there is this discrepancy between the Jiménez et al. (2009) room-temperature value and the previous studies, it was expected that the values calculated from this work would be lower than the values of Jiménez et al. (2009).

### 4.3.2 Experimental

The apparatus and experimental procedure has been fully described in Chapter 2 of this thesis; therefore, only a brief outline is given here.

The bath gas used was $N_2$, and the pressure was kept constant at 50 Torr. The gases were delivered to a pre-mixing chamber before entering the reactor cell via calibrated mass flow controllers (MKS instruments). The concentrations of the aldehyde and $N_2$ gas mixtures were kept constant throughout ($CH_3CHO = 0.50\%$

; $(CH_3)_2CHCH_2CHO = 0.18\%$) in glass bulbs.  Nitrogen dioxide (6% in $N_2$) was used as the radical precursor, utilising the photo-dissociation at 355 nm to produce $O(^3P)$ (4.11).  Reaction 4.12 is well known for $R=CH_3$ with the most recent review article by Demore et al. (1997) giving it a rate coefficient of $(4.47 \pm 0.02) \times 10^{-13}$ $cm^3$ $molecule^{-1}$ $s^{-1}$.  However, it is not known for $(CH_3)_2CHCH_2CHO + O$, but the rate is know for Reaction 4.12 when R = $C_2H_5$ $((4.72 \pm 0.13) \times 10^{-13}$ $cm^3$ $molecule^{-1}$ $s^{-1}$) and for when R = $C_3H_7$ $((5.71 \pm 0.15) \times 10^{-13}$ $cm^3$ $molecule^{-1}$ $s^{-1}$) (Singleton, Irwin, and Cvetanovic 1977).  Therefore it can be assumed that for $(CH_3)_2CHCH_2CHO + O$ the rate will be very similar to these other reactions and would be very fast.

$$NO_2 \xrightarrow{355nm} O^{\cdot} + NO \tag{4.11}$$

$$RCHO + O^{\cdot} \rightarrow RCO + OH \tag{4.12}$$

The OH radicals formed by RCHO + O, were probed using 282 nm LIF – see Chapter 2 for more information.  As pseudo first order conditions [RCHO] > [OH] were used the LIF-profiles can be analysed by Equation 4.13 which was used previously for the calculation of Cl rate coefficients and also in the determination OH yields, discussed in Chapter 3.

$$[OH](t) = A(e^{-Bt} - e^{-Ct}) \tag{4.13}$$

Experiments were conducted using a range of either $CH_3CHO$ or $(CH_3)_2CHCH_2$ CHO which allowed the pseudo first-order decay traces to be obtained.  The bimolecular rate coefficient was determined from the gradient of a plot of pseudo first-order rate coefficient versus [RCHO].

The experiments at 283 K at a pressure of 50 Torr used two $NO_2$ concentrations $(4.4 \times 10^{13}$ and $1.0 \times 10^{14}$ molecule $cm^{-3}$), with the range of the [RCHO] found in

Table 4.16: The range of the reagent concentrations used in experimental runs, investigating the OH rate coefficients of $CH_3CHO$ and $(CH_3)_2CHCH_2CHO$ at 293 K.

| | Concentrations / $10^{13}$ molecule $cm^{-3}$ | |
| --- | --- | --- |
| | **$CH_3CHO$** | **$(CH_3)_2CHCH_2CHO$** |
| **Low [NO$_2$]** | 7.5 – 35.4 (5) | 7.4 – 34.7(5) |
| **High [NO$_2$]** | 7.1 – 33.6 (5) | 7.7 – 101 (11) |

*Notes:* The values in brackets represent the number of experimental traces recorded at that particular [NO$_2$] and using that specific aldehyde.

Table 4.16. The values in the brackets, found in Table 4.16, represent the number of traces recorded using that aldehyde at that particular [NO$_2$]. LabVIEW settings were kept constant throughout, with 520 points being taken in total in each scan, one point per time shot and 5 scans to average the data, reducing noise. The total time of the scan was adjusted depending on the concentration of the aldehyde, ensuring that there were good quality data on both the rise and the decay.

The rate coefficients were also investigated at higher temperatures of 370 and 430 K. The experimental set-up was kept similar to the room-temperature investigations – LabVIEW acquisition software was kept consistent with 500 shots, 5 scans and 1 shot per time. The heating tape was used, discussed further in Chapter 2, and was set to 413 K to give a temperature of 370 K in the cell and 498 K to give a temperature of 430 K. Similar to before, experiments were carried out at two NO$_2$ concentrations at both 370 K ($2.1 \times 10^{13}$ and $4.9 \times 10^{13}$ molecule $cm^{-3}$) and 430 K ($3.2 \times 10^{13}$ and $3.2 \times 10^{13}$ molecule $cm^{-3}$), with the range of aldehyde concentrations used shown in Table 4.17. Unfortunately due to time constraints, no data were recorded for $CH_3CHO$ at higher [NO$_2$].

Table 4.17: The range of the reagent concentrations used in experimental runs, investigating the OH rate coefficients of $CH_3CHO$ and $(CH_3)_2CHCH_2CHO$ at 370 and 430 K.

| | Concentrations of Reagents / $10^{13}$ molecule cm $^{-3}$ | | | |
|---|---|---|---|---|
| | **$CH_3CHO$** | | **$(CH_3)_2CHCH_2CHO$** | |
| | **370 K** | **430 K** | **370 K** | **430 K** |
| **Low [$NO_2$]** | 3.6 – 47 (6) | 3.1– 29(6) | 1.2 –6.9 (6) | 0.7–5.4 (6) |
| **High [$NO_2$]** | 1.7 – 34 (6) | N/A | 1.2 –16 (6) | 0.7 –7.9 (8) |

*Notes:* The values in brackets represent the number of experimental traces recorded at that particular [$NO_2$] and using that specific aldehyde. Unfortunately due to time constraints, no data were recorded for $CH_3CHO$ at higher [$NO_2$].

### 4.3.3 Room-Temperature Results

Room-temperature experiments were carried out first to validate the method and analysis, as both compounds already have rate constants associated with them at room temperature. The same fit (Equation 4.13) used previously for the calculation of Cl rate coefficients, and explained in detail in Chapter 3, was used to fit the experimental runs. This time, however, a second fit was used in the analysis (Equation 4.14). The second fit included a fourth parameter ($D$) which allowed the error of the baseline to be reduced. The room-temperature experiments aimed to show the effect of these two fits and confirm the validity of this method for the calculation of OH rate coefficients.

$$[OH](t) = A(e^{-Bt} - e^{-Ct}) + D \tag{4.14}$$

Experimental traces containing $NO_2$ and $N_2$ with $CH_3CHO$ and with $(CH_3)_2CH$ $CH_2CHO$ show clear traces of the production and decay of OH. More scatter is visible for the $CH_3CHO$ data (Figure 4.17), which could be due to a variety of factors including laser stability, amount of OH produced and electrical noise from other parts of the laboratory. Figure 4.17 displays the data overlaid with both the 3-parameter and 4-parameter fit, agreeing well with each other.
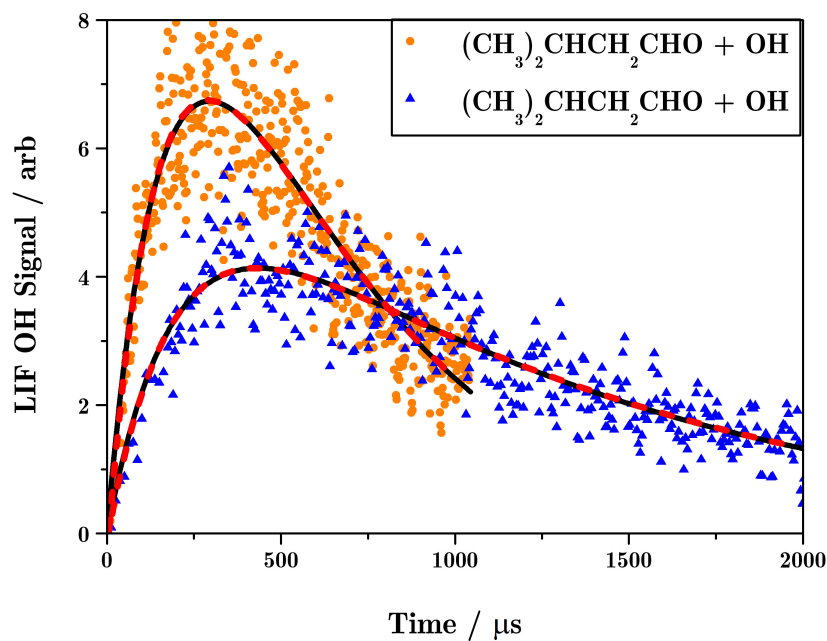
Figure 4.17: LIF traces of $(CH_3)_2CHCH_2CHO$ + OH with $[(CH_3)_2CHCH_2CHO]$ = $4.2 \times 10^{14}$ molecule $cm^{-3}$ (orange circles) and $3.5 \times 10^{14}$ molecule $cm^{-3}$ (blue triangles) together with the non linear fits: 3-parameter fit (black line) and 4-parameter fit (red dashed line).
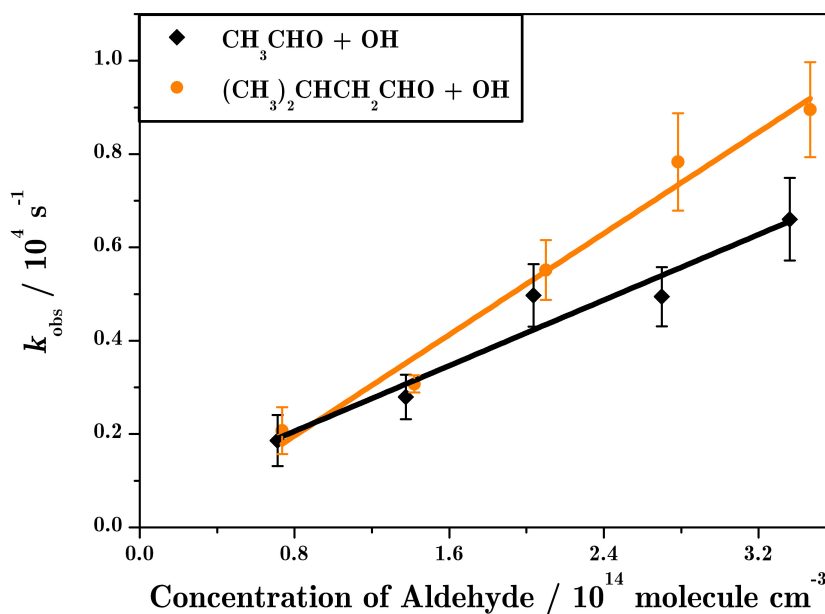


Figure 4.18: Results from the non-linear fits at 293 K, for $CH_3CHO$ + Cl (black diamond) and $(CH_3)_2CHCH_2CHO$ + Cl (orange circles) at the lower $[NO_2]$.

The closeness between the two types of fit enhanced the confidence in these results. All the data were primarily analysed using the two fits, to determine the accuracy of the data – if the two fits overlapped this validated the data set for further analysis. The data discussed in this section (4.3) all passed this analysis test; however, the values given are from the 3-parameter fits – the 4-parameter fit was used solely as a check.

Figure 4.18, where $k_{obs}$ refers to the value from parameter $C$, shows the results from non-linear fits at five different [RCHO] for both $CH_3CHO$ + OH and $(CH_3)_2CH$ $CH_2CHO$ + OH at the lower [$NO_2$] – the results at the higher [$NO_2$] were very similar. The reliability of this method looks excellent since the data points follow clear linear trends with not much scatter. The lines shown on the plot are the results from the least-squares analysis which fall, as expected, in the middle of the data points.

Table 4.18 displays the results from the least-squares analysis from the data collected at room temperature with both concentrations of $NO_2$. The experimental results for the rate coefficient of $CH_3CHO$ + OH show a good agreement with the previous literature value of $1.53 \times 10^{-11}$ cm$^3$ molecule$^{-1}$ s$^{-1}$ (Atkinson and Pitts 1978). The experimental values for both the experiments at high and low [$NO_2$] are within their errors to the literature value, which indicates good validity to this experiment. This agreement with the literature was expected, as values from previous studies show good agreement with each other as discussed previously.

There is a larger difference between the results of $(CH_3)_2CHCH_2CHO$ + OH when the different $NO_2$ concentrations were used. The value calculated from the results at the low [$NO_2$] is much larger than the high [$NO_2$] result, but both are lower than the literature value in Table 4.18. As discussed previously there is a large range for the rate coefficient of $(CH_3)_2CHCH_2CHO$ + OH in the literature: (1.83 - 3.09) $\times 10^{-11}$ cm$^3$ molecule$^{-1}$ s$^{-1}$. The literature value included in Table 4.18 is at the higher end of the range; so it was expected that this work's results would fall below

Table 4.18: Results from the least squares analysis of OH rate coefficients with: $CH_3CHO$ and $(CH_3)_2CHCH_2CHO$ at 293 K.

| Reaction (+ OH) | Rate Coefficients / $10^{-11}$ cm$^3$ molecule$^{-1}$ s$^{-1}$ | | |
| | Literature | Experimental | |
| | | Low [NO$_2$] | High [NO$_2$] |
| --- | --- | --- | --- |
| $CH_3CHO$ | $1.53^1$ | $1.8 \pm 0.3$ | $1.7 \pm 0.3$ |
| $(CH_3)_2CHCH_2CHO$ | $3.10^2$ | $2.7 \pm 0.3$ | $1.2 \pm 0.2$ |

*Notes:* [1]= Atkinson, Baulch, Cox, Crowley, Hampson, Hynes, Jenkin, Kerr, et al. (2007) [2]= Jiménez et al. (2009).

this as discussed previously.

The result from the low [NO$_2$] falls in the middle of all the previous literature results, which is ideal, but the discrepancy between the two results could be due to the increased amount of OH produced by the higher [NO$_2$] which could have led to an increased uncertainty.

## 4.3.4 Temperature Dependent Results

Two higher temperatures were investigated: 370 and 428 K. These experiments were run on a different day to the previous room temperature experiment, therefore a room temperature run for $CH_3CHO$ + OH was completed first to check that everything was working – Figure 4.19. The data gave the result of $(1.5 \pm 0.3) \times 10^{-11}$ cm$^3$ molecule$^{-1}$ s$^{-1}$ for the rate coefficient which is in close agreement to the literature value – $1.53 \times 10^{-11}$ cm$^3$ molecule$^{-1}$ s$^{-1}$ (Atkinson, Baulch, Cox, Crowley, Hampson, Hynes, Jenkin, Kerr, et al. 2007).

The same analysis process was carried out for the higher temperature results. Figure 4.20 displays the results from a kinetic trace which was investigating the $CH_3CHO$ + OH rate coefficient at 370 K. The non-linear fit was able to follow the data trend extremely well, with both the 3 and 4-parameter fits giving similar results. The result from each non-linear fit (from each experimental run at a different aldehyde
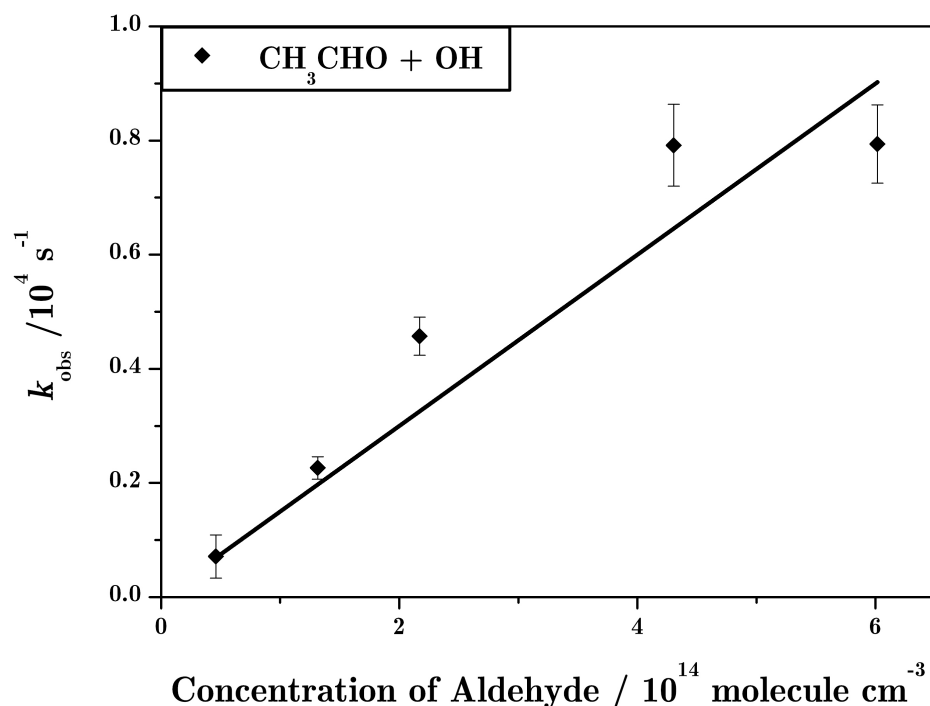
Figure 4.19: Results from the experimental run of $CH_3CHO + OH$ at 293 K and a pressure of 50 Torr (67 mbar). The black line indicates where the least-squares fit of the 3-parameter fit falls.

concentration) was used to create a plot to allow the least-squares fit analysis to be carried out.

Figure 4.21 displays the results of non-linear fits alongside the least-squares fit of the data points. The results show there to be slight deviation and scatter between the points, although in general they follow a linear fit. The difference in the range of aldehyde concentrations used for the two reactions was because of the concentration and amounts available to use. For all the experiments, the aim was to use the largest range possible for the [RCHO] but unfortunately for this experiment there was just not enough $(CH_3)_2CHCH_2CHO$ compared to $CH_3CHO$.

The results from the least-squares linear fit, found in Table 4.19, show that the rate coefficient for both $CH_3CHO + OH$ and $(CH_3)_2CHCH_2CHO + OH$ do agree with the literature, which states that the rate increases as the temperature increases. There is quite a large difference for the $(CH_3)_2CHCH_2CHO + OH$ rate at 370 K with the
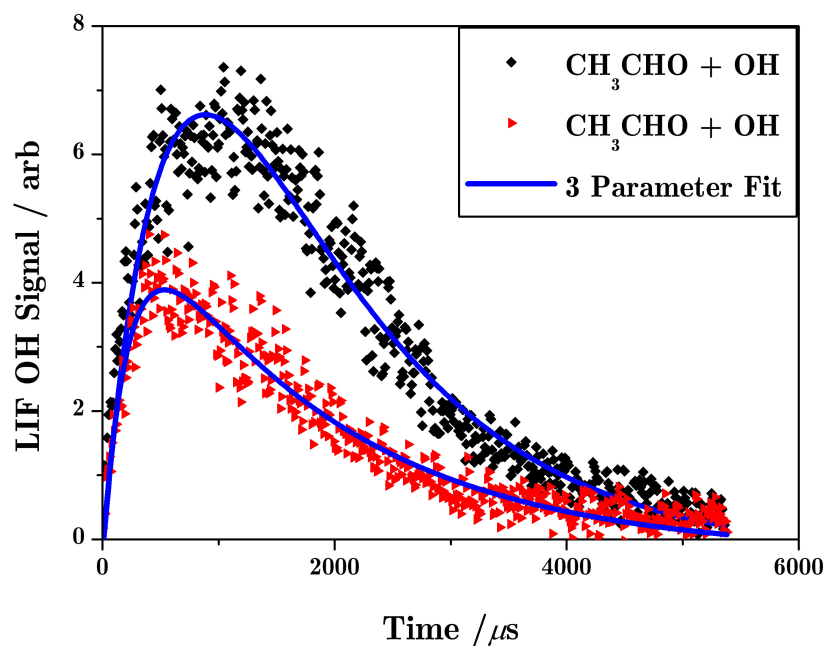
Figure 4.20: LIF traces of $CH_3CHO + OH$ with $[CH_3CHO] = 3.8 \times 10^{14}$ molecule $cm^{-3}$ (black diamonds) and $1.6 \times 10^{14}$ molecule $cm^{-3}$ (red triangles) together with the non linear fits using the 3-parameter fit (blue line) at 50 Torr and 370 K.
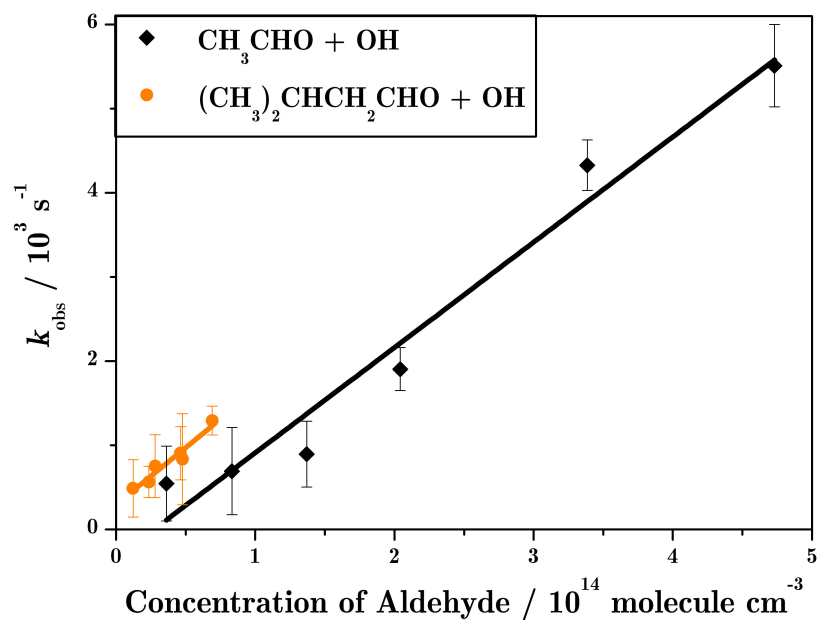


Figure 4.21: Results from the experimental runs of $CH_3CHO + OH$ (black diamonds) and $(CH_3)_2CHCH_2CHO + OH$ (orange circles) at 370 K and a pressure of 50 Torr. The lines indicate where the least squares fit falls for both reactions.

Table 4.19: Results from the least-square analysis of OH rate coefficients with: $CH_3CHO$ and $(CH_3)_2CHCH_2CHO$ at two temperatures: 370 and 430 K.

| | Rate Coefficient / $10^{-11}$ cm$^3$ molecule$^{-1}$ s$^{-1}$ | | | |
| --- | --- | --- | --- | --- |
| | **CH$_3$CHO + OH** | | **(CH$_3$)$_2$CHCH$_2$CHO + OH** | |
| | **370 K** | **430 K** | **370 K** | **430 K** |
| **Literature** | 1.2[1] | 1.05[1] | 2.2[2] | 1.86[2] |
| **Low [NO$_2$]** | $1.3 \pm 0.2$ | $0.94 \pm 0.1$ | $1.4 \pm 0.2$ | $0.68 \pm 0.2$ |
| **High [NO$_2$]** | $1.1 \pm 0.1$ | N/A | $3.7 \pm 0.9$ | $0.93 \pm 0.06$ |

*Notes:* Literature values – [1]= Atkinson, Baulch, Cox, Crowley, Hampson, Hynes, Jenkin, Kerr, et al. (2007) data from and [2] = Jiménez et al. (2009).

higher [NO$_2$] giving a much larger rate coefficient. Interestingly, the higher [NO$_2$] gives a larger result for both $(CH_3)_2CHCH_2CHO$ + OH measurements. However, it is not possible to say that this is fully due to the higher [NO$_2$], it is extremely likely that the $CH_3CHO$ + OH rate coefficient does not follow this trend.

An Arrhenius plot was created, Figure 4.22, to display the results of the temperature dependency rate coefficient study using the lower [NO$_2$] results. The lower [NO$_2$] results have less scatter in their data then the higher concentration results, therefore should give more reliable results. The plot allowed for the determination of the pre-exponential factor and the activation energy for the two RCHO + OH reactions, shown in Table 4.20.

Table 4.20: Results from the Arrhenius of $CH_3CHO$ + OH and $(CH_3)_2CHCH_2CHO$ + OH.

| Reaction (+ Cl) | Pre-Exponential factor $A$ | Activation Energy $Ea$ / J mol$^{-1}$ |
| --- | --- | --- |
| CH$_3$CHO | $(3.9 \pm 1.2) \times 10^{11}$ | $67 \pm 9$ |
| (CH$_3$)$_2$CHCH$_2$CHO | $(3.8 \pm 1.5) \times 10^{11}$ | $74 \pm 60$ |

As previous literature studies have suggested, there is a relationship between temperature and the OH rate coefficient. As the temperature rises, this causes the rate coefficient to increase.
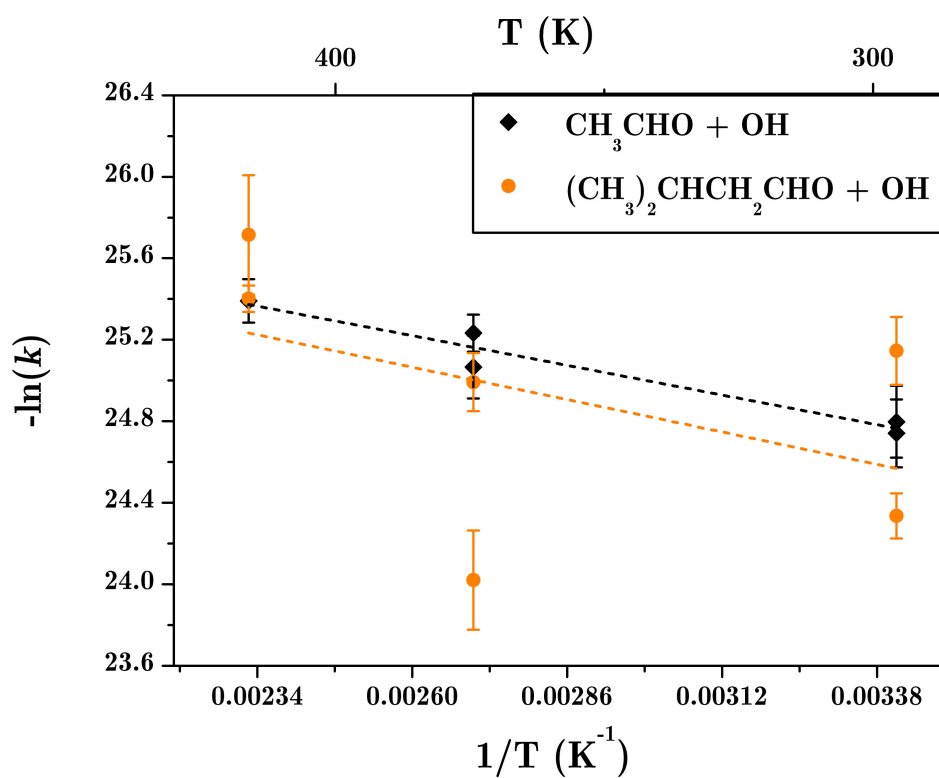
Figure 4.22: Arrhenius plot of two different RCHO + Cl at three different temperatures: $CH_3CHO$ + Cl (black diamonds) and $(CH_3)_2CHCH_2CHO$ + Cl (orange circles).

## 4.4    Summary

This chapter shows the ability of the apparatus to use OH as a spectroscopic marker for the determination of both Cl and OH rate coefficients.  In both cases reaction proceeds via pseudo first-order conditions and, from recording $k_{obs}$ at different [RCHO], the rate coefficient was calculated.

During the study, the effect that the precursor concentration has on the reliability of the rate coefficient was observed.  If the concentrations were too low, this increased the scatter of the recorded data since less OH was detected - affecting the reproducibility of the results.  However, too much and the numerous radicals in the system make the kinetics too complex, decreasing the accuracy.

The room-temperature results for both Cl and OH coefficients were compared to and agreed with previous literature studies, which showed these results to have high reproducibility and accuracy.  For example, this work gave the rate coefficient of $CH_3CHO$ + Cl to be $(8.8 \pm 1.3) \times 10^{-11}$ cm$^3$ molecule$^{-1}$ s$^{-1}$, while the literature $= (8.0 \pm 0.6) \times 10^{-11}$ cm$^3$ molecule$^{-1}$ s$^{-1}$ (Atkinson et al. 2004), and $C_2H_5CHO$ + Cl to be $(1.4 \pm 0.2) \times 10^{-10}$ cm$^3$ molecule$^{-1}$ s$^{-1}$, while the literature $= (1.3 \pm 0.3) \times 10^{-10}$ cm$^3$ molecule$^{-1}$ s$^{-1}$ (Atkinson et al. 2004).  The OH rate coefficients gave similar results with this work calculating a rate of $(1.8 \pm 0.3) \times 10^{-11}$ cm$^3$ molecule$^{-1}$ s$^{-1}$ for $CH_3CHO$ + OH while the literature gave $(1.5 \pm 0.1) \times 10^{-11}$ cm$^3$ molecule$^{-1}$ s$^{-1}$ (Atkinson et al. 2001).

This study calculated two new room-temperature Cl rate coefficients:  $C_2H_5CH(CH_3)$ CHO + Cl $(1.2 \pm 0.3) \times 10^{-10}$ cm$^3$ molecule$^{-1}$ s$^{-1}$, and $(CH_3)_2CHCH_2CHO$ + Cl $(3.1 \pm 0.6) \times 10^{-10}$ cm$^3$ molecule$^{-1}$ s$^{-1}$.  The results follow the trend set by other aldehyde + Cl rates.

The Cl and OH rate coefficients were also investigated at higher temperatures, giving similar results. This work has shown that with an increase of temperature the rate

increases. Though this has been known for the OH rate coefficients, this is new knowledge for the Cl rate coefficients. Future work should include more temperature experiments so an Arrhenius relationship can be fully expressed for both Cl and OH rate coefficients - since this study only examined three temperatures and therefore the Arrhenius relationship is not well constrained.

# Bibliography

Atkinson and Arey (2003). "Atmospheric Degradation of Volatile Organic Compounds".
In: *Chemical Reviews Reviews* 103.3, pp. 4605–4638.

Atkinson, Baulch, Cox, Crowley, Hampson, Hynes, Jenkin, Kerr, et al. (2007).
*IUPAC Subcommittee for Gas Kinetic Data Evaluation.* URL: www.iupac-kinetic.
ch.cam.ac.uk.

Atkinson, Baulch, Cox, Crowley, Hampson, Hynes, Jenkin, Rossi, et al. (2004).
"Evaluated kinetic and photochemical data for atmospheric chemistry: Part
1 - gas phase reactions of $O_x$, $HO_x$, $NO_x$ and $SO_x$ species". In: *Atmospheric
Chemistry and Physics Discussions* 3.6, pp. 6179–6699.

Atkinson and Pitts (1978). "Kinetics of the reactions of the OH radical with HCHO
and $CH_3CHO$ over the temperature range 299–426°K". In: *The Journal of Chemical
Physics* 68.8, p. 3581.

Audley, Baulch, and Campbell (1981). "Gas-phase Reactions of Hydroxyl Radicals
with Aldehydes in Flowing $H_2O_2$ +$NO_2$ + CO Mixtures". In: *Journal of the
Chemical Society, Faraday Transactions 1: Physical Chemistry in Condensed
Phases* 77, pp. 2541–2549.

Bartels, Hoyermann, and Lange (1989). "An Experimental Study of the Reactions
$CH_3CHO$ + Cl, $C_2H_4O$ + Cl, and $C_2H_4O$ + F in the Gas-Phase". In: *Berichte
der Bunsengesellschaft/Physical Chemistry Chemical Physics* 93.4, pp. 423–427.

Carter (2010). "Development of the SAPRC-07 chemical mechanism". In: *Atmospheric
Environment* 44.40, pp. 5324–5335.

Cuevas et al. (2006). "Temperature-dependence study of the gas-phase reactions of atmospheric Cl atoms with a series of aliphatic aldehydes". In: *Atmospheric Environment* 40.21, pp. 3845–3854.

D'Anna et al. (2001). "Kinetic study of OH and NO radical reactions with 14 aliphatic aldehydes". In: *Physical Chemistry Chemical Physics* 3, pp. 3057–3063.

Demore et al. (1997). *Chemical Kinetics and Photochemical Data for Use in Stratospheric Modeling Evaluation Number 12 NASA Panel for Data Evaluation*. Tech. rep.

Jenkin et al. (2018). *Estimation of rate coefficients and branching ratios for gas-phase reactions of OH with aliphatic organic compounds for use in automated mechanism construction*. Vol. 30. February, pp. 1–37. ISBN: 1892972018. DOI: `10.5194/acp-2018-146`. URL: `https://www.atmos-chem-phys-discuss.net/acp-2018-146/`.

Jiménez et al. (2009). "Influence of temperature on the chemical removal of 3-methylbutanal, trans-2-methyl-2-butenal, and 3-methyl-2-butenal by OH radicals in the troposphere". In: *Atmospheric Environment* 43.26, pp. 4043–4049.

Kegley-Owen et al. (1999). "Tunable diode laser studies of the reaction of Cl atoms with $CH_3CHO$". In: *International Journal of Chemical Kinetics* 31.11, pp. 766–775.

Keller-Rudek et al. (2013). "The MPI-Mainz UV/VIS spectral atlas of gaseous molecules of atmospheric interest". In: *Earth System Science Data* 5.2, pp. 365–373.

Kerr and Sheppard (1981). "Kinetics of the Reactions of Hydroxyl Radicals with Aldehydes Studied under Atmospheric Conditions". In: *Environmental Science and Technology* 15.8, pp. 960–963.

LeCrâne et al. (2004). "Atmospheric chemistry of pivalaldehyde and isobutyraldehyde: Kinetics and mechanisms of reactions with Cl atoms, fate of $(CH_3)_3CC(O)$ and $(CH_3)_2CHC(O)$ radicals, and self-reaction kinetics of $(CH_3)_3CC(O)O_2$ and $(CH_3)_2CHC(O)O_2$ radicals". In: *Journal of Physical Chemistry A* 108.5, pp. 795–805.

Martinez et al. (1992). "The near U.V. absorption spectra of several aliphatic aldehydes and ketones at 300 K". In: *Atmospheric Environment Part A-General Topics* 26.5, pp. 785–792.

Michael, Keil, and Klemm (1985). "Rate Constants for the Reaction of Hydroxyl Radicals with Acetaldehyde from 244–528 K". In: *The Journal of Chemical Physics* 83.4, p. 1630.

Morris, Stedman, and Niki (1971). "Mass-spectrometric study of the reactions of the hydroxyl radical with ethylene, propylene, and acetaldehyde in a discharge-flow system". In: *Journal of the American Chemical Society* 93.15, pp. 3570–3572.

Niki et al. (1985). "FTIR study of the Kinetics and Mechanism for Chlorine Atom Initiated Reactions of Acetaldehyde". In: *Journal of Physical Chemistry* 6, pp. 588–591.

Payne et al. (1990). "Rate constant for the reaction of atomic chlorine with acetaldehyde from 210 to 343 K". In: *The Journal of Physical Chemistry* 94.18, pp. 7190–7193.

Rayez, Rayez, and Villenave (2011). "Theoretical approach of the mechanism of the reactions of chlorine atoms with aliphatic aldehydes". In: *Computational and Theoretical Chemistry* 965.2-3, pp. 321–327.

Rodríguez et al. (2005). "Kinetic study of the gas-phase reaction of atomic chlorine with a series of aldehydes". In: *Atmospheric Chemistry and Physics* 5.12, pp. 3433–3440.

Seakins, Orlando, and Tyndall (2004). "Rate coefficients and production of vibrationally excited HCl from the reactions of chlorine atoms with methanol, ethanol, acetaldehyde and formaldehyde". In: *Physical Chemistry Chemical Physics* 6.9, pp. 2224–2229.

Semmes et al. (1985). "Kinetics of the reactions of hydroxyl radical with aliphatic aldehydes". In: *International Journal of Chemical Kinetics* 17.3, pp. 303–313.

Singleton, Irwin, and Cvetanovic (1977). "Arrhenius parameters for the reactions of $O(^3P)$ atoms with several aldehydes and the trend in aldehydic C-H bond dissociation energies1". In: *Canadian Journal of Chemistry* 55.18, pp. 3321–3327.

Sivakumaran and Crowley (2003). "Reaction between OH and CH3CHO". In: *Physical Chemistry Chemical Physics* 5.1, pp. 106–111.

Smith and Ravishankara (2002). "Role of hydrogen-bonded intermediates in the bimolecular reactions of the hydroxyl radical". In: *Journal of Physical Chemistry A* 106.19, pp. 4798–4807.

Taylor, Yamada, and Marshall (2006). "The reaction of OH with acetaldehyde and deuterated acetaldehyde: Further insight into the reaction mechanism at both low and elevated temperatures". In: *International Journal of Chemical Kinetics* 38.8, pp. 489–495.

Thévenet, Mellouki, and Le Bras (2000). "Kinetics of OH and Cl reactions with a series of aldehydes". In: *International Journal of Chemical Kinetics* 32.11, pp. 676–685.

Tyndall, Orlando, et al. (1999). "Rate Coefficients for the Reactions of Chlorine Atoms with Methanol and Acetaldehyde". In: *International Journal of Chemical Kinetics* 31.11, pp. 776–784.

Tyndall, Staffelbach, et al. (1995). "Rate coefficients for the reactions of OH radicals with Methylglyoxal and Acetaldehyde". In: *International Journal of Chemical Kinetics* 27.10, pp. 1009–1020.

Vöhringer-Martinez et al. (2007). "Water catalysis of a radical-molecule gas-phase reaction". In: *Science* 315.5811, pp. 497–501.

Wallington et al. (1988). "Gas phase reaction of Cl atoms with a series of oxygenated organic species at 295 K". In: *International Journal of Chemical Kinetics*.

Wang et al. (2003). "Kinetic study of the reaction of acetaldehyde with OH". In: *Journal of Physical Chemistry A* 107.49, pp. 10834–10844.

Zhu et al. (2008). "Rate Coefficients for the OH + Acetaldehyde ($CH_3CHO$) Reaction Between 204 and 373 K". In: *International Journal of Chemical Kinetics* 40.10, pp. 635–646.

# Chapter 5

# New Source of OH from Peroxy Radicals

## 5.1   Background

During this PhD, OH yields from RCO + $O_2$ (Chapter 3) and RC(O)$O_2$ + HO$_2$ (Chapter 6) reactions were studied. Chapters 1 and 3 cover the importance of peroxy radicals to both the atmosphere and combustion chemistry. Previously, in both this work and literature studies, when examining the OH yields from RCO + $O_2$ reactions, the OH fluorescence has been recorded only over the time period 0 – 1000 $\mu$s. The majority of the OH was observed within the first 500 $\mu$s, it then sharply decreased to 0, staying there till 1000 $\mu$s – this was expected. It had been assumed that this zero amount of OH would continue as previous literature had no indication of anything else happening (Papadimitriou et al. 2015; Gross, Dillon, and Crowley 2014).

For the studies of RC(O)$O_2$ + HO$_2$, higher concentrations of chlorine radicals were used and LIF signals were recorded over a longer time scale, up to 10,000 $\mu$s. A few experiments in this study had previously used these conditions (higher [Cl]

and longer time scale) in the absence of $HO_2$ where OH from $RCO + O_2$ was expected to decay quickly. Figure 5.1 shows one such trace using a large initial [Cl] $= 10^{13}$ molecule $cm^{-3}$. The kinetic simulation, Kintecus (Ianni 2017), follows the experimental data well at first, corresponding to OH production from $CH_3CO + O_2$. When the Kintecus levels drop to zero, there seems to be an unknown secondary OH source. This secondary OH product was observed in this study whenever elevated [Cl] was used and was not consistent with known OH production from $RCO + O_2$ or $RC(O)O_2 + HO_2$.

This chapter presents the experimental results of the studies which have been conducted to explore the origin and implications of this secondary OH. Studies were carried out to determine how the concentrations of $Cl_2$ and RCHO affect this secondary OH; these will be discussed alongside the results of studies investigating the OH dependency on photolysis laser power.
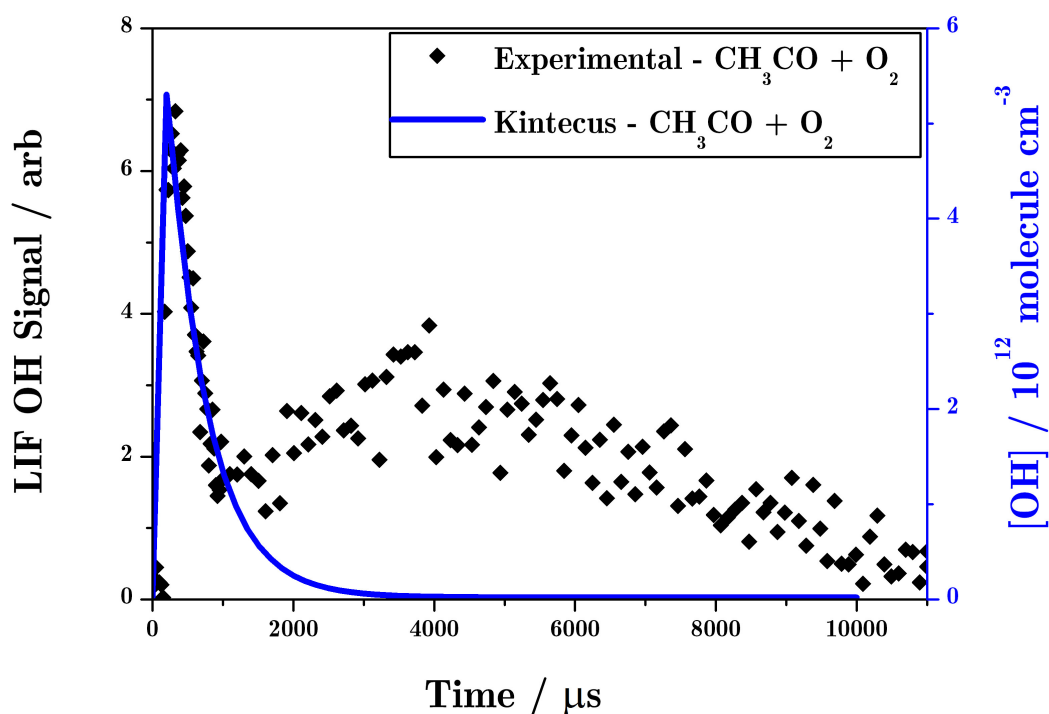


Figure 5.1: Experimental results from $CH_3CO + O_2$ (black diamonds) at 100 Torr with the concentrations (in molecule $cm^{-3}$): $CH_3CHO = 2.5 \times 10^{14}$, $Cl_2 = 9.2 \times 10^{14}$, $Cl \approx 2 \times 10^{13}$, $N_2 = 3.1 \times 10^{18}$, and $O_2 = 1.2 \times 10^{17}$. The line indicates the Kintecus simulation for these experimental conditions (Ianni 2017).

## 5.2    OH LIF Excitation Spectra

To confirm that the signal seen in Figure 5.1 was OH, a LIF Excitation Spectrum was recorded, Figure 5.2. Similar conditions were applied to the experiment as used for the collection of data of Figure 5.1, with the pressure at 100 Torr and concentrations (molecule $cm^{-3}$) of: $CH_3CHO = 1.3 \times 10^{14}$, $Cl_2 = 9.2 \times 10^{14}$, $Cl \approx 2 \times 10^{13}$, $N_2 = 3.1 \times 10^{18}$, and $O_2 = 1.2 \times 10^{17}$. The time delay between the photolysis and probe laser was 3500 $\mu$s, where Kintecus predicts no OH production from $CH_3CO$ + $O_2$ (Figure 5.1). The data from Figure 5.2 demonstrate the fluorescence to be OH, though due to a low signal-to-noise ratio, the peaks are not as well-defined as the previously recorded OH LIF Excitation Spectra (Chapter 3).
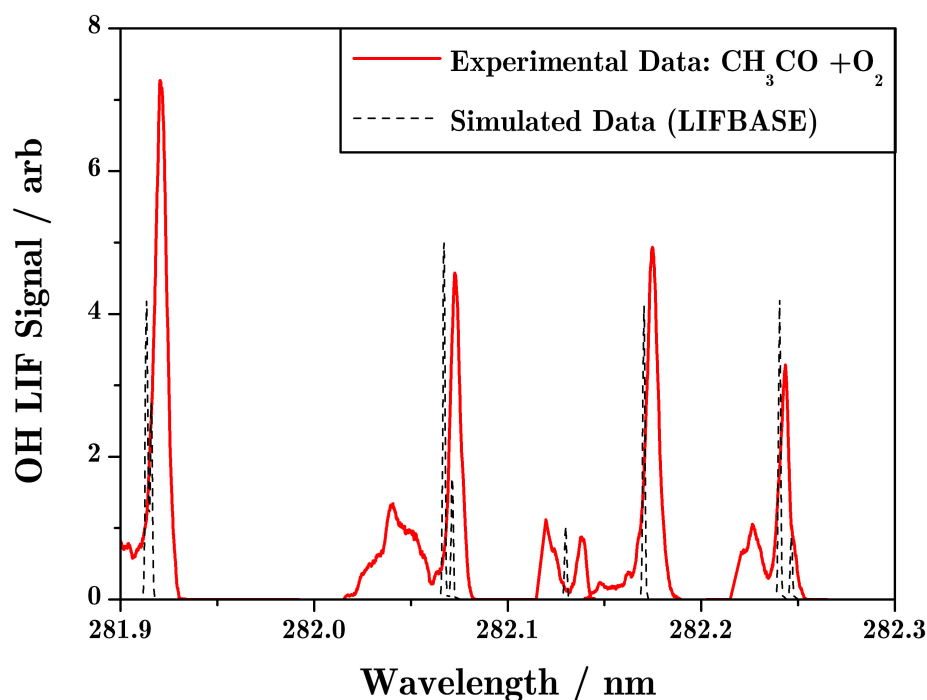


Figure 5.2: LIF Excitation Spectra of $CH_3CO$ + $O_2$ at the longer time period with conditions of: 100 Torr and concentrations (in molecule $cm^{-3}$) of $CH_3CHO = 1.3 \times 10^{14}$, $Cl_2 = 9.2 \times 10^{14}$, $Cl \approx 2 \times 10^{13}$, $N_2 = 3.1 \times 10^{18}$, and $O_2 = 1.2 \times 10^{17}$.

Kinetic traces repeated at different wavelengths further confirmed that it was OH. A trace was recorded at a wavelength of 281.91 nm, where previous kinetic traces were

recorded for the results shown in Chapter 3. Afterwards the probe laser was tuned to a wavelength of 282.01 nm, where OH does not fluoresce. Figure 5.3 displays these results. As expected the off–resonance, at a wavelength of 282.01 nm, does not show any OH fluorescence. It can therefore be concluded that the species which caused the fluorescence at the later time period was OH.
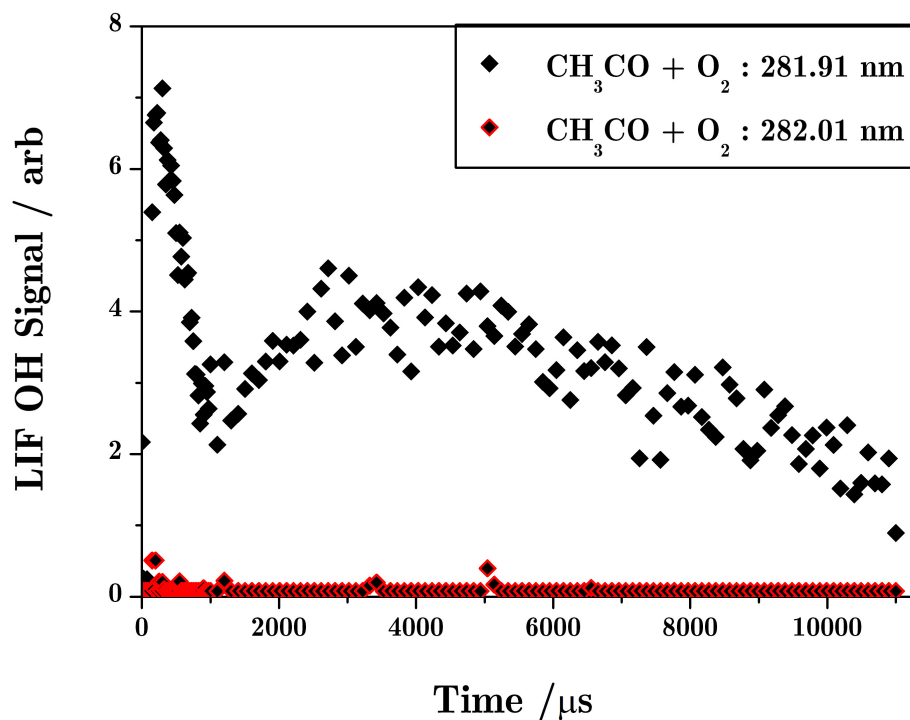


Figure 5.3: Kinetic traces of $CH_3CO + O_2$ at 100 Torr with $[CH_3CHO] = 2.5 \times 10^{14}$, $[Cl_2] = 9.2 \times 10^{14}$, $[Cl] \approx 2 \times 10^{13}$, $[N_2] = 3.1 \times 10^{18}$ and $[O_2] = 1.2 \times 10^{17}$. Two traces are shown: one with the probe laser tuned to 281.91 nm (black diamonds) and the other at 282.01 nm (black and red diamonds) where no OH fluorescence is seen.

## 5.3 Concentration Dependence

Figure 5.4 shows the dependence that the concentration of $CH_3CHO$ has on the production of OH. The pressure was kept constant at 100 Torr, as was the concentration (in molecule cm$^{-3}$) of the other gases: $Cl_2 = 9.2 \times 10^{14}$, $Cl \approx 2 \times 10^{13}$, $N_2 = 3.1 \times 10^{18}$, and $O_2 = 1.2 \times 10^{17}$. Figure 5.4 shows that as the concentration of $CH_3CHO$ increased the OH signal correspondingly reduced. This is expected due to more $CH_3CHO$ being available to react with the OH – considered to be the largest loss channel for OH.
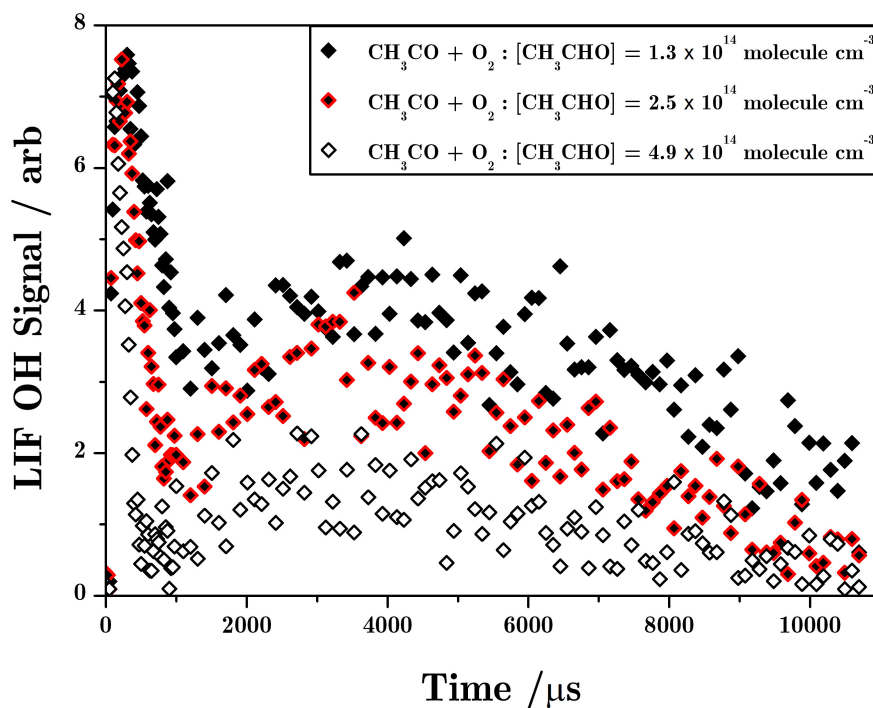


Figure 5.4: The dependence of the concentration of $CH_3CHO$ on the OH formation from the reaction $CH_3CO + O_2$ at 100 Torr. Three different concentrations (in molecule cm$^{-3}$) of $CH_3CHO$ are shown: $1.3 \times 10^{14}$, $2.5 \times 10^{14}$ and $4.9 \times 10^{14}$. Other gases were kept constant: $[Cl_2] = 9.2 \times 10^{14}$, $[Cl] \approx 2 \times 10^{13}$ , $[N_2] = 3.1 \times 10^{18}$ and $[O_2] = 1.2 \times 10^{17}$.

To estimate a quantitative result, the three data sets acquired from altering the $CH_3CHO$ concentration were fitted using Equation 5.1 in MATLAB (previously used and discussed in Chapter 3). Figure 5.5 shows the fit for the data when $[CH_3CHO]$

$= 1.3 \times 10^{14}$ molecule cm$^{-3}$. The points from $0 - 1000$ $\mu$s are removed from the data to allow the code to only fit the secondary rise and decay of OH. This type of fit was repeated for the other two traces with the numerical (un-scaled) OH yield for these reactions shown in Table 5.1. These results show that increasing the [CH$_3$CHO] decreases the OH yield of the reaction.

$$[OH](t) = A(e^{-Bt} - e^{-Ct}) \tag{5.1}$$
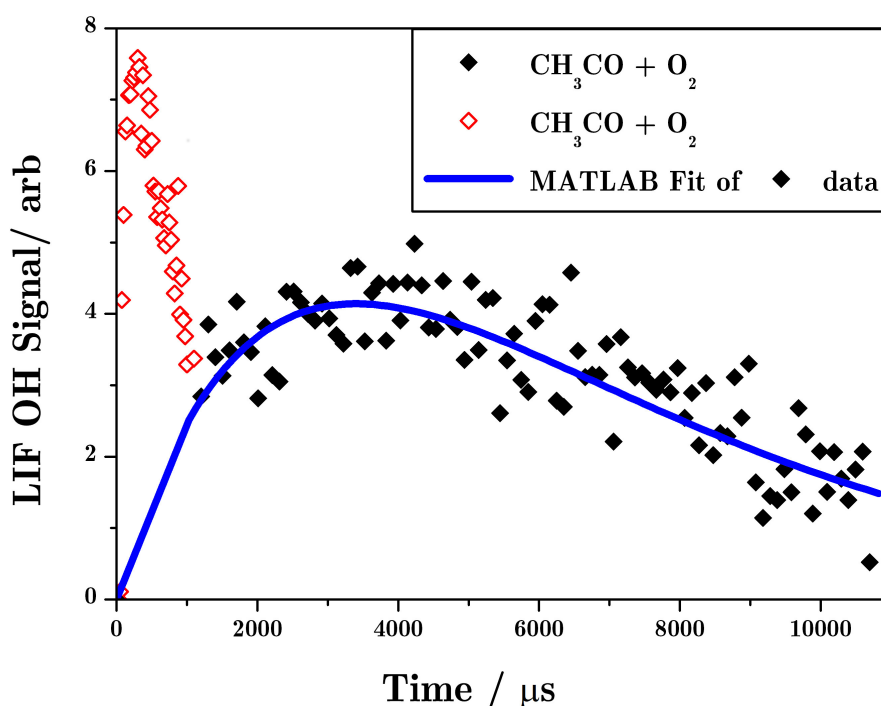


Figure 5.5: Experimental result (black diamonds) of the CH$_3$CO + O$_2$ reaction at 100 Torr with [CH$_3$CHO] $= 1.3 \times 10^{14}$, [Cl$_2$] $= 9.2 \times 10^{14}$, [Cl] $\approx 2 \times 10^{13}$ , [N$_2$] $= 3.1 \times 10^{18}$ and [O$_2$] $= 1.2 \times 10^{17}$. The blue line shows the MATLAB fit (previously used and discussed in Chapter 3) which has calculated by removing the first part of the data so only the secondary OH producing reaction is analysed.

Figure 5.6 shows the dependence that the concentration of chlorine has on the OH; two different concentrations are shown : [Cl$_2$] / [Cl] $= 9.2 \times 10^{14}$/ $2 \times 10^{13}$ molecule cm$^{-3}$ and [Cl$_2$] / [Cl] $= 1.8 \times 10^{15}$/ $3 \times 10^{13}$ molecule cm$^{-3}$. The pressure was kept constant at 100 Torr as was the concentration (molecule cm$^{-3}$) of the other gases: [CH$_3$CHO] $= 4.9 \times 10^{14}$, [N$_2$] $= 3.1 \times 10^{18}$, and [O$_2$] $= 1.2 \times 10^{17}$. Figure 5.6

Table 5.1: The numerical OH Yield (unscaled) results of the three reactions shown in Figure 5.4, showing how [CH$_3$CHO] affects the secondary OH producing reaction.

| | [CH$_3$CHO] / molecule cm$^{-3}$ | | |
| --- | --- | --- | --- |
| | $1.3 \times 10^{14}$ | $2.5 \times 10^{14}$ | $4.9 \times 10^{14}$ |
| Unscaled OH Yield | $3.3 \times 10^5$ | $2.4 \times 10^5$ | $1.2 \times 10^5$ |

shows that by increasing the [Cl] the OH signal is increased. This suggests that the secondary OH channel is directly affected by the chlorine radicals.
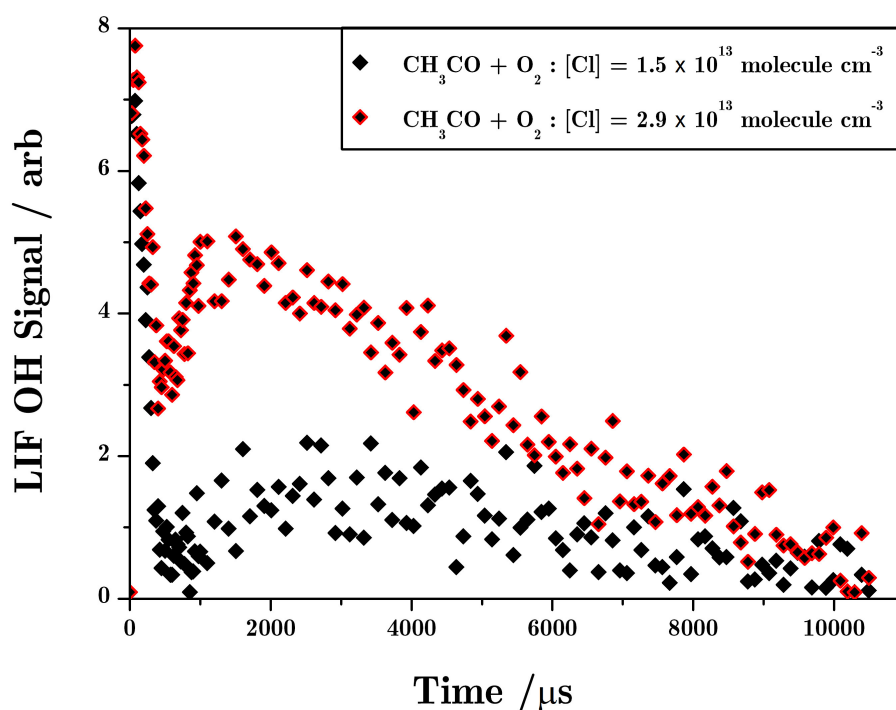


Figure 5.6: The dependence of the concentration of chlorine on the OH formation from the reaction CH$_3$CO + O$_2$ at 100 Torr. Two different concentrations of chlorine are shown: [Cl$_2$] / [Cl] = $9.2 \times 10^{14}$/ $2 \times 10^{13}$ molecule cm$^{-3}$ (black diamonds) and [Cl$_2$] / [Cl] = $1.8 \times 10^{15}$/ $3 \times 10^{13}$ molecule cm$^{-3}$ (red and black diamonds) while the other gases were kept constant: [CH$_3$CHO] = $4.9 \times 10^{14}$ molecule cm$^{-3}$, [N$_2$] = $3.1 \times 10^{18}$ molecule cm$^{-3}$ and [O$_2$] = $1.2 \times 10^{17}$ molecule cm$^{-3}$.

Figure 5.7 shows the dependence that the concentration of O$_2$ has on the OH; three different concentrations (in molecule cm$^{-3}$) are shown : $2.8 \times 10^{16}$, $1.1 \times 10^{17}$, and $2.2 \times 10^{17}$. The pressure was kept constant at 100 Torr as was the concentration of the other gases (in molecule cm$^{-3}$): [CH$_3$CHO] = $4.9 \times 10^{14}$, [N$_2$] = $3.1 \times 10^{18}$,

$[Cl_2] = 1.4 \times 10^{15}$, and $[Cl] \approx 2 \times 10^{13}$ molecule $cm^{-3}$. Figure 5.7 shows that the secondary OH channel is only slightly affected by the change in the $[O_2]$; the traces from the different concentrations follow similar curves that are close to each other.
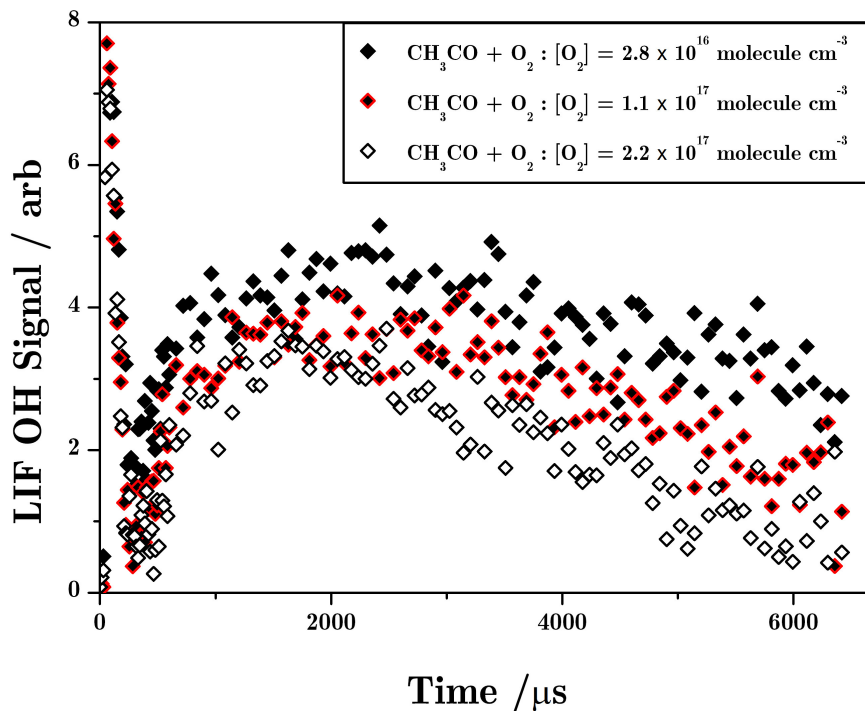


Figure 5.7: The dependence of the concentration of $O_2$ on the OH formation from the reaction $CH_3CO + O_2$ at 100 Torr. Three different concentrations of $O_2$ are shown: $2.8 \times 10^{16}$ molecule $cm^{-3}$ (black filled diamonds), $1.1 \times 10^{17}$ molecule $cm^{-3}$ (black and red diamonds) and $2.2 \times 10^{17}$ molecule $cm^{-3}$ (black empty diamonds) while the other gases were kept constant: $[CH_3CHO] = 4.85 \times 10^{14}$ molecule $cm^{-3}$, $[N_2] = 3.1 \times 10^{18}$ molecule $cm^{-3}$, $[Cl_2] = 1.4 \times 10^{15}$ molecule $cm^{-3}$ and $[Cl] \approx 2 \times 10^{13}$ molecule $cm^{-3}$.

## 5.4　Laser Power Dependence

To help determine whether this secondary OH producing reaction is a radical + radical reaction or not, laser power experiments were carried out. Initially a hollow metal tube was placed in the 355 nm beam path, which has no effect on the beam (laser power = 0.22 W). Then metal gauze was inserted into the tube, which partially blocked the beam, reducing the power. Two gauzes were used, allowing experiments to be additionally carried out at 0.13 W and 0.06 W, without having to change the Q-switch and flashlamp timings on the photolysis laser. The gauze allowed these photolysis laser power experiments to be run back-to-back, meaning they all had the same conditions so the experiments could be directly compared. Two types of experiments are discussed here, both carried out at 100 Torr. The first was when the photolysis laser power was altered the chlorine flow was also altered to keep the chlorine radicals constant; the second experiment altered the photolysis laser power with all the flows kept constant so that the radical concentration changed with the power change.

Table 5.2: The concentrations of the gases in the mixtures for the three traces using different power, shown in Figure 5.8. The chlorine radical concentration was kept constant by altering the $Cl_2$ flow.

| Gas | Concentrations / molecule $cm^{-3}$ | | |
| --- | --- | --- | --- |
| | 0.21 W | 0.13 W | 0.06 W |
| $N_2$ | $3.1 \times 10^{18}$ | $3.1 \times 10^{18}$ | $3.1 \times 10^{18}$ |
| $O_2$ | $1.2 \times 10^{17}$ | $1.2 \times 10^{17}$ | $1.5 \times 10^{17}$ |
| $CH_3CHO$ | $2.5 \times 10^{14}$ | $2.5 \times 10^{14}$ | $2.5 \times 10^{14}$ |
| $Cl_2$ | $6.5 \times 10^{14}$ | $1.2 \times 10^{15}$ | $2.3 \times 10^{15}$ |
| Cl | $1 \times 10^{13}$ | $1 \times 10^{13}$ | $1 \times 10^{13}$ |

Figure 5.8 shows results of the effect that the photolysis laser power change has on the OH yield of the secondary OH producing reaction when the chlorine radical concentration stays constant (conditions found in Table 5.2). The results show that the data recorded for these three runs are very similar, showing that the change in the $[Cl_2]$ has little/no effect on the OH yield. This indicates that the secondary OH
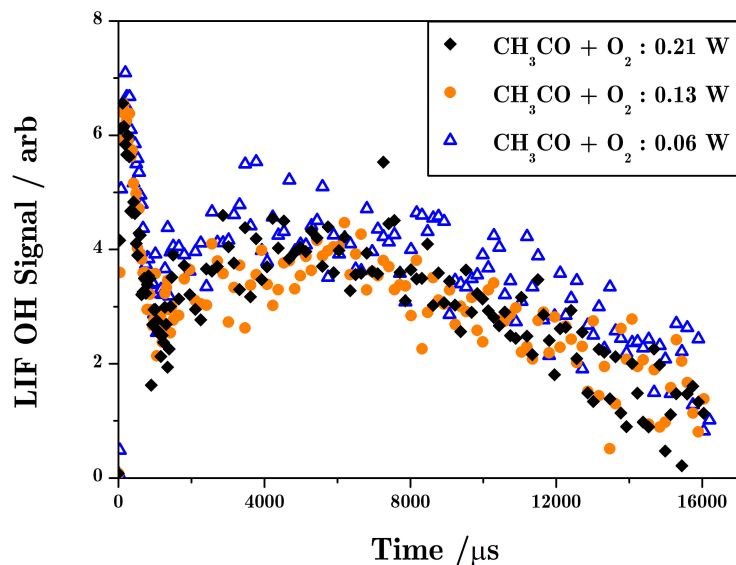
Figure 5.8: Three kinetic traces at different photolysis laser powers: 0.21 W (black diamonds), 0.13 W (orange circles) and 0.06 W (blue triangles). Table 5.2 contains the concentrations used in these traces with the [Cl] kept constant $\approx 1 \times 10^{13}$ molecule cm$^{-3}$.
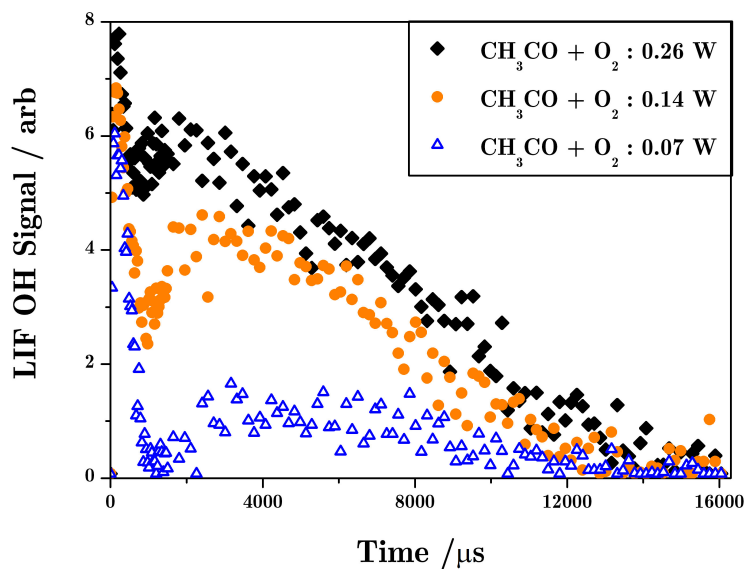


Figure 5.9: Three kinetic traces at different photolysis laser powers (and different [Cl] in molecule cm$^{-3}$): 0.21 W ($3 \times 10^{13}$; black diamonds), 0.13 W ($2 \times 10^{13}$; orange circles) and 0.06 W ($9 \times 10^{12}$; blue triangles). Flows of gases were kept constant with their concentrations found in Table 5.3 .

is unlikely to be produced by the reaction of $Cl_2$ + $CH_3$.

Figure 5.9 displays the effect the concentrations of the radical species has on the OH yield of the secondary OH producing reaction. All the gas flows stay constant throughout this experiment, causing the radicals in the system to change with the change in the laser power. The concentrations of each species for the three different laser powers are presented below in Table 5.3. The results show that the data recorded for these three runs differ greatly, showing that the change in the chlorine radical concentration has an effect on the OH yield.

Table 5.3: The concentrations of the gases (in molecule $cm^{-3}$) in the mixtures for the three traces shown in Figure 5.9. The flows of all gases were kept constant which allowed the radical concentration to change with the power changes.

| Compound | Power | | |
|---|---|---|---|
| | **0.26 W** | **0.14 W** | **0.07 W** |
| $N_2$ | $3.1 \times 10^{18}$ | $3.1 \times 10^{18}$ | $3.1 \times 10^{18}$ |
| $O_2$ | $1.1 \times 10^{17}$ | $1.1 \times 10^{17}$ | $1.1 \times 10^{17}$ |
| $CH_3CHO$ | $2.5 \times 10^{14}$ | $2.5 \times 10^{14}$ | $2.5 \times 10^{14}$ |
| $Cl_2$ | $1.8 \times 10^{15}$ | $1.8 \times 10^{15}$ | $1.8 \times 10^{15}$ |
| $Cl$ | $3 \times 10^{13}$ | $2 \times 10^{13}$ | $9 \times 10^{12}$ |

## 5.5 Pressure Dependence

It was important to look at the difference that pressure makes on this reaction. It was difficult to keep the number of Cl radicals the same throughout these experiments as traces were recorded at a range of pressures from 100 Torr – 300 Torr. Though they were kept as similar as possible to allow for direct comparisons, the concentrations of all the compounds are found in Table 5.4. To be able to fully compare these experiments directly to each other, they were recorded back-to-back with the PMT kept constant. The results shown in Figure 5.10 indicate that this secondary OH producing channel is not pressure dependent by qualitative analysis.
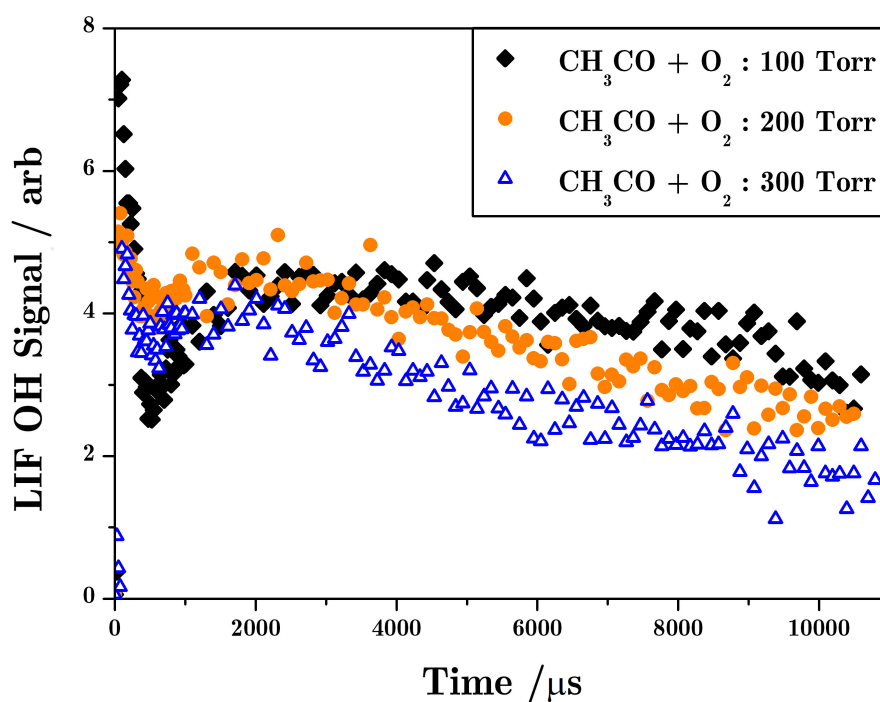


Figure 5.10: Three kinetic traces at different pressures: 100 Torr (black diamonds; $[Cl] = 1.5 \times 10^{13}$ molecule $cm^{-3}$), 200 Torr (orange circles; $[Cl] = 2.9 \times 10^{13}$ molecule $cm^{-3}$) and 300 Torr (blue triangles; $[Cl] = 3.3 \times 10^{13}$ molecule $cm^{-3}$). The other concentrations of the gases are found in Table 5.4.

To estimate quantitative results from these data, these kinetic traces were recorded with kinetic traces of NO + $HO_2$ – well known OH producing reaction (Atkinson et al. 2004). Figure 5.11 shows a kinetic trace of both $CH_3CO + O_2$ and NO +

Table 5.4: The concentrations (in molecule cm$^{-3}$ of the gases in the mixtures for the kinetic traces at the three different pressures (100, 200 and 300 Torr) shown in Figure 5.9.

| Compounds | Pressure | | |
| --- | --- | --- | --- |
| | 100 Torr | 200 Torr | 300 Torr |
| N$_2$ | $3.1 \times 10^{18}$ | $6.3 \times 10^{18}$ | $9.3 \times 10^{18}$ |
| O$_2$ | $8.7 \times 10^{16}$ | $1.7 \times 10^{17}$ | $3.5 \times 10^{17}$ |
| CH$_3$CHO | $6.2 \times 10^{14}$ | $4.3 \times 10^{14}$ | $6.3 \times 10^{14}$ |
| Cl$_2$ | $9.3 \times 10^{14}$ | $1.9 \times 10^{15}$ | $2.1 \times 10^{15}$ |
| Cl | $1.5 \times 10^{13}$ | $2.9 \times 10^{13}$ | $3.3 \times 10^{13}$ |

HO$_2$ at 100 Torr, with the NO + HO$_2$ trace being fit by a Kintecus simulation (Ianni 2017). This Kintecus model allowed the conversion of the LIF OH signal into OH concentration (molecule cm$^{-3}$) and is discussed further in Chapter 6 where the reactions included in the Kintecus model are presented. The MATLAB fit of the CH$_3$CO + O$_2$ data (explained further in Section 5.3: Concentration Dependence) was used to generate a estimated OH yield which was in the units of LIF signal. A conversion from LIF signal to concentration (from the NO + HO$_2$) was applied to obtain the approximated OH yield in concentration. This allowed a ratio between the [Cl] and the concentration of OH yield. These results are plotted in Figure 5.12 - the error bars on this plot represent two standard deviations. This pressure dependence study has shown that pressure hardly affects the OH yield, it also has shown how to roughly quantify the amount of OH produced from the secondary source.
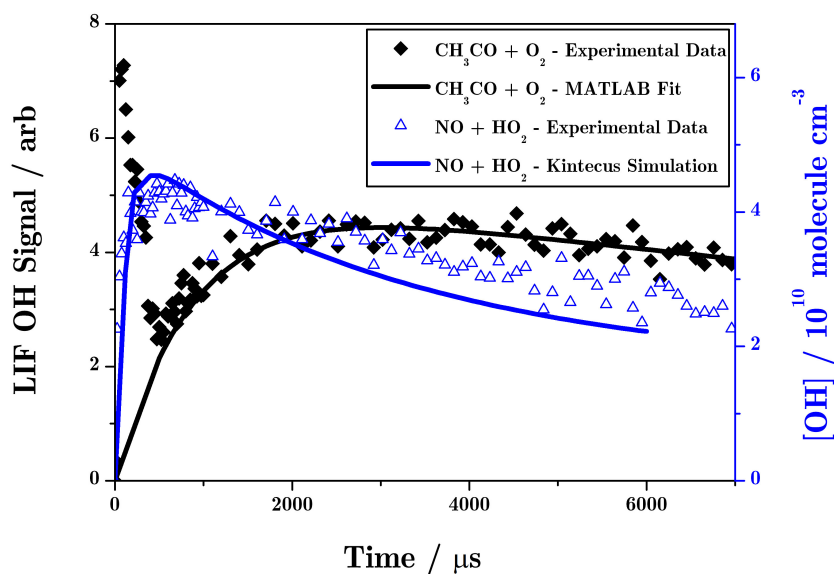
Figure 5.11: Experimental data from kinetic traces of $CH_3CO + O_2$ (black diamonds) and $NO + HO_2$ (blue triangles) at 100 Torr. The black line represents the MATLAB fit of the $CH_3CO + O_2$ data, whereas the blue line represents the Kintecus kinetic simulation of the $NO + HO_2$.
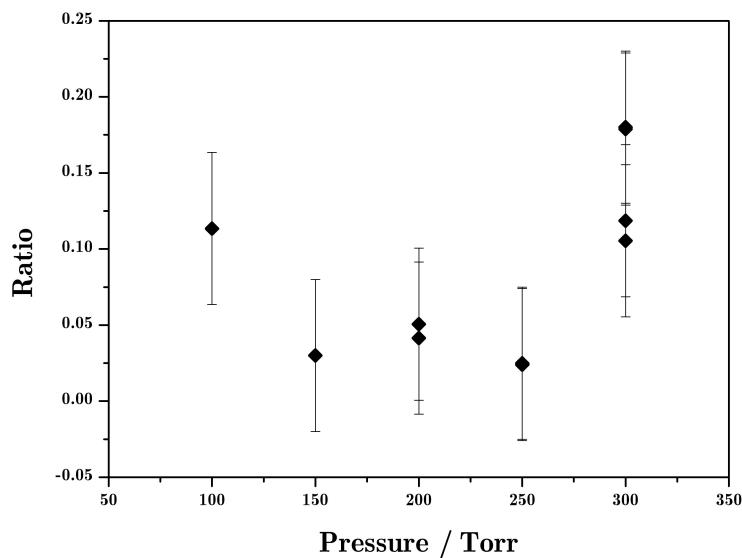


Figure 5.12: The ratio showing how much of the chlorine radicals form the secondary OH at different pressures from the reaction of $CH_3CO + O_2$. The error bars represent the two standard deviation of each of the data points.

## 5.6    Temperature Dependence

The temperature dependence of this secondary OH producing reaction was examined, with a set of experiments recorded at 294 K between the pressures of 100 - 300 Torr then repeated at 375 K with the 100 and 300 Torr results shown in Figures 5.13 and 5.14. The $CH_3CO + O_2$ data were recorded back-to-back with a trace of $NO + HO_2$, which allowed the two traces to be compared.

The 100 Torr results (Figure 5.13) show the traces of $NO + HO_2$ to be closely overlapped - this reaction has been shown to be stable over a wide temperature range (200 – 400 K) from numerous literature studies, therefore it is a good reaction to compare results with. However, the $CH_3CO + O_2$ results do differ across the two temperatures. The OH produced from $CH_3CO + O_2$ between the time period of 0 - 1000 $\mu$s is from the known OH production route of $CH_3CO + O_2$ (Chapter 3). This is where the difference occurs between the two temperatures - the peak of OH is greater from the results at 375 K, indicting a higher OH yield at higher temperature.

However, the secondary OH production from $CH_3CO + O_2$ (1000 - 10000 $\mu$s) does not change with temperature at 100 Torr (Figure 5.13), suggesting that this reaction does not have a temperature dependence. Further results at 300 Torr (Figure 5.14) indicate that the temperature dependence  does not change with pressure. As qualitatively there seems to be no difference between the two $CH_3CO + O_2$ traces at the different temperatures at the higher pressure. In comparison the $NO + HO_2$ reaction differs more at 300 Torr, though this is expected from the literature because of the increase in pressure.
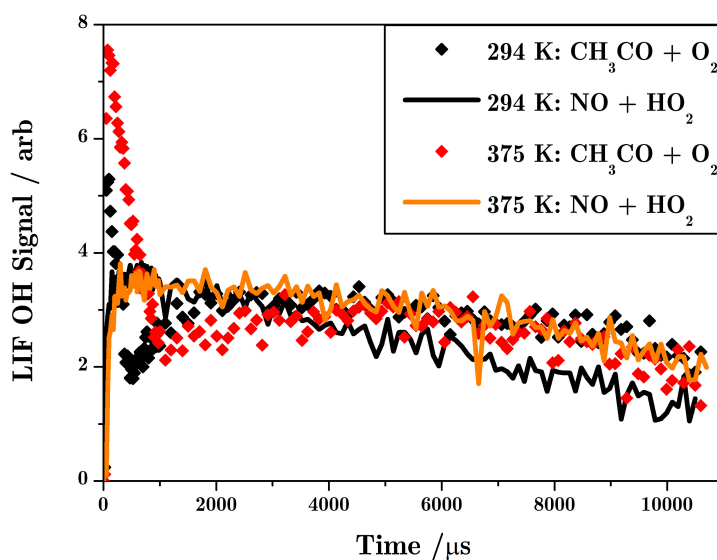
Figure 5.13: Results from $CH_3CO + O_2$ and $NO + HO_2$ at 100 Torr and at two temperatures – 294 K (black diamonds -$CH_3CO + O_2$; black line – $NO + HO_2$) and 375 K (red diamonds -$CH_3CO + O_2$; orange line – $NO + HO_2$).
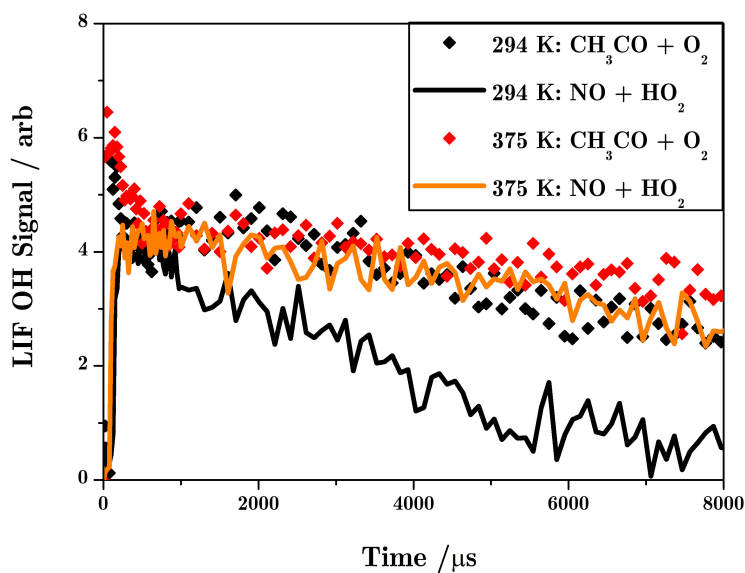


Figure 5.14: Results from $CH_3CO + O_2$ and $NO + HO_2$ at 300 Torr and at two temperatures – 294 K (black diamonds – $CH_3CO + O_2$; black line – $NO + HO_2$) and 375 K (red diamonds -$CH_3CO + O_2$; orange line - $NO + HO_2$).

## 5.7   Results from other Peroxys

Two other reactions were examined to see if all RCO + $O_2$ produce this secondary OH. The reactions looked at were:  $C_2H_5CO$ + $O_2$ and $(CH_3)_2CHCH_2CO$ + $O_2$. Figure 5.15 shows the data collected for the reaction $C_2H_5CO$ + $O_2$ at 100 Torr; it shows that this reaction does produce this secondary OH similar to $CH_3CO$ + $O_2$ shown in Figure 5.4. The dependence that the concentration of $C_2H_5CHO$ has on the OH was analysed, shown in Figure 5.15. The pressure was kept constant at 100 Torr as was the concentration (in molecule $cm^{-3}$ of the other gases: $[Cl_2]$ = 9.2 × $10^{14}$, $[Cl]$ = 2 × $10^{13}$, $[N_2]$ = 3.1 × $10^{18}$, and $[O_2]$ = 1.2 × $10^{17}$. Similar to $CH_3CO$ + $O_2$, the reaction of $C_2H_5CO$ + $O_2$ shows that by increasing the $[C_2H_5CHO]$ the OH signal is reduced.
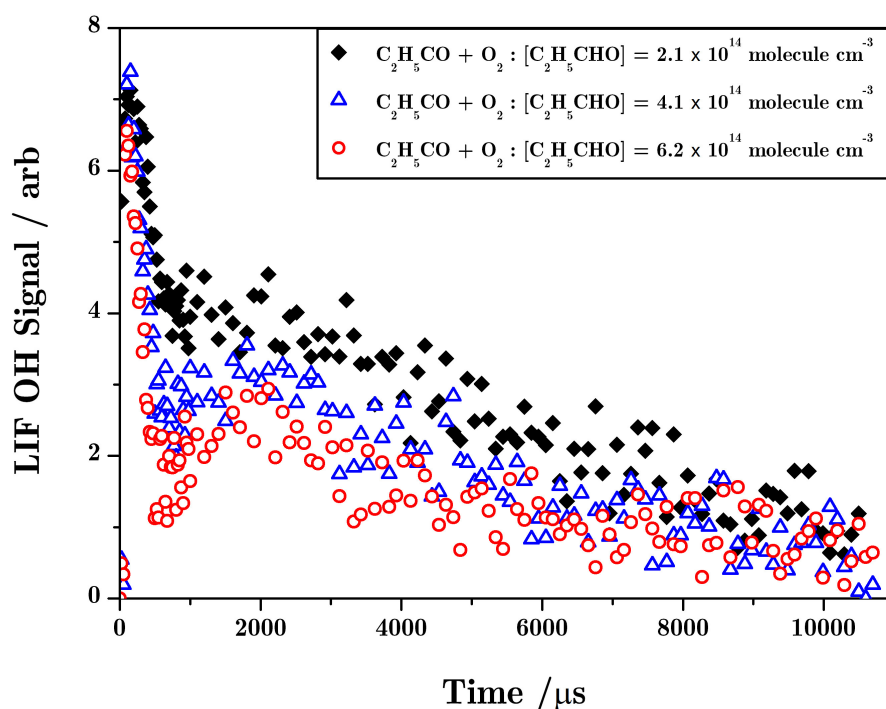


Figure 5.15: The dependence of the concentration of $C_2H_5CHO$ on the OH formation from the reaction $C_2H_5CO$ + $O_2$ at 100 Torr. Three different concentrations (in molecule $cm^{-3}$) of $C_2H_5CHO$ are shown:  2.1 × $10^{14}$, 4.1 × $10^{14}$, and 6.2 × $10^{14}$ while the other gases were kept constant: $[Cl_2]$ = 9.2 × $10^{14}$, $[Cl]$ ≈ 2 × $10^{13}$, $[N_2]$ = 3.1 × $10^{18}$, and $[O_2]$ = 1.2 × $10^{17}$.

Figure 5.16 shows the data collected for the reaction $(CH_3)_2CHCH_2CO + O_2$ at 100 Torr. This chemistry does produce secondary OH similar to $CH_3CO + O_2$ and $C_2H_5CO + O_2$. The dependence that the concentration of $(CH_3)_2CHCH_2CHO$ has on the OH was analysed, shown in Figure 5.16. The pressure was kept constant at 100 Torr as was the concentration (in molecule $cm^{-3}$) of the other gases: $[Cl_2] = 9.2 \times 10^{14}$, $[Cl] \approx 2 \times 10^{13}$, $[N_2] = 3.1 \times 10^{18}$, and $[O_2] = 1.2 \times 10^{17}$. Similar to $CH_3CO + O_2$ and $C_2H_5CO + O_2$ the signal from the OH is reduced when $[(CH_3)_2CHCH_2CHO]$ is increased. However, there is less OH produced compared to the $CH_3CO + O_2$ and $C_2H_5CO + O_2$ reactions as the OH signal reduces substantially as soon as the $[(CH_3)_2CHCH_2CHO]$ is increased.
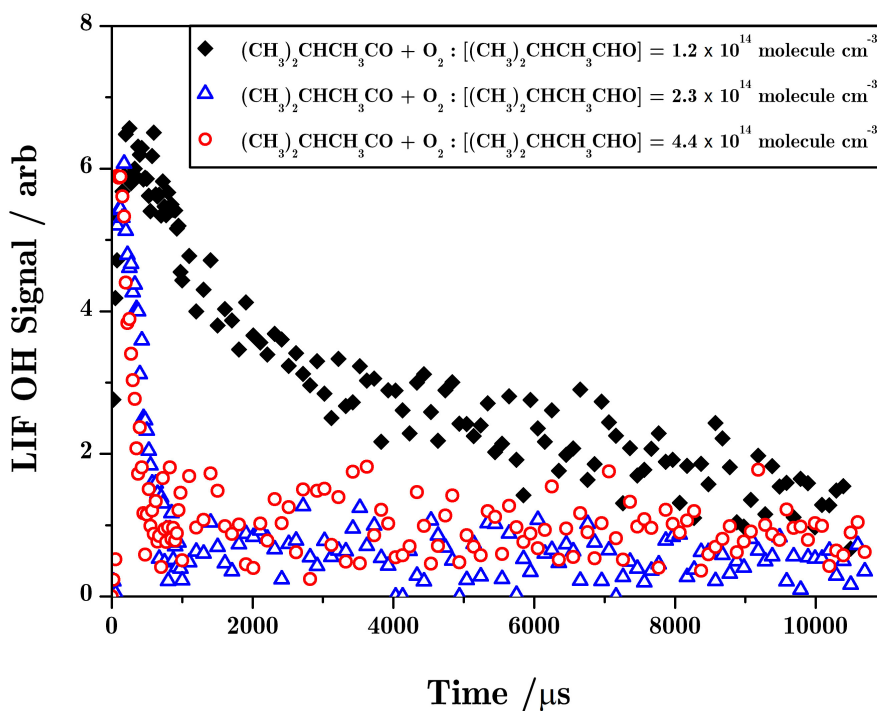


Figure 5.16: The dependence of the concentration of $(CH_3)_2CHCH_2CHO$ on the OH formation from the reaction $(CH_3)_2CHCH_2CO + O_2$ at 100 Torr. Three different concentrations (in molecule $cm^{-3}$) of $(CH_3)_2CHCH_2CHO$ are shown: $1.2 \times 10^{14}$, $2.3 \times 10^{14}$, and $4.5 \times 10^{14}$ while the other gases were kept constant: $[Cl_2] = 9.2 \times 10^{14}$, $[Cl] \approx 2 \times 10^{13}$, $[N_2] = 3.1 \times 10^{18}$, and $[O_2] = 1.2 \times 10^{17}$.

## 5.8   Summary

The discussions in this chapter have shown the numerous types of experiments which have been carried out to clarify a previously unknown source of OH. The results from these experiments have proven that this secondary OH formation is substantial and occurs at various different pressures and temperatures as well as in different reactions. It has shown that the secondary OH reaction is neither pressure or temperature dependent, suggesting that the reaction does not proceed via a chemical activated mechanism - which the RCO + $O_2$ reactions do in Chapter 3.

The results from the experiments on radical dependency also suggest that this secondary OH reaction is controlled by the amount of Cl radicals in the system. At first when investigating the source of this OH, there were a few potential reactions. However, as there was no $O_2$ dependency shown in experiments this removed any reactions with $O_2$ to be the source of OH including: $CH_3$ + $O_2$ and $CH_3O$ + $O_2$. Other reactions that could lead to formation of OH are: $CH_3O_2$ + $CH_3$, $CH_3$ + $RO_2$, $RO_2$ + $RO_2$, or $RO_2$ + $CH_3O_2$. The conclusion that was reached at the end of these studies was that the source of the unknown OH came from a secondary reaction and was most likely caused by a high concentration of $RO_2$. To be able to fully determine what reaction causes this OH further investigations are needed to into the products of this reaction. Unfortunately this experiment can only record OH fluorescence therefore studies on other instruments, such as FTIR, should be carried out to probe what products are made and how the amounts change due to varying conditions.

# Bibliography

Atkinson et al. (2004). "Evaluated kinetic and photochemical data for atmospheric chemistry: Part 1 - gas phase reactions of $O_x$, $HO_x$, $NO_x$ and $SO_x$ species". In: *Atmospheric Chemistry and Physics Discussions* 3.6, pp. 6179–6699.

Gross, Dillon, and Crowley (2014). "Pressure dependent OH yields in the reactions of $CH_3CO$ and $HOCH_2CO$ with $O_2$." In: *Physical Chemistry Chemical Physics* 16.22, pp. 10990–10998.

Ianni, James C (2017). *Kintecus*. URL: www.kintecus.com.

Papadimitriou et al. (2015). "$CH_3CO$ + $O_2$ + M (M = He, $N_2$) Reaction Rate Coefficient Measurements and Implications for the OH Radical Product Yield". In: *Journal of Physical Chemistry A* 119.28, pp. 7481–7497.

# Chapter 6

# Peroxy Radicals with Hydroperoxyl Radicals

Peroxy radicals ($RO_2$) play a key role in not only atmospheric chemistry but also in auto-ignition chemistry. The majority of $RO_2$ are formed in the atmosphere via the reaction of primary organic pollutants with tropospheric oxidants, forming an alkyl radical which then reacts with $O_2$. Acyl radicals ($RC(O)O_2$) are one type of $RO_2$, generally more reactive than other $RO_2$ due to their carbonyl bond (C=O) in the molecule. Chapter 3 has shown how chemically activated $RC(O)O_2$ breaks down to form OH, with the OH yield depending on the R group of the $RC(O)O_2$ and the pressure of the system. This chapter describes the work undertaken to investigate the OH product yield in the reactions between $RC(O)O_2$ and hydroperoxyl radicals ($HO_2$). The reaction of $CH_3C(O)O_2 + HO_2$ has already been extensively studied in the literature but this chapter will show the ability this apparatus has to determine the yields of OH from two other $RC(O)O_2$, using $CH_3C(O)O_2 + HO_2$ as a comparison.

## 6.1 Background

The reactions of $RO_2$ + $HO_2$ were studied due to their atmospheric importance – as described in Chapter 1. $RO_2$ are critical in the production of tropospheric $O_3$, acting as an oxidant to convert NO to $NO_2$ without using $O_3$ – otherwise it would be a null cycle where the amount of $O_3$ produced is equal to the amount used – see Equation 6.1.

$$NO + O_3 \rightarrow NO_2 + O_2$$
$$NO_2 + h\nu \rightarrow NO + O \qquad (6.1)$$
$$O + O_2 \rightarrow O_3$$
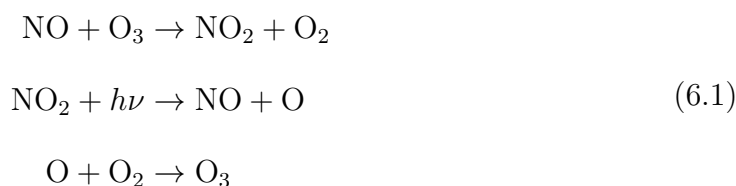
In the atmosphere OH and $HO_2$ are in rapid steady state, and therefore are collectively known as $HO_x$. Figure 6.1 displays a simple $HO_x$ cycle, which shows how OH and $HO_2$ interchange in the troposphere – only the main routes in the cycle are shown. Atmospheric $HO_2$ is commonly produced via the oxidation of VOCs with OH which in turn produces $RO_2$ then RO which reacts with $O_2$ to form $HO_2$ and $R'CHO$. The most common loss of $HO_2$ in the atmosphere occurs via the reaction with NO to form $NO_2$ and OH.

Interest in $RC(O)O_2$, principally the acetyl peroxyl ($CH_3C(O)O_2$), came about because of their important role in radical termination processes, especially in their reactions with $HO_2$ (Equation 6.2a) – when Equations 6.2b and 6.2c were unknown. These reactions were shown to inhibit the generation of $O_3$ and OH by causing a disruption to the $HO_x$ cycle. They also were found to produce organic hydrogen peroxides (ROOH, Equation 6.2b) and peracids ($RC(O)OOH$, Equation 6.2a). The reaction between $CH_3C(O)O_2$ and $HO_2$ has been studied previously with well-established yields for the radical terminating products – the peracid and $O_3$ (Niki et al. 1985; Moortgat, Veyret, and Lesclaux 1989; Horie and Moortgat 1992; Crawford et al. 1999; Tomas, Villenave, and Lesclaux 2001).
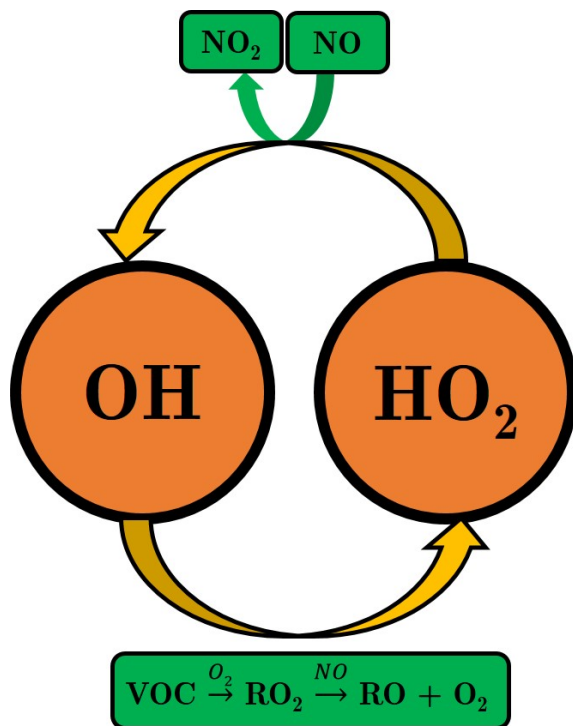
Figure 6.1: The $HO_x$ cycle which occurs in the atmosphere, converting OH to $HO_2$ and vice versa.

$$CH_3C(O)O_2 + HO_2 \rightarrow CH_3C(O)O_2H + O_2 \qquad (6.2a)$$

$$\rightarrow CH_3C(O)OH + O_3 \qquad (6.2b)$$

$$\rightarrow CH_3C(O)O + O_2 + OH \qquad (6.2c)$$
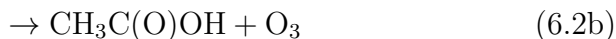
All four of these previous studies report ratios between the peracid pathway and the $O_3$ pathway to be about $0.75 : 0.25$. Three different techniques were used to obtain this ratio: Moortgat, Veyret, and Lesclaux (1989), and Tomas, Villenave, and Lesclaux (2001) fitted a kinetic model for the recorded data of $[CH_3C(O)O_2]$ from flash photolysis; Horie and Moortgat (1992) carried out a FTIR study to determine the branching ratio; whereas Niki et al. (1985) used FTIR to determine product yields. Crawford et al. (1999) carried out a flash photolysis and FTIR smog chamber study to calculate a branching ratio and a rate coefficient; however, this is the only study which presents substantially different results from the previous literature

with a branching ratio of less than half of the previous literature values and a rate coefficient 2-3 times larger than previously reported values.

It was only recently, when ozone production rates were examined in the Nashville urban plume by Thornton et al. (2002), that it was indicated that these reactions may not exclusively terminate radical chemistry. This was first suggested to explain the differences observed for the rate coefficient of $RC(O)O_2 + HO_2$ to the previous literature values.

Hasson, Tyndall, and Orlando (2004) were first to propose an OH product yield (0.4 ± 0.16) for $CH_3C(O)O_2 + HO_2$ by indirect product product analysis. Considering the amount of OH produced in the reaction, the authors noted how this OH generation may have caused a serious underestimation of the rate coefficient seen by Thornton et al. (2002). The OH product yield was calculated by FTIR and HPLC end-product analysis.

In contrast, a study by LeCrâne et al. (2006) agreed with the original thinking: the majority of the reaction of $CH_3C(O)O_2 + HO_2$ proceeds via a radical termination process with the yield of OH being less than 0.1. This, however, was followed by a FTIR study using end product analysis by Jenkin, Hurley, and Wallington (2007). Jenkin et al. (2007) obtained a OH product yield of (0.43 ± 0.1), in excellent agreement with the study of Hasson, Tyndall, and Orlando (2004). The difference between these studies highlights the effect that the different methods have on investigating the OH yield. Le Crane et al. (2006) used two complementary approaches: one experimental and one theoretical. The theoretical approach used quantum chemistry calculations performed using the density functional theory (DFT) method with the three-parameter hybrid functional B3LYP associated with the 6-31G(d,p) basis set. The results from these calculations differ from the results from the study of Hasson et al. (2005) that calculated the energies of all the structures using the CBS-QB3 method, which has a higher accuracy than the method used by Le Crane et al. (2006). The experimental technique used by Le

Crane et al. (2006) was flash photolysis combined with UV absorption, using the hydroxycyclohexadienyl radical ($HOC_6H_6$) which is formed when high concentrations of benzene were added to the system to scavenge OH radicals. $HOC_6H_6$ absorbs strongly at 290 nm, ideal for absorption spectroscopy; however, the irreversible reaction of $HOC_6H_6 + O_2$ would have been a major loss process and since there was no discussion on how this was controlled, it was concluded that this could have be the origin of their discrepancy with the OH yield.

To eliminate this discrepancy in the literature, i.e. how much OH is produced in the reaction of $CH_3C(O)O_2 + HO_2$, Dillon and Crowley (2008) utilised the technique of pulsed laser photolysis coupled with calibrated laser induced fluorescence to directly detect OH as a product. This gave the OH product yield to be (0.5 $\pm$ 0.2). This increase in the OH yield when compared with the previous literature studies is attributed to previous studies using indirect techniques rather than the direct technique used here.

More recent studies were also able to combine the direct technique of recording the OH fluorescence along with monitoring the concentrations of radical precursors. Gross, Dillon, Schuster, et al. (2014) used a combination of LIF which allowed the time-resolved OH concentration measurement and transient absorption spectroscopy (TAS) to determine the initial concentration of the reactant peroxy radicals, e.g. the $HO_2$ radical. This study gave the OH product yield to be (0.61 $\pm$ 0.09), with the increase of the OH yield being due to the higher accuracy; both the OH and $HO_2$ concentrations were able to be monitored, thus reducing the errors in the OH yield calculation. It also gave the first results for the reaction of $CH_3C(O)O_2 + DO_2$: the yield for the OH producing channel increasing to (0.80 $\pm$ 0.14) when $DO_2$ was used.

The most recent study on the $CH_3C(O)O_2 + HO_2$ reaction by Winiberg et al. (2016) combined the advantages of the previous chamber studies (e.g. Jenkin, Hurley, and Wallington (2007)) and the direct OH detection experiments (e.g. Dillon and Crowley (2008)). Their experiments were carried out in the HIRAC simulation

chamber at Leeds University where it was possible to detect products from all three branching pathways simultaneously. FAGE (Fluorescence Assay by Gas Expansion) could detect both OH and $HO_2$ radicals, which combined with FTIR, gas chromatography and an $O_3$ analyser offered unprecedented, detailed coverage of all the key species. Radical precursors, such as $HO_2$, were analysed alongside secondary products which further constrained the system. This study gave the OH yield to be $(0.51 \pm 0.12)$.

It is possible to illustrate the effect of changing to a direct method on the investigation of the $CH_3C(O)O_2 + HO_2$ by examining the rate coefficients given by previous literature studies, Table 6.1. The more recent studies on $CH_3C(O)O_2 + HO_2$ which use direct methods to study the OH radical, show that the rate coefficient is faster than first thought.

Table 6.1: A comparison of the rate coefficients for the reaction $CH_3C(O)O_2 + HO_2$ found in the literature, alongside the technique each study used.

| Literature | Analytical Technique | Cl Rate Coefficients / $10^{-11}$ cm$^3$ molecule$^{-1}$ s$^{-1}$ |
|---|---|---|
| Moorgat et al. (1989) | Flash photolysis UV absorption | $1.4 \pm 0.12$ |
| Crawford et al. (1999) | FTIR | $3.62 \pm 0.5$ |
| Tomas et al. (2001) | Flash photolysis UV absorption | $1.42 \pm 0.07$ |
| Le Crane et al. (2005) | Flash photolysis UV absorption | $1.5 \pm 0.08$ |
| Dillon et al. (2008) | PLP-LIF | $1.4 \pm 0.5$ |
| Gross et al. (2014) | FTIR, LIF | $2.1 \pm 0.4$ |
| Winiberg et al. (2016) | FTIR, FAGE GC-FID | $2.4 \pm 0.4$ |

## 6.2    Experimental

Three $RC(O)O_2$ + $HO_2$ reactions, where R = $CH_3$, $C_2H_5$, and $(CH_3)_2CHCH_2$ (Equations 6.2, 6.3 and 6.4), were investigated with the results analysed in this chapter. The majority of the data collection occurred at two different pressures (100 and 200 Torr) and at a temperature of 293 K, but some preliminary high-temperature experiments and results are also discussed in this chapter.

$$C_2H_5C(O)O_2 + HO_2 \rightarrow OH + Products \tag{6.3}$$

$$(CH_3)_2CHCH_2C(O)O_2 + HO_2 \rightarrow OH + Products \tag{6.4}$$
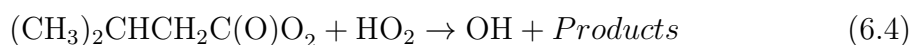
Radical generation was again initiated by the photolysis of $Cl_2$ at 355 nm, similar to the experiments investigating the RCO + $O_2$ reaction. The Cl radicals react with $CH_3OH$ to generate $CH_2OH$ and HCl (Equation 6.5), the $CH_2OH$ radicals formed go on to react with $O_2$ to form HCHO and the $HO_2$ radicals - critical for this experiment (Equation 6.6).

$$CH_3OH + Cl \rightarrow CH_2OH + HCl \tag{6.5}$$

$$CH_2OH + O_2 \rightarrow HO_2 + HCHO \tag{6.6}$$

$$CH_2OH + Cl_2 \rightarrow ClCH_2OH + Cl \tag{6.7}$$
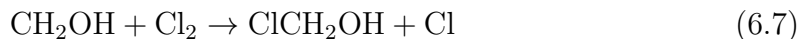
An excess of $CH_3OH$ and $O_2$ was used in the cell to reduce the unwanted secondary radical chemistry from Equations 6.7, 6.8a and 6.8b by helping drive the reaction of $CH_2OH$ reacting with $O_2$ rather than $Cl_2$. It also increases the amount of $CH_3OH$ reacting with Cl radicals rather than Cl + $HO_2$. The excess of these species allow assumptions of the kinetics to take place, resulting in the simplification of the system's kinetics.

$$Cl + HO_2 \rightarrow HCl + O_2 \tag{6.8a}$$

$$\rightarrow ClO + OH \tag{6.8b}$$

## 6.3 Calibration Reactions and Preliminary Experiments

To allow the conversion of fluorescence intensities into absolute [OH], PLP-LIF experiments were run back-to-back with a calibration reaction. There was no need for a calibration reaction for the previous RCO + $O_2$ experiments (Chapter 3), as a direct comparison was used to convert OH yields from the well-known $CH_3CO$ + $O_2$ to unknown RCO + $O_2$. For the studies of $RC(O)O_2$ + $HO_2$ two calibration methods were used: one was an external calibration (NO + $HO_2$ - Equation 6.9), and the other an internal calibration ($CH_3C(O)O_2$ + $HO_2$).

$$HO_2 + NO \rightarrow OH + NO_2 \tag{6.9}$$

There were advantages and disadvantages for both types of calibrations due to the different reactions they use. The NO + $HO_2$ reaction is a major reaction found in the atmosphere, therefore numerous studies have recorded the rate coefficient for this reaction. The earliest review to examine this reaction was Atkinson, Baulch, Cox, Hampson, et al. (1989) who gave the rate coefficient to be $(8.29 \pm 1.20) \times 10^{-12}$ $cm^3$ molecule$^{-1}$ s$^{-1}$, and the most recent review by Atkinson et al. (2004) gave it to be $(8.91 \pm 0.45) \times 10^{-12}$ $cm^3$ molecule$^{-1}$ s$^{-1}$, giving only a small difference in the rate between the two reviews. This illustrates how well constrained and understood this reaction is, which is the opposite of the $CH_3C(O)O_2$ + $HO_2$ reaction. For the latter there has been a literature discrepancy, with its rate coefficient and the branching ratios of its products, discussed in the previous section. It is a suitable

calibration reaction as the yield of OH is known to be close to unity (98.4%) and conveniently the rate coefficient is $(8.5 \pm 0.45) \times 10^{-12}$ cm$^3$ molecule$^{-1}$ s$^{-1}$ (Atkinson et al. 2004). This rate coefficient for HO$_2$ + NO is similar to other RO$_2$ + HO$_2$ reactions, for example the rate coefficient for CH$_3$C(O)O$_2$ + HO$_2$ is $(2.4 \pm 0.4) \times$ $10^{-11}$ cm$^3$ molecule$^{-1}$ s$^{-1}$ (Winiberg et al. 2016). Another advantage for the NO + HO$_2$ reaction is that it is a simpler system than the CH$_3$C(O)O$_2$ + HO$_2$ reaction: there is only one radical precursor to form the HO$_2$, whereas in the CH$_3$C(O)O$_2$ + HO$_2$ reaction the CH$_3$C(O)O$_2$ also needs to be formed. This means that the kinetics of the system for NO + HO$_2$ would be easier to model with less secondary radical reactions occurring. Theses two advantages give strong support to using the NO + HO$_2$ reaction for a calibration.

However, the NO + HO$_2$ kinetics are different to the RC(O)O$_2$ + HO$_2$ reactions that are studied here, notably with the OH taking longer to decay in the NO + HO$_2$ traces. This is mostly due to different types of species the OH signal. In the RC(O)O$_2$ + HO$_2$ reactions, the concentration of the RCHO precursor is larger than the [NO] as it is the concentrations of RC(O)O$_2$ and NO which are kept similar, so the difference in OH yields can be directly compared. This causes the higher [RCHO] to decay the OH away at a faster rate than the NO calibration reaction. This disadvantage of the NO + HO$_2$ is an advantage for using the CH$_3$C(O)O$_2$ + HO$_2$ reaction as a calibration.

This is because all RC(O)O$_2$ + HO$_2$ reactions seem to follow a similar kinetic profile, therefore it could be more accurate and reliable to use an internal calibration of CH$_3$C(O)O$_2$ + HO$_2$ when investigating other RC(O)O$_2$ + HO$_2$ reactions. The advantages for both calibration reactions meant that both reactions were used at first to determine which performed better in this experimental set-up.
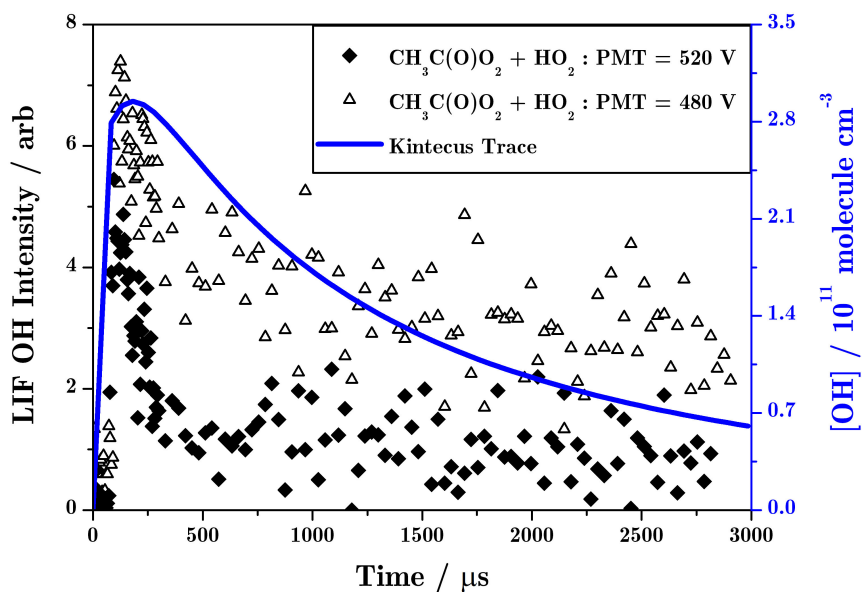
Figure 6.2: Two experimental traces at 100 Torr with different PMT settings (520 V = black diamonds, and 480 V = triangles) from the reaction of $CH_3C(O)O_2 + HO_2$ alongside the Kintecus model (blue line). The concentrations (in molecule $cm^{-3}$): $[CH_3CHO] = 2.7 \times 10^{14}$, $[CH_3OH] = 1.9 \times 10^{15}$, $[O_2] = 3.2 \times 10^{17}$, $[Cl_2] = 1.5 \times 10^{15}$, and $[Cl] \times 3 \times 10^{13}$.
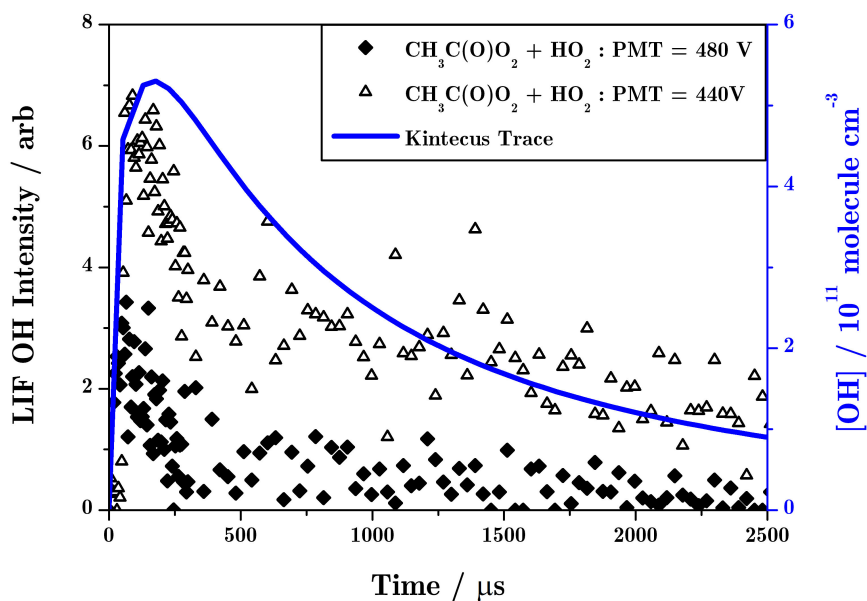


Figure 6.3: Two experimental traces at 100 Torr with different PMT settings (480 V = black diamonds, and 440 V = triangles) from the reaction of $CH_3C(O)O_2 + HO_2$ alongside the Kintecus model (blue line). The concentrations (in molecule $cm^{-3}$): $[CH_3CHO] = 2.7 \times 10^{14}$, $[CH_3OH] = 1.9 \times 10^{15}$, $[O_2] = 3.2 \times 10^{17}$, $[Cl_2] = 2.2 \times 10^{15}$, $[Cl] \times 4 \times 10^{13}$.

The first preliminary experiments solely tested out the ability to record the OH from the two different reactions and to examine the difference between the data and the relevant Kintecus outputs. The first batch of results from these experiments displayed an effect due to the PMT. Figures 6.2 and 6.3 show this effect: when the PMT voltage is altered, it affects the shape of the OH decay even when all other conditions are constant. Figures 6.2 and 6.3 show experimental data at the same conditions (100 Torr; concentrations in molecule cm$^{-3}$: $[CH_3CHO] = 2.7 \times 10^{14}$, $[CH_3OH] = 1.9 \times 10^{15}$, $[O_2] = 3.2 \times 10^{17}$). The concentrations (molecule cm$^{-3}$) of $Cl_2$, and therefore $[Cl]$, were altered so for Figure 6.2 $[Cl_2] = 1.5 \times 10^{15}$ ($[Cl] \times 3 \times 10^{13}$) and for Figure 6.3 $[Cl_2] = 2.2 \times 10^{15}$ ($[Cl] = 4 \times 10^{13}$). The conclusion from these results was that this effect could be due to alteration of the LabVIEW programme making it harder to determine when the PMT is being overloaded with fluorescence. To combat this problem an oscilloscope was set up alongside the PicoScope, which allowed the LIF signal to be examined in greater detail during an experimental run. This meant that for the future experiments it was certain that the PMT was not overloaded, avoiding the problem seen in Figures 6.2 and 6.3.

After fixing this problem, the first preliminary experiments were carried out on the NO + $HO_2$ calibration reaction – Figures 6.4 and 6.5 display the results of these experiments. Small flows of NO were added to the $Cl_2$, $CH_3OH$, $N_2$ and $O_2$ photolysis mixture to generate well-characterised amounts of OH. A Kintecus model was created for the NO + $HO_2$ reaction; the rate coefficients and reactions used are found in Table 6.2. To test the new model, the concentration of NO was varied to confirm that the Kintecus model was able to constrain the OH production from reaction 6.9 correctly.
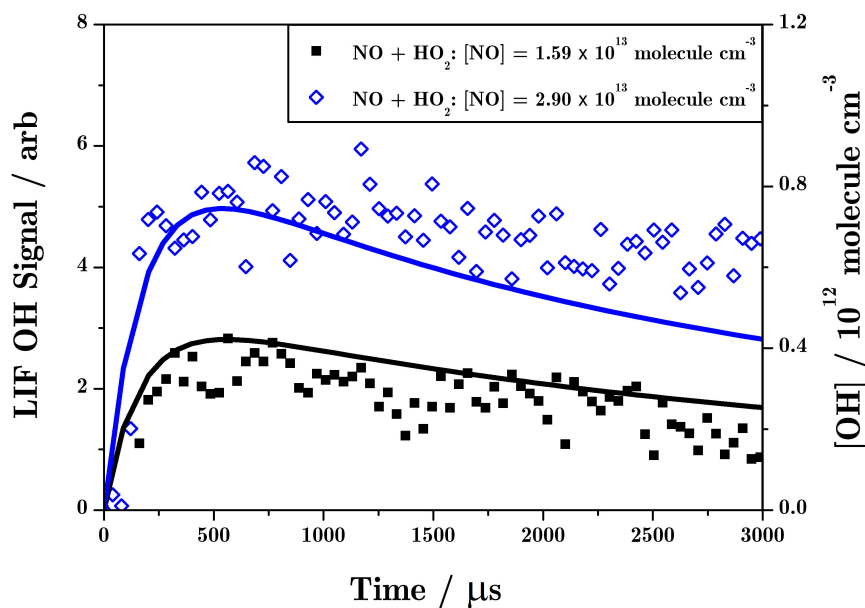
Figure 6.4: Experimental data from the NO + HO$_2$ reaction at two different [NO] (in molecule cm$^{-3}$): blue diamonds = $1.58 \times 10^{13}$; black squares = $2.90 \times 10^{13}$ ; lines represent the Kintecus fits. The concentrations (in molecule cm$^{-3}$) of the other species were kept constant: [Cl$_2$] = $1.9 \times 10^{15}$, [Cl] $\times 2 \times 10^{13}$, [CH$_3$OH] = $3.4 \times 10^{15}$, [O$_2$] = $5.0 \times 10^{16}$ .
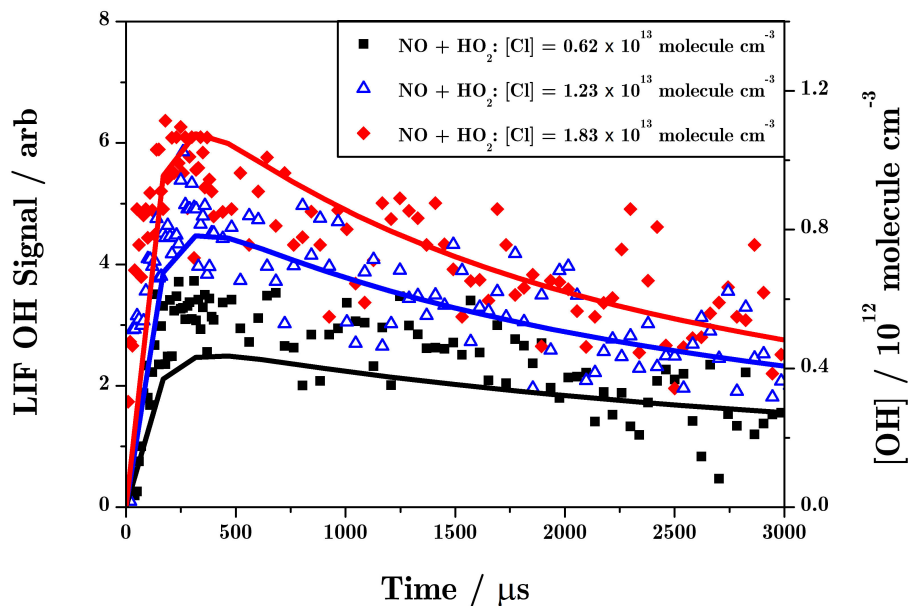


Figure 6.5: Experimental data from the NO + HO$_2$ reaction at three different [Cl] (in molecule cm$^{-3}$): red diamonds $\times 2 \times 10^{13}$; blue triangles $\times 1 \times 10^{13}$; black squares $\times 6 \times 10^{12}$ ; lines represent the Kintecus fits. The concentrations (in molecule cm$^{-3}$) of the other species were kept constant: [NO] = $8.5 \times 10^{13}$; [CH$_3$OH] = $8.8 \times 10^{15}$; [O$_2$] = $7.3 \times 10^{16}$.

Figure 6.4 displays some of the results from changing the [NO]; the experimental results at two different concentrations ($1.58 \times 10^{13}$ and $2.90 \times 10^{13}$ molecule cm$^{-3}$) are shown alongside the equivalent Kintecus traces. The concentrations (in molecule cm$^{-3}$) of the other species were kept constant: $[Cl_2] = 1.9 \times 10^{15}$; $[Cl] \times 2 \times 10^{13}$; $[CH_3OH] = 3.4 \times 10^{15}$; $[O_2] = 5.0 \times 10^{16}$. The result, shown in Figure 6.4, is that the Kintecus model follows well with the experimental results but deviates slightly with the later decay of OH. This effect was greater with the higher [NO] and therefore the explanation of this deviation could be the increase of OH in the system making the kinetics more complicated.

The experimental results at three different concentrations of Cl ($2 \times 10^{13}$, $1 \times 10^{13}$, and $6 \times 10^{12}$ molecule cm$^{-3}$) are shown alongside the equivalent Kintecus traces - Figure 6.5. The concentrations (in molecule cm$^{-3}$) of the other species were kept constant while the [Cl] was altered: $[NO] = 8.5 \times 10^{13}$; $[CH_3OH] = 8.8 \times 10^{15}$; $[O_2] = 7.3 \times 10^{16}$. There is some deviation again between the experimental results and the Kintecus traces but overall the Kintecus traces match with the experimental data for both set of reactions.

Figure 6.6 shows an example of a Kintecus run, displaying the change in the concentrations of OH, NO, HO$_2$, and Cl over time of 0 - 50 $\mu$s. It clearly shows that the Cl initiates the OH production, with the [Cl] falling sharply at the start. The other compound which has a concentration at time zero is NO, however, NO reacts away much slower than Cl. As it was important to have [NO] > [HO$_2$] to make sure that the majority of HO$_2$ reacts with NO, the change in the concentration of [NO] in Figure 6.6 is small in comparison to the total [NO] and therefore the decrease in the concentration cannot be seen in the plot. OH and HO$_2$ are formed by radical reactions initiated by Cl and therefore do not intercept the $y$-axis. The plot clearly shows the relationship between the [OH] and [HO$_2$]: both rising at similar rates. This is expected since the reaction of NO + HO$_2$ forms OH. If the plot was zoomed out, the concentrations of NO and HO$_2$ would decrease at similar rates with OH increasing.
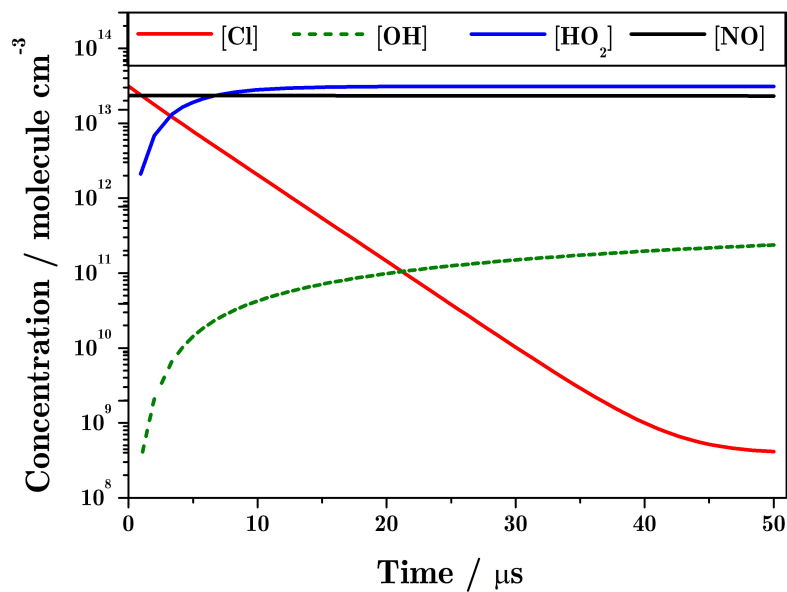
Figure 6.6: Plot of how the concentration of Cl, OH, $HO_2$, and NO changes over time produced by the NO + $HO_2$ Kintecus model (Ianni 2017).

The system broadly characterised the OH from NO + $HO_2$ but clearly some of the radical - radical reactions are difficult to quantify accurately and reliably, due to the uncertainties in the two lasers (power and drift from 282 nm).

Table 6.2: The reactions with their associated rate coefficients (in $cm^3$ molecule$^{-1}$ s$^{-1}$) at 298 K that were included in the NO + HO$_2$ Kintecus model.

| Reaction | Literature | Rate Coefficients |
|---|---|---|
| ***NO$_x$ Reactions*** | | |
| NO + HO$_2$ → OH + NO$_2$ | Atkinson et al. (2004) | $8.64 \times 10^{-12}$ |
| NO + OH → HONO | Atkinson et al. (2004) | $3.32 \times 10^{-11}$ |
| NO$_2$ + OH → HONO$_2$ | Atkinson et al. (2004) | $3.00 \times 10^{-11}$ |
| NO$_2$ + OH → HONO$_2$ | Atkinson et al. (2004) | $3.50 \times 10^{-11}$ |
| HONO + OH → H$_2$O + NO$_2$ | Atkinson et al. (2004) | $6.05 \times 10^{-12}$ |
| NO + CH$_3$O → CH$_3$ONO | Atkinson (1997) | $3.60 \times 10^{-11}$ |
| NO$_2$ + CH$_3$O → HCHO + HONO | Atkinson et al. (1989) | $3.01 \times 10^{-13}$ |
| HOCH$_2$O + NO → HOCH$_2$ONO | Veyret et al. (1982) | $4.00 \times 10^{-11}$ |
| HOCH$_2$O$_2$ + NO → HOCH$_2$O + NO$_2$ | Veyret et al. (1982) | $5.60 \times 10^{-12}$ |
| ClO + NO → Cl + NO$_2$ | Atkinson et al. (2004) | $1.69 \times 10^{-11}$ |
| ***CH$_3$OH Reactions*** | | |
| CH$_3$OH + Cl → CH$_2$OH + HCl | Atkinson et al. (2006) | $5.50 \times 10^{-11}$ |
| CH$_3$OH + OH → CH$_2$OH + H$_2$O | Atkinson et al. (2006) | $7.50 \times 10^{-13}$ |
| CH$_3$OH + OH → CH$_3$O + HCl | Atkinson et al. (2006) | $1.32 \times 10^{-13}$ |
| CH$_2$OH + O$_2$ → HCHO + HO$_2$ | Atkinson et al. (2006) | $9.31 \times 10^{-12}$ |
| CH$_3$O + O$_2$ → HCHO + HO$_2$ | Atkinson et al. (2006) | $1.83 \times 10^{-15}$ |
| HCHO + OH → HCO + H$_2$O | Atkinson et al. (2006) | $8.54 \times 10^{-12}$ |
| HCO + O$_2$ → HO$_2$ + CO | Atkinson et al. (2006) | $5.20 \times 10^{-12}$ |
| HCHO + HO$_2$ → HCCH$_2$O$_2$ | Atkinson et al. (2006) | $8.12 \times 10^{-14}$ |
| HCCH$_2$O$_2$ → HCHO + HO$_2$ | Atkinson et al. (2006) | $1.12 \times 10^{-21}$ |
| HOCH$_2$O + O$_2$ → HC(O)OH + HO$_2$ | Veyret et al. (1982) | $3.5 \times 10^{-14}$ |
| ***HO$_x$ Reactions*** | | |
| HO$_2$ + HO$_2$ → H$_2$O$_2$ + O$_2$ | Atkinson et al. (2004) | $2.04 \times 10^{-12}$ |
| OH + HO$_2$ → H$_2$O + O$_2$ | Atkinson et al. (2004) | $1.12 \times 10^{-10}$ |
| OH + H$_2$O$_2$ → H$_2$O + HO$_2$ | Atkinson et al. (2004) | $1.68 \times 10^{-12}$ |
| OH + OH → H$_2$O$_2$ | Atkinson et al. (2004) | $5.48 \times 10^{-12}$ |
| OH + OH → O + H$_2$O | Atkinson et al. (2004) | $1.49 \times 10^{-12}$ |
| O + HO$_2$ → OH + O$_2$ | Atkinson et al. (2004) | $5.78 \times 10^{-11}$ |
| OH + O$_3$ → HO$_2$ + O$_2$ | Atkinson et al. (2004) | $4.10 \times 10^{-14}$ |
| O$_3$ + HO$_2$ → OH + 2O$_2$ | Atkinson et al. (2004) | $1.96 \times 10^{-15}$ |
| ***ClO$_x$ Reactions*** | | |
| Cl$_2$ + OH → HOCl + Cl | Atkinson et al. (2007) | $6.10 \times 10^{-14}$ |
| HCl + OH → H$_2$O + Cl | Atkinson et al. (2007) | $7.52 \times 10^{-13}$ |
| Cl + HO$_2$ → HCl + O$_2$ | Atkinson et al. (2007) | $3.49 \times 10^{-11}$ |
| Cl + HO$_2$ → ClO + OH | Atkinson et al. (2007) | $9.10 \times 10^{-12}$ |
| ClO + OH → Cl + HO$_2$ | Atkinson et al. (2007) | $1.90 \times 10^{-11}$ |
| ClO + OH → HCl + O$_2$ | Atkinson et al. (2007) | $1.21 \times 10^{-12}$ |
| ClO + HO$_2$ → HOCl + O$_2$ | Atkinson et al. (2007) | $6.99 \times 10^{-12}$ |

*Notes:* Literature used: Atkinson et al. (2004) Atkinson (1997), Atkinson et al. (2006), Atkinson, Baulch, Cox, Crowley, Hampson, Hynes, Jenkin, Kerr, et al. (2007), and Veyret, Rayez, and Lesclaux (1982).

## 6.4 Acetyl Peroxyl with Hydroperoxyl Radicals

As mentioned previously, the $CH_3C(O)O_2$ + $HO_2$ has been well characterised and therefore it is used here to test the apparatus to confirm that it is possible to obtain accurate results in this set up. As previously alluded to, the Kintecus software (Ianni 2017) played a critical role in the analysis, with two models being created: a simple and a more complex version. The $HO_x$ and the $ClO_x$ reactions, shown in Table 6.2, which were used in the NO + $HO_2$ Kintecus model, were included in these models. Table 6.3 displays the $CH_3CHO$ and $CH_3C(O)O_2$ reactions that were included at first for the simpler $CH_3C(O)O_2$ + $HO_2$ model.

Table 6.3: The reactions with their associated rate coefficients (units: $cm^3$ $molecule^{-1}$ $s^{-1}$) at 298 K that were included in the first Kintecus model of $CH_3C(O)O_2$ + $HO_2$.

| Reaction | Literature | Rate Coefficients |
|---|---|---|
| **$CH_3CHO$ Reactions** | | |
| $CH_3CHO + Cl \rightarrow CH_3CO + HCl$ | Atkinson et al. (2006) | $8.00 \times 10^{-11}$ |
| $CH_3CHO + OH \rightarrow CH_3CO + H_2O$ | Atkinson et al. (2006) | $1.47 \times 10^{-11}$ |
| $CH_3CHO + OH \rightarrow CH_2CHO + H_2O$ | Atkinson et al. (2006) | $7.72 \times 10^{-13}$ |
| $CH_3CO + O_2 \rightarrow CH_3C(O)O_2$ | Gross et al. (2014) | $9.70 \times 10^{-12}$ |
| $CH_3CO + O_2 \rightarrow OH + product$ | Gross et al. (2014) | $3.00 \times 10^{-13}$ |
| $CH_3CO + Cl_2 \rightarrow CH_3COCl + Cl$ | Tyndall et al. (1999) | $4.30 \times 10^{-11}$ |
| **$CH_3C(O)O_2$ Reactions** | | |
| $CH_3C(O)O_2 + HO_2 \rightarrow$ $CH_3C(O)O + O_2 + OH$ | Winiberg et al. (2016) | $5.20 \times 10^{-12}$ |
| $CH_3C(O)O_2 + HO_2 \rightarrow$ $CH_3C(O)O_2H + O_2$ | Winiberg et al. (2016) | $8.12 \times 10^{-14}$ |
| $CH_3C(O)O_2 + HO_2 \rightarrow$ $CH_3C(O)OH + O_3$ | Winiberg et al. (2016) | $1.12 \times 10^{-21}$ |
| $2CH_3C(O)O_2 \rightarrow$ $2CH_3C(O)O + O_2$ | Atkinson et al. (2007) | $3.5 \times 10^{-14}$ |

*Notes:* Reactions used along with the $HO_x$ and $ClO_x$ reactions, shown in Table 6.2 for the NO + $HO_2$ Kintecus model (Ianni 2017). Literature from: Atkinson et al. (2006), Gross, Dillon, Schuster, et al. (2014), Tyndall et al. (1999), and Atkinson, Baulch, Cox, Crowley, Hampson, Hynes, Jenkin, Kerr, et al. (2007).

Figure 6.7 shows an example of a Kintecus run, displaying the change in the concentrations of OH, $CH_3C(O)O_2$, $HO_2$, and Cl over time. Similar to the NO + $HO_2$ reaction, it is clearly shown that the Cl initiates the OH production, with the [Cl] falling sharply at the start of the time. There is a close link between the $[CH_3C(O)O_2]$, $[HO_2]$, and [OH] which is expected since OH is formed by $HO_2$ + $CH_3C(O)O_2$.

To examine the effect that the secondary reactions have on the OH production, a second Kintecus model was created – the more 'complex' model. Table 6.4 contains the reactions that were added to the model along with their associated rate coefficients. To display the difference that this causes in the model, Figure 6.8 displays a trace from both models using the same concentrations of all the species - the black dashed lines represent the equivalent species form the simple model. Though a slight difference is expected between the two Kintecus models, the concentrations of the species used in the experiments (and applied in these Kintecus models) mean that the difference is negligible - shown in Figure 6.8. This is important for future experiments on unknown $RC(O)O_2$ + $HO_2$ as the larger compounds do not have the rate coefficients for the equivalent reactions listed in Table 6.4.
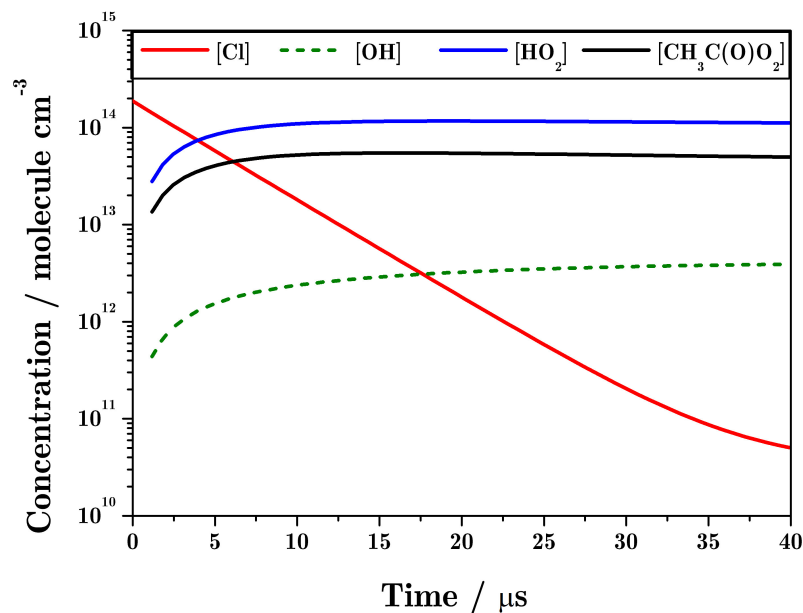
Figure 6.7: Plot of how the concentration of Cl, OH, HO$_2$, and CH$_3$C(O)O$_2$ changes over the time of 0 - 40$\mu$s produced by the simple CH$_3$C(O)O$_2$ + HO$_2$ Kintecus model (Ianni 2017).
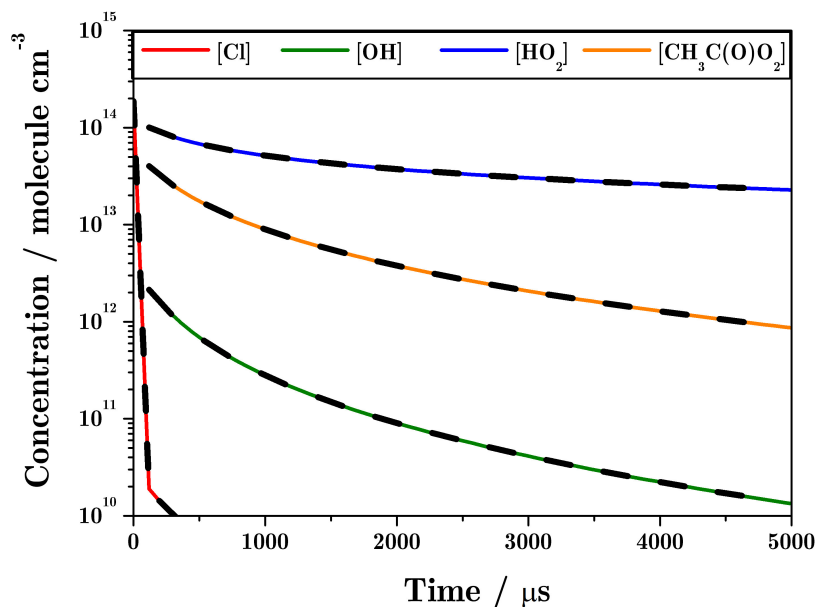


Figure 6.8: Plot of the concentrations of Cl, OH, HO$_2$, and CH$_3$C(O)O$_2$ from the two different CH$_3$C(O)O$_2$ + HO$_2$ Kintecus models - the simple model is shown in dotted lines (Ianni 2017).

Table 6.4: The reactions with their associated rate coefficients (units: $cm^3$ molecule$^{-1}$ s$^{-1}$) at 298 K that were included in the second more complex Kintecus model for $CH_3C(O)O_2 + HO_2$(Ianni 2017).

| Reaction | Literature | Rate Coefficients |
|---|---|---|
| **$CH_3CHO$ Reactions** | | |
| $CH_2CHO + Cl_2 \rightarrow$ $CH_3C(O)Cl + Cl$ | Morajkar et al. (2014) | $9.00 \times 10^{-11}$ |
| $2CH_2CHO \rightarrow$ $CH_3C(O)C(O)CH_3$ | Morajkar et al. (2014) | $1.81 \times 10^{-11}$ |
| $CH_3CHO + HO_2 \rightarrow$ $CH_3CH(OH)O_2$ | Morajkar et al. (2014) | $1.50 \times 10^{-14}$ |
| $CH_3 + Cl_2 \rightarrow$ $CH_3Cl + Cl$ | Eskola et al. (2008) | $1.55 \times 10^{-12}$ |
| $CH_3 + O_2 \rightarrow CH_3O_2$ | DeMore et al. (1997) | $4.49 \times 10^{-31}$ |
| **$CH_3C(O)O_2$ Reactions** | | |
| $CH_3O_2 + HO_2 \rightarrow$ $CH_3O_2H + O_2$ | Atkinson et al. (2007) | $5.17 \times 10^{-11}$ |
| $CH_3O_2 + HO_2 \rightarrow$ $HCHO + H_2O + O_2$ | Atkinson et al. (2007) | $5.72 \times 10^{-11}$ |
| $HOCH_2O_2 + HO_2 \rightarrow$ $HOCH_2O + OH + O_2$ | Atkinson et al. (2007) | $2.87 \times 10^{-12}$ |
| $HOCH_2O_2 + HO_2 \rightarrow$ $HOCH_2O_2H + O_2$ | Atkinson et al. (2007) | $7.18 \times 10^{-12}$ |
| $HOCH_2O_2 + HO_2 \rightarrow$ $HC(O)OH + H_2O + O_2$ | Atkinson et al. (2007) | $4.31 \times 10^{-12}$ |
| $2CH_3O_2 \rightarrow$ $CH_3OH + HCHO + O_2$ | Atkinson et al. (2007) | $2.21 \times 10^{-13}$ |
| $2HOCH_2O_2 \rightarrow$ $HC(O)OH + CH_2(OH)_2 + O_2$ | Atkinson et al. (2007) | $7.37 \times 10^{-13}$ |
| $2HOCH_2O_2 \rightarrow$ $2HOCH_2O + O_2$ | Atkinson et al. (2007) | $5.50 \times 10^{-12}$ |
| $CH_3C(O)O_2 + CH_3O_2 \rightarrow$ $CH_3C(O)O + CH_3O + O_2$ | Atkinson et al. (2007) | $9.92 \times 10^{-12}$ |
| $CH_3C(O)O_2 + CH_3O_2 \rightarrow$ $H_3C(O)OH + HCHO + O_2$ | Atkinson et al. (2007) | $1.10 \times 10^{-12}$ |
| $2CH_3O_2 \rightarrow 2CH_3O + O_2$ | Atkinson et al. (2007) | $1.37 \times 10^{-13}$ |

*Notes:* Used along with reactions found in Table 6.3 and the $HO_x$ and $ClO_x$ reactions, shown in Table 6.2 from the NO + $HO_2$ Kintecus model (Ianni 2017). Literature from: Atkinson, Baulch, Cox, Crowley, Hampson, Hynes, Jenkin, Kerr, et al. (2007), Morajkar et al. (2014), Eskola et al. (2008), and Demore et al. (1997).

## 6.4.1 OH LIF Excitation Spectra

A LIF Excitation Spectrum, Figure 6.9, confirmed that the signal seen in previous experiments (Figures 3 -4) was OH. Similar conditions were applied to the experiment as used for the collection of data for the previous kinetic traces, with the pressure at 100 Torr and the concentrations of the species (in molecule cm$^{-3}$): $[CH_3CHO] = 2.8 \times 10^{14}$, $[Cl_2] = 3.6 \times 10^{15}$, $[Cl] \approx 6 \times 10^{13}$, $[N_2] = 2.8 \times 10^{18}$, $[CH_3OH] = 1.0 \times 10^{15}$, and $[O_2] = 3.2 \times 10^{17}$. The time delay between the photolysis and probe laser was kept constant at 500 $\mu$s. The data from Figure 6.9 show the fluorescence to be OH, with the experimental data following the simulated data from LIFBASE well (Luque and Crosley 1999). The largest difference between the two data sets is the peak broadening seen in the experimental data which has been discussed previously in Chapter 3.
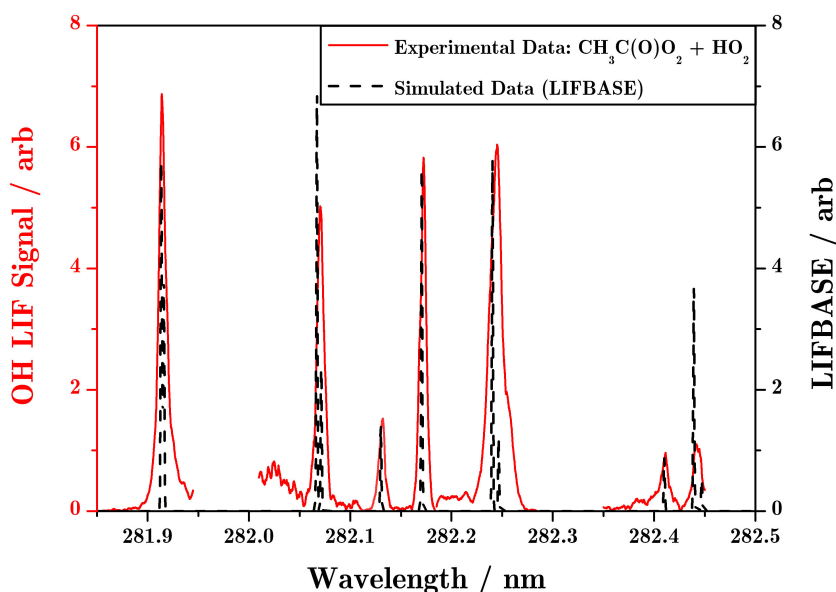


Figure 6.9: LIF Excitation Spectra of $CH_3C(O)O_2 + HO_2$ (red line) at 100 Torr with the concentrations (in molecule cm$^{-3}$): $[CH_3CHO] = 2.8 \times 10^{14}$, $[Cl_2] = 3.6 \times 10^{15}$, $[Cl] \approx 6 \times 0^{13}$, $[N_2] = 2.8 \times 10^{18}$, $[CH_3OH] = 1.0 \times 10^{15}$ and $[O_2] = 3.2 \times 10^{17}$; simulated data from LIFBASE (black dashed line) (Luque and Crosley 1999).

## 6.4.2   Determination of OH Yield

To determine the OH yield of the $CH_3C(O)O_2$ + $HO_2$ reaction, the experimental data of the back-to-back reactions (with NO + $HO_2$) was plotted alongside Kintecus traces, seen in Figure 6.10; summary of the concentrations used in these experiments is found in Table 6.5. Since the NO + $HO_2$ was reasonably well characterised, the $y$-axis on the graph was constrained to the fit of the Kintecus trace to the experimental data. The Kintecus model for $CH_3C(O)O_2$ + $HO_2$ was then run at various values for the OH yield, with the results added on the graph to determine which trace fits best with the experimental data.
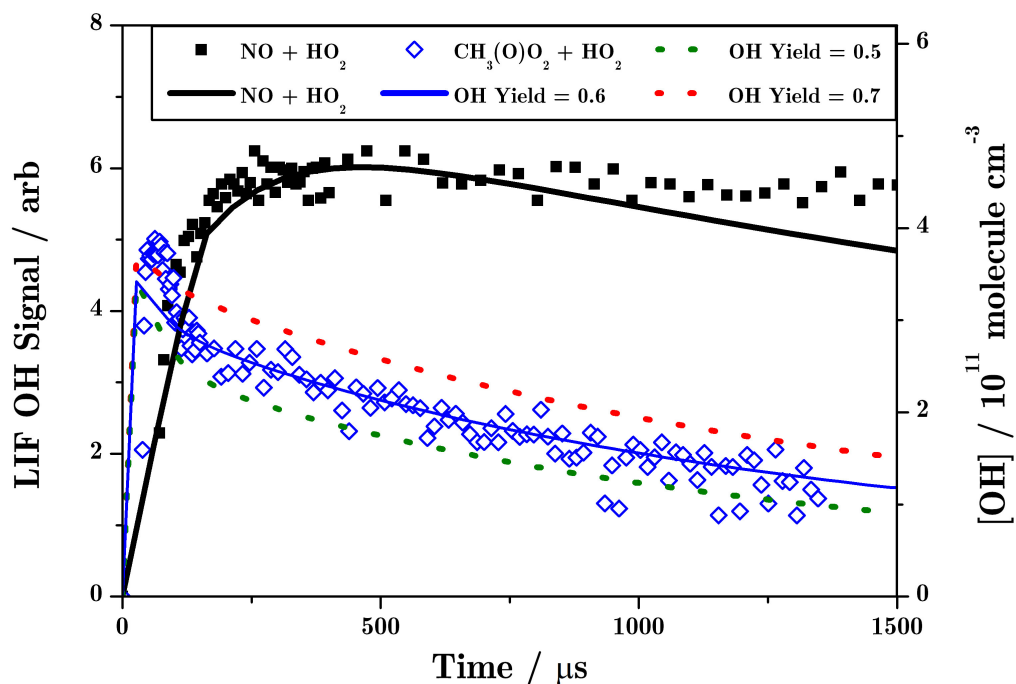


Figure 6.10: Experimental traces at 100 Torr of $CH_3C(O)O_2$ + $HO_2$ (blue diamonds) and NO + $HO_2$ (black squares, Kintecus in the black line). Three Kintecus traces indicating different OH yields of $CH_3C(O)O_2$ + $HO_2$ are shown: 0.7 = red dotted line; 0.6 = blue line; 0.5 = green dotted line (Ianni 2017). The concentrations of the species are found in Table 6.5.

Table 6.5: Summary of the concentrations used for each species from the investigation of the OH yield from the reaction of $CH_3C(O)O_2 + HO_2$ at 294 K when using $NO + HO_2$ calibration reaction.

| Concentration/ | Reaction | |
|---|---|---|
| molecule $cm^{-3}$ | $CH_3C(O)O_2 + HO_2$ | $NO + HO_2$ |
| $N_2$ | $2.6 \times 10^{18}$ | $2.8 \times 10^{18}$ |
| $O_2$ | $2.7 \times 10^{17}$ | $2.8 \times 10^{17}$ |
| $CH_3CHO$ | $9.1 \times 10^{14}$ | N/A |
| NO | N/A | $3.1 \times 10^{14}$ |
| $CH_3OH$ | $3.9 \times 10^{15}$ | $4.1 \times 10^{15}$ |
| $Cl_2$ | $3.3 \times 10^{15}$ | $3.0 \times 10^{15}$ |
| Cl | $5 \times 10^{13}$ | $4 \times 10^{13}$ |

Figure 6.10 displays the $CH_3C(O)O_2 + HO_2$ experimental data fitting best with the Kintecus trace using the OH yield of 0.6, as a comparison the traces of a OH yield of 0.7 and 0.5 are also shown (Ianni 2017). The experimental data clearly falls on the Kintecus trace which relates to $CH_3C(O)O_2 + HO_2$ having a OH yield of (0.6 ± 0.1) which is in line with previous literature (Dillon and Crowley 2008; Gross, Dillon, Schuster, et al. 2014; Winiberg et al. 2016).

Previous literature has shown this reaction to show no pressure dependence, especially in the pressure range that this apparatus works at (Dillon and Crowley 2008; Gross, Dillon, Schuster, et al. 2014). However, two preliminary data sets were collected at higher pressure (200 Torr) with Figure 6.11 showing the back-to-back experiment between $CH_3C(O)O_2 + HO_2$ and $NO + HO_2$. The $CH_3C(O)O_2 + HO_2$ Kintecus model has an OH yield of 0.6, which follows the experimental data reasonably well except for the middle portion of the trace ($400 - 800$ $\mu s$). However, this deviation could be due to the secondary OH production that is mentioned in Chapter 5 and which has not yet been fully determined, and therefore is not included in the Kintecus model. A quick comparison between the results at 100 Torr (Figure 6.10) and 200 Torr (Figure 6.11) showed that this rough analysis gave the OH yield for $CH_3C(O)O_2 + HO_2$ to be the same at both pressures ($\approx 0.6$).
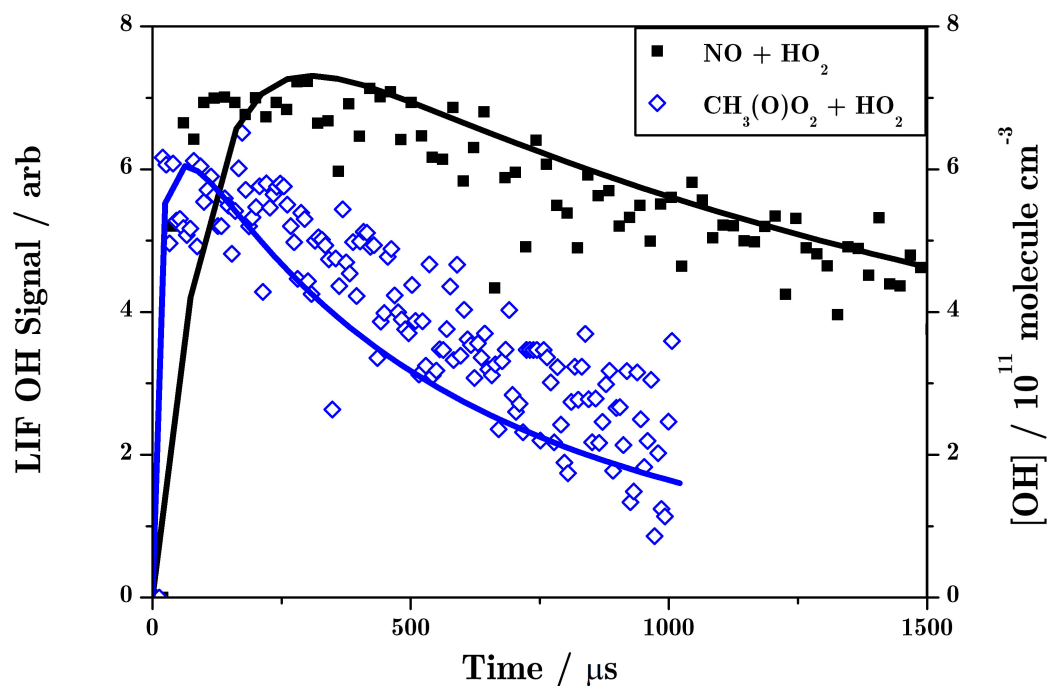
Figure 6.11: Experimental trace at 200 Torr of $CH_3C(O)O_2 + HO_2$ (blue diamonds, Kintecus trace with 0.6 OH yield: blue line) and $NO + HO_2$ (black squares, Kintecus in the black line) (Ianni 2017). The concentrations (in molecule $cm^{-3}$) were $[Cl] \approx 5 \times 10^{13}$ and $[CH_3OH] = 3.9 \times 10^{15}$ for both reactions with $[CH_3CHO] = 6.9 \times 10^{14}$ and $[NO] = 4.3 \times 10^{14}$.

At different concentrations the yield fluctuated due to a changeable noise signal, which gave a range of 0.5 - 0.6 for the OH yield. Therefore the preferred value for the OH yield from the reaction of $CH_3C(O)O_2 + HO_2$ was calculated to be $(0.55 \pm 0.2)$.

### 6.4.3 Temperature

This section examines the effect that an increase in temperature has on results from back-to-back experiments for the reactions of $NO + HO_2$ and $CH_3C(O)O_2 + HO_2$ at 100 Torr. A heating tape was utilised to run experiments between the temperatures 293 and 410 K – explained further in Chapter 2. The data shown and discussed here are from just two temperatures: 326 and 395 K, as they are able show an overall trend – results from other temperatures experiments are found in Appendix D. The concentrations of the species used at 326 and 395 K were kept very similar, and are found in Table 6.6.

Table 6.6: The concentrations of the species in the experiments run at 326 K and 395 K.

| Concentration / molecule cm$^{-3}$ | | | | | | |
|---|---|---|---|---|---|---|
| $O_2$ | $Cl_2$ | $CH_3CHO$ | $CH_3OH$ | $NO$ | $RC(O)O_2$ | $Cl$ |
| $3.0 \times 10^{18}$ | $3.5 \times 10^{15}$ | $3.7 \times 10^{14}$ | $2.5 \times 10^{15}$ | $1.3 \times 10^{14}$ | $1.2 \times 10^{13}$ | $5 \times 10^{13}$ |

Figure 6.12 displays the results from the two reactions at 326 K, which shows a resemblance with the results at 293 K (Figure 6.10). Similar to the results at 293 K, the conversion between the OH LIF signal and the concentration of OH was achieved by the calibration of the $NO + HO_2$ using the Kintecus model. This then allowed the OH yield of $CH_3C(O)O_2 + HO_2$ to be analysed; for this analysis it was assumed that the rate coefficient for the reaction of $CH_3C(O)O_2 + HO_2$ stayed constant when the temperature was increased, or only a small negligible change occurred. If temperature does affect the rate coefficient it would mostly likely cause the rate coefficient to occur faster; but since it is a rapid reaction already at room temperature, it was assumed that this difference would not have a large impact. The assumption was that any difference in the rate coefficient would be overshadowed by any changes in the OH yield. When other similar rate coefficients whose temperature dependence was known were examined (for example $NO + HO_2$), the effect that

temperature has is shown to be small, e.g. for $NO + HO_2$ in the temperature range of 295 to 400 K the range of the rate coefficient is: $8.5 \times 10^{-12} - 6.8 \times 10^{-12}$ cm$^3$ molecule$^{-1}$ s$^{-1}$ (Atkinson et al. 2004). The rate coefficient used in the Kintecus model for $CH_3C(O)O_2 + HO_2$ was kept at $2.4 \times 10^{-11}$ cm$^3$ molecule$^{-1}$ s$^{-1}$ as per Winiberg et al. (2016), which is the most recent study of this rate coefficient and is in line with previous literature values (Gross et al. 2014).

Table 6.7 displays the reactions that were included in the higher temperature Kintecus model – the values were taken from the same literature as referenced in Tables 6.2, 6.3, and 6.4. The reactions are shown in a colour code in Table 6.7 with the reactions in black indicating reactions whose rate coefficients are unknown for the temperature range studied, whilst the green represents known temperature rate coefficients. As shown, numerous rate coefficients have not been measured at high temperature, adding to the unknown chemistry that the Kintecus model is unable to constrain. It also increases the uncertainty of the analysis and therefore it is not possible to give results quantitatively, as there are too many unknowns.

Table 6.7: Reactions that were included in the higher temperature Kintecus model for both $NO + HO_2$ and $CH_3C(O)O_2 + HO_2$ reactions - black indicates reactions whose rate coefficients are not known for the temperatures studied; green represents known temperature rate coefficients.

| Reactions | | | | |
|---|---|---|---|---|
| **CH$_3$OH** | **HO$_x$** | **ClO$_x$** | **CH$_3$CHO / CH$_3$C(O)O$_2$** | **NO** |
| CH$_3$OH + Cl | HO$_2$ + HO$_2$ | Cl$_2$ + OH | CH$_3$CHO + Cl | NO + HO$_2$ |
| CH$_3$OH + OH | OH+ HO$_2$ | HCl +OH | CH$_3$CHO + OH | NO$_2$ + OH |
| CH$_2$OH + O$_2$ | H$_2$O$_2$ + OH | Cl+ HO$_2$ | CH$_3$CO + O$_2$ | HONO + OH |
| CH$_3$O + O$_2$ | OH+ OH | ClO + OH | CH$_3$CO + Cl$_2$ | NO + CH$_3$O |
| CH$_2$OH + Cl$_2$ | HO$_2$ + O | ClO + HO$_2$ | CH$_3$O$_2$ + HO$_2$ | NO$_2$ + CH$_3$O |
| HCHO + OH | O$_3$ + OH | | 2CH$_3$O$_2$ | HOCH$_2$O+NO |
| CHO + O$_2$ | O$_3$ + HO$_2$ | | 2CH$_3$C(O)O$_2$ | HOCH$_2$O$_2$+NO |
| HOCH$_2$O$_2$ | | | CH$_3$C(O)O$_2$+HO$_2$ | ClO + NO |
| HOCH$_2$O + O$_2$ | | | CH$_3$C(O)O$_2$+CH$_3$O$_2$ | |
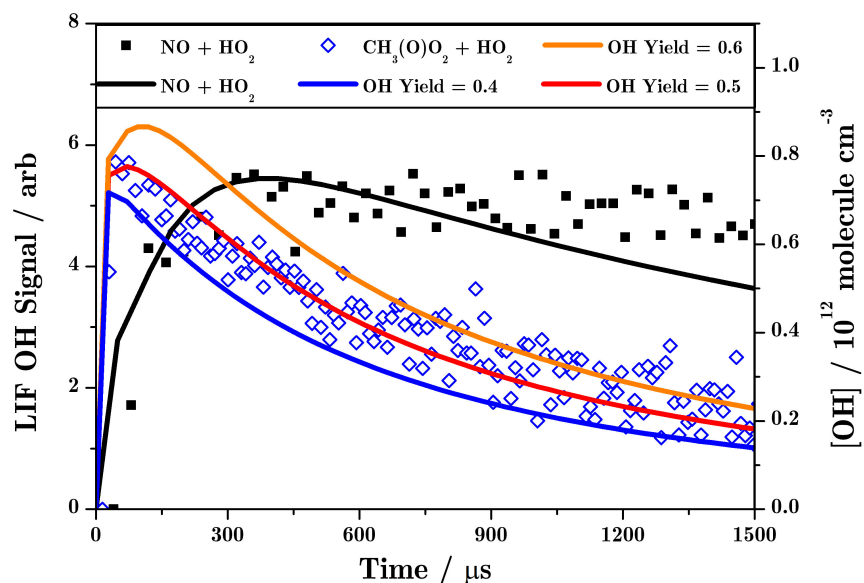
Figure 6.12: Kinetic traces of $CH_3C(O)O_2 + HO_2$ (blue diamonds) and $NO + HO_2$ (black squares) at 100 Torr and a temperature of 326 K. The concentrations of the species in the experimental run are found in Table 6.6 and these are used for the Kintecus traces (straight lines).
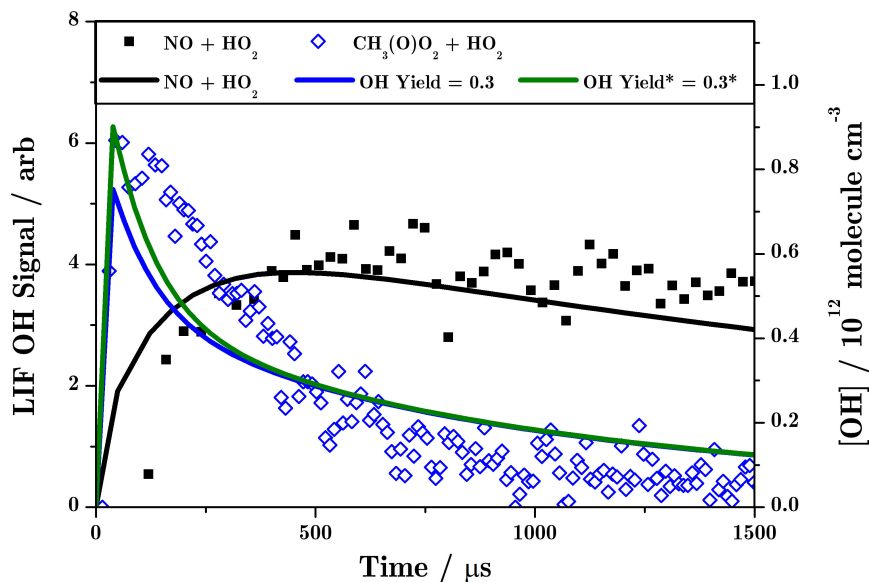


Figure 6.13: Kinetic traces of $CH_3C(O)O_2 + HO_2$ (blue diamonds) and $NO + HO_2$ (black squares) at 100 Torr and a temperature of 395 K. The concentrations of the species in the experimental run are found in Table 6.6 and these are used for the Kintecus traces (straight lines), the green line is a trace where the OH yield for $CH_3CO + O_2$ has been altered from 0.03 to 0.06.

At 293 K the OH yield for $CH_3C(O)O_2 + HO_2$ was shown to be $(0.55 \pm 0.20)$, which was modelled to the data from 326 K (Figure 6.12). The results show that the OH decay at 326 K fits best when the Kintecus model gives a OH yield of 0.5, which is a slight decrease from the result at 293 K. This provides an indication that the OH yield decreases at higher temperature; however, as the errors of the results are so large this drop in the OH yield is not considered significant enough to indicate any temperature dependence. When the temperature is increased further to 395 K (Figure 6.13), the change in the OH decay profile for the reaction $CH_3C(O)O_2 + HO_2$ changes substantially, causing the traces that form the Kintecus model to fit poorly (red, orange and blue lines). From preliminary experiments on the $CH_3CO + O_2$ reaction at high temperature (Chapter 3) it was suggested that the yield of this reaction increases with temperature. These results were collected at 100 Torr where the OH yield from $CH_3CO + O_2$ is approximately 0.03 (Gross, Dillon, and Crowley 2014). If this yield is increased to 0.06 (green line in Figure 6.13) this alters the Kintecus model to produce a larger amount of OH at the shorter time-scale which improves the Kintecus and experimental data overlap.

Looking at the data qualitatively it is clear that the OH yield for the $CH_3C(O)O_2 + HO_2$ reaction increases when the temperature is increased. The shape of the OH decay changed substantially when the temperature increased from 326 K to 395 K, decaying faster at higher temperatures. This change can occur from either the OH decay reactions occurring at a faster rate at a higher temperature or from a lower OH yield. It is mostly likely to be due to both. These preliminary experiments indicate that the OH yield from $CH_3CO + O_2$ changes substantially at higher temperatures and needs to be examined in great detail in order for the OH yield from $CH_3C(O)O_2 + HO_2$ to be calculated at high temperatures. These results also show that the OH yield decreases when the temperature increases for the $CH_3C(O)O_2 + HO_2$ reaction.

## 6.5 Other Peroxy Radicals with Hydroperoxyl Radicals

Once the technique of the apparatus and analysis had been proven to work for the reaction of $CH_3C(O)O_2$ + $HO_2$, two other $RC(O)O_2$ + $HO_2$ reactions were investigated $C_2H_5C(O)O_2$ + $HO_2$ (Equation 6.3) and $(CH_3)_2CHCH_2C(O)O_2$ + $HO_2$ (Equation 6.4), with their OH yield being examined at both room and higher temperatures. The last part of this section will discuss the results from the preliminary reactions of $(CH_3)_2CHC(O)O_2$ + $HO_2$, $(CH_3)_3CHC(O)O_2$ + $HO_2$, and $C_2H_5CH(CH_3)$ $C(O)O_2$ + $HO_2$ which were recorded alongside $CH_3C(O)O_2$ + $HO_2$ traces at room temperature.

As alluded to in the previous sections, the accuracy of the Kintecus models is of paramount importance for the analysis if OH yields are to be determined using the technique shown in previous section when analysing the results of $CH_3C(O)O_2$ + $HO_2$. The analysis of the OH yield from $(CH_3)_2CHCH_2C(O)O_2$ + $HO_2$ was only possible due to the recent results shown and discussed in Chapter 4. The rate coefficients discussed in Chapter 4 showed that previously the reaction of $(CH_3)_2CHCH_2CHO$ + Cl (Equation 6.10) had no previous literature value and therefore would have made the Kintecus model for this reaction contain too many uncertainties. The rate coefficient was determined to be $(3.1 \pm 0.6) \times 10^{-10}$ $cm^3$ $molecule^{-1}$ $s^{-1}$.

$$(CH_3)_2CHCH_2CHO + Cl \rightarrow (CH_3)_2CHCH_2CO + HCl \qquad (6.10)$$
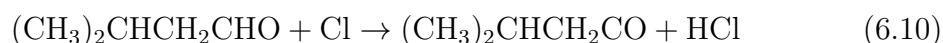
## 6.5.1   OH LIF Excitation Spectra

To confirm that OH is produced from $C_2H_5C(O)O_2$ + $HO_2$ and $(CH_2)_2CHCH_2C(O)O_2$ + $HO_2$, LIF Excitation Spectra were recorded – Figures 6.14 and 6.15. The time delay between the photolysis and probe laser was 500 $\mu$s, with the conditions for both set of reactions kept similar at 100 Torr. The data from Figures 6.14 and 6.15 show that OH is produced from these reactions – the first time this OH production has been seen from these reactions.

## 6.5.2   Room-Temperature Traces

Experiments were carried out similar to the ones previously with $CH_3C(O)O_2$ + $HO_2$ but this time analysing the difference between the OH yield of $CH_3C(O)O_2$ + $HO_2$, $C_2H_5C(O)O_2$ + $HO_2$, and $(CH_2)_2CHCH_2C(O)O_2$ + $HO_2$. Figure 6.16 displays the data alongside Kintecus traces with the conversion between LIF OH intensity to OH concentration calculated by the NO + $HO_2$ calibration reaction at 100 Torr. The $CH_3C(O)O_2$ + $HO_2$ data agreed with the Kintecus model when a OH yield of 0.5 was used. Qualitatively it was possible to recognise that the reaction of $C_2H_5C(O)O_2$ + $HO_2$ gave a similar amount of OH to $CH_3C(O)O_2$ + $HO_2$; however, the reaction of $(CH_2)_2CHCH_2C(O)O_2$ + $HO_2$ produced substantially less OH that the other two reactions. It was possible to compare the results like this due to the conditions being kept similar throughout the runs, with the range of concentrations (in molecule cm$^{-3}$) of : $RC(O)O_2$ = 1.5 - 1.9 $\times$ 10$^{13}$; $HO_2$ = 4.1 - 4.5 $\times$ 10$^{13}$; $CH_3OH$ = 1.3 $\times$ 10$^{15}$; $O_2$ = 3.3 $\times$ 10$^{17}$. The Kintecus traces displayed in Figure 6.16 are all of the $CH_3C(O)O_2$ + $HO_2$ but with different OH yields to estimate a value for the $C_2H_5C(O)O_2$ + $HO_2$ and $(CH_2)_2CHCH_2C(O)O_2$ + $HO_2$ OH yields to be 0.7 and 0.1 respectively. This estimate for the OH yield for $(CH_2)_2CHCH_2C(O)O_2$ + $HO_2$ holds true for other data sets, for example Figure 6.17; however, for $C_2H_5C(O)O_2$ + $HO_2$ there are large discrepancies in the data. This was evident in Figures 6.16
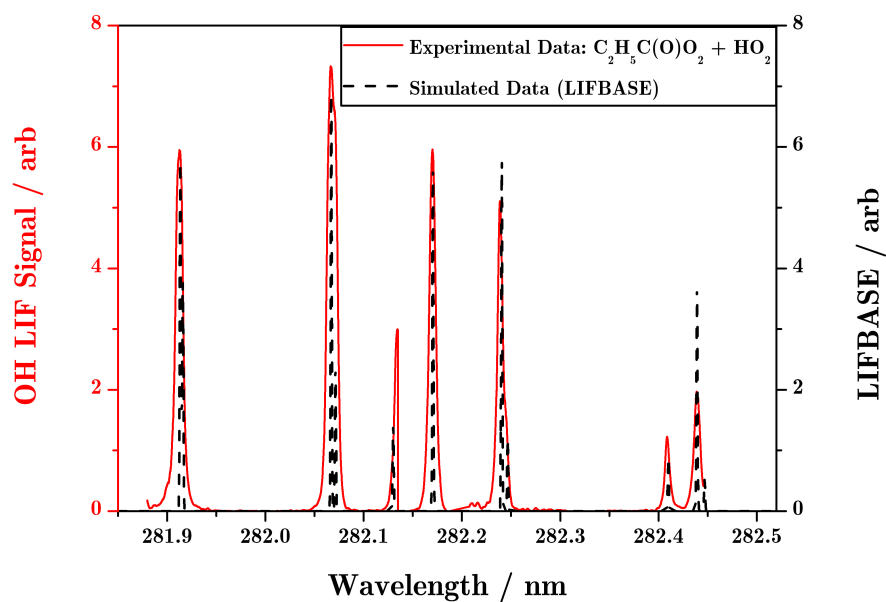
Figure 6.14: LIF Excitation Spectra of $C_2H_5C(O)O_2$ + $HO_2$ at 100 Torr with concentrations (molecule cm$^{-3}$) of $C_2H_5CHO = 1.6 \times 10^{14}$, $Cl_2 = 3.8 \times 10^{15}$, $Cl \approx 7 \times 10^{13}$, $N_2 = 2.9 \times 10^{18}$, $CH_3OH = 1.0 \times 10^{15}$, and $O_2 = 2.9 \times 10^{17}$.
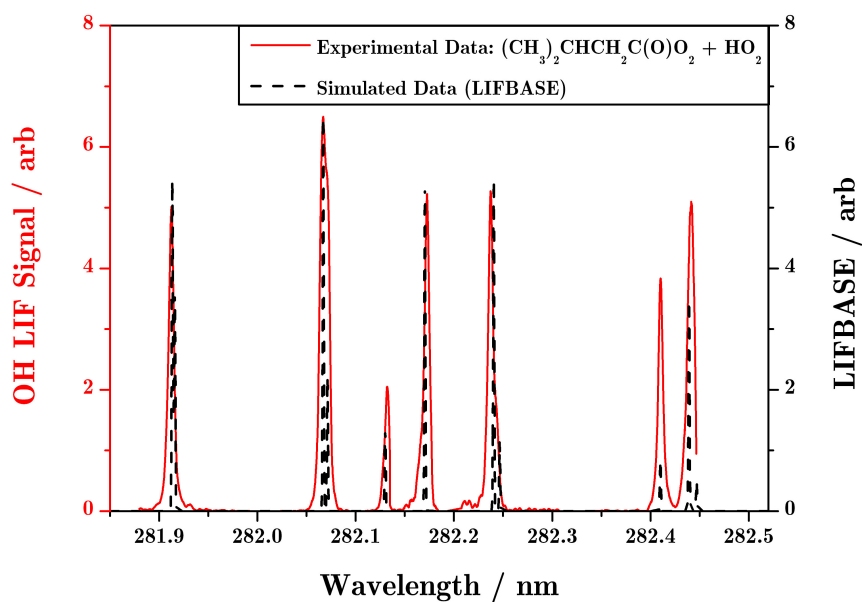


Figure 6.15: LIF Excitation Spectra of $(CH_3)_2CHCH_2C(O)O_2$ + $HO_2$ at 100 Torr with concentrations (molecule cm$^{-3}$) of $(CH_3)_2CHCH_2CHO = 1.6 \times 10^{14}$, $Cl_2 = 3.8 \times 10^{15}$, $Cl \approx 7 \times 10^{13}$, $N_2 = 2.9 \times 10^{18}$, $CH_3OH = 1.0 \times 10^{15}$, and $O_2 = 2.9 \times 10^{17}$.
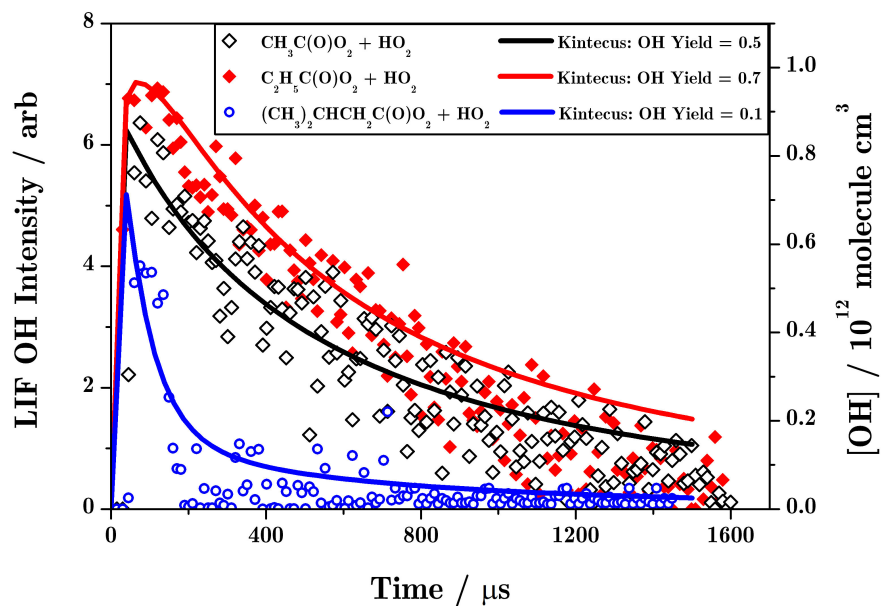
Figure 6.16: Kinetic traces of $CH_3C(O)O_2$ + $HO_2$ (black diamonds), $C_2H_5C(O)O_2$ + $HO_2$ (red diamonds), and $(CH_3)_2CHCH_2C(O)O_2$ + $HO_2$ (blue circles) at 100 Torr and a temperature of 293 K. Kintecus traces (straight lines).
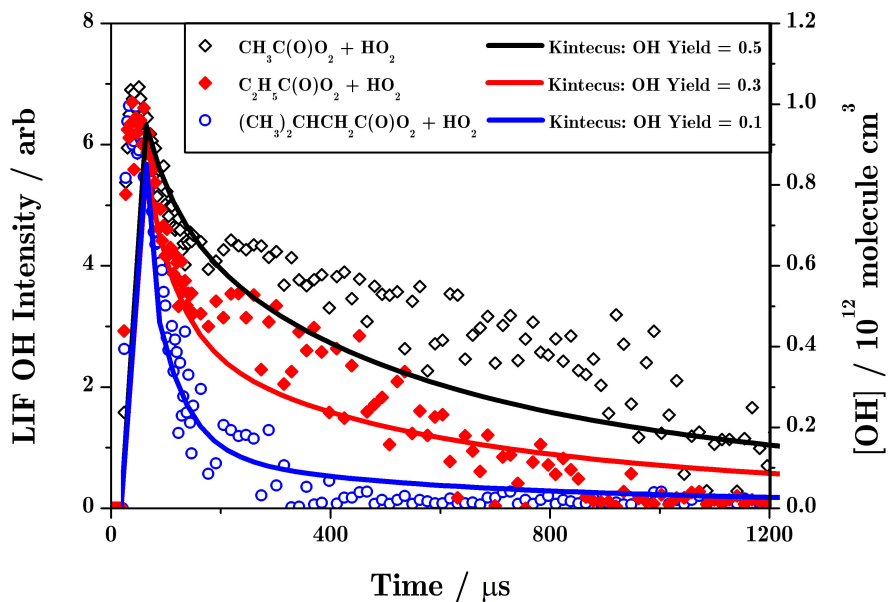


Figure 6.17: Kinetic traces of $CH_3C(O)O_2$ + $HO_2$ (black diamonds), $C_2H_5C(O)O_2$ + $HO_2$ (red diamonds), and $(CH_3)_2CHCH_2C(O)O_2$ + $HO_2$ (blue circles) at 100 Torr and a temperature of 293 K. Kintecus Traces shown as lines, colours matching the data points.

and 6.17 where the OH yield for $C_2H_5C(O)O_2 + HO_2$ was shown to be both higher and lower than $CH_3C(O)O_2 + HO_2$. The concentration of $C_2H_5C(O)O_2$ was found to be partly responsible for this large range of the OH yield for $C_2H_5C(O)O_2 + HO_2$ - estimated from 0.3 to 0.7. The higher $[C_2H_5C(O)O_2]$ gave a larger OH yield, shown in Figure 6.17 (where $[C_2H_5C(O)O_2] = 3.2 \times 10^{13}$ molecule $cm^{-3}$) whereas the results shown in Figure 6.16 are when $[C_2H_5C(O)O_2] = 1.5 \times 10^{13}$ molecule $cm^{-3}$. This indicated that the system that was modelled in Kintecus, was a simplified version of what was actually happening in the reactor cell.

### 6.5.3   High-Temperature Traces

Similarly to the previous section, back-to-back experiments were carried out on $NO + HO_2$, $CH_3C(O)O_2 + HO_2$, $C_2H_5C(O)O_2 + HO_2$ and $(CH_2)_2CHCH_2C(O)O_2 + HO_2$ at temperatures between 293 and 400 K. Figures 6.18 and 6.19 display the results from two of these experiments (326 and 395 K) to show the trend that temperature seems to have on the OH yields of these reactions. Here the three types of $RC(O)O_2 + HO_2$ are compared to each other; the $NO + HO_2$ traces have not been included in the figures for clarity but they were used to calibrate the OH LIF intensity to OH concentration.

The data at 326 K (Figure 6.18) showed similar trends to what was seen at room temperature (Figure 6.16 and 6.17) with the $CH_3C(O)O_2 + HO_2$ and $C_2H_5C(O)O_2 + HO_2$ data overlapping. They seem to have a similar OH yield at approximately $0.5 \pm 0.1$, which was a slight decrease and was in line with the previous results at this temperature. However, $(CH_2)_2CHCH_2C(O)O_2 + HO_2$ shows the opposite trend; comparing the room temperature and 326 K results it is possible to see that the amount of OH produced from the $(CH_2)_2CHCH_2C(O)O_2 + HO_2$ reaction has increased substantially in comparison with the other $RC(O)O_2 + HO_2$ reaction.

Figure 6.19 displays the data from the experiment at 395 K, showing the substantial effect that temperature has on the OH yield of $(CH_2)_2CHCH_2C(O)O_2 + HO_2$. The
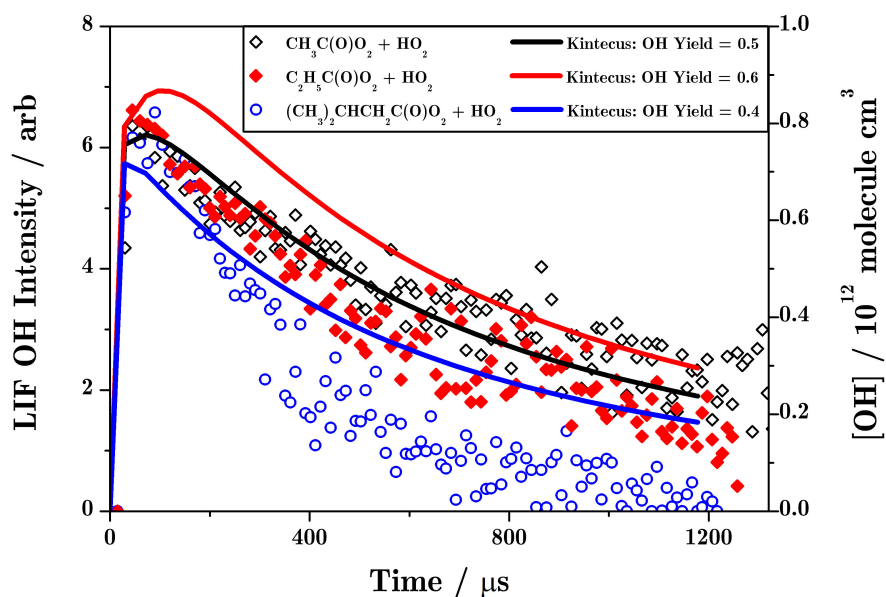
Figure 6.18: Kinetic traces of $CH_3C(O)O_2$ + $HO_2$ (black diamonds), $C_2H_5C(O)O_2$ + $HO_2$ (red diamonds) and $(CH_3)_2CHCH_2C(O)O_2$ + $HO_2$ (blue circles) at 100 Torr and a temperature of 326 K. The straight lines represent Kintecus traces of $CH_3C(O)O_2$ + $HO_2$.
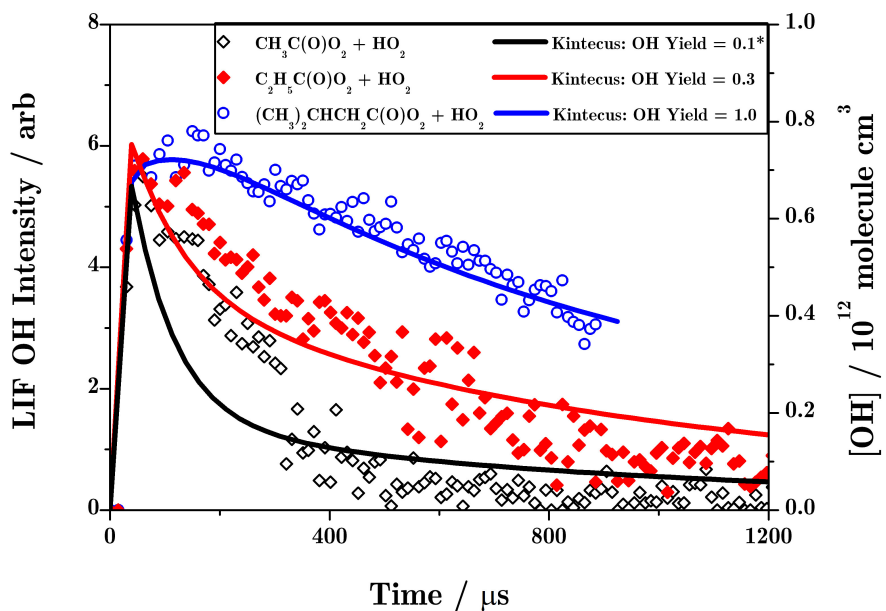


Figure 6.19: Kinetic traces of $CH_3C(O)O_2$ + $HO_2$ (black diamonds), $C_2H_5C(O)O_2$ + $HO_2$ (red diamonds) and $(CH_3)_2CHCH_2C(O)O_2$ + $HO_2$ (blue circles) at 100 Torr and a temperature of 395 K. The straight lines represent Kintecus traces of $CH_3C(O)O_2$ + $HO_2$, with the black line the yield of the $CH_3CO$ + $O_2$ reaction being doubled to 0.06 to fit.

comparison between Figures 6.18 and 6.19 indicates how much the OH yield for $(CH_2)_2CHCH_2C(O)O_2$ + $HO_2$ increased with an increase in temperature - only when the yield was set to 1.0 the Kintecus model able to get close to the experimental data. This, however, was the opposite trend than the other two $RC(O)O_2$ + $HO_2$ reactions, which are both shown to decrease with increasing temperature, with $CH_3C(O)O_2$ + $HO_2$ decreasing at a faster rate than $C_2H_5C(O)O_2$ + $HO_2$. A reason for this difference could be due to the ability of the $RC(O)O_2$ being able to stabilise the intermediate better with a larger molecule at higher temperatures therefore making the pathway to the OH yield more favourable.

### 6.5.4   Preliminary Results on other Peroxys

Figure 6.20 displays the preliminary results of the reactions: $(CH_3)_2CHC(O)O_2 +$ $HO_2$, $(CH_3)_3CHC(O)O_2 + HO_2$, and $C_2H_5CH(CH_3)C(O)O_2 + HO_2$ which were run alongside $CH_3C(O)O_2 + HO_2$ traces at room temperature. The LabVIEW data collection programme was altered slightly from before to examine the baseline parameter hidden deep in the code. It is easy to see the improvement that this has given to the data when Figure 6.20 is compared to Figures 6.16 and 6.17. Unfortunately, due to time constraints, it was not possible to repeat the past experiments with this new changed parameter to improve the accuracy of the results. However, future experiments will be able to make use of the improvement in the code to obtain more reliable and accurate results.

These results show that for the reaction of $RC(O)O_2 + HO_2$ there is OH production regardless of the chain length or branching in the chain. They indicate that OH yields for the three larger $RC(O)O_2$ are very similar but are all smaller than the OH yield from $CH_3C(O)O_2 + HO_2$. Out of the three larger $RC(O)O_2 + HO_2$ reactions shown here, Figure 6.20 shows that OH decays slower for $(CH_3)_2CHC(O)O_2$ than for $(CH_3)_3CHC(O)O_2$ and $C_2H_5CH(CH_3)C(O)O_2$. This could suggest that $(CH_3)_2CH$ $C(O)O_2 + HO_2$ produces more OH than the other two reactions, as the OH decay is mostly constrained by the reaction of the parent aldehyde with $OH - (CH_3)_2CHCHO$, $(CH_3)_3CHCHO$, and $C_2H_5CH(CH_3)CHO$ with OH have similar rate coefficients.

Figure 6.21 shows the results of $CH_3C(O)O_2 + HO_2$ and $(CH_3)_2CHC(O)O_2 + HO_2$ along with Kintecus traces to estimate the OH yields. The Kintecus model, which gave a OH yield of $(0.6 \pm 0.2)$ for the reaction of $CH_3C(O)O_2 + HO_2$, internally calibrates the system allowing rough a Kintecus model to predict a OH yield of $(0.3 \pm 0.2)$ for $(CH_3)_2CHC(O)O_2 + HO_2$. The Kintecus model estimated very low OH yields for $(CH_3)_3CHC(O)O_2 + HO_2$ and $C_2H_5CH(CH_3)C(O)O_2 + HO_2$ between 0.1 and 0.2, these traces can be found in Appendix D.
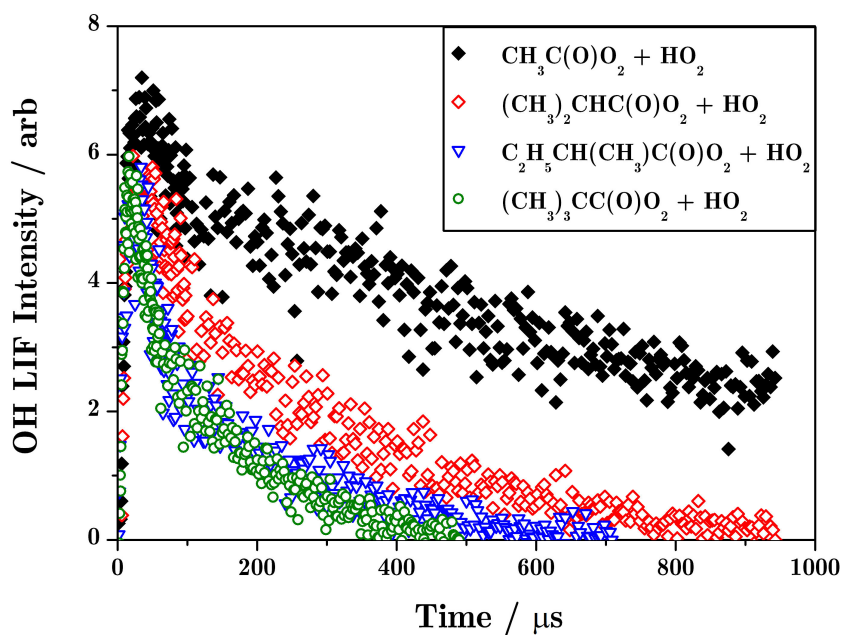
Figure 6.20: Results of $CH_3C(O)O_2$ + $HO_2$ (black diamonds), $(CH_3)_2CHC(O)O_2$ + $HO_2$ (red diamonds), $(CH_3)_3CC(O)O_2$ + $HO_2$ (green circles) and $C_2H_5CH(CH_3)C(O)O_2$ + $HO_2$ (blue triangles) at 100 Torr and 293 K. The conditions were kept similar throughout with [RCHO] = $6.3 \times 10^{14}$, [$Cl_2$] = $1.4 \times 10^{16}$, [Cl] $\approx$ $2 \times 10^{14}$ , [$N_2$] = $5.4 \times 10^{18}$, [$CH_3OH$] = $3.2 \times 10^{15}$ and [$O_2$] = $8.4 \times 10^{17}$.
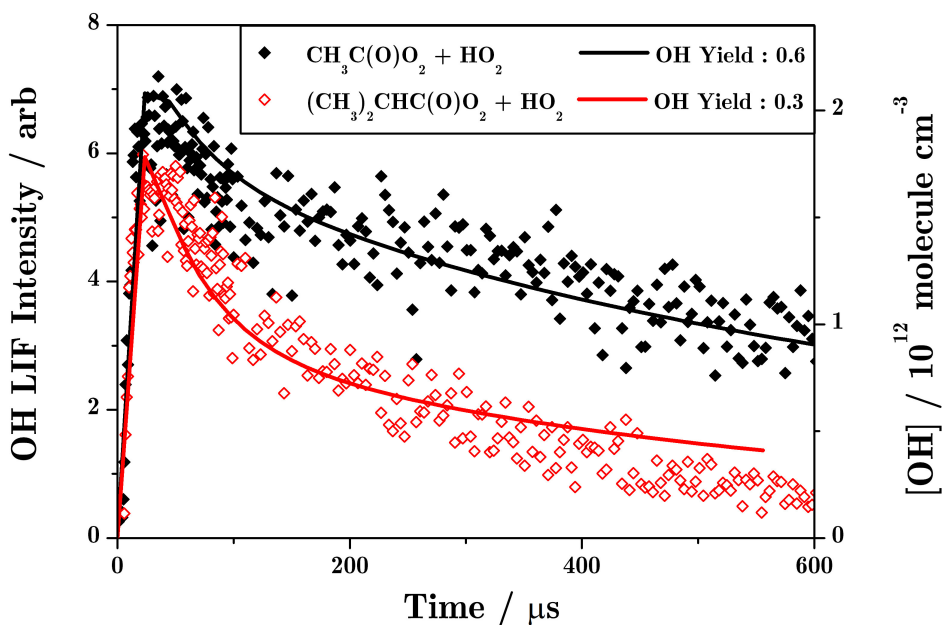


Figure 6.21: Results of $CH_3C(O)O_2$ + $HO_2$ (black diamonds) and $(CH_3)_2CHC(O)O_2$ + $HO_2$ (red diamonds) alongside Kintecus traces, same conditions as Figure 6.20 (Ianni 2017).

## 6.6    Deuterated Hydroperoxyl Radicals

It was possible to study the $RC(O)O_2 + HO_2$ reaction using $DO_2$ instead by including $CD_3OD$ instead of $CH_3OH$. This allowed only the OD formed by the $RC(O)O_2 + DO_2$ reactions to be examined, rather than analysing the OH from the $RC(O)O_2 + HO_2$ reaction which could be complicated by the OH production from $RCO + O_2$ reactions (discussed in Chapter 3). It also allowed the isolation of any secondary OH, such as from $RCO + O_2$ but also the unknown OH production examined in Chapter 5. The concentration of $CD_3OD$ used in experimental runs was very similar to that of $CH_3OH$, meaning back-to-back reactions were carried out and it was possible to compare results from $RC(O)O_2 + HO_2$ and $RC(O)O_2 + DO_2$ reactions.

### 6.6.1    OD LIF Excitation Spectra

To confirm that it is possible to alter the experiment to detect OD instead of OH, LIF Excitation Spectra were carried out, Figures 6.22 and 6.23. Similar conditions were applied to the experiment as used for $RC(O)O_2 + HO_2$ experiments, with the pressure at 100 Torr and the concentrations (in molecule $cm^{-3}$) of: $Cl_2 = 3.8 \times 10^{15}$, $Cl \approx 7 \times 10^{13}$ , $N_2 = 2.9 \times 10^{18}$, $CD_3OD = 1.3 \times 10^{15}$ and $O_2 = 2.9 \times 10^{17}$. The data from Figures 6.22 and 6.23 show that the fluorescence recorded follows the spectra of OD and therefore can confirm that it is possible to switch from detecting OH to OD, and vice versa, by tuning the doubling crystal of the dye laser to a higher frequency.

### 6.6.2    Comparison between OH and OD Production

An interesting comparison is made when analysing results from back-to-back experiments using both $HO_2$ and $DO_2$. Figure 6.24 displays the results from the reaction of: $CH_3C(O)O_2 + HO_2$ when the OH fluorescence is recorded (black
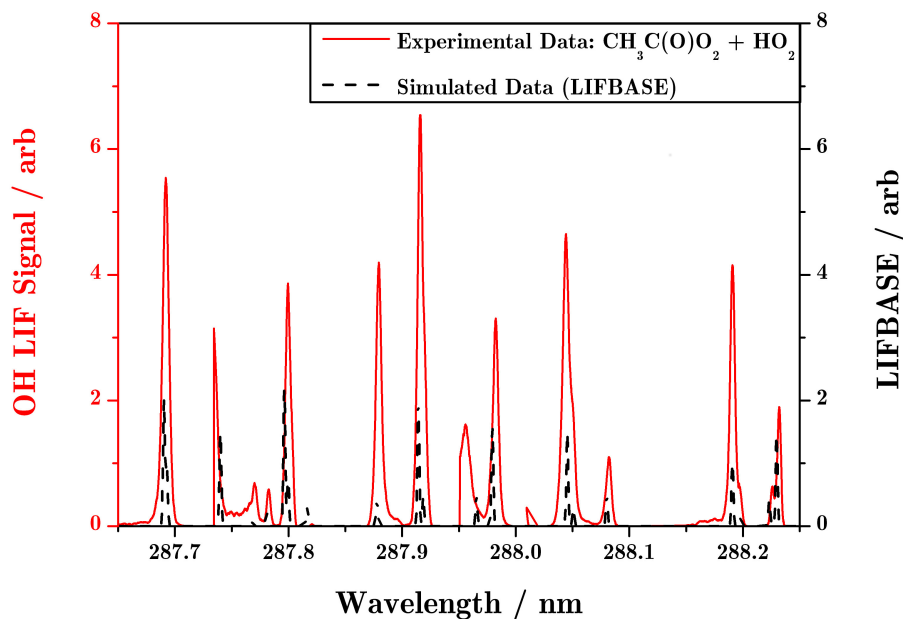
Figure 6.22: LIF OD Excitation Spectra of $CH_3C(O)O_2$ + $DO_2$ at 100 Torr with the concentrations (in molecule $cm^{-3}$): $[CH_3CHO] = 1.6 \times 10^{14}$, $[Cl_2] = 3.8 \times 10^{15}$, $[Cl] \times 7 \times 10^{13}$, $[N_2] = 2.9 \times 10^{18}$, $[CD_3OD] = 1.3 \times 10^{15}$ and $[O_2] = 2.9 \times 10^{17}$. Experimental data in the red line alongside simulated data from Luque and Crosley (1999) in the dotted black line.
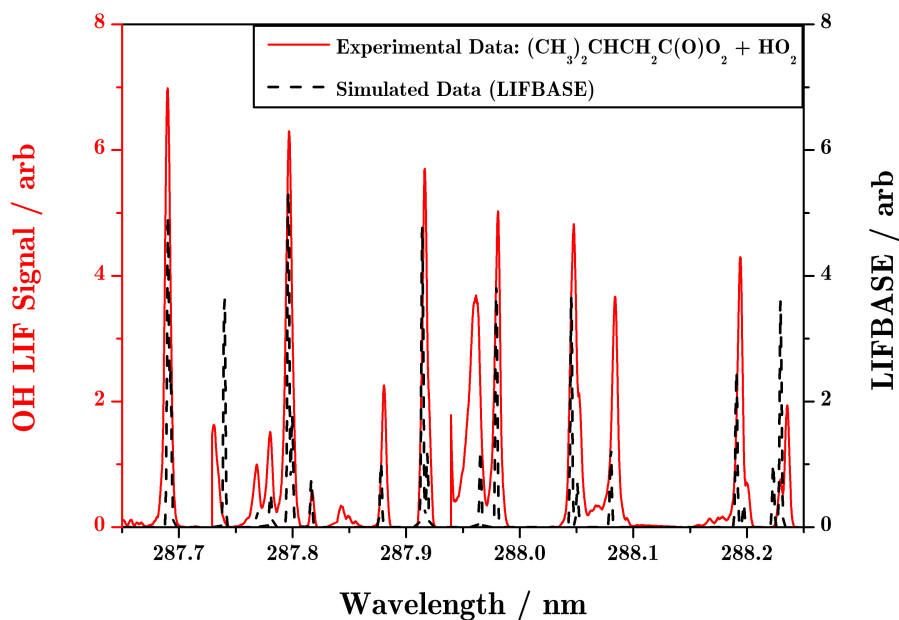


Figure 6.23: LIF OD Excitation Spectra of $(CH_3)_2CHCH_2C(O)O_2$ + $DO_2$ at 100 Torr with the concentrations (in molecule $cm^{-3}$): $[(CH_3)_2CHCH_2CHO] = 8.6 \times 10^{13}$, $[Cl_2] = 3.8 \times 10^{15}$, $[Cl] \times 7 \times 10^{13}$, $[N_2] = 2.9 \times 10^{18}$, $[CD_3OD] = 1.3 \times 10^{15}$ and $[O_2] = 2.9 \times 10^{17}$. Experimental data in the red line alongside simulated data from Luque and Crosley (1999) in the dotted black line.

diamonds); $CH_3C(O)O_2$ + $DO_2$ when the OH fluorescence is recorded (blue circles); $CH_3C(O)O_2$ + $DO_2$ when the OD fluorescence is recorded (red triangles). This allows the distinction between the OH being produced by the fast $RCO$ + $O_2$ (blue circles) and the slower $RC(O)O_2$ + $HO_2$ (red triangles), which is normally hard to distinguish as the OH production from both reactions is combined to produce a kinetic trace (black diamonds).

This analysis was repeated for the $C_2H_5C(O)O_2$ + $HO_2$ / $DO_2$ and $(CH_3)_2CHCH_2$ $C(O)O_2$ + $HO_2$ / $DO_2$ reactions, shown in Figures 6.25 and 6.26. As expected, similar results were recorded for $CH_3C(O)O_2$ + $HO_2$/ $DO_2$ reactions, although there was greater noise in the $C_2H_5C(O)O_2$ + $HO_2$ / $DO_2$ data caused by less OH production.

However, $(CH_3)_2CHCH_2C(O)O_2$ + $HO_2$/ $DO_2$ demonstrate that (Figure 6.26) the red triangles unexpectedly do not follow the decay of the black triangles despite the same decay occurring in the equivalent $(CH_3)_2CHCH_2C(O)O_2$ + $HO_2$/ $DO_2$ reactions. This indicates that there could be an extra OD/OH recycling effect which is not seen in the smaller $RC(O)O_2$ + $HO_2$ reactions but is more prominent in the larger $RC(O)O_2$ + $HO_2$ reaction.

Figure 6.27 displays a comparison between the kinetic traces of $CH_3C(O)O_2$ + $HO_2$, $CH_3C(O)O_2$ + $DO_2$, NO + $HO_2$ and NO + $DO_2$. As the two data sets (OH and OD) were collected at different wavelengths and at different times of the day, they cannot be analysed directly on the same axis. As the NO + $HO_2$ reaction should give the same amount of OH as OD given by NO + $DO_2$ the data from these two traces were overlaid so the difference between $CH_3C(O)O_2$ + $HO_2$ and $CH_3C(O)O_2$ + $DO_2$ could be examined. The data in Figure 6.27 indicates that the $CH_3C(O)O_2$ + $DO_2$ has a higher yield than that of $CH_3C(O)O_2$ + $HO_2$. This agrees with Gross, Dillon, Schuster, et al. (2014) who have given the OD yield of $CH_3C(O)O_2$ + $DO_2$ to be $0.8 \pm 0.14$, compared to $0.61 \pm 0.09$ OH yield of $CH_3C(O)O_2$ + $HO_2$.
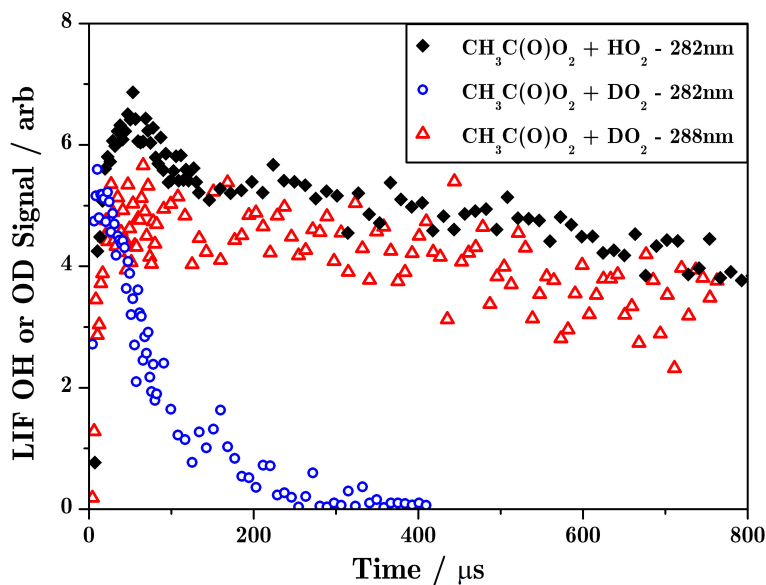
Figure 6.24: A comparison of kinetic traces of $CH_3C(O)O_2 + HO_2$ and $CH_3C(O)O_2$ + $DO_2$ at 100 Torr. The concentrations (in molecule $cm^{-3}$) were: $[CH_3CHO] = 1.6 \times 10^{14}$, $[Cl_2] = 3.8 \times 10^{15}$, $[Cl] \approx 7 \times 10^{13}$ , $[N_2] = 2.9 \times 10^{18}$, $[CD_3OD]$ or $[CH_3OH] = 1.0 \times 10^{15}$ and $[O_2] = 2.9 \times 10^{17}$.
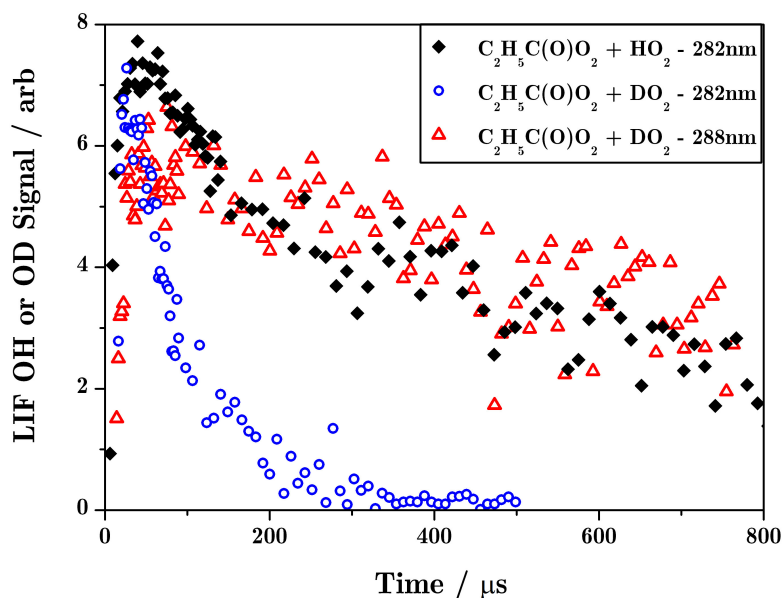


Figure 6.25: A comparison of kinetic traces of $C_2H_5C(O)O_2 + HO_2$ and $C_2H_5C(O)O_2$ + $DO_2$ at 100 Torr. The concentrations (in molecule $cm^{-3}$) were: $[C_2H_5CHO] = 1.2 \times 10^{14}$, $[Cl_2] = 3.8 \times 10^{15}$, $[Cl] \approx 7 \times 10^{13}$ , $[N_2] = 2.9 \times 10^{18}$, $[CD_3OD]$ or $[CH_3OH] = 1.0 \times 10^{15}$ and $[O_2] = 2.9 \times 10^{17}$.
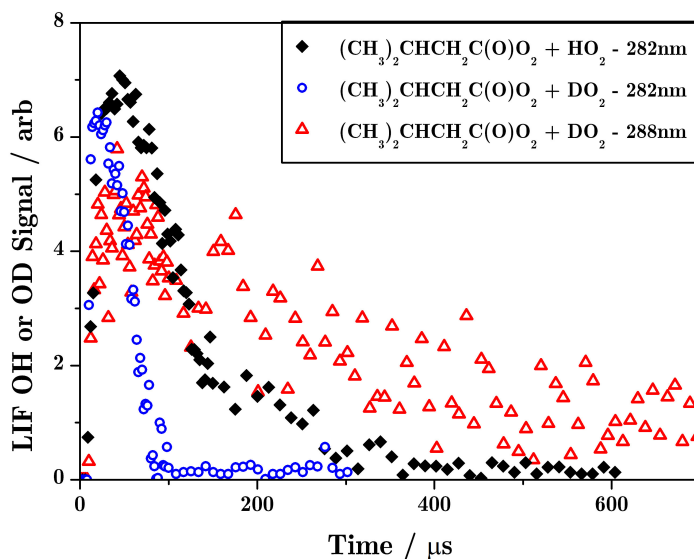
Figure 6.26: A comparison of kinetic traces of $(CH_3)_2CHCH_2C(O)O_2 + HO_2$ and $(CH_3)_2CHCH_2C(O)O_2 + DO_2$ at 100 Torr. The concentrations (in molecule cm$^{-3}$) were:$[(CH_3)_2CHCH_2CHO] = 8.6 \times 10^{13}$, $[Cl_2] = 3.8 \times 10^{15}$, $[Cl] \approx 7 \times 10^{13}$ , $[N_2]$ $= 2.9 \times 10^{18}$, $[CD_3OD]$ or $[CH_3OH] = 1.0 \times 10^{15}$ and $[O_2] = 2.9 \times 10^{17}$.
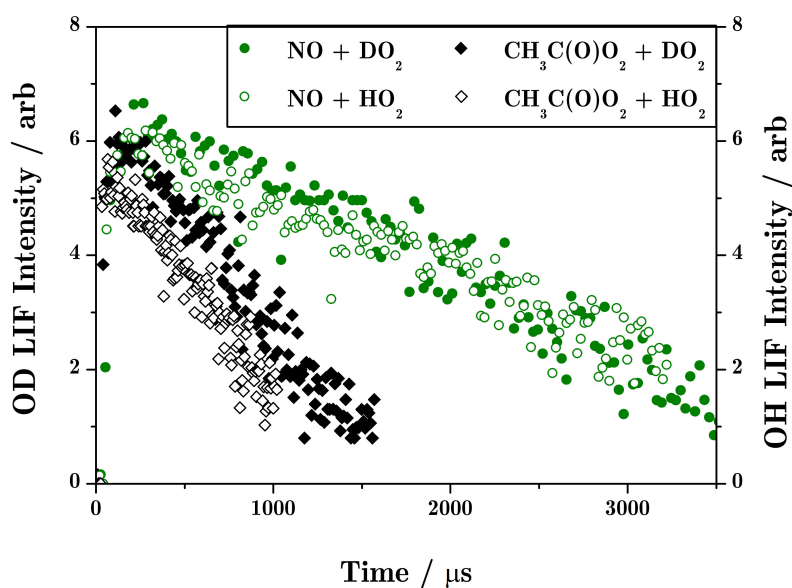


Figure 6.27: A comparison of kinetic traces of $CH_3C(O)O_2 + HO_2$ (filled black diamonds), $CH_3C(O)O_2 + DO_2$ (empty black diamonds), $NO + HO_2$ (filled green circles) and $NO + DO_2$ (empty green circles) at 100 Torr. The concentrations (in molecule cm$^{-3}$) were: $[CH_3CHO] = 3 \times 10^{14}$, $[NO] = 2 \times 10^{13}$, $[Cl_2] = 5 \times 10^{15}$, $[Cl] \approx 6 \times 10^{13}$ , $[N_2] = 3.1 \times 10^{18}$, $[CD_3OD]$ or $[CH_3OH] = 1.0 \times 10^{15}$ and $[O_2] = 2.9 \times 10^{17}$.

### 6.6.3 Temperature Effect
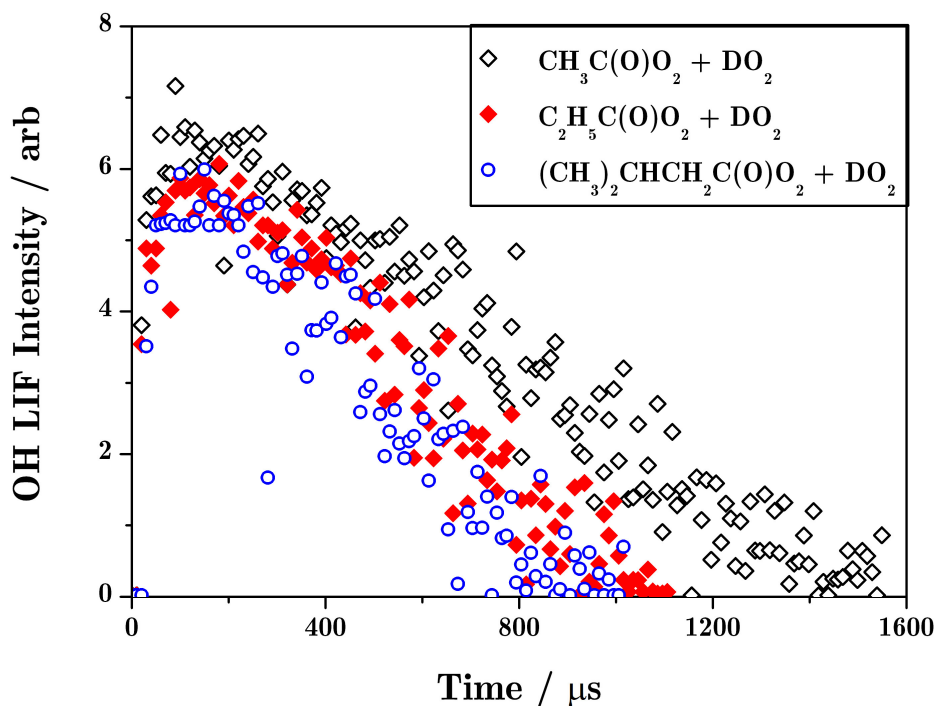


Figure 6.28: Data from the experimental runs of $CH_3C(O)O_2$ + $DO_2$ (black diamonds), $C_2H_5C(O)O_2$ + $DO_2$ (red diamonds) and $(CH_3)_2CHCH_2C(O)O_2$ + $DO_2$ (blue circles) at 100 Torr and 360 K. The concentrations (in molecule $cm^{-3}$) were:[RCHO] = $7 \times 10^{14}$, $[Cl_2]$ = $4 \times 10^{15}$, [Cl] $\approx 6 \times 10^{13}$ , $[N_2]$ = $2 \times 10^{18}$, $[CD_3OD]$ = $2.0 \times 10^{15}$ and $[O_2]$ = $2.1 \times 10^{17}$.

Similar to the $RC(O)O_2$ + $HO_2$, the preliminary experiments were carried out at higher temperature on the $RC(O)O_2$ + $DO_2$ reactions. Figure 6.28 displays the data from experimental runs of $CH_3C(O)O_2$ + $DO_2$, $C_2H_5C(O)O_2$ + $DO_2$, and $(CH_3)_2CHCH_2C(O)O_2$ + $DO_2$ at 100 Torr with a temperature of 360 K. Comparing the difference from room temperature results to 360 K, the yield of $(CH_3)_2CHCH_2$ $C(O)O_2$ + $DO_2$ increased so it was similar to the OD yields of the other two reactions.

This is the trend that was also seen in previous results of this work in the $RC(O)O_2$ + $HO_2$ reactions: compounds which have a larger OH yield in the $RC(O)O_2$ + $HO_2$ at room temperature decrease at higher temperature; whereas compounds which have

small OH yields at room temperature increase with increasing temperature. This trend is due solely to the $RC(O)O_2 + HO_2$ with the $RC(O)O_2 + DO_2$ reactions proving that the observed trend is not due to the $RCO + O_2$ reaction (Chapter 3) or the unknown secondary OH producing reaction (Chapter 5).

## 6.7   Summary

This chapter has shown that OH production from $RC(O)O_2 + HO_2$ is universal in the six $RC(O)O_2 + HO_2$ reactions studied here. OH has been analysed for the first time from the reactions of $C_2H_5C(O)O_2 + HO_2$ and $(CH_3)_2CHCH_2C(O)O_2 + HO_2$. Figure 6.20 also displays the first preliminary experiments on $(CH_3)_2CHC(O)O_2 + HO_2$, $(CH_3)_3CC(O)O_2 + HO_2$, and $C_2H_5CH(CH_3)C(O)O_2 + HO_2$, showing OH production from these reactions. Preliminary temperature experiments indicate that the OH yield for these reactions alter with the change in temperature. The smaller compounds which have a higher OH yield at room temperature $(0.5 - 0.7)$ decrease as the temperature increases. Contrasting with the larger compounds which have a low OH yield at room temperature $(0.1 - 0.3)$ increasing with a temperature rise. This trend is also seen for the reactions of $RC(O)O_2 + DO_2$, where it is possible to distinguish between the OH formed by the $RCO + O_2$ reactions and other $RC(O)O_2 + HO_2$ reactions.

# Bibliography

Atkinson (1997). "Atmospheric reactions of alkoxy and -hydroxyalkoxy radicals".
In: *International Journal of Chemical Kinetics* 29, pp. 99–111.

Atkinson, Baulch, Cox, Crowley, Hampson, Hynes, Jenkin, Kerr, et al. (2007).
*IUPAC Subcommittee for Gas Kinetic Data Evaluation*. URL: www.iupac-kinetic.
ch.cam.ac.uk.

Atkinson, Baulch, Cox, Hampson, et al. (1989). "Evaluated kinetic and photochemical
data for atmospheric chemistry : Volume III". In: *Journal of Physical and Chemical
Reference Data* 18.2, pp. 881–1097.

Atkinson et al. (2004). "Evaluated kinetic and photochemical data for atmospheric
chemistry: Part 1 - gas phase reactions of $O_x$, $HO_x$, $NO_x$ and $SO_x$ species". In:
*Atmospheric Chemistry and Physics Discussions* 3.6, pp. 6179–6699.

— (2006). "Evaluated kinetic and photochemical data for atmospheric chemistry:
Volume II; gas phase reactions of organic species". In: *Atmospheric Chemistry
and Physics* 6.11, pp. 3625–4055.

Crawford et al. (1999). "Kinetics and mechanism of the acetylperoxy plus $HO_2$
reaction". In: *Journal of Physical Chemistry A* 103.3, pp. 365–378.

Demore et al. (1997). *Chemical Kinetics and Photochemical Data for Use in Stratospheric
Modeling Evaluation Number 12 NASA Panel for Data Evaluation*. Tech. rep.

Dillon and Crowley (2008). "Direct detection of OH formation in the reactions of
$HO_2$ with $CH_3C(O)O_2$ and other substituted peroxy radicals". In: *Atmospheric
Chemistry and Physics* 8.16, pp. 4877–4889.

Eskola et al. (2008). "Rate constants and hydrogen isotope substitution effects in the $CH_3$ + HCl and $CH_3$ + $Cl_2$ reactions". In: *Journal of Physical Chemistry A* 112.32, pp. 7391–7401.

Gross, Dillon, and Crowley (2014). "Pressure dependent OH yields in the reactions of $CH_3CO$ and $HOCH_2CO$ with $O_2$." In: *Physical Chemistry Chemical Physics* 16.22, pp. 10990–10998.

Gross, Dillon, Schuster, et al. (2014). "Direct kinetic study of OH and $O_3$ formation in the reaction of $CH_3C(O)O_2$ with $HO_2$." In: *The Journal of Physical Chemistry. A* 118.6, pp. 974–85.

Hasson, Tyndall, and Orlando (2004). "A product yield study of the reaction of $HO_2$ radicals with ethyl peroxy ($C_2H_5O_2$), acetyl peroxy ($CH_3C(O)O_2$), and acetonyl peroxy ($CH_3C(O)CH_2O_2$) radicals". In: *Journal of Physical Chemistry A* 108.28, pp. 5979–5989.

Horie and Moortgat (1992). "Reactions of $CH_3C(O)O_2$ radicals with $CH_3O_2$ and $HO_2$ between 263 and 333 K. A product study". In: *Journal of the Chemical Society, Faraday Transactions* 88.22, pp. 3305–3312.

Ianni, James C (2017). *Kintecus*. URL: www.kintecus.com.

Jenkin, Hurley, and Wallington (2007). "Investigation of the radical product channel of the $CH_3C(O)O_2$ + $HO_2$ reaction in the gas phase". In: *Physical Chemistry Chemical Physics*, pp. 3149–3162.

LeCrâne et al. (2006). "A reinvestigation of the kinetics and the mechanism of the $CH_3C(O)O_2$ + $HO_2$ reaction using both experimental and theoretical approaches." In: *Physical Chemistry Chemical Physics* 8.18, pp. 2163–2171.

Luque and Crosley (1999). "LIFBASE: Database and Spectral Simulation Program (Version 1.5), SRI International Report MP 99-009". In:

Moortgat, Veyret, and Lesclaux (1989). "Kinetics of the reaction of $HO_2$ with $CH_3C(O)O_2$ in the temperature range 253-368 K". In: *Chemical Physics Letters* 160.4, pp. 443–447.

Morajkar et al. (2014). "Direct measurement of the equilibrium constants of the reaction of formaldehyde and acetaldehyde with HO2 radicals". In: *International Journal of Chemical Kinetics.*

Niki et al. (1985). "FTIR study of the Kinetics and Mechanism for Chlorine Atom Initiated Reactions of Acetaldehyde". In: *Journal of Physical Chemistry* 6, pp. 588–591.

Thornton et al. (2002). "Ozone production rates as a function of $NO_x$ abundances and $HO_x$ production rates in the Nashville urban plume". In: *Journal of Geophysical Research* 107.D12, pp. 1–17.

Tomas, Villenave, and Lesclaux (2001). "Reactions of the Hydroperoxyl Radical with Acetaldehyde and Acetylperoxy Radical in the Gas Phase". In: *J. Phys. Chem. A* 105.14, pp. 3505–3514.

Tyndall et al. (1999). "Rate Coefficients for the Reactions of Chlorine Atoms with Methanol and Acetaldehyde". In: *International Journal of Chemical Kinetics* 31.11, pp. 776–784.

Veyret, Rayez, and Lesclaux (1982). "Mechanism of the photooxidation of formaldehyde studied by flash photolysis of formaldehyde oxygen nitric oxide mixtures". In: *Journal of Physical Chemistry* 86.17, pp. 3424–3430.

Winiberg et al. (2016). "Direct measurements of OH and other product yields from the $HO_2 + CH_3C(O)O_2$ reaction". In: *Atmospheric Chemistry and Physics* 2.2, pp. 4023–4042.

# Chapter 7

# Concluding Remarks

## 7.1  Concluding Remarks and Implications

The first chapter of this thesis discussed the importance of peroxy radicals ($RO_2$) in both the atmosphere and in biofuels. Recently the production of OH from the formation of $CH_3C(O)O_2$, when $CH_3CO$ reacts with $O_2$, has increased the interest and importance of the RCO + $O_2$ reactions. Especially the importance in biofuel oxidation studies in the lab.

The new PLP-LIF system that was set up in this project, Chapter 2, was able to detect OH from RCO + $O_2$ reactions. This enabled a study of RCO + $O_2$ reactions to be carried out, Chapter 3. The results from this study demonstrated that OH is a general feature of RCO + $O_2$ reactions, when R = alkyl chain. The first set of experiments focused on clarifying a literature discrepancy between Romero et al. (2005) and Zügner et al. (2010) for the OH yield of $C_2H_5CO$ + $O_2$. The results from these studies agreed with the values from Zügner et al. (2010), who suggested that the source of $C_2H_5CO$ in study by Romero et al. (2005) produced very 'hot' radicals from the direct photolysis of 3-pentanone which caused the OH yield to be over estimated significantly.

The study investigated how the OH yield changed due to the length and shape of the carbon chain. Pressure-dependent (13 to 120 Torr of $N_2$) OH yields were determined for the first time for R = $CH_3CH_2CH_2$, $(CH_3)_2CH$, $(CH_3)_3C$, $CH_3CH_2CH_2CH_2$, $(CH_3)_2CHCH_2$, and $CH_3CH_2CH(CH_3)$. The OH yield was observed to decrease with increasing chain length and to display a complex dependency on the degree of branching within the R group. The studies on different branched RCO gave rise to the conclusion that the OH yield is dependent on two properties: the energy of the transition state and the carbon-hydrogen bond strength. To illustrate how the C-H bond affected the OH yield, the formation of the 6-remembered immediate was key. In the formation of the intermediate if a primary hydrogen is attacked rather than a secondary or tertiary, the OH yield is higher. The lowest yield came from the attack of a tertiary hydrogen. It is the combination of both effects that controls the OH yield in the RCO + $O_2$ reaction.

The other peroxy radical reaction shown to been of importance in Chapter 1, was the reaction of $RC(O)O_2$ + $HO_2$. Previous literature had only shown the reaction where R = $CH_3$ to have a OH yield of 0.5 - 0.6 (Gross et al. 2014; Winiberg et al. 2016; Dillon and Crowley 2008). The OH yield is much higher for the $CH_3C(O)O_2$ + $HO_2$ than the $CH_3CO$ + $O_2$ and has a larger impact on atmospheric chemistry - see Chapter 1. The work which was carried out in this project has shown that OH production from $RC(O)O_2$ + $HO_2$ is universal in all $RC(O)O_2$ + $HO_2$ reactions. This is important as this causes termination reactions to be slower for a whole class or $RO_2$. OH has been analysed for the first time from the reactions of $C_2H_5C(O)O_2$ + $HO_2$ and $(CH_3)_2CHCH_2C(O)O_2$ + $HO_2$, with OH observed for the first time from the reactions of $(CH_3)_2CHC(O)O_2$ + $HO_2$, $(CH_3)_3CC(O)O_2$ + $HO_2$ and $C_2H_5CH(CH_3)C(O)O_2$ + $HO_2$.

When the analysis of the results from Chapters 3 (RCO + $O_2$) and 6 ($RC(O)O_2$ + $HO_2$) was carried out, Kintecus models were created. For the smaller compounds all the rate coefficients were known, but unfortunately there were some unknown ones for the larger compounds. Chapter 4 discussed the results from the investigation

into the OH and Cl rate coefficients of aldehydes. For the first time the apparatus used its ability to detect OH, as a spectroscopic marker, for the determination of Cl rate coefficients. Though this is a very indirect measurement the rate coefficients recorded agreed well with previous literature, giving confidence in these results. This project was able to calculate two new room-temperature Cl rate coefficients: $C_2H_5CH(CH_3)CHO$ + Cl $(1.2 \pm 0.3) \times 10^{-10}$ $cm^3$ molecule$^{-1}$ s$^{-1}$, and $(CH_3)_2CHCH_2CHO$ + Cl $(3.1 \pm 0.6) \times 10^{-10}$ $cm^3$ molecule$^{-1}$ s$^{-1}$. The photolysis of $NO_2$ at 355 nm was used as the source of OH for the investigation of OH + RCHO rate coefficients. The results from these studies show good agreement with previous studies for example the rate coefficient for OH + $CH_3CHO$ + OH from this study was $(1.8 \pm 0.3) \times 10^{-11}$ $cm^3$ molecule$^{-1}$ s$^{-1}$ which is in good agreement to the value of $(1.5 \pm 0.2) \times 10^{-11}$ $cm^3$ molecule$^{-1}$ s$^{-1}$ from the review by Atkinson et al. (2007).

The investigation into the rate coefficients was not the only area which had to be examined further when the project focused on the $RC(O)O_2$ + $HO_2$ reactions rather than $RCO + O_2$. Chapter 5 presented data of a brand new source of OH; there have been no previous literature studies indicating that this was a possibility.

This new OH source was noticed first when higher radical concentrations were used in the preliminary experiments of $RC(O)O_2$ + $HO_2$. The chapter showed the evidence that this OH formation is substantial and occurred at various different pressures and temperatures as well as using different precursors. The results also suggested that this secondary OH reaction is controlled by the amount of radicals in the system, therefore a possibility of the source is from a self reaction with $RC(O)O_2$ + $RC(O)O_2$.

These reactions have importance in biofuels, as mentioned previously, therefore it is crucial to examine the effect temperature has on them. The OH yield for the $RC(O)O_2$ + $HO_2$ reactions was examined at different temperatures where preliminary experiments indicated that the OH yield does alter with the change in temperature. The smaller compounds (e.g. $CH_3C(O)O_2$) which have a higher OH yield at room

temperature (0.5 – 0.7) decreased as the temperature increases. Whereas the larger compounds (e.g. $(CH_3)_2CHCH_2C(O)O_2$) which have a low OH yield at room temperature (0.1 – 0.3) increase with a temperature rise. This trend is also seen for the reactions of $RC(O)O_2 + DO_2$, where it is possible to distinguish between the OH formed by the $RCO + O_2$ reactions and other $RC(O)O_2 + HO_2$ reactions. This indicated that the OH yield for the $RCO + O_2$ reactions increases for all compounds as the temperature increases.

## 7.2 Future Work

The reactions of $RCO + O_2$ clearly show the production of OH. However, the reasons why the yield changes so much with the different types of branching is not fully understood. To ascertain why these differences are seen, quantum chemistry calculations should be carried out to determine the mechanism of the larger RCO compounds with $O_2$. Future work should also examine the temperature effect on the $RCO + O_2$ reactions; since the results from this thesis have shown that the OH yield from $RCO + O_2$ dominates over the $RC(O_2)O + HO_2$. Therefore it is vital that future work is carried out to quantify the OH yield of $RCO + O_2$ at higher temperatures which will allow the temperature effect on the $RC(O)O_2 + HO_2$ to be analysed more accurately, which is where it is more relevant for combustion chemistry.

For the rate coefficients, future studies should examine higher temperatures which would allow a well constrained Arrenhius relationship to be determined. This is not only important for combustion chemistry, but as higher concentrations of Cl has been observed over continental cities it is important to understand their temperature dependency. Especially since, previously, this class of Cl coefficients were unknown to have a temperature dependence.

# Bibliography

Atkinson et al. (2007). "Evaluated kinetic and photochemical data for atmospheric chemistry : Volume III – gas phase reactions of inorganic halogens". In: *Atmospheric Chemistry and Physics* 7, pp. 981–1191.

Dillon and Crowley (2008). "Direct detection of OH formation in the reactions of $HO_2$ with $CH_3C(O)O_2$ and other substituted peroxy radicals". In: *Atmospheric Chemistry and Physics* 8.16, pp. 4877–4889.

Gross et al. (2014). "Direct kinetic study of OH and $O_3$ formation in the reaction of $CH_3C(O)O_2$ with $HO_2$." In: *The Journal of Physical Chemistry. A* 118.6, pp. 974–85.

Romero et al. (2005). "OH formation from the $C_2H_5CO + O_2$ reaction: An experimental marker for the propionyl radical". In: *Chemical Physics Letters* 408.4-6, pp. 232–236.

Winiberg et al. (2016). "Direct measurements of OH and other product yields from the $HO_2 + CH_3C(O)O_2$ reaction". In: *Atmospheric Chemistry and Physics* 2.2, pp. 4023–4042.

Zügner et al. (2010). "OH yields for $C_2H_5CO + O_2$ at low pressure: Experiment and theory". In: *Chemical Physics Letters* 495.4-6, pp. 179–181.

# Abbreviations

| | |
|---|---|
| **CCD** | Charge coupled device |
| **DF-RF** | Discharge Flow Resonance |
| **FT-IR** | Fourier Transform Infrared Spectroscopy |
| **GC** | Gas Chromatography |
| **HO$_2$** | Hydroperoxy Radical |
| **HPLC** | High performance liquid chromatography |
| **IUPAC** | International Union of Pure and Applied Chemistry |
| **KDP** | Potassium Dihydrogen Phosphate |
| **LIF** | Laser Induced Fluorescence |
| **LTC** | Low Temperature Combustion |
| **MFC** | Mass Flow Controller |
| **MS** | Mass Spectrometry |
| **NO$_x$** | Nitrogen Oxides |
| **OH** | Hydroxyl Radical |
| **PLP** | Pulsed Laser Photolysis |
| **PMT** | Photomultipler Tube |
| **pptv** | parts per trillion |
| **RO$_2$** | Peroxy Radicals |
| **SAR** | Structure Activity Relationship |
| **sccm** | Standard Cubic Centimetre (s) per minute |
| **VOC** | Volatile Organic Compounds |
| **YAG** | Yttrium aluminium garnet |